A Low Cost Direct Writing Process for Flexible Circuit and Interconnect Fabrication

David Ewan Gray Watson

Submitted for the degree of Doctor of Philosophy

Heriot-Watt University

School of Engineering and Physical Sciences

Institute of Sensors, Signals and Systems

October 2014

Abstract

This thesis investigates the development of a low cost fabrication process for flexible electronics and interconnects. By using a ‘direct writing’ process, the use of vacuum-based metal evaporation and photoresist steps is not necessary and so less complex equipment is needed.

The process forms silver embedded on top of a polyimide substrate and was first tested using a UV laser to perform writing before switching to a blue laser due to excessive substrate degradation observed from UV exposures. The blue light was combined with a biologically friendly photo reducing agent, which was found to be much more efficient at the creation of silver. The methods of silver formation by various means are the main focus of investigation in this thesis but process expansion and improvement were the main goals. To this end, a chemical, rather than light-based, process for silver creation was found to produce more consistent silver coatings, however the patterning by this method was found to be more challenging. The process was also extended to a different substrate in polyetherimide.

Dedication

To all the cohorts of my family. And all my friends too, why not?

Acknowledgements

I would like to thank my supervisor Professor Marc Desmulliez for giving me the opportunity to carry out this work, for his patience and for his assistance and guidance for the last what seems like eternity. I would also like to thank my examiners, Professor Andrew Holmes and Doctor Resh Dhariwal for taking the time to scrutinise this work.

I would also like to thank all who work and have worked within the Microsystems Engineering Centre and all those from elsewhere in the University that I've come into contact with. As well as getting lots of useful advice and having many helpful discussions, it has also been fun and generally a great place to be and I am thankful for all the friendships I've made, although there are perhaps too many to name here. I would however like to thank Jack Ng for his previous work on the subject, which helped focus my research, and Yves Lacrotte for his bonhomie. Thanks too to Lorna Johnston for her support and infinite patience while this work was being finished. I'd also like to give a special thanks to Mark Leonard for always being able to provide solutions to problems and get things done. His help has been invaluable.

Finally I'd like to thank the Engineering and Physical Sciences Research Council for funding my work.

HERIOT WATT UNIVERSITY

ACADEMIC REGISTRY
Research Thesis Submission

Name*:*	David Ewan Gray Watson		
School/PGI:	EPS / ISSS		
Version: *(i.e. First, Resubmission, Final)*	Final	Degree Sought (Award **and** Subject area)	PhD Electrical Engineering

Declaration

In accordance with the appropriate regulations I hereby submit my thesis and I declare that:

1) the thesis embodies the results of my own work and has been composed by myself
2) where appropriate, I have made acknowledgement of the work of others and have made reference to work carried out in collaboration with other persons
3) the thesis is the correct version of the thesis for submission and is the same version as any electronic versions submitted*.
4) my thesis for the award referred to, deposited in the Heriot-Watt University Library, should be made available for loan or photocopying and be available via the Institutional Repository, subject to such conditions as the Librarian may require
5) I understand that as a student of the University I am required to abide by the Regulations of the University and to conform to its discipline.

* *Please note that it is the responsibility of the candidate to ensure that the correct version of the thesis is submitted.*

Signature of Candidate*:*		Date:	27.01.2015

Submission

Submitted By *(name in capitals):*	DAVID WATSON
Signature of Individual Submitting:	
Date Submitted:	

For Completion in the Student Service Centre (SSC)

Received in the SSC by *(name in capitals):*			
Method of Submission *(Handed in to SSC; posted through internal/external mail):*			
E-thesis Submitted (**mandatory for final theses)**			
Signature:		Date:	

Contents

Chapter 1

Chapter 2

Chapter 5

Chapter 6

Chapter 7

List of Figures

Chapter 1

Chapter 2

Chapter 3

Chapter 4

Chapter 5

Chapter 6

Chapter 7

List of Tables

Chapter 1

Chapter 2

Chapter 3

Chapter 4

Chapter 5

Chapter 6

Chapter 7

List of Abbreviations

ABS	Acrylonitrile Butadiene Styrene
AFA-LIFT	Absorbing Film Assisted LIFT
$AgNO_3$	Silver nitrate
ATR-FTIR	Attenuated Total Reflection Fourier Transform Infrared spectroscopy
ATRP	Atom Transfer Radical Polymerisation
BA-LIFT	Blister Actuated LIFT
CIJ	Continuous Inkjet
CTE	Coefficient of Thermal Expansion
CVD	Chemical Vapour Deposition
CW	Continuous Wave
DI	Deionised Water
DMAB	Dimethylamino-Borane complex
DOD	Drop on Demand
DRL	Dynamic Release Layer
FET	Field Effect Transistor
FTIR	Fourier Transform InfraRed spectroscopy
HAZ	Heat Affected Zone
IOP	Institute of Physics
IPA	Isopropanol
IPMC	Ionic Polymer Metal Composites
ITO	Indium Tin Oxide
KOH	Potassium Hydroxide
LbL	Layer-by-Layer
LCLD	Laser-induced Chemical Liquid Deposition
LCVD	Laser Chemical Vapour Deposition
LDW	Laser Direct Writing
LEEP	Laser Enhanced Electroless Plating
LIBT	Laser Induced Backwards Transfer
LIFT	Laser Induced Forward Transfer
LSPR	Localised Surface Plasmon Resonance
LTCC	Low Temperature Co-fired Ceramic
MACP	Matrix Assisted Catalytic Printing
MAPLE-DW	Matrix Assisted Pulse Laser Evaporation-Direct Write
MCP	Micro Contact Printing
MISEC	MIcroSystems Engineering Centre
MPEG	Methyoxy Polyethylene Glycol
NaOH	Sodium Hydroxide
NMP	N-Methylpyrrolidone
NP	Nanoparticle
OLED	Organic Light Emitting Diode
OTFT	Organic Thin Film Transistor
PAA	Poly(amic acid)
PAA2	Poly(acrylic acid)
PCB	Printed Circuit Board
PDMS	Polydimethylsiloxane
PEG	Polyethylene Glycol
PEN	Polyethylene Naphthalate
PFN	Polyfluorene
PI	polyimide
PEDOT-PSS	Poly(3,4-ethylenedioxythiophene) Polystyrene Sulfonate
PEI	Polyetherimide
PET	Polyethylene Terephthalate
PMDA-ODA	Pyromellitic dianhydride-oxydianiline
PMETAC	Poly[2-(methacryloyloxy)ethyltrimethylammonium chloride]
PMMA	Poly(methyl methacrylate)
PTFE	Polytetrafluoroethylene
PV	Photovoltaic
PVA	Poly(vinyl alcohol)
PVD	Physical Vapour Deposition
PVK	Poly(N-vinyl carbazole)
PVP	Polyvinylpyrrolidone
R2R	Roll to Roll
RFID	Radio Frequency IDentification
RIE	Reactive Ion Etching
SPEEK	Sulfonated Poly(ether-ether)ketone
TFT	Thin Film Transistor
TP	Triazene Polymer
ULSI	Ultra-large-scale integrated circuit

List of Publications by the Candidate

Journal

D.E. Watson, J.H.-G. Ng, K.E. Aasmundtveit, M.P.Y. Desmulliez,
"In-Situ Silver Nanoparticle Formation on Surface-Modified Polyetherimide Films,"
IEEE Transactions on Nanotechnology, vol.13, no.4, pp. 736–742, July 1 2014

J. H.-G. Ng, D. E. G. Watson, J. Sigwarth, A. McCarthy, K. A. Prior, D. P. Hand, W. Yu, R. W. Kay, C. Liu, and M. P. Y. Desmulliez,
"On the Use of Silver Nanoparticles for Direct Micropatterning on Polyimide Substrates,"
IEEE Transactions on Nanotechnology, vol. 11, no. 1, pp. 139–147, 2012.

Conference

D. E. Watson, J. H.-G. Ng, and M. P. Y. Desmulliez,
"Additive photolithography based process for metal patterning using chemical reduction on surface modified polyimide,"
18th European Microelectronics and Packaging Conference (EMPC), 2011, Brighton, UK, 2011, pp. 1–7.

D. E. Watson, J. H.-G. Ng, J. Sigwarth, J. Bates, and M. P. Y. Desmulliez,
"Silver nanocluster formation using UV radiation for direct metal patterning on polyimide,"
3rd Electronic System-Integration Technology Conference (ESTC), 2010, Berlin, Germany, 2010, pp. 1–4.

J. H.-G. Ng, D. E. G. Watson, J. Sigwarth, A. McCarthy, H. Suyal, D. P. Hand, T. Y. Hin, and M. Desmulliez,
"An additive method for photopatterning of metals on flexible substrates,"
36th International MATADOR Conference, Manchester, UK, 2010, pp. 389–392.

Patent

J. H.-G. Ng, M. P. Y. Desmulliez, and D. E. G. Watson,
"Additive metallisation process,"
U.S. Patent PCT/GB2012/000116

Chapter 1 – Introduction

1.1 Introduction to plastic electronics and applications

Electronic systems have been part of our life for many years now, yet thanks to technological advances our interactions with such devices are only set to increase as they become more pervasive and central to everyday life. Plastic and flexible electronics have long been seen as an alternative way to fabricate devices from the more traditional silicon-based processes, particularly since the first organic thin film transistor (OTFT) was demonstrated [1]. The most compelling reason for this is one of production cost. Plastics are cheaper to process as they do not rely on expensive patterning techniques that require a vacuum environment or high pressure and temperature conditions. As such, plastics are more amenable to large-scale production than silicon-based fabrication routes for reasons of both machine size and ease of automated substrate transfer between process steps, roll-to-roll (R2R) processing being a prime example of this. Although plastic electronics cannot compete with inorganic devices in terms of minimum feature size, a number of areas and applications exist where circuit components and devices can replace them or reduce fabrication complexity. These include printed circuit board (PCB) interconnects, moulded interconnect device (MID) fabrication, multichip module packaging and various space applications [2, 3], not to mention more recent, and rapidly expanding, markets such as flexible displays and organic light emitting diodes (OLED), radio frequency identification (RFID), e-paper and chemical or biological sensors based on organic field effect transistor (FET) technology.

Having seen that plastic electronics are capable of contributing to a wide range of applications, it is worth finding out in slightly more detail just how big their potential impact is. Combining this information with a look at a few of the production methods will reveal the motivation behind this project. This is discussed in the following section.

1.2 Motivation for the work

The numerous wide-ranging applications of plastic electronics imply that there must be some level of commercial exploitation through organisations with processing plants. Indeed, a report from the Institute of Physics (IOP) commissioned by the UK Government in 2008 highlights the role that plastic electronics can play in the key challenges over the coming decades, as well as providing numerous job opportunities [4].

More recently, market research from consultancy agency IDTechEx shows rapid growth in the plastic and printed electronics market [5]. This is highlighted in Figure 1.1 below, however this forecast also includes printed electronics on non-flexible substrates such as silicon and glass. Nevertheless it does indicate the growth potential and displays the market share of non-rigid substrates increasing from 6% to 33% over the period.

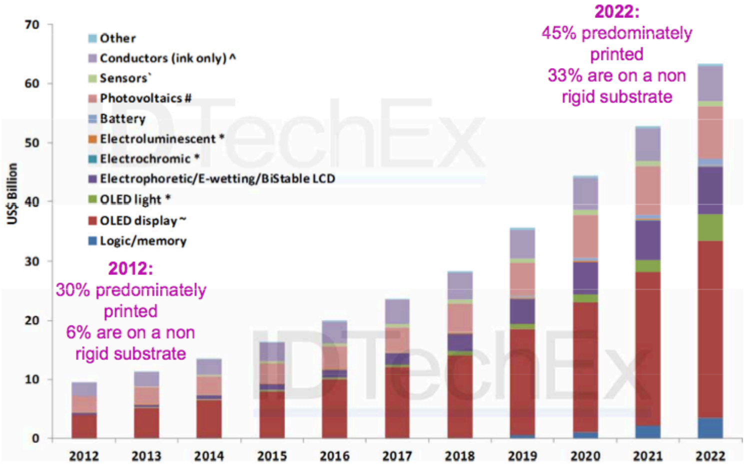

Figure 1.1: *Ten year forecast for plastic electronics (© IDTechEx 2012).*

It is clear that the development and exploitation of a robust fabrication process that can challenge current production methods could prove very profitable, not only economically but also in terms of job creation and furthering common knowledge. It must then be decided which production route to focus on.

Large amounts of research, evaluated in the following chapter, have been carried out to find and develop the myriad of fabrication routes of flexible substrate electronics. The motivation of this thesis is to further understand and improve additive metallisation of polyimide substrates. Such substrates exhibit excellent mechanical and thermal properties, making them suitable for many applications. However, more 'traditional' circuit fabrication techniques rely on expensive equipment such as vacuum chambers, so a more cost effective solution is desirable.

Each technique has its own relative merits and drawbacks when it comes to the key parameters of feature size, cost of raw materials, equipment and waste disposal, turnaround times, dielectric-conductor adhesion and conductivity and environmental impact. Of the various techniques enabling the metallisation of plastics, the goal of which is to produce flexible circuitry and interconnects for any given application, a direct write method was found to be the most promising to develop to meet the demands of ever decreasing feature sizes and the push for faster, cheaper and more efficient production methods. This method utilises polyimide as a substrate, ubiquitous throughout the majority of the sectors highlighted in Figure 1.1 above. A brief summary of the leading candidates is provided here, following on from a survey previously carried out by Ng *et al.* [6].

1.3 Overview of the process and contribution to the field

Traditionally, plastic electronics have been manufactured using chemical vapour deposition (CVD). This process requires the use of photoresist patterning and chemical etching before the plastic substrate is placed in a vacuum, where metal is deposited uniformly across the sample. The photoresist is then removed to leave the plastic substrate with patterned metal tracks. While this allows for fine feature sizes, the process is somewhat slow and the complex vacuum equipment is relatively expensive. Another fabrication option is by subtractive methods. Here a metal coating is uniformly applied over the substrate before layering a patternable photoresist on top of this. This is then photopatterned and etched, the difference being that rather than growing metal, any exposed metal after patterning of the resist is stripped away in a further etching step. Since the majority of the original metal layer is etched away, this process is not highly efficient and expensive as large volumes of waste containing expensive metals are created as by-products, which require treatment or disposal.

For these reasons, additive techniques such as inkjet printing of metallic nanoparticles suspended in solution for subsequent sintering, laser based thermal formation mechanisms and photochemical methods are seen as less complex and lower cost alternatives. Of these techniques, a method employing surface modification with subsequent in situ silver nanoparticle growth was chosen in this thesis, both due to the opportunity for new research being identified and also the potential of this method for continuing the downward trend in feature size. The number of processing steps is significantly reduced compared to the traditional CVD and subtractive routes. Furthermore, the absence of a lithographic step means that a given circuit design can be prototyped and tested more quickly without the expense of repeated revisions to expensive quartz photomasks. Comparing to other additive methods such as inkjet, the use of a focussed laser circumvents some of the problems such as irregular line patterning and the 'coffee ring' effect, where metallic droplets form small circular patterns after sintering instead of solid lines, resulting in poor conductivity. A more detailed analysis of the current literature in the field of additive micro fabrication highlighting such issues is given in Chapter 2. Since the process investigated within this thesis is somewhat disruptive, potential problems and hurdles to be overcome are also discussed.

1.4 Layout of the thesis

With the background and motivation for the current work laid out above, the remaining chapters further these arguments in greater detail. Chapter 2 reviews both the academic literature of recent similar and competing processes and also investigates state of the art technology as used by current manufacturers within the plastic and printed electronics industry. It concludes by summarising these findings and fostering the argument for further development of the process investigated by this thesis as a viable commercial manufacturing technology.

Chapter 3 provides an in-depth discussion of the process, with more technical details on the prior art carried out by the MIcroSystems Engineering Centre (MISEC) research group at Heriot-Watt University. It then describes recent investigations into polymer degradation, caused by exposure to UV light, which creates adhesion problems at the metal-plastic interface. This highlights one of the main uninvestigated challenges facing the process if it is to be put into action in an industrial setting.

The following two chapters, Chapters 4 and 5, examine techniques to remove or significantly reduce such degradation. Firstly, the UV-based photo reduction of silver ions within the plastic substrate to their zero valent state is compared to a chemical reduction process, combined with a novel and previously untested photolithography patterning technique and the findings are contrasted and compared with the laser based characterisations of the previous chapter. At the same time, a new water-based photoresist is investigated as a possible supplementary fabrication route.

Secondly, and perhaps more importantly, modifications to the photo-reduction based process are explored. A lower energy, visible laser is used in conjunction with new electron donors, previously unexplored in the fields of microfabrication and plastic electronics. Taking inspiration from nature, these alterations promise to offer both a significant increase in the speed of the process and a reduction in chemical and waste disposal costs. These new electron donor chemicals within the photosystems studied are tested and compared with their efficacy when within the photosystem as a whole. Results are compared to the existing process.

Chapter 6 examines the suitability of the process for application to different substrates. A brief review of substrates is presented before experimental results on the identified potential candidates are analysed. Different polyimides are tested along with polyetherimide, a close analogue of polyimide that has not previously received a great deal of attention.

The final chapter, Chapter 7, provides conclusions of the experiments carried out, from the challenges discovered and the process alterations to circumvent these, to the investigations of new substrates. Also outlined here are potential future avenues for this work, all with the aim of bringing the technology to an industrially useable level. A diagrammatical overview of the thesis showing how the chapters contribute to the field can be seen in Table 1.1 below. This highlights the areas investigated and thus shows the contribution of this work to the field of plastic and flexible electronics.

This introductory chapter has described briefly what plastic electronics are and their applications, the motivation for the work and its contribution to the field, outlined the process by which this is realised and finally provided a synopsis. The themes touched on in the first three sections of this chapter are expanded upon in greater detail and put into the context of current and prior research in the following chapter.

Chapter	Topic	Highlights	Contribution / outcomes
1	Introduction	• Overview of field • Motivation for work • Layout of thesis	
2	Literature review	• Definition and scope of direct writing and metallisation • Discussion of various competing techniques • In depth discussion of metallisation of polyimide	• Places work of thesis in context of field as a whole • Discussion of relative merits of available techniques
3	Direct writing tests and degradation investigation	• UV laser direct write tests • Degradation due to laser energy investigated and characterised	• Direct writing process demonstration • Detailed investigation of physical effects during process
4	Alternative metallisation route	• Silver tracks created using chemical-based as opposed to photo-based methods • New low cost, environmentally friendly photo-resist tested	• Process diversification • Novel photoresist process development
5	Biologically inspired fabrication	• Lower energy blue light used with chlorophyll to mimic photosynthesis for photo-reduction	• Process advancement using novel, biologically based material • Facile, low cost modification of process
6	New substrate material	• Polyetherimide tested and developed as alternate substrate	• Substrate choice increased, therefore diversifying the process
7	Conclusion	• Summary of thesis • Future research avenues	• Pigments of LHC-II/PS-I/PS-II tested for electron transfer ability • New cellulose substrate

Table 1.1: *Layout of thesis and contribution to the field.*

Chapter 2:
Review of direct writing and metallisation processes

2.1 Definition and scope of direct writing and metallisation

As discussed in the introductory chapter, there is great interest in developing techniques that simplify and diversify circuit fabrication methods, by creating processes that are lower in cost and developing new materials for use as non- or semi-conducting substrates. Two such terms often used to describe a large group of techniques that aim to achieve this are ‘direct metallisation’ and 'direct writing'. The former covers the coating of an entire surface with metal, or the deposition or creation of metal tracks onto a non-conducting substrate. Direct writing on the other hand can be used to describe processes which deposit virtually any material, from metals and plastics right through to biological materials such as cells and proteins. Both direct metallisation and direct writing are seen as having potential to replace more traditional fabrication methods, which use photolithographic methods and require exposure of the substrate, photoresist or both through a photomask. These established approaches also most often favour vapour phase deposition for conductive metal track creation, which requires a vacuum chamber.

The aim of this chapter is to provide a taxonomy of direct writing and direct metallisation techniques and show how these overlap in the context of flexible circuit fabrication. It is also intended for use as a background for the work in subsequent chapters of this thesis, to show where the research carried out contributes to the literature. Examples are used to give the reader an idea of the various processes involved while their merits and drawbacks are discussed. Suggestions of particularly useful review papers for some of the larger sub-topics (in relation to the present work) are also given where deemed appropriate. The remainder of this section outlines the layout of the chapter, a summary of which is shown in Figure 2.1 below.

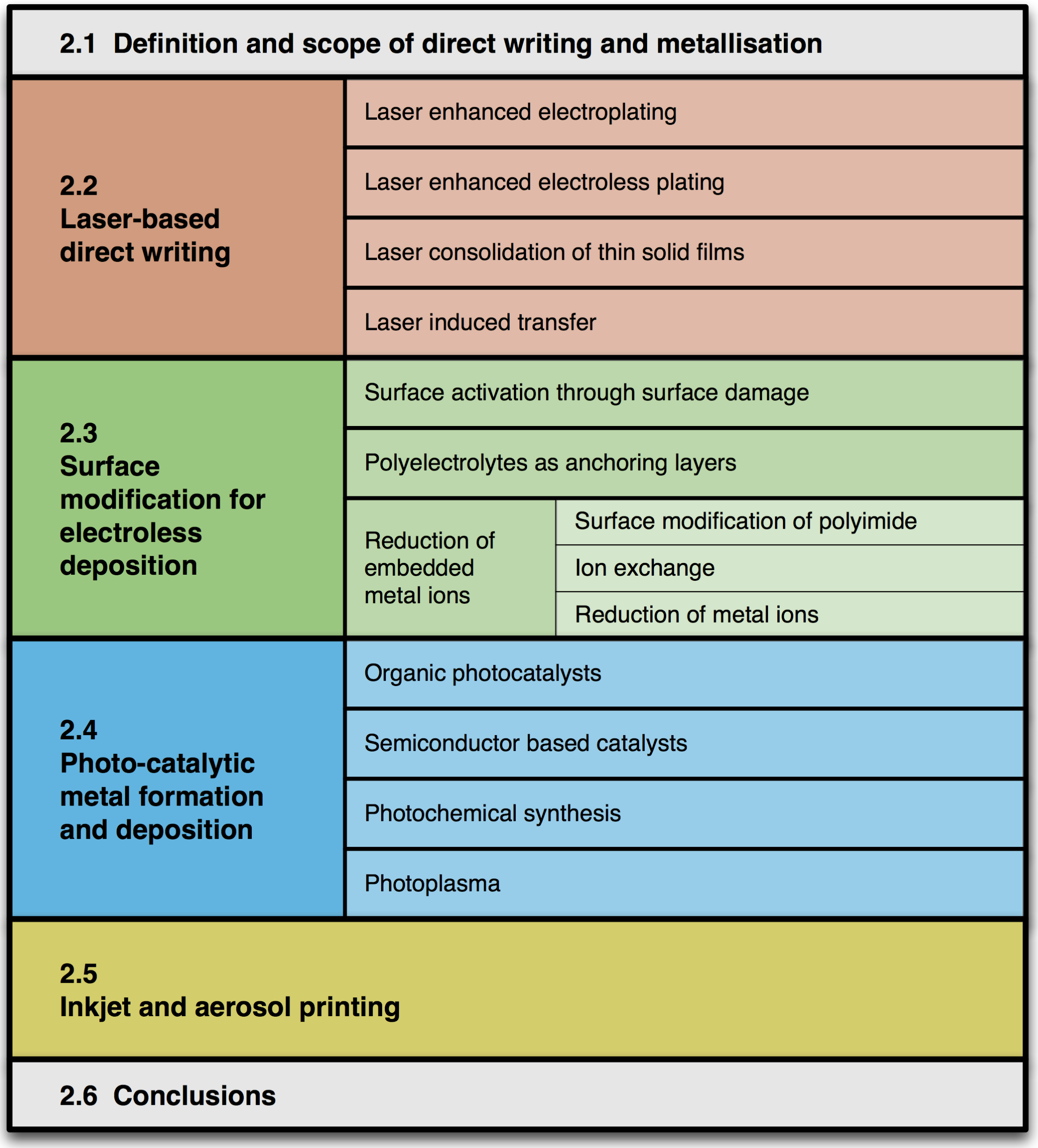

2.1 Definition and scope of direct writing and metallisation		
2.2 Laser-based direct writing	Laser enhanced electroplating	
	Laser enhanced electroless plating	
	Laser consolidation of thin solid films	
	Laser induced transfer	
2.3 Surface modification for electroless deposition	Surface activation through surface damage	
	Polyelectrolytes as anchoring layers	
	Reduction of embedded metal ions	Surface modification of polyimide
		Ion exchange
		Reduction of metal ions
2.4 Photo-catalytic metal formation and deposition	Organic photocatalysts	
	Semiconductor based catalysts	
	Photochemical synthesis	
	Photoplasma	
2.5 Inkjet and aerosol printing		
2.6 Conclusions		

Figure 2.1: *Schematic of the chapter layout.*

Section 2.2 focuses on direct writing methods using lasers. Since the cost of laser systems has greatly decreased in recent years, they have been exploited in the field of direct writing in several novel ways.

Section 2.3 looks at metallisation of substrates through surface modification., with particular attention paid to the techniques used later in this thesis.

Section 2.4 looks at photo-catalytic metal formation and deposition, how light is used to create metallic particles, structures and coatings and how this is utilised in the present work. Subsections within this section are intended to clearly differentiate the physical and chemical mechanisms involved.

Section 2.5 discusses inkjet printing and its derivatives. Although such a method is not used for experiments in this thesis, it is perhaps the most widespread direct writing technology and therefore the source of most competition. It is also often used as a processing step in some of the methods from the previous sections.

Finally, Section 2.6 sums up the findings of the chapter and provides reasoning for the work undertaken in subsequent chapters. Although this thesis is aimed at developing a technique that employs lasers, as presented in Chapters 3 and 5, the novel way in which laser energy is exploited combined with the anchoring mechanisms of the metal particles within the substrate do not fit neatly under the definition of the various laser-based processes discussed in Section 2.2. Rather, it is a hybrid technique encompassing reduction of metal ions through light induced excitation of organic photocatalysts for which the source of light is not confined to being a laser medium. As such, it sits abreast sections 2.3 and 2.4, with some overlap into Section 2.2 as discussed later.

2.2 Laser-based direct writing

Laser-based direct writing (LDW) broadly refers to the controlled deposition of materials via a laser-based process without the use of photomasks or lithographic procedures. Typically metal tracks are written but other materials such as semiconductors, polymers and ceramics have also been deposited. Some maskless laser based techniques have existed since the 1970s, with von Gutfeld *et al.* pioneering a technique to enhance electroplating by thermally assisted laser excitation in 1979 [7] so it is perhaps the oldest of processes that can be classified as direct write. Since then the field of LDW has expanded considerably, with techniques being developed that utilise precursors in various states of matter. Depending on the process, a chemical, electrochemical or physical reaction will be induced by a laser beam, resulting in the deposition of material onto the substrate.

A review by Hon *et al.* splits LDW into numerous categories, underlining the diversity of the topic [8]. Laser chemical vapour deposition (LCVD) methods are discussed for example, but, by adhering to the definition at the beginning of this chapter, such methods were not considered due to the complex vacuum based equipment required. However, Kwok and Chiu employed an LCVD system without a vacuum setup for the purpose of creating carbon nanotubes [9], although their setup still requires somewhat complex equipment for processing samples in the gas phase. Other examples from Hon *et al.*, such as multi-photon polymerisation [10] and laser tweezer particle trapping [11] focus more on polymer forming and manipulation or deposition of biomaterials such as proteins and cells [12] and so do not fall within the scope of a direct metallisation process. Of direct relevance to this work are the following branches of LDW, which provide competing technologies against which to benchmark the process developed in this thesis:

α. Laser enhanced or activated electroplating
β. Laser enhanced electroless plating
γ. Laser consolidation of thin solid films
δ. Laser-induced transfer

2.2.1 Laser enhanced electroplating

Von Gutfeld *et al.* were the first to apply this technique to plate gold, copper and nickel in the late 1970s and early 1980s [7]. A laser beam was focussed onto the cathode within an electroplating bath, causing highly localised heating that resulted in plating rates increasing by up to 3 orders of magnitude. Scanning was performed manually and estimated to be approximately 1 $mm{\cdot}s^{-1}$. More recently, Wee and Li deposited copper tracks with a width of a few hundred microns onto stainless steel using this method [13]. However the scan speeds here were slower, in the range of 0.1 – 0.3 $mm{\cdot}s^{-1}$, and the linewidth and track height both increased approximately linearly with the number of passes. There are few other recent reports of laser enhanced electroplating in the literature. This is perhaps due to there being a number of negative effects to overcome if consistent patterning is to be achieved. Such effects include the turbulence generated from the laser which can cause bubbling and disrupt the process. Diffraction of the laser beam within the electrolyte solution and heat diffusion, will also impact upon the resolution of features.

2.2.2 Laser enhanced electroless plating

Laser enhanced electroless plating (LEEP) also referred to in the literature as laser-induced chemical liquid deposition (LCLD), shares many characteristics with laser enhanced electroplating [14]. The substrate to be patterned is submersed in an electroless plating solution. A laser is then directed at a point on the substrate, causing a local rise in temperature. When the temperature is high enough the solution will decompose, allowing the metal ions to be reduced to their elemental state upon the substrate. Electroless plating has received more attention than electroplating in recent years, in part due to requiring less complex equipment since electroless deposition does not require an anode, cathode and voltage monitoring. Using this method, Chen *et al.* found deposition rates to be increased by about 5 orders of magnitude over standard electroless deposition [15]. The final copper tracks were 2 – 12 μm wide for a height of 0.24 – 1.2 μm with a resistivity twice that of bulk copper, however laser scanning speed was low, with 0.8 $mm\cdot s^{-1}$ being the maximum achieved. Manshina *et al.* also produced well defined copper tracks with width of about 30 – 80 μm [16], however the scan speed was still low, at 0.01 $mm\cdot s^{-1}$. Speeds of up to 0.4 $mm\cdot s^{-1}$ were demonstrated for a variety of metal complexes by Kordás *et al.* [17]. Despite the relatively slow scanning rates, investigations into the effect different reducing agents added into the electroless solution have on deposited copper have been carried out. Kochemirovsky *et al.* measured the effects of formaldehyde, ethanol and various polyols on the deposited copper [18] and found that the addition of polyols caused a large decrease in resistivity, with xylitol providing the greatest decrease of around 3 orders of magnitude. Such an increase in quality of deposition indicates that there is a good possibility of process improvement and therefore scanning speeds can be expected to increase.

2.2.3 Laser consolidation of thin solid films

The state of the metallic precursor need not be limited to liquid or gas; solid films have also been under investigation for many years. One notable early example by Gross *et al.* uses palladium onto quartz via a thin film of the organo-metallic composite palladium acetate [19]. The deposition mechanism is based on the photothermal, or pyrolitic, decomposition of the thin film precursor and subsequent fusing or sintering of the metallic particles to form a continuous track, while the organic portion is burned off. The process has the advantage over LCVD of being suitable for a vacuum-free environment, however the resulting compounds could be hazardous so appropriate precautions should be taken. Similarly, removal of thin film deposits on unexposed areas of the substrate requires harsh chemicals such as sulfuric acid.

More recently Aminuzzaman *et al.* demonstrated 6 μm wide conductive tracks on a polyimide substrate with a resistivity 2 orders of magnitude larger than bulk silver from a silver nanoparticle ink suspension [20]. However, the write speed of 200 $\mu m \cdot s^{-1}$ was not an improvement on the 2 $mm \cdot s^{-1}$ achieved by Gross *et al.*. On the same substrate, a faster write speed of 4.3 $mm \cdot s^{-1}$ was successfully employed to produce 55 μm wide tracks by Kim *et al.* [21]. Sample preparation involved coating the polyimide in a copper formate solution and allowing it to dry. A 20 ns pulsed laser of 355 nm wavelength was then scanned across the surface, which served two functions. Firstly, the energy imparted triggered decomposition of the dried precursor into hydrogen, carbon dioxide and copper and secondly, it caused breaking of chemical bonds in the polyimide, turning it hydrophilic. This is due to polyimide being highly absorbent in the UV region and has the effect of improved copper-polyimide adhesion. The reported resistivity was 107 μΩ·cm, 2 orders of magnitude greater than bulk, but this is still low enough to use in certain applications without the need for subsequent electroless plating, although the track shape visible in Figure 2.2 below was also somewhat irregular and could be improved.

A possible way to improve this is to alter the energy dose. Joo and Baldwin followed the above technique and investigated laser and thermal sintering processes for the creation of a conductive film [22]. To compare an entire sheet of thermally sintered film, a laser beam of 3 mm diameter was raster scanned across the substrate. It was found that increasing the laser power from 1 W to around 2 W resulted in smoother copper deposits and lowered sheet resistance, in a similar way to increasing the sintering temperature from 160 to 220^{o}C. Resistivity was found to be greater than in Kim *et al.*, at 1410 μΩ·cm and 1300 μΩ·cm for thermal and laser methods respectively, yet the thickness of copper here was only 1 μm, compared to 8.5 μm in the older study. Another possible reason for the smoother copper deposit was the copper nanoparticle precursor used. The melting temperature of nanoparticle inks is considerably less because of the well-known thermodynamic size effect [23], which reduces the spreading of the deposited metal. The sintering of metallic NPs has also recently been tested as a possible alternative to gold plating by Watanabe [24] and also for fabrication of transparent conductive thin films by Watanabe and Qin [25].

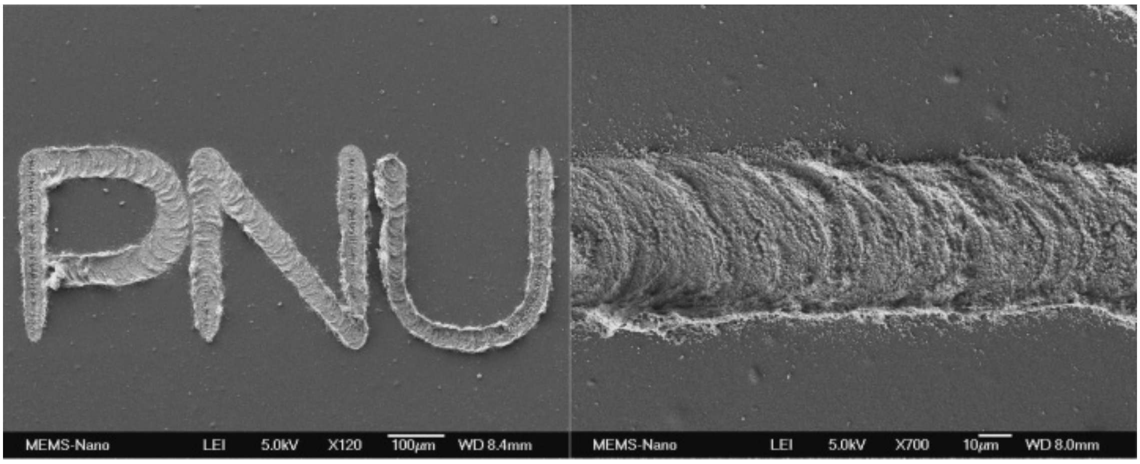

Figure 2.2: *SEM images of copper tracks on polyimide formed by laser decomposition of copper formate [21].*

Laser consolidation of thin films is a promising technique in terms of feature size, conductivity and freedom from subsequent electroless plating. It still however remains a relatively slow direct writing process. Also, the metal-containing precursor is coated over the whole substrate before the laser targets small areas to metallise. This is profligate in the sense that there are large areas of 'unwritten' precursor remaining after laser writing, which somewhat wastefully require removal after laser scanning. Further, substrate choice and precursor formation are highly specific, in that they must be selected to have enough optical absorption at the laser wavelength to initiate decomposition of the thin film coating.

2.2.4 Laser induced transfer

The first instance of using laser induced transfer targeted the deposition of copper onto a silicon substrate and was carried out by Bohandy *et al.* in 1986 [26]. Now more widely known as laser induced forward transfer (LIFT), the process consists of transferring a thin film onto a substrate from a donor support substrate positioned anywhere from a few microns to a few millimetres above. The basic principle, shown in Figure 2.3(a) below, relies on the choice of a material for the donor support that is optically transparent at the wavelength of the used laser. Typically an excimer laser or other deep UV source is used. The incoming laser beam passes through the donor support, focussing on the thin film of material on the underside, causing the film to detach and transfer onto the acceptor substrate below. As well as being relatively straightforward, the thermal and optical characteristics of the acceptor substrate are not important, allowing thereby the choice of any substrate to be deposited upon. Although the tracks created by Bohandy *et al.* were rather irregular and not particularly conductive, with reported resistivities between 3 and 50 times that of bulk copper, this was comparable with other laser techniques available at the time. Furthermore, the 30 μm linewidths indicated that refinement of this process could prove highly worthwhile.

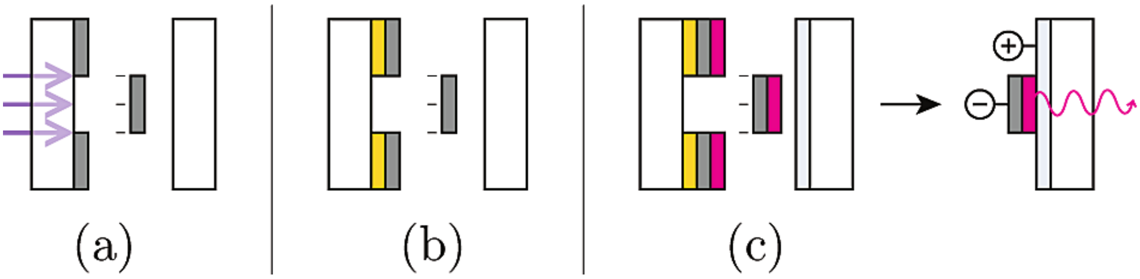

Figure 2.3: *LIFT principle. Donor substrate on left, receiver on right. (a) Original method, (b) addition of a sacrificial layer (yellow) and (c) sacrificial method used to create OLEDs [27].*

More recent literature shows that this is demonstrably the case: as well as the 'pure' LIFT process, five similar but distinct adaptations are also presented here. As well as deposition of metals, LIFT has also been developed for transfer of metal oxides, such as zinc oxide [28] and titanium dioxide [29]. Experiments by Boutopolous *et al.* demonstrated LIFT for transferring silver nano particles still in suspended liquid phase [30]. In doing so they also highlighted how modifying the process with the addition of a titanium dynamic release layer (DRL) placed between carrier substrate and thin film source improved both final deposition uniformity by reducing the exit velocity of the material to be transferred and increased the range of laser fluence that would initiate ejection, resulting in a finer level of control. As well as aiding in liquid phase transfers, the addition of a DRL to the LIFT process has also enabled more diverse material patterning, with solid metal transfer, such as aluminium [31], and sample hydrogels containing biological materials [32].

Perhaps more interestingly in terms of practical application is the deposition of functioning organic circuit components, such as the OLED by Fardel *et al.* as shown in Figure 2.3(c) above [27]. The receiver substrate used was a non-conductive glass slide. Square pixels of approximately 350 µm were transferred successfully with a configuration of zero gap between donor and receiver substrates however gap sizes of 0.5 mm and 1 mm showed that the integrity of the transferred element decreased with increasing size, although this gap was deliberately created to allow for imaging of the process in action. Similarly, an OTFT was developed by Kim *et al.* using silver as the electrodes, pentacene as the semi conductor and poly-4-vinylphenol as the dielectric [33] with reported contact resistances comparable to pentacene-based OTFTs produced by alternate methods with gold electrodes. However the procedure of preparing and coating the organic chemicals results in a larger number of processing steps.

The ability to transfer different materials was also put to effective practical use by Shaw-Stewart *et al.* in 2012, where a functioning polymeric LED (PLED) 500 x 500 µm pixel was fabricated [34]. For the receiver substrate a glass wafer coated with layers of indium-doped tin oxide (ITO), PEDOT:PSS and PVK was used. LIFT was then employed to transfer first a 700 x 700 µm electron-interface layer (made from the polyelectrolyte PFN) and second a 500 x 500 µm aluminium layer. A triazene polymer (TP) DRL was used in both instances. The fact that the pixel components were transferred wholly with one pulse from the laser meant that enhanced beam shaping and a mask were necessary, adding complexity to the experimental setup.

Two adaptations to LIFT similar to the DRL approach are absorbing film assisted LIFT (AFA-LIFT) and blister actuated LIFT (BA-LIFT). Both were developed to protect mechanically or thermally sensitive materials, such as biological samples from the high levels of heat experienced by the transfer material in a standard LIFT process [35, 36]. Looking first at AFA-LIFT, this process uses a thin silver layer between the donor substrate and transfer material to absorb the majority of energy from the laser and convert it into kinetic energy. This forms a diffuse halo consisting of silver vapour and microparticles that carries the sensitive biological samples, for example, away from the heat affected zone, thus protecting it from overheating. Although successfully protecting the transfer material, this method introduces extra debris and vapour that is not desirable on the target substrate and could lead to contamination. Characterised by Smausz *et al.* [37], this phenomenon is something that a DRL-based approach can also suffer from depending on the material used. The second adaptation similar to the DRL approach, developed by Brown *et al.* and termed BA-LIFT, circumvents this problem [38]. Polyimide is used as the release layer, which in this case is not intended to disintegrate or vaporise but merely incubate a sealed blister adjacent to the donor substrate, as shown in Figure 2.4. The creation of such a blister mechanically forces the transfer material away from the opposite underside of the polyimide and onto the target substrate. Since polyimide absorbs strongly at UV wavelengths [39] and is of low thermal diffusivity, using a thick enough layer in conjunction with the correct laser fluence will prevent any laser or heat energy from affecting the transfer material. Furthermore, any ablated PI remains trapped within the blister. At a few microns thickness, the energy absorbing layers are generally thicker than DRL- and AFA-LIFT methods, which are in the region of tens to a few hundred nanometres. Clearly the shape of the deposit will be affected by the shape of blister, which is, in turn, affected by numerous factors ranging from beam shape, size and fluence, to thin film thickness and absorbance.

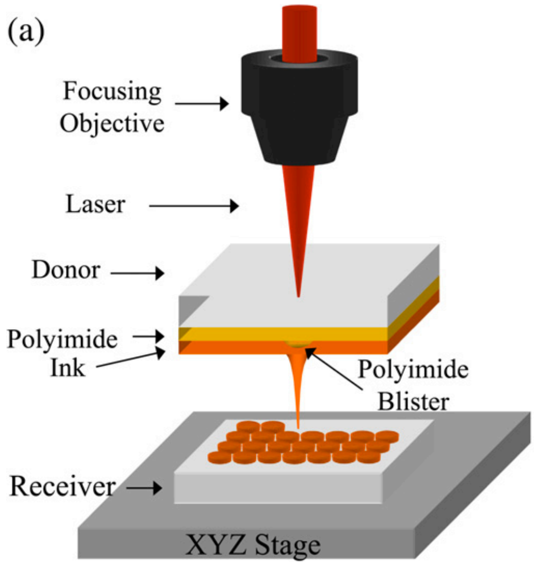

Figure 2.4: *BA-LIFT experimental setup [40].*

Nevertheless, parameter tuning is possible: Kattamis *et al.* demonstrated the printing of photoluminescent compounds onto an ITO-on-glass substrate to create coloured voxels with initial spot sizes of 80 µm, further optimised to approximately 10 µm [40]. As well as the varying parameters already mentioned, they also highlight the difference the composition of the transfer material can make, with the complex used to pattern a green voxel creating a much less regular shape than the red voxel complex, shown in Figure 2.5. Formulating such complexes is non-trivial, requiring specific chemical quantities on top of subsequent necessary precise mixing with a solvent before it is applied to the donor substrate. While the BA-LIFT process is straightforward in itself, there are numerous pre- and post-processing steps, which require a great deal of work to optimise.

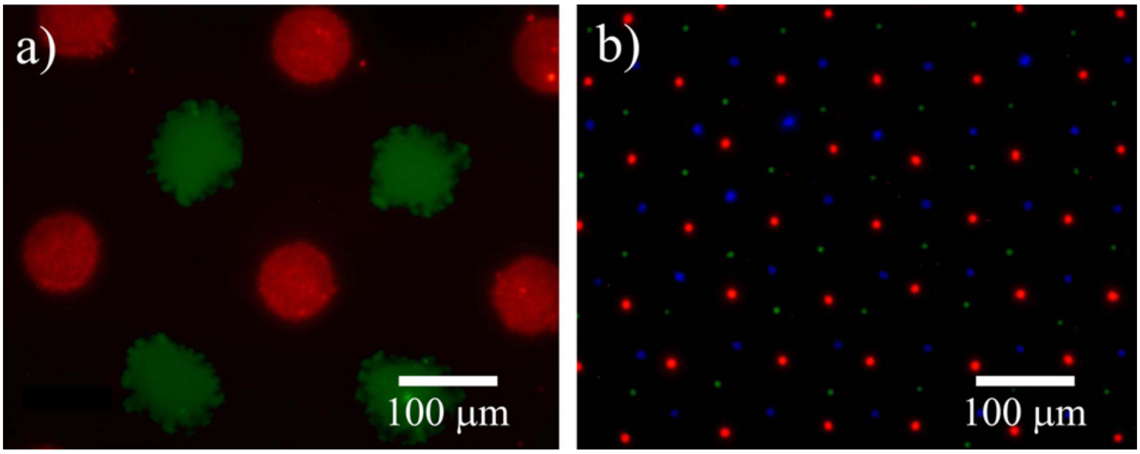

Figure 2.5: *Voxels printed by BA-LIFT technique [40].*

Pique *et al.* first demonstrated the versatility of a fourth different refinement to LIFT by depositing both metallic and organic materials onto a variety of substrates [41]. Their method, termed matrix-assisted pulse-laser evaporation direct write (MAPLE-DW), combines the already described LIFT process with the material preparation concepts seen in MAPLE – a laser-assisted vacuum deposition technique. Here a solution is formed by dissolving an organic compound in a matrix material, most often a volatile solvent such as alcohol. This solution is then frozen to form a target film for the laser. When the laser strikes the film the solvent vaporises rapidly and part of the thermal energy absorbed by the solvent transfers to the organic molecules. Upon exposure to the gas-target interface, the organic molecules are removed from the surface of the target in the gas phase, where they then form a new film on an acceptor substrate placed opposite the target, while the solvent is pumped away. As well as fabricating a variety of circuit components with this method, they showed an order of magnitude improvement in transfer rate over LIFT. They successfully patterned ~30–50 µm wide silver tracks, however the resistivity was approximately 1,000 times greater than that of bulk. Also 10 passes of the laser were required, so this increase in speed did not serve a practical end in this case. This work did however open the doors to numerous potential applications of the process.

As with most LIFT processes, biomaterials have been a major application area, with Riggs *et al.* providing a recent in-depth review of MAPLE-DW for biomaterial deposition [42]. Although deviating slightly from the scope of this thesis, it is worth highlighting the level of interest in the area for potential future applications of the work carried out in this thesis. More in keeping with the discussion at hand is the work on electronic components, such as resistors, capacitors, interconnects or inductors, on polymer substrates as demonstrated by Chrisey *et al.* [43]. Of particular note is the relatively uniform silver track, approximately 40 μm wide and 8 μm high. This resolution is greater than that achievable by screen printing and the conductivity of approximately 2.5 times bulk silver, while not ideal, is in the same region as screen printing.

Low temperature co-fired ceramic (LTCC) has also been used as the target substrate. Zhang *et al.* [44] utilised MAPLE-DW when printing an inductor and band-pass filter. Although details of the filter were not divulged, the inductor possessed a linewidth of 100 μm. 50 μm test patterns were also presented but this was before the ceramic firing step, which causes shrinkage in the substrate, so it is not clear what effect this had on the tracks. More recently, Kinzel *et al.* demonstrated 20 μm wide silver lines on LTCC [45], and although the track appeared to have irregular edges and uneven continuity, a resistivity of 6.25 μΩ·cm was reported – a magnitude of the same order as bulk silver. Furthermore the write speed of this track was 70 $mm \cdot s^{-1}$, a clear improvement over other LIFT processes.

Mir-Hosseini *et al.* demonstrated the fifth and final variation to the LIFT process covered by this thesis, termed laser induced backward transfer (LIBT) [46]. Here the laser is directed through a target substrate suspended above the material to be transferred. The transfer material melts and vaporises and some is then deposited on the target substrate above. While successfully used to deposit a thin layer of tin oxide from a tin powder bed at a high scan speed of 300 $mm \cdot s^{-1}$, this technique is seriously constrained by the target substrate requiring to be transparent to the laser light. Although Kuznetsov *et al.* also demonstrated the viability of LIBT for transferring gold nanodroplets of diameter between 300 nm and 1 µm with a view to fabricating devices for sensing applications [47], there have been limited other applications in the literature since.

One of the disadvantages of most LIFT methods is that ablated materials in various forms can interfere with both the ejection and deposition of the material to be transferred. These interactions have been noted to be both problematic and complex in nature [48], although techniques such as BA-LIFT alleviates this. Moreover, while the choice of transfer material is theoretically limitless, a good deal of effort is required to achieve acceptable deposition for new materials. This is in part down to the high sensitivity of the process to laser fluence and the gap size between donor and acceptor substrates [49]. However as discussed above, the application of a dynamic release layer or matrix assisted pulsed laser evaporation can result in greater control. Furthermore, models of the process [50, 51], or specific applications of it, have recently been proposed, which will be of assistance when tailoring the process to new materials. A final large drawback of LIFT processes is that although the transfer process itself does not necessarily require a vacuum environment, and indeed MAPLE-DW has been widely used in ambient environments, coating the donor substrate with a thin film, particularly in the case of metal precursors, often does. This adds both a layer of complexity and expense onto the overall process. The write speed is generally relatively poor too, although this may not present such a problem for biological applications, where dimensions may be smaller.

As can be seen from the examples of laser-based direct writing above, there are numerous applications spanning large domains, from nanometre up to centimetre and above. Laser energy is being harnessed for circuit fabrication but for this specific application its speeds are not yet at an industrially scalable level and more work is needed to find optimum solutions.

2.3 Surface modification for electroless deposition

Laser direct write processes can be effective but the features produced are often irregular due to the thermal effects of the laser. One way to mitigate this is to use a process that is not thermally driven, allowing more uniform metallic area formation, onto which further metal can be added via electroless plating. Electroless plating is an isotropic process and so will produce regular, controllable deposits, with unwanted increase of the patterns in the horizontal direction. The primary advantage of electroless over electroplating is that a nonconductive substrate can be used, providing a suitable seed layer is created to catalyse the plating reaction. This reaction is typically referred to as activation.

This section looks at some of the techniques used to create active seed sites on non-conductive substrates. These can be broadly grouped into the following categories:

α. Surface activation through substrate damage
β. Polyelectrolytes as anchoring layers
γ. Reduction of embedded metal ions

2.3.1 Surface activation through substrate damage

In this method, one of the first investigated to produce active catalytic sites on a substrate, active sites are generated by opening chemical bonds within the molecular structure of the substrate or by the explusion then redeposition of charged species onto the substrate, whose release originates from the rapid and high temperature reactions created during laser melting or ablation. Numerous substrates were subjected to this process by Shafeev, with aluminium oxide, diamond, silicon carbide and zirconium dioxide all successfully 'activated' [52]. LTCC [53], polyimide [54] and aluminium nitride [55] surface activation have also been demonstrated with the latter taking advantage of the substrate's 'inbuilt' aluminium to act as a catalyst for copper plating to demonstrate through hole via formation. While this method is straightforward to apply, the high power laser required causes undesirable machining of the substrate and thermal diffusion also hinders the achievable minimum feature size. Pulsed lasers have long been used to reduce the heat affected zone (HAZ) for a variety of laser machining applications and this was shown to aid the surface modification process by Xu *et al.* [56]. A femtosecond laser was used to ablate a groove in a glass substrate and create silver particles within the groove from a silver nitrate coating, enabling the creation of 15 µm wide electrolessly plated copper filled tracks. Small cavities within the plated tracks could however be seen and edge irregularities on the surface were still present. Similarly Song *et al.* produced well-formed gold tracks embedded in quartz glass by first ablating a 20 µm wide, 15 µm deep trench with a femtosecond laser at high fluence before coating with silver nitrate and scanning the same trench at a lower laser power to reduce any silver ions within it [57]. This silver seeding was then used to electrolessly fill the groove with gold. Resistivity was estimated from resistance measurements at one order of magnitude greater than bulk gold. Although the recessed nature of the gold tracks is excellent in terms of adhesion, the choice of gold is expensive and the scan speed for the ablation step was only 1 $mm \cdot s^{-1}$, with the speed for silver reduction not quantified but reported as slower still.

A different technique to activate the substrate was demonstrated by Zhou *et al.* [58], where a mercury arc lamp was used as a light source through a photomask to selectively activate polycarbonate to produce gold electrodes. Even though this UV light source was low intensity compared to laser sources, it was enough to create carboxyl groups by photochemical oxidation of the methyl groups in the polymer chain. Tin ions were chemisorbed onto these carboxyl groups before silver ions were then adsorbed onto the tin ions. When the substrate was subsequently placed in an electroless gold plating bath based on formaldehyde, immediate reduction of the silver ions occurred, resulting in the instant creation of a seed layer for electroless gold plating to commence. Cyclic voltammetry on the electrodes showed reasonable agreement with a commercial electrode and the sensors have subsequently been employed in microfluidic systems for determining glucose and lactate concentrations [54].

Surface modification has also proved a fertile topic for flexible electronic fabrication, with electrolessly plated silver on both polyester [59] and polyethylene terephthalate (PET) [60] being notable current examples that do not rely on complex equipment or particularly complicated chemical formulations.

However the focus here is on textile-based applications, which, although an area of large contemporary interest, is in its infancy.

2.3.2 Polyelectrolytes as anchoring layers

As an alternative to the above additive method, polyelectrolytes can be used to additively build up a film on a substrate layer by layer. Polyelectrolytes are polymers, which contain an electrolyte group within their repeating unit and so will become charged when dissolved in an aqueous solution. The electrostatic attraction between two such molecules of opposite charge can be exploited to create a charged thin film, onto which metallic particles may adhere, thus producing a seed layer for electroless plating. A synopsis of polyelectrolyte multilayers, also known as layer-by-layer assembled films (LbL), provides the basis of the process description [61]. Firstly the target substrate must be prepared so that the first polyelectrolyte will adhere to it. For inorganic materials such as glass, this can be achieved by immersion in a sulphuric acid-hydrogen peroxide solution, commonly referred to as piranha solution. Since this is not suitable for certain organic substrates, such as FR4 for example, plasma treatment provides an alternative. The prepared substrate is then alternately dipped into oppositely charged polyelectrolyte solutions, with each submersion adding a new layer of polymer. Both gold and silver nanoparticles in polyelectrolyte film deposition have been demonstrated, with sizes in the tens of nanometers range [62, 63], which could be used as catalysts for subsequent electroless plating.

One popular method for patterning that selectively deposits the polyelectrolyte is microcontact printing (MCP). This is a soft lithography process that uses a master stamp of polydimethylsiloxane (PDMS) to deposit material in the desired location. Azzaroni *et al.* took this route to deposit 'initiator domains' containing thiol and silane functional groups onto both gold and silicon dioxide coated substrates [64]. A polyelectrolyte was then bound to these through a process known as atom transfer radical polymerisation (ATRP), resulting in a positive polyelectrolyte being anchored at the patterned areas. Submersion in a palladium salt solution then resulted in $PdCl_4^{2-}$ anions becoming tethered to the polyelectrolyte. Finally the sample was placed in an electroless bath for 30 – 60 seconds, where the $PdCl_4^{2-}$ ions catalysed copper deposition of height 1 – 2 μm. Since the original PDMS stamp can be created by photolithography, this allows fine feature sizes, as demonstrated here. Tracks of width 1–2 µm displaying very high uniformity were produced. Copper has also been selectively patterned onto a PET substrate by Huang *et al.* [65], while Kimura *et al.* used this process to deposit nickel onto polyimide and glass, reporting 7 µm linewidths [66].

Zabetakis and Dressick provided a comprehensive investigation into various routes of selective surface treatment and electroless plating for interconnect applications with a focus on sub-micron scales [67]. Although much of the finer resolution samples were created by reactive ion etching (RIE), which required a vacuum, very well defined 20 µm wide nickel tracks on oxygen plasma activated polyimide were also created by flood UV exposure through a photomask, but little extra information on performance was given.

The two main requirements of polyelectrolyte anchoring layers are good adhesion and appropriate catalyst seed layer. However both requirements are sensitive to the pH of the solution, the concentration of each of its constituents, the molecular weight of the polymer chains, and the ratio between the chain length of polyanion and polycation. More knowledge of the underlying chemistry is required however. Skirtach *et al.* [68] and Parakhonskiy *et al.* [63] investigated the formation of silver and gold nanoparticle aggregates and the effect concentration has on their formation, while various modelling strategies and methods were recently discussed by Cerda *et al.* [69]. A recent study by Carrillo and Dobrynin uses molecular dynamic simulations of nanoparticle adhesion [70].

LbL assembly is time-consuming due to the several repeated dippings but advances on the technique have helped to reduce or even eliminate this problem. Garcia *et al.* demonstrated a 'one-shot' technique to deposit a copper NP seed layer onto an acrylonitrile-butadiene-styrene (ABS) substrate through adhesion of the polyelectrolyte poly(acrylic acid) (PAA2) [71]. The '2-in-1' approach taken by de Saint Aubin *et al.*, deposits the conductive polymer (poly(3,4-ethylenedioxythiophene)-poly(styrene sulfonate)) PEDOT-PSS, widely used in photovoltaic and organic electronic applications, onto silicon or quartz substrates in one step [72]. They observed that although PEDOT-PSS is molecularly charged, it can also be defined as zwitterionic - that is each molecule will contain both a positive and a negative charge simultaneously. Although this negates the need for a series of alternate dipping steps, they still require a number of spin coating stages for a desired thickness, indicating that the process may still require time.

More directly relevant to interconnects are the following two papers. Basarir recently pushed the boundaries of patterning by fabricating 10 μm wide gold features on a silicon substrate [73]. A PDMS stamp was coated with polyelectrolytes before being transferred via MCP to the substrate. Samples were then immersed in a gold NP solution for various times to allow the final electroless plating step. Not only was ohmic behaviour in the resulting gold tracks demonstrated, but resistivity was close to bulk. Gold, however, is expensive and ten alternating polyelectrolyte layer applications were needed. Further, the overall area treated was not discussed, highlighting a larger issue with LbL; that of patterning at the large scale. For an acceptably low manufacturing variation between individual structures on a given stamp, there are limits to how large this stamp can be.

Progress with this technique is being made in many areas, particularly at the nano scale for biological applications. Both Barbey *et al.* [74] and Azzaroni [75] provide exhaustive and in depth discussions of the many applications of polyelectrolytes and recent trends within the field. At the micro and meso scale for circuit and interconnect fabrication however, unless a suitably rapid or large area process to reliably pattern substrates can be found, industrial level throughput will not be realised. Recent research by Guo *et al.* however, addresses this problem [76]. They developed a technique known as matrix-assisted catalytic printing (MACP), which operates in a similar vein to the MAPLE direct write technique introduced in 2.2.4 above. An inorganic catalyst salt, ammonium tetrachloropalladate $(NH_4)_2PdCl_4$, is mixed into a carrier matrix polymer, polyethylene glycol (PEG), and then deposited onto a substrate with a thin coating of receiving polymer matrix, PMETAC, in this case. When the two polymer matrices come into contact, the catalyst salt diffuses into the receiving polymer and becomes immobilised. Electroless deposition is then carried out to metallise the printed seed areas. Patterning was carried out by dip pen lithography, inkjet printing and screen printing, which demonstrates the overlap between techniques for metallisation discussed at the beginning of this chapter and shows how they can be combined to produce better results. These methods are discussed in more detail in Section 2.5. The use of each of these patterning techniques also emphasises the suitability of MACP for a range of applications from the nano to macro scale. Furthermore, the PMETAC used to coat the substrates enhances adhesion of the electrolessly deposited metal and the immobilised palladium-based catalyst is a suitable seed for gold, silver, copper and nickel, with resistivities of approximately three times the bulk values for each reported. As well providing different options for conductor choice, various materials can be chosen for the substrate. Guo *et al.*'s focus appears to be on flexible, foldable and stretchable materials, with PET, PI, PDMS, cotton and cellulose paper all demonstrated as appropriate candidates for the process. While these results are highly encouraging, the patterning steps used have their own inherent drawbacks as discussed in Section 2.5.

2.3.3 Reduction of embedded metal ions in polyimide

The process typically involves three steps: chemical modification of the surface to create active sites, ion-exchange to embed metal ions at the active sites followed by in-situ reduction of these ions to form metallic areas within the substrate itself. Instead of the metal seed material in an anchored coating on the surface, this method creates a better anchoring mechanism between the subsequently electrolessly plated metal and the substrate. Furthermore, it negates the use of a carrier medium for the foreign metal material, such as a solvent, anion solution or organic complex solution, which can leave residues that affect the conductivity of the metal deposit.

Since this section deals with the direct metallisation technique explored in this thesis, the background theory is described in greater detail when discussing previous work in this field. A sub-section is devoted to each of the steps mentioned above, with a focus on silver formation within polyimide throughout, before example results and the current state of the art are discussed.

Polyimides are selected as prime candidate substrates for the embedded ion reduction technique because of their versatility and widespread use in electronics and microsystems technology. They have very high mechanical strength, are chemically unreactive, highly resistant to heat and radiation and are often bio-compatible. They are however more expensive than other flexible materials such as PET or PEN, but are often the only choice in harsh environment applications, such as those founds in space or biomedicine. Pyromellitic dianhydride-oxydianiline (PMDA-ODA) was the first commercially available polyimide. Originally introduced by DuPont under the trade name Kapton® in the 1960s, there are now a number of different commercially available polyimides in different forms, developed to suit different fabrication flows or final device operation. Most often seen in the form of a dark orange-brown roll or sheet, it is also available as a liquid of tunable viscosity, useful for different screen printing, spin-coating and spray-coating methods, and as a powder for producing non-standard parts and shapes through sintering techniques such as hot compression moulding or isostatic pressing. Various properties can be tuned to suit specific applications without adversely affecting the excellent mechanical, chemical and thermal attributes. Examples of such tailored polyimides are the optically transparent material by MGC Chemicals, the fast-curing or high rigidity polymer from RBI Plastics, the high elasticity, low curing temperature films from Mantech and the photo-patternable resins from HD Microsystems, of which there are both positive and negative photoresist types.

The critical point of interest with respect to this thesis is that at least one of the monomers contains an imide ring, hence the name of this particular family of plastics. This ring contains a C–N bond, which can be cleaved through alkaline hydrolysis, creating a suitable surface for subsequent ion exchange and metallisation. Therefore this treatment can in theory be applied to a large variety of polyimides.

PI circuit fabrication is more commonly a subtractive process. Typically a metallic layer, usually copper, chrome or titanium, is deposited onto the PI substrate, either by lamination or sputtering. Dry film photoresist can then be laminated onto this and UV-lithographic steps of exposure, development and etching can be performed to remove metal from selected areas and thus pattern the substrate. In circuit design, the ratio of area of bare substrate to area of metallised substrate is often high, meaning that this subtractive process can be very wasteful.

2.3.3.1 Surface modification of PI

Alkaline hydrolysis of polyimide with a potassium hydroxide (KOH) solution was first reported by Lee *et al.* [77]. This treatment results in a surface layer of potassium polyamate, with the K^+ ions occupying vacancies in between the polymeric molecules at the cleaved C–N bond sites, discussed further below. A proposed mechanism of this reaction was given by Stephans *et al.* [78], reproduced in Figure 2.6 below.

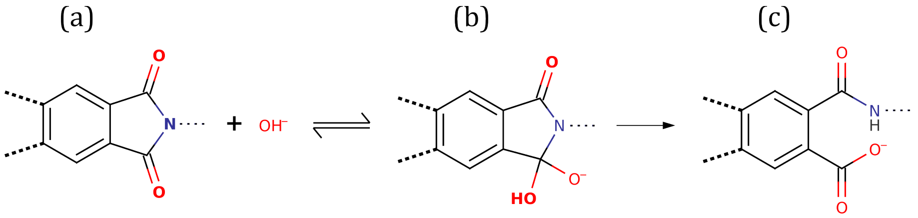

Figure 2.6: *Polyimide imide ring cleavage mechanism proposed by Stephans* et al. *[78]*

The hydroxyl OH^- ions diffuse from the alkaline solution into the polyimide substrate, where they nucleophilically attack the carbonyl carbon atom of the imide group, creating an intermediary anion, or activated complex as shown in Figure 2.6(b). Cleaving of the C–N bond is completed by the transfer of a proton from the oxygen to nitrogen atom, creating the carboxyl functional group COO^-. This resulting polyamate molecule can then be neutralised to create poly(amic acid), PAA. Plechaty *et al.* found that this reaction was diffusion controlled, that is to say that the formation of the final products from the activated complex, or the reaction from (b) to (c) in Figure 2.6, happens far more rapidly than the diffusion of OH^- ions into the polyimide in (a) to (b) [79]. Since the reaction begins at the surface of the polyimide then continues into the bulk of the material, with the hydrolysed layer taking an amorphous gel-like form, this amorphous layer was postulated to hinder diffusion of the OH^- ions deeper into the polyimide. As this polyamate layer grows, the rate of cleaving decreases, making this in effect a self-limiting reaction. However, this was contradictory to later experimental results from Okumura *et al.* [80]. In 2003, they performed depth profile analysis and found that modification depth increased with KOH immersion time. Using a 5 M KOH solution at 80°C, they observed modification depths of approximately 0.5, 2 and 8 μm for immersion times of 5, 10 and 30 minutes respectively. They did however agree with Stephans *et al.* with respect to finding that removal of this gel-like polyamate was not easy. Mechanical agitation was often required for removal, indicating that, under the right conditions such as limited immersion duration, there was strong adhesion between the amorphous hydrolysed polyimide and the untouched PI bulk underneath. When the OH^- ions cleave the imide ring, nearby K^+ ions become electrostatically immobilised by the newly created COO^- group, thus the polyamate layer can be more accurately designated as potassium polyamate and is primed for the following ion-exchange step. The reimidisation is basically this same reaction in reverse, and the reaction route is thermal rather than chemical.

2.3.3.2 Ion exchange

A short outline of this process is provided here for the introduction and understanding of relevant literature. More details can be found in the following chapter. An ion exchange material will contain a functional group that is either acidic (having a negative charge) or basic (having a positive charge) and is also either weak or strong. The carboxylic group described above is weakly acidic and can adsorb potassium or silver ions, with a selective preference of silver. This means that when a PI film with a modified PAA surface containing K^+ ions adsorbed at COO^- sites along the polymer chain is immersed in a solution of silver nitrate, the Ag^+ cation will displace the K^+ cation since it has a greater affinity. The functional COO^- sites within the polymer chain were quantified by Thomas in 1996 [81]. Qi *et al.* more recently demonstrated that, as well as silver carboxylate being formed, silver ions also bonded strongly with other functional groups along the polymer chain, such as the carbonyl and amide groups [82]. They also reported cross-linking of the PAA due to the silver ions and even a small amount of self-reduced silver particles. Further study of these phenomena would help optimise the metallisation process. Nevertheless, the COO^- group in the PAA is still thought to be predominant point at which Ag^+ ions become immobilised. There have been numerous successful demonstrations of embedded silver nanoparticles resulting from this process, some examples of which are presented in the following section.

2.3.3.3 Reduction of metal ions

The reduction of metal ions refers to the process whereby a positive ion gains an electron, reducing it to its zero-valent state. Therefore an electron source is required from which electrons can be transferred. If carried out in a solution, the Ag^+ ions will be floating freely and electron donor molecules can be mixed in. Transfer of electrons into a semi-rigid substrate matrix of PAA however, is more complicated and there are different ways by which to initiate reduction, namely electro, photo, chemical and thermal.

Electrochemical reduction is the process used in electroplating baths, where the electrode to be plated is immersed in the bath and functions as a cathode. The anode is made of the metal to be plated and a voltage is then applied across the two electrodes. If the cathode has a greater reduction potential than metal ions in the bath, this drives metal to be deposited onto the surface of the cathode. Chemical reduction is usually performed by reducing agents, or electron donors, dissolved in solution. When a metal object with suitable surface energy is placed in or in contact with this solution, reduction will occur. This is the basis of the investigations in Chapter 4. Thermal reduction is performed simply by elevating the temperature of the ions in a hydrogen rich atmosphere, such as air. While this is not the metallisation method used in this thesis, the reimidisation stage of the process in this thesis does require raising the temperature to reform certain polymer bonds. This effect forms a large part of the studies of Chapter 3. Finally photoreduction is the process where electrons in the vicinity of metal ions are excited by incident photons to an energy level, which will trigger reduction. Photoreducing agents can be used to assist this process. Photoreduction is more usually carried out in the liquid phase, with reactants and reducing agents in a single beaker for example. The following examples show how the different reduction routes have been applied to solid substrates, with more on photocatalytic reactions in the liquid phase in the next section.

One of the first successful demonstrations of this technique was given by Ikeda *et al.* in 2001 [83]. After the ion exchange of copper ions from a copper sulphate solution into the PAA matrix, TiO_2 colloids of approximately 20 nm diameter were then adsorbed on its surface. Exposure to a UV lamp through a photomask caused selective reduction of the copper ions. The resulting metallic layer possessed a conductivity of 1,120 μΩ·cm, which although not close to bulk, was claimed to be sufficient to act as an electroplating seed. Resolution however, was excellent for a photomask process, with 5 μm linewidths demonstrated. The main drawback is that colloidal TiO_2 precursors require a great deal of 'tuning'. Numerous factors affect electron transfer from the semiconductor crystals to the copper ions, such as nanoparticle size, size distribution and crystalline structure. It can be said that the full mechanisms are not yet completely understood. Although promising then, TiO_2 is not entirely suitable for the process without a fair degree of adjustment first and a catalyst with fewer critical variable parameters would be simpler.

Soon after publishing these findings, the same research group used water as an alternative photocatalytic layer [2]. After hydrolysis then ion exchange of polyimide in $AgNO_3$, the modified plastic was irradiated through a photomask with a UV lamp at 315 nm for one hour. Irradiance was given as 260 $mW \cdot cm^{-2}$. Before photomask exposure, a thin layer of water was pipetted onto the surface of the substrate for some samples. Without water small metal islands were formed through charge transfer from carboxylate ions to silver ions, creating carboxyl radicals and silver atoms. With water present on the surface, protonation of the carboxyl radicals from the water molecules resulted in the formation of carboxylic acid and hydroxyl radicals. It was postulated that the new presence of this acid on the top surface of the substrate could cause the more deeply bound Ag^+ ions to transport towards the upper surface by ion exchange with H^+ ions. Therefore more silver atoms are photoreduced in the presence of water at the top of the substrate. Even with the layer of water between substrate and photomask, 500 nm feature sizes were achieved with a resistivity of 14,000 μΩ·cm. Although the addition of an aqueous layer had a positive impact on silver formation, as well as requiring far less preparation than a TiO_2 colloidal solution, the process of handling and coating a substrate with a liquid when using laser or photomask equipment is cumbersome. An electron donor compound that could be used in the solid phase was proposed by Ng *et al.* to circumvent these issues [84]. Here they adapted a work using a liquid phase technique developed by Mallick *et al.* [85], which is discussed further in Section 2.4 below. After the usual imide ring opening and ion-exchange steps, embedding silver ions in this case, the surface was spin coated with methoxy polyethylene glycol (MPEG) in ethanol solution. After allowing the solvent to evaporate, the films were then either patterned with a photomask and broadband UV lamp (250 – 450 nm) or by continuous wave (CW) lasers at 325 or 375 nm. The photopatterned substrates were then placed in an electroless copper bath to form conductive tracks. The seed pattern created by laser was used to plate tracks of 100 μm while the photomask produced feature sizes as low as 15 μm. While the laser tracks appeared very well formed, the maximum scan speed was only 0.1 $mm \cdot s^{-1}$ and conductivity was not reported. It was however given as 3.1 $\mu\Omega \cdot cm$ for 50 μm photomask-produced test structures of 275 nm height, which is close to the bulk copper value of 1.7 $\mu\Omega \cdot cm$. Although the exposure time of 90 minutes was slightly longer than the water assisted report, the intensity of excitation was over 5 times less, at 48 $mW \cdot cm^{-2}$, suggesting an improvement in processing time when using MPEG as a reduction assisting agent. Ng *et al.*'s work here is essentially the basis for the experiments carried out in this thesis, and Chapters 3 to 6 investigate how to expand and improve this process.

Similarly, Chen *et al.* also employed a laser to induce photoreduction of Ag^+ ions in a PI substrate [86]. A pulsed rather than continuous wave laser at 266 nm was used and no electron donor material was applied, meaning any reduction would be attributed to laser excitation of the silver ions, although exactly how this process occurred was not explained. A range of scan speeds between 0.1 and 0.5 $mm \cdot s^{-1}$ were used to create a seed layer for electroless copper deposition. Although silver was produced, ablation damage to the PI was also reported, raising the possibility that broken bonds within the etched area of polymer could activate electroless plating of copper. Although they attained a linewidth of 30 μm, the highest speed with which conductive, unbroken tracks were achieved was 0.2 $mm \cdot s^{-1}$.

As touched upon before, (sub)processes for direct metallisation can overlap or be combined. Akamatsu's group, who are particularly active in ion-exchange and in-situ reduction, showed a novel combination of this with an ink-jet printing process [87]. Here, rather than modifying the entire PI film and ion-exchanging in ions to be selectively reduced, a KOH solution was printed at 5 $mm \cdot s^{-1}$ onto the pristine substrate. In other words, only part of the substrate was selectively modified. This has the advantage of minimising both the disruption to the integrity of the polyimide and the volume of ion exchange material used. Furthermore the reduction step can then be performed chemically, that is by straightforward submersion in a suitable liquid. In this case copper sulfate and dimethyl amine borane (DMAB) solutions were chosen as the respective ion-exchange and reduction solutions. Also, the lack of surface modification in unpatterned areas means that reimidisation is unnecessary. Resistivity values for the patterened tracks were not given but a value of 1.84 μΩ·cm was reported for a completely metallised PI sheet of unspecified dimensions. Although passing the Scotch tape test and achieving a 50 μm linewidth, a typical value for ink-jet processes, the inherent problems of ink-jet printing arise, such as the required fine-tuning of the properties of the dispensing liquid. In a similar method, Su *et al.* reported copper metallisation of selectively KOH modified PI [88]. Rather than printing the KOH, an unnamed 'alkali-proof' ink was screen-printed before KOH treatment. TEM and SEM images of the resulting metallic layers are comparable to other efforts but there is no discussion of adhesion or conductivity, although it is stated that the aim was to create a seed layer. The screen printing method only achieved 200 μm features and there have been no follow up reports by the group.

Another variation on the theme reported by the Akamatsu group was to selectively ink-jet print a PAA precursor solution onto a glass substrate [89], to be used as both an anchoring layer for embedded ions, and a glue to enhance adhesion of the final electrodeposited metal to the substrate. Since a PAA precursor was used, ion exchange could be performed directly without surface modification. The modification step was in effect replaced by the printing of the PAA precursor. After the PAA was printed, the solvent was evaporated and submersion in nickel acetate allowed an ion exchange reaction to occur. Chemical reduction was performed with sodium borohydride solution, with unreacted ions subsequently rinsed out with citric acid. Annealing and reimidisation were then performed before copper was electroplated onto the seed layer. While the patterns were low resolution at 300 μm, this did allow for resistivity very close to bulk value. The nickel seed layer appeared to be uniform enough to provide a regular copper deposition, but any adhesion results were not provided, with the final copper-PI films only being described as “highly adhesive” to the glass substrate.

Yet another variation on this fabrication theme was to use a PDMS stamp to first create trenches on the surface of the PAA, before forming a nickel seed layer for copper electrodeposition [90]. The entire surface was overplated with copper to ensure all trenches were filled, with the excess then polished down to the level of the substrate. This method produced tracks of approximately 5 x 5 μm in cross section with excellent uniformity and aspect ratio and resistivity only 2 μΩ·cm away from bulk values. Furthermore, due to the 'damascene' profile of the tracks, adhesion was further enhanced by virtue of interlocking contact mechanisms on three sides rather than one. While showing very promising results, the changes and additions to the process result in several more preparation steps. Furthermore, handling a PAA precursor requires more care than a PI film. In film form, the polyimide does not need to be cast onto a flat substrate and could be processed reel-to-reel, indicating a greater suitability to industrial scale fabrication.

Closely related to this, Yoon *et al.* used the same microcontact printing approach to pattern PI film with KOH for subsequent palladium ion exchange followed by electroless nickel and electroless gold [91]. 20 μm tracks were demonstrated, however no conductivity tests were reported and adhesion tests caused a high degree of damage to the plated tracks.

Investigations to further understand and characterise the modification-ion-exchange-reduction are still ongoing, with Cui *et al.* providing a thorough discourse on the chemical reduction of silver on polyimide [92], and much work has also been carried out to diversify and expand the process. Recently, Ikeda *et al.* successfully chemically reduced silver in transparent polyimide [93]. While no patterning was reported, this is of significant interest for visual applications, especially given recent excitement over curved and flexible displays. Other materials to be reduced from embedded ions in polyimide include tin compounds [94], copper oxide [95], magnetic iron oxides [96] and cobalt for use as a moisture sensor [97]. Graphene and CNTs have also been incorporated in the process by Zheng *et al.* offering promise in the area of conductive and semi-conductive polymers [98]. Another interesting application of the process was shown by Han *et al.*, where rather than casting PAA in a thin film form it was squeezed through a spinneret plate, in a similar manner to a garlic crusher, and collected in a bath of deionised water where the extruded fibres coagulated [99]. The resulting long strands were then passed into a standard ion-exchange bath before being thermally treated to achieve both imidisation of the PAA and reduction of the silver ions. Final fibre diameters were about 10 μm, however the silver was not particularly continuous and only found to be conductive after extended heat treatment, which in turn caused the fibres to become very brittle. This was attributed to thermo-oxidative degradation of the PI structure, catalysed by the silver NPs, an effect which was also observed during the course of experiments carried out for this thesis. As such, it is discussed in depth in the following chapter in Section 3.5.

Song *et al.* recently designed a MEMS polymer actuator based on sulfonated polyimide using the thermal reduction route [100]. Such actuators have a variety of applications from artificial muscles to biomimetic robotics and were previously fabricated using ion polymer metal composites (IPMC), which typically involved several processing steps including vacuum metal deposition or harmful chemicals. As well as being far simpler to produce by the embedded ion reduction method, performance compared to a 'standard' sensor, based on the Nafion polymer, was much improved. Displacements 6 times greater under a 0.1 Hz AC applied voltage were shown. Nickelised PI films have also been used as the substrate and cathode in a facile all-solution process to create inverted photo-voltaic (PV) cells, currently a burgeoning area of research [101]. It was found that nickel NPs increased absorbance by up to approximately 33% depending on the wavelength of incident light. This was attributed to the fact that the chemically reduced nickel was more granular than the standard aluminium that it replaced, resulting in greater light scattering and therefore additional absorption of energy from the reflected light. Finally Tian *et al.* utilised silver NPs in a PI film as a bistable layer to demonstrate nonvolatile memory behaviour [102]. Since their aim was to tightly limit the silver NP size to less than 10 nm, they opted for photo-based reduction, which allows greater control than chemical or thermal options. Although NPs at this size will not conduct, the theory is for the small isolated islands of silver to trap electrons. To test the device, a thin Ag NP doped PI film was coated onto an ITO-on-glass substrate, with gold islands then added on top to allow a voltage to be applied.

They noted that despite the numerous current transition mechanisms in the literature such as ohmic conduction, Schottky emission, tunnel or field emission, none was found to fit the characteristic of their device in both on and off states.

Surface modification and selective metallisation is a large field of research with many potential applications. Although silver NPs can have a negative effect on a PI substrate, they still offer a means to selectively pattern metals quickly without complexity. For reducing the metal ions, photoreduction appears to offer most control. Photo-based methods are not limited to solid substrates, indeed such methods were originally carried out with the substrate immersed in a solution, much like laser-assisted electroplating methods discussed previously. Many circuit fabrication techniques exploiting photo-chemical reduction and photo-catalytic processes have been attempted. These efforts are explored in the next section.

2.4 Photo-catalytic metal formation and deposition

This section looks specifically at photo-initiated reduction of metal ions. It is included not only because it is the origin of the use of MPEG in the present work, but also because it has spawned various other means of direct metallisation worthy of consideration. Furthermore it encompasses not just laser triggered reactions but also those initiated by lower intensity sources. As this photoreduction process continues and more metal ions are reduced, they begin to form small aggregates and grow into nanoparticles, with a continuous metal layer forming if enough source ions are present. As witnessed above, the donor material is often referred to as the photocatalyst or photo-reducing agent and can be organic or inorganic in composition. The remainder of this section is split into three sub-sections: Organic catalysts, semiconductor catalysts and photoreduction of organometallic compounds.

2.4.1 Organic photocatalysts

As mentioned in Section 2.3.3 above, Ng *et al.* pioneered the use of MPEG in solid form as a photocatalyst. This was an adaptation of work by Mallick *et al.* [85]. By using a 'one-pot' synthesis technique, meaning that all reagents, catalysts and products are in the same container, the experimental setup is simplified. The reactants and reagents were placed in a quartz cuvette, such as would fit into a UV-vis spectrophotometer, to allow for monitoring of the reaction. Once UV irradiation at 254 nm was applied, an absorbance band around 400 – 450 nm, the region of silver plasmonic resonance, was seen to form and expand, indicating the presence and growth of silver NPs. The resulting NPs were less than 100 nm in diameter and could be extracted via centrifugation, filtration and evaporation of the residual solution. While there is a sizeable amount of literature on the creation of silver NPs in solution, the liquid nature is difficult to work with. As such, work has been carried out to use other more easily manageable materials.

A gel based photocatalyst as opposed to liquid based was used by Deng *et al.* to demonstrate a practical, low cost process for forming metallic structures [103]. Firstly a CAD file of the pattern to be created was printed onto office paper using a standard inkjet printer and black ink, resulting in 200 μm patterns. A commercial black and white slide maker was then used to reproduce these patterns onto a special photographic film. This film consists of a 100 μm thick polyester backing, with a 2 μm thick coating of silver-halide-containing gelatin. Isolated silver NPs formed in the exposed areas were used as a seed layer for subsequent electroless deposition. In the paper, Deng *et al.* also demonstrated electrolessly plated gold with resistivity about 3.5 times that of bulk for 50 μm tracks, although 30 μm features were also shown. They also created a rudimentary 3 electrode microfluidic sensing device by attaching a PDMS block with pre-patterned microchannel to the surface. The chemistry of the reaction was not discussed, perhaps due to gelatin having a large number of constituent compounds and both UV source and the silver-halide photographic film being proprietary. Also, gelatin is not a particularly suitable substrate for any long term application. However it could find some application and freestanding electrolessly plated nickel structures were created. Although not prevalent in circuit fabrication circles, silver halides are still a popular medium in the print industry and also a popular choice of precursor for silver NP formation for various applications. Tian *et al.* provide an in depth review of this subset of photocatalytic materials, with particular focus on controlling the morphology at the nanoscale [104].

Matsubayashi *et al.* also utilised the photocatalysis in a novel manner to create ordered silver nanoclusters within PMMA [105]. Silver salts were mixed into the polymer precursor, which was then spin coated onto a reflective substrate. When placed under a monochromatic UV source, this substrate then reflected light that had passed through the PMMA. Standing waves are assumed to have been created and confined within the substrate, which could in turn shift metal ions and ion clusters into specific layers inside the polymer thus creating rows of NP a few hundred nanometers apart. It was also reported that the addition of a small amount of 4-tert-butylcatechol enhanced silver formation. While the intensity at the surface was only 26 $mW\cdot cm^{-2}$ and thus irradiation times were several hours, it presents a novel way to form optical components if not conductive tracks.

Fleancu *et al.* also recently created a similar complex involving gold nanoparticles, terming the process 'microemulsion assisted photoreduction' [106]. Although patterning or ordering of the NPs was not carried out, different concentrations of PEG in the mixture were used as an additive to control size of NPs from 2.5 – 30 nm for a given UV irradiation time up to 2 hours. Extending exposure after this time was also found to increase particle size up to 75 nm. The emulsion form of this mixture makes it a candidate for use in conjunction with other patterning techniques such as inkjet printing.

2.4.2 Semiconductor based catalysts

Semiconductors can also be employed as photo-reducing agents. As well as being dispersed in colloidal form throughout a solution or matrix similar to polymeric catalysts above, semiconductor materials can also be used as the substrate, as the reduction takes place directly on the substrate surface. While the semiconductor preparation adds complexity to the process, typical examples such as silicon and titanium dioxide in particular are abundant and very well researched. They function as a photocatalyst by creating electron-hole pairs when exposed to radiation that is of greater energy than their intrinsic bandgap energy. How long excited electrons stay in the conduction band is critical to the photocatalysic process, with adsorption of free metal ions onto the substrate surface and the transfer rate of charge carriers within the semiconductor itself, which affects how quickly electrons will diffuse to the surface from the bulk of the material. When in a liquid solution, molecules of oxygen and hydroxyl groups are easily adsorbed onto TiO_2 surfaces, which hinder the recombination of excited electron-hole pairs long enough to increase the likelihood of interfacial charge transfer with adjacent metal ions.

The study of the photocatalytic properties of TiO_2 is a Brobdingnagian field in its own right, evidenced by Carp *et al.*'s pre-eminent review from 2004 [107]. A more recent notable example is also given by Fujishima [108]. Much of the push behind this research comes from microsystems and solar cell industries. Due to the abstruse nature of electron transfer mechanisms however, more research is necessary to fully understand the effects that phenomena such as surface defects, doping and epitaxial growth have on photocatalytic efficiency. A recent example of patterning by this method was presented by Riassetto [109]. A precursor gel of tetraisopropyl orthotitanate mixed with ethanol, water and hydrochloric acid was spin coated onto glass substrates before heating to create the TiO_2 films. This method is often referred to as a sol-gel process. The substrate was then placed in a metallic acid solution, where exposure from a UVA lamp centred around 365 nm reduced the metal onto the TiO_2 surface. The size of the resulting NPs was shown to be tightly controllable between 2 and 20 nm but the durations of exposure required varied from 30 minutes to several hours, although the exposure time could be shortened by increasing the source irradiance. Also the liquid nature of the reaction hinders the ease of patterning as explained earlier. This problem was circumvented by Byk *et al.* [110], who created a titania-palladium composite for a similar process, with metallic ions embedded within the complex. The amorphous gel-like nature of this composite allowed patterning by placing a photomask between UV source and coated substrate, which in this case was glass. One minute exposure to a Hg-Xe UV lamp with intensity of either 8 or 30 $mW{\cdot}cm^{-2}$ created palladium NPs 2–3 nm in diameter, which were then used as a seed layer for electroless nickel. The different intensities conferred different properties to the Pd NPs, with the lower and higher values producing active and inactive Pd_0 respectively. Thanks to this effect, the same photomask could be used both negatively and positively. In the first case, the exposed active Pd_0 was used as the seed, while in the second, the exposed areas became inactive but it was found nickel could still be deposited on the unexposed Pd^{2+} ions. Adhesion of nickel was reported to be good for deposited heights or less than 2 µm, but values for conductivity were not given. Also despite the claimed 10 µm minimum feature size, the smallest displayed was 40 µm. Finally the use of palladium is becoming less popular, due to the relatively harsh nature of reactants and waste products.

Photocatalysis can also be the driving force in the LIFT process, inducing decomposition of material surrounding the semi conductor particles. Details of this method and examples have been discussed in Section 2.2.4 above.

2.4.3 Photochemical synthesis

Photochemical synthesis is the term given to reduction of organometallic complexes. Such complexes consist of a metal core bonded to organic ligands, typically by the latter donating an electron pair to the former. Given the right formulation these compounds can, when irradiated by a suitable energy source, decompose or cleave the organic-metal bond, resulting in a neutral metal atom and organic radicals. Its roots can be traced back to Baum *et al.*'s work on projection printing in 1986, where UV laser was shone through a photomask onto one side of a quartz substrate, causing photolysis of a gold organometallic complex in the vapour phase on the opposite side of the substrate [111]. Although equipment to store the organometallic vapour at the right pressure was slightly complicated and sheet resistivities reported were several orders of magnitude greater than bulk values attributed to carbon contamination, 2 µm features were deposited, proving the concept and laying the foundation for future developments.

Dicks *et al.* improved on this with well-defined 10 µm platinum test structures on silicon substrate through a photomask, which possessed resistivity only one order of magnitude greater than bulk [112]. Despite the organometallic patterning method eliminating several process steps from standard metal photolithography, it required a 2 hour exposure to reduce the metal ions and over 12 hours for their subsequent annealing and organic residue evaporation, rendering it a lengthy overall process.

By creating and deploying a silver precursor, Byun *et al.* further improved on this by creating 5 µm patterns after only 90 seconds of broadband UV exposure, also through a photomask [113]. While encouraging, the lowest resistivity of the 4 different precursors under test was still 5 orders of magnitude greater than bulk. Furthermore, this process was also time consuming, with preparation of the organometallic complex requiring painstaking drop-wise mixing of reagents followed by 4 hours of stirring and two filtration steps. This is perhaps one of the main drawbacks with the organometallic method, in that it requires large and specific knowledge of the properties and behaviour of inorganic and organic compounds to formulate the complexes. It is not without its uses however, as it has been used to pattern sulfonated poly(ether-ether)ketone (SPEEK), part of the PEEK family of plastics which have been traditionally some of the most difficult materialls to metallise. By mixing the SPEEK with PVA, a popular matrix for metallic nanoparticles, Korchev *et al.* created a substrate that could be doped with silver ions via ion-exchange with the hydroxyl groups of the PVA [114]. UV irradiation then caused radical generation of SPEEK molecules, which were found to aid in the photoreduction process. Although this method requires few steps, the exposure time was 30 minutes and so not ideal, but the simple readily available chemicals used allow preparation time to be significantly reduced.

Bernabo *et al.* also took advantage of PVA as a carrier matrix for silver NPs, curing a thin film of it to create a novel strain sensor [115]. By embedding specially formulated anisotropic silver nanorods and casting the PVA in a certain direction before curing, the nanorods would align well in this direction. This feature gives the film dichroic properties: if observed through a linear polariser, depending on the angle of the incident polarisation light in relation to the casting direction, the film will take on a different colour, which can be used to detect strains within the film for example.

NPs/colloids in solutions are also a source for ink-jet and aerosol printing. In that regard, Kim *et al.* successfully removed the use of finely tuned NP precursors by mixing either gold or silver acids with sodium borohydride, a relatively simple compound [116]. Mixing this with polyvinylpyrrolidone (PVP) resulted in a stable liquid complex, from which metallic aggregates of 2 – 10 nm were produced by laser irridation at UV (355 nm) or green (532 nm) wavelengths. By changing the excitation wavelength and exposure time, the size and distribution uniformity were controlled. However, exposure times were required to be as high as 30 minutes. Also, while this is particularly useful work at the nano scale, it still requires a means to allow patterning at the micro and meso scales.

2.4.4 Photoplasma

As well as using chemicals in liquid or gel forms, plasmas have also recently been used as photocatalysts. When a plasma electrode is subjected to a current, electrons in the plasma become more mobile. By placing such an electrode in close proximity to a substrate or coating containing metallic cations, a reduction reaction can be initiated. Charbonnier *et al.* benchmarked such a technique against chemical and deep-UV methods for electroless nickel plating without the use of a palladium catalyst on a variety of substrates [117]. They found that, although most efficient at reducing nickel ions, plasma treated samples would not initiate plating in a low phosphorous content electroless bath, while chemically reduced samples would. For a high phosphorous bath however, plating for both was comparable and adhesion was generally excellent for all substrates tested other than PTFE. Further, the plasma method took a maximum of 60 seconds, with around 15 – 30 seconds found to produce both fastest reduction and best nickel concentration on the surface. They also noted however that deposits over 0.2 μm in height were highly prone to cracking, although this could also be attributed to the bath chemistry. During UV reduction tests the organometallic precursor, nickel acetate, was found to be too stable for UV decomposition so no deposits were formed by this route.

While the work by Charbonnier *et al.* did not address how to achieve site-selective reduction, Lee *et al.* have recently developed an original, more 'immediate' version of the plasma method, performable at atmospheric pressure which does [118]. Comparable in equipment setup to laser-based processes, a plasma beam is scanned across a target material consisting of metal ions embedded in either PMMA or PVA. This polymer-ion mixture is coated onto a silicon substrate, which acts as a grounding electrode for the plasma during patterning. The plasma is created by directing argon gas downwards at the target material through a stainless steel capillary tube perpendicular to the substrate. A large voltage of around 2 kV is then applied to ignite the plasma, which is stabilised to a constant current. The process was shown to work for PMMA and PVA polymers with a variety of metals (Ag, Au, Pt, Ir, Ru) and carries high potential for increasing its scope. Furthermore, the plasma 'beam' could be on constantly and so it has potential for upscaling. However the 150 μm lines produced were rather ragged at the edges and no conductivity measurements were discussed, although this does not preclude the patterned metal from being used for plasmonic or electroless plating applications. Also, the maximum scan speed reported was 30 mm·min^{-1}: a long way short of large scale production. It is nevertheless a promising avenue for further research since the setup is not overly expensive, with argon being relatively cheap, or the cheapest noble gas at any rate, and also the work is recent so improvements can be anticipated.

While some photo-based methods, such as one-pot and other liquid precursor techniques are not suited to large scale production, the ideas here can and have been extended to gel and solid complexes. Formation of metals on the nano scale, while not comprehensively understood, has been studied and performed extensively, and while NPs and metal colloids have a wealth of applications, their application at the micro and larger scales most often requires deployment as part of a longer fabrication chain, in conjunction with processes such as inkjet printing. Although not the direction of this thesis, a particularly informative tutorial style review paper on the function of light in colloidal NP formation was very recently published by Grzelczak and Liz-Marzán [119], with a more exhaustive summary of the field supplied by Sakamoto *et al.* [120]. The work of this thesis however, is to further characterise and expand the process as first laid out by Ng *et al.*, described in Section 2.3, which adapted a liquid based photo-reductive process to create a solid layer as electron donor. Before discussing the work of this thesis in the next chapter however, it is necessary to look at a final category of competing technology, which has perhaps gained most prominence of all direct writing processes.

2.5 Inkjet and aerosol printing

Inkjet printing is an enticing choice for circuit fabrication for several reasons. It is substrate indiscriminate, has low material and waste costs and can be performed at low temperature when compared to silicon processes. This last point allows materials such as plastics to be patterned which, due to their diverse nature, paves the way for substrates with novel attributes, such as having flexible, bendable or even stretchable properties. Furthermore, inkjet printers have been commercially mass-produced for upwards of 30 years, which considerably lowers the cost of equipment. Predictably then, several efforts have been made to modify the process for various uses, including circuit fabrication. There are two main principles by which inkjet printing operates: continuous inkjet printing (CIP) and drop on demand (DOD). CIP, the more mature of the two methods, works by expelling a continuous stream of liquid through a nozzle. Such a jet has a natural inclination to break up into droplets due to surface tension, a phenomenon known as Plateau-Rayleigh instability. Droplet size can be controlled by encouraging this effect through the application of modulated disturbance to either the nozzle or the ink, typically in the form of periodic current passed through a small heating element or via a piezoelectric transducer. The jet is aimed through a charging electrode, inducing a charge on each drop, which can be varied by changing the potential of the electrode. The drops then pass through a steady electric field, which deflects them depending on the magnitude of their charge. Uncharged particles pass straight through the field and are collected in a 'gutter', while charged particles will be deposited on the substrate at a position dependent on their charge. This is shown in diagrams from Martin *et al.* 2008 in Figure 2.7(a) below [121].

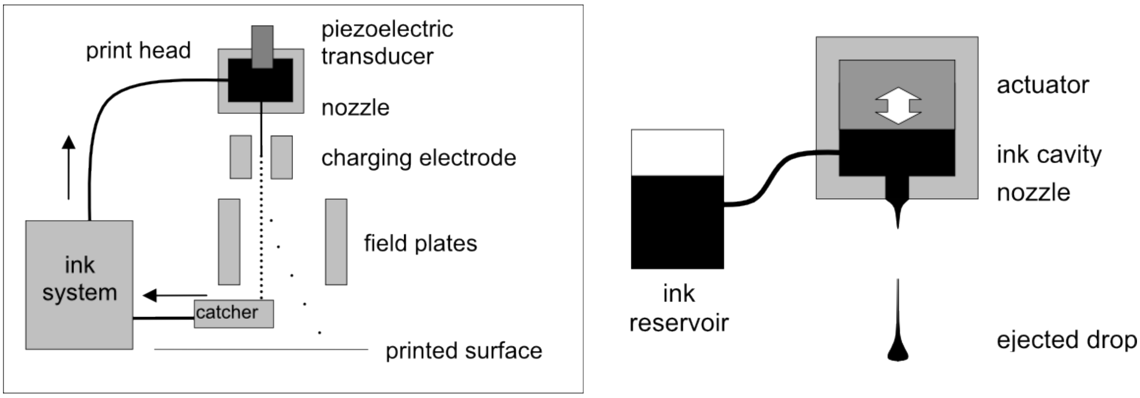

Figure 2.7: *Different inkjet printing methods. (a) Continuous Inkjet and (b) Drop on demand [121].*

Even with the gutter connected to the ink source to allow for recycling of unprinted ink to reduce waste, this introduces the potential for contamination from the external environment. Combined with the fact that the material to be printed must also respond to an electric field, this means that this choice limits the range of printable materials. Although CIJ has been utilised for some materials such as 3D ceramics printing, DOD has proven to be far more popular for fabricating functional materials such as circuits [122]. In this method, shown in Figure 2.7(b) above, drops are only expelled from the ink cavity when they are required for printing, eliminating the need to recycle the ink. Drop expulsion from the ink well is triggered by a pulse from a thermal or piezoelectric actuator. Thermal actuation is the predominant means employed in standard office or home-based printers, involves the vaporisation of a small amount of ink to create the pressure necessary for droplet ejection. This method limits the choice of material for the ink as a degree of volatility is required. Furthermore, DOD typically produces finer feature sizes than CIJ. Thus it is not surprising that the majority of inkjet printing for circuit fabrication processes use piezoelectric DOD methods, as there are no such limitations on material choice.

While substrate material choice for printed circuits is not limited, preparation of ink has many constraining factors. For printing of organometallic complexes or metal-containing matrices, the formulation must be such that metal deposits are conductive, or at least possess sufficient surface energy to initiate subsequent electroless plating. This will have an effect on the density, viscosity and surface tension of the liquid. Key parameters for inkjet printing are best characterised by the dimensionless Reynolds and Weber numbers, *Re* and *We* respectively:

$$Re = \frac{\rho v D}{\mu}, \tag{2.1}$$

where ρ = liquid density, v = fluid velocity, D = pipe diameter (for circular pipes) and μ = dynamic viscosity and

$$We = \frac{\rho v^2 l}{\sigma}, \qquad , \tag{2.2}$$

where l = droplet diameter and σ = surface tension. The sensitivity of the inkjet process is highlighted by Figure 2.8, taken from Derby [122], where the Ohnesorge number, *Oh*, is third useful fluid flow comparator, defined as:

$$Oh = \frac{\sqrt{We}}{Re}, \tag{2.3}$$

which gives a value indicating the relative impacts of fluid viscosity and surface tension. These factors have an influence throughout the ink transfer process, affecting droplet generation, flight of ejected droplets, droplet-substrate interaction and post-printing mechanisms of drying/evaporation/solidification. Therefore the 'window' for an acceptable in formulation is somewhat limited. However, as pointed out above, the process has been the subject of much study and many successful examples of its application exist, as the following examples show.

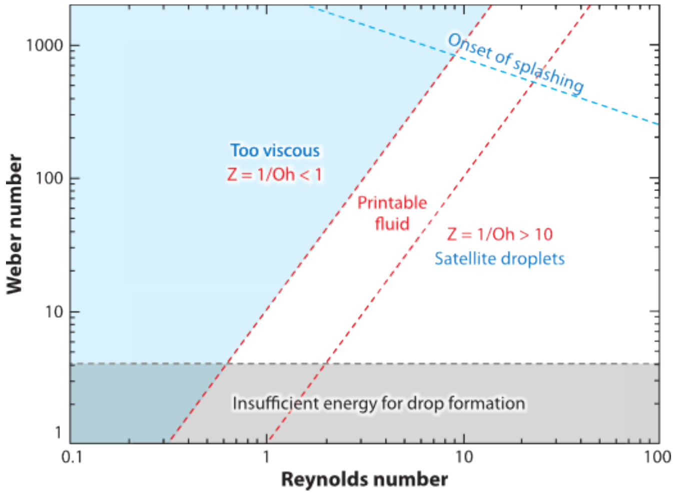

Figure 2.8: *Plot highlighting window of ideal ink characteristics. Red dashed lines represent constant Ohnesorge numbers [122].*

A final step often necessary in the printing of conductive tracks is post-print sintering. Since the ink viscosity is crucial for droplet ejection, impact on substrate and spreading, the percentage loading of metallic NPs or organometallic complexes cannot be too large. This has the negative effect of constraining potential conductivity due to reduced number of electron pathways at lower metal content. This can be compensated for, at least partially, by sintering, which causes metal particles to become more densely packed, thus reducing porosity. Temperatures of 200°C and above are usually required for sintering however, a temperature that narrows the choice of substrates, especially when dealing with plastic and flexible candidates.

Non-thermal routes for sintering or metal growth, such as by microwave, laser-assisted sintering and chemical means have been explored however. An example of the latter was recently demonstrated by Chen *et al.* [123]. A toluene solution containing silver NPs was prepared and printed onto transparent PET using a commercially available 5,760 dpi desktop printer. The printed nanoparticles exhibited good size distribution at 6.2 ± 0.57 nm on average, as seen in Figure 2.9(a) below. Further, no adverse effects on deposit stability were found after storage for 30 days at -25°C. Subsequent silver reduction by submersion in hydrazine solution showed relatively uniform covering at the nano scale, seen in Figure 2.9(b). At the micro scale however, the 212 μm wide tracks showed poor uniformity, seen in Figure 2.9(c). While this qualitatively suggested excessive porosity, the calculated resistivity of 26,200 μΩ·cm, 4 orders of magnitude greater than bulk, confirmed significant room for improvement. Sintering at the relatively low temperature of 100°C, necessarily low to protect the PET substrate, improved upon this by an order of magnitude but this is still less than ideal, and also negates somewhat the reasons for choosing an alternative metal growth method. Furthermore, hydrazine is a particularly undesirable chemical, registering high on the scales for volatility, toxicity and harmfulness to the environment.

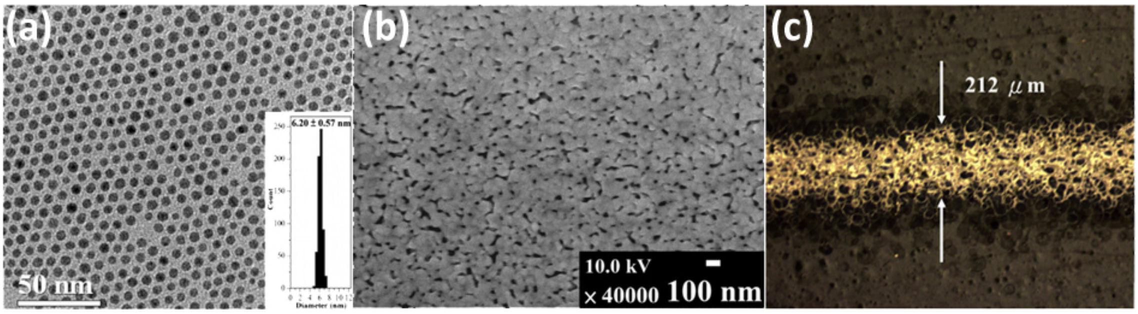

Figure 2.9: *(a) TEM image of silver NP ink suspension, (b) SEM image of chemically reduced silver track and (c) microscope image of test track [123].*

However, better results using thermal sintering on PET using ink consisting of silver nitrate dissolved in a solution of ethanol, ethylene glycol and 1-dimethylamino-2-propanol (DP) were demonstrated by Wu *et al.* [124]. As well as these chemicals being more readily available the DP acts as a reducing agent for the silver when heat is applied, allowing thermal sintering to occur at a temperature favourable to the PET substrate – up to 100°C. This method showed improved resistivity, only one order of magnitude more than bulk silver for 100 μm wide lines. The same group had previously deposited 50 – 60 μm silver tracks onto PI by the same method, allowing a higher sintering temperature of 200°C to be used [125]. The resistivity was slightly larger however, but of the same magnitude at 27 μΩ·cm. Although ozone treatment was applied to the hydrophobic PI film before printing in order to improve adhesion, little information is given other than reporting it achieved the highest rating of 5B (or 100% coverage remaining) in the ASTM-3359D Scotch tape test. Figure 2.10 taken from the first paper gives an indication of the challenges of refining the inkjet process through modification of nozzle size and droplet spacing.

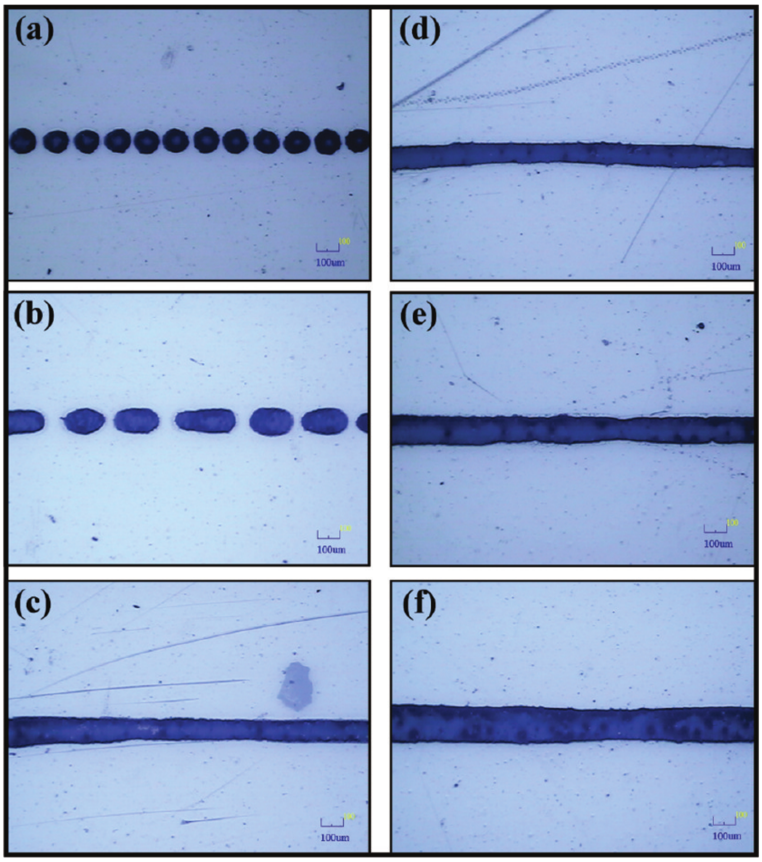

Figure 2.10: *Effect of droplet spacing on printed track integrity. Droplet spacings of 140, 120, 100, 80, 60 and 40 µm correspond to images (a–f) respectively [124].*

Another recent set of results dealing with inkjet-printed metal adhesion to PI was published by Lee and Choa [126]. Firstly they created a 15% by weight copper complex ink by placing copper electrodes in a solution consisting of dilute formic and acetic acids and ammonium hydroxide solutions and applying a voltage to generate copper ions from the source electrodes. Varying amounts of 3-amino-propyl-trimethoxy-silane, APS, a member of a family of silane compounds relatively well known for their adhesion promoting qualities, were then added. Before printing the PI substrate was plasma etched to create hydrophilic hydroxyl groups through breaking of C–C and C–H bonds, similar to the KOH treatment central to work described in this thesis, albeit acting on different chemical bonds and with more expensive equipment. When in solution, the APS forms silanol groups, and then an oxane bond with the plasma-created hydroxyl groups on the PI surface as well as CuSi$^+$ being easily formed from the reaction between Cu$^+$ and SiH, both of which aid adhesion. Finally the substrates were annealed at 200^{o}C for

2 hours in a hydrogen atmosphere. Although best resistivity was obtained with 0% APS, this also proved to have poorest adhesion of the range tested as tested by the same formal peel test above. While the resistivity increased with increasing APS up to 4% wt, the peel strength reached a peak of 4B, or >95% remaining coverage, at 3% wt, suggesting this to be the optimum trade-off. Results from the adhesions tests can be seen in Figure 2.11 below. Although the resistivity of this solution was found to be approximately 20 μΩ·cm, the minimum linewidth was 100 μm and plasma etching treatment requires an expensive plasma chamber, which in turn requires a specific gas rather than open air.

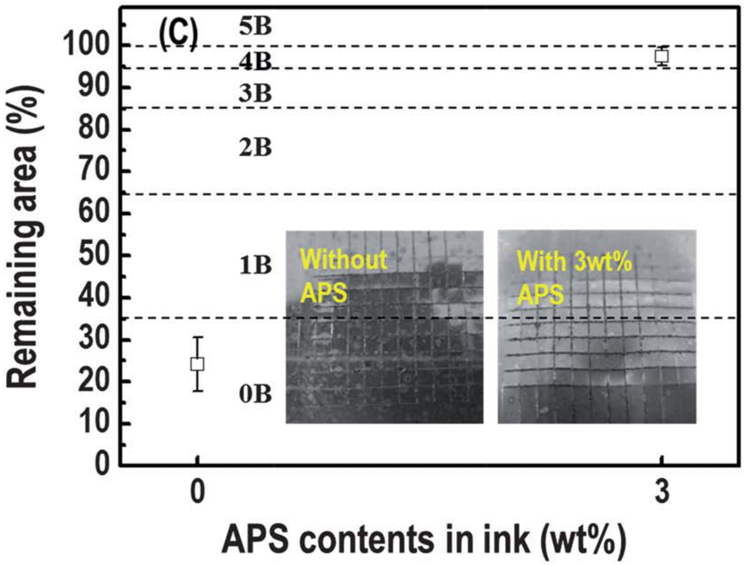

Figure 2.11: *Adhesion test example results from Lee and Choa [126]. Addition of APS to ink is necessary for adhesion.*

Finer feature sizes are possible by this method however as shown by Choi *et al.* who fabricated a silver temperature sensor on PET with approximately 30 μm linewidth and 60 μm gap [127]. They employed electrohydrodynamic forces below the nozzle on the liquid in the ink reservoir to extract ink from the nozzle and form droplets, a method which allows reduction of droplet size to one third the diameter of the nozzle. This has the advantage of allowing more viscous ink, enabling higher concentrations of metal nanoparticles to be printed. Indeed, the proprietary ink Choi *et al.* used contained 55% wt silver NPs, although the reported resistivity of 25 μΩ·cm was comparable but did not improve upon resistivity of the previously discussed papers. Furthermore, mention is made of multiple passes being employed but this is not quantified, making it difficult to judge the overall speed of printing. Also no parameters are provided for the post-print IR curing stage, so its effects are unclear. No mention is made of adhesion either. Choi *et al.* did place the printing equipment within a roll-to-roll manufacturing system commonly used for processing PET substrates. This highlights the increasing suitability of inkjet printing for circuits at an industrial scale.

Much finer resolution of approximately 1 µm of printed silver tracks was demonstrated in 2007 by Murata [128], as shown in Figure 2.12(a) below. Here proprietary ink containing 57 – 62 %wt silver NPs was printed onto various substrates. Unfortunately due to the lack of information, details of the printing equipment are also presumed to be commercially sensitive. It cannot be a DOD system, since the minimum volume for piezoelectric DOD printing is generally accepted to be approximately 1 pL or a 12 µm diameter drop [122], and the drop will then spread upon contact with the substrate, increasing the size. It is then predicted that some form of bespoke EHD system, similar to that employed by Choi *et al.* above, was used to manipulate the ink into small drop sizes. No experimental values for the resistivity are given, although the ink specification claims to be approximately twice that of bulk after curing. Such curing requires temperatures of 250^{o}C or above however, ruling out its use on more delicate substrates. The resulting 50 µm interconnects shown in Figure 2.12(b) appear reasonably well formed.

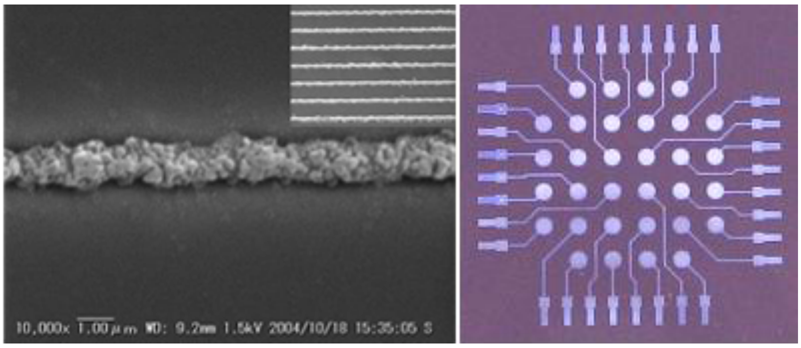

Figure 2.12: *(a) 1 µm inkjet printed tracks, (b) 50 µm interconnects [128].*

Aerosol jet promises improved feature sizes and faster write speeds. Although papers and patents for aerosol jet printing can be found as early as the mid 1970s, mature systems arose only in the last 10 – 15 years for practical applications. In the Optomec system, ink is placed in an atomizer, which converts the liquid into a dense aerosol consisting of droplets 1 – 5 µm in diameter. This is achieved either ultrasonically or pneumatically depending on the viscosity of the ink. These droplets are then carried from the atomizer chamber to the deposition nozzle by a nitrogen gas flow. The geometry of the nozzle is specially designed with an extra input for 'sheath' gas expelled in an annular flow, which collimates the aerosol output 'beam' in the middle as illustrated in Figure 2.13(a) [129].

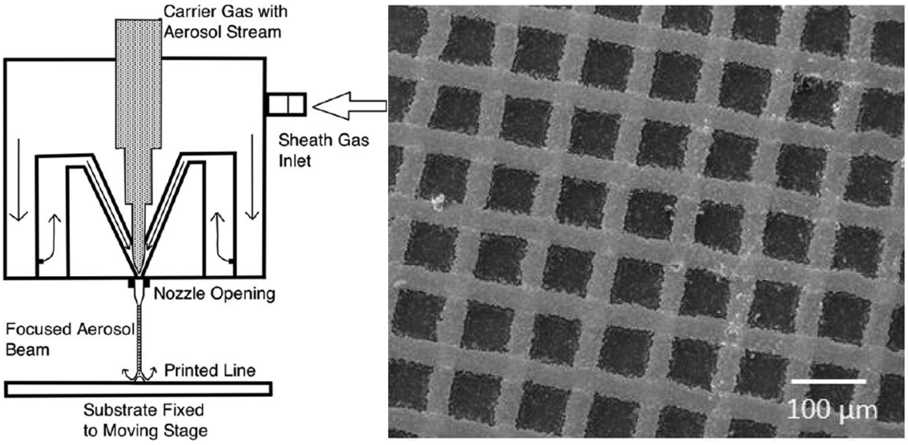

Figure 2.13: *(a) Aerosol printing nozzle, (b) printed tracks [129].*

In their study, Mahajan *et al.* printed proprietary silver NP ink on silicon and PI substrates as shown in Figure 2.13(b). As well as successfully depositing 20-100 µm wide lines at a speed of 100 mm·s^{-1} for a resistivity only twice that of bulk silver, they provided a thorough characterisation of the four key process variables: nozzle diameter, carrier gas flow rate, translation stage speed and focussing ratio defined as the ration of the sheath gas flow rate over the carrier gas flow rate. While some of the complications of drop formation in earlier printing techniques are negated by aerosol spray, the effect of the gas flow rate requires fine tuning. They also reported that, for higher scan speeds, printed lines were initially snakelike before straightening out. Furthermore, higher speeds were noted to require higher carrier gas flow rates, although it is doubtful this would be of great importance. As well as being capable of micro-scale features down to 10 µm [130], print heads are available to increase linewidth to 5 mm, making this option particularly attractive for rapid prototyping of devices requiring different sized interconnections. This technique has been used successfully in several applications of great current interest, such as the work from Jones *et al.* or Ha *et al.* on TFT [131, 132], PV development by Yang *et al.* [133] and strain gauge fabrication by Li *et al.* [134]. A summary with further applications of aerosol jet was also recently given by Hoey *et al.* [135].

From the examples given in this section, it can be seen that ink-based technologies have a lot to offer the world of direct metallisation. Although 'traditional' branches such as CIJ and DOD may be reaching their fundamental limits in terms of minimum feature size, the EHD and aerosol techniques that have evolved from them strive to remain at the forefront of fabrication methods. This has been aided by several major equipment suppliers being well established in the inkjet printing business. Furthermore, it is a simple method to quickly generate design variations and prototypes, for example when combined with a CAD system. Ink formulation, especially when dealing with metallic NPs, can be complex, although this is maturing. Despite this, and although the systems for aerosol are somewhat complex and not at a competitive price level to a low power laser, this is perhaps therefore the area from which greatest competition for the technology developed in this thesis will come.

2.6 Chapter conclusions

Following a thorough review of relevant literature, a platform has been provided for the work to be undertaken in following this chapters. Although the process under investigation is not strictly bound within a single category as defined by Figure 2.1, it can be seen from several of the examples given that it is not uncommon for modern fabrication methods to combine different techniques. It can also be seen that there is a great variety of different technologies available and therefore there is great competition to get any new technologies recognised and adopted. The main merits and drawbacks of the primary electronic fabrication methods are compared with the work in this thesis in Table 2.1 below. The various direct write and direct metallisation processes discussed are summarised in terms of their feature sizes and write speed capabilities are shown in Table 2.2 below.

The work in this thesis can be described as a combination of reduction of embedded metal ions catalysed by organic photo-catalytic agents. By this definition the process can be described as a hybrid form of direct metallisation consisting of surface modification, discussed in Section 2.3, and photo-catalytic metal formations, discussed in Section 2.4. As shown in the following chapters it is versatile enough that it can not only be employed as a laser direct write process, discussed in Section 2.2, but it will also be shown that low intensity lights can be used for large area exposure thanks to the investigations of this work. Subsequent chapters investigate the effects of various process parameters on the substrate and metal formation and look to develop and diversify the process to maximise its range of potential applications.

Criterion	**Industrial process**			
	Photolithography	**Vacuum deposition**	**Printed electronics**	**DW process of this thesis**
Type	Subtractive	Additive	Additive	Additive
Cost	High	Moderate	Low	Low
Speed	High	Low	Varies	Low
Processing temperature	High	High	Low	Medium
Environmental	High volume hazardous waste	Some hazardous waste	Low volume waste, may not be hazardous	Low volume, low hazard waste
Resolution	Very high	Low	Low for most applications	Low
Status	Well established	Well established	Emerging	In development
Example products	CPUs, memory	OLED, surface coatings	RFID, PV, other applications arising	Interconnects, flexible passive components

Table 2.1: *General merits of circuit fabrication technologies.*

Direct write / metallisation process	Mechanism	Linewidth (µm)	Write speed (mm·s^{-1})	Materials	Selected Ref(s)
Laser based					
Laser activated electroplating	Enhanced chemical reaction due to localised heating	0.1 – 300	10	Metals on Metal	13
LEEP	Thermal decomposition of plating bath components	2 – 150	0.4	Metal/ceramic on inorganic substrates	15 – 18
Laser consolidation of thin solid films	Melting/fusion of materials onto substrates	10 – 50	2	Metals & ceramics on metal or ceramic	19 – 21, 24, 25
Laser induced transfer					
LIFT	Material transfer by vapourising a carrier matrix	10 – 100	50	Numerous	28, 29 33
MAPLE-DW	Material transfer by vapourising a carrier matrix	1–100	70	Numerous	41, 44, 45
LIBT	Deposition from liquid/vapour via irradiation through underside of transparent substrate	5 – 200	300	Metals & ceramics on transparent substrates	46
Surface modification					
Surface activation through substrate damage	Opening of chemical bonds on substrate surface	15	1	Metals on organic & inorganic substrates	52 – 57
Polyelectrolyte anchoring layers	Multilayer build up of alternately charged polyelectrolyte layers	1 – 20	n/a	Metals on organic & inorganic substrates	64 – 66
MACP	Diffusion of catalytic salt onto substrate from carrier matrix polymer	1 – 150	Depends on writing method	Various	76
Reduction of embedded metal ions	Metallic growth from ions embedded in substrate	20	50	Metals grown on organic substrates	2, 6, 82 – 84, 86 – 102
Photo-catalytic metal formation and deposition					
Organic	Light-triggered metal growth	30	photomask exposure	Metals on/in organic substrates	103
Semiconductor based	Semiconductor enhanced photoreduction	40	0.6	Metal on inorganic	110
Photochemical synthesis	Metal cores bound to organic ligands	5	photomask long	Metal on polymers or semiconductors	113
Photoplasma	Current passed through electrode to mobilise electrons in plasma	150	0.5	Various	118
Droplet based					
Inkjet	Droplet deposition by either breakup of continuous jet or individual droplet generation on demand	20+	50	Liquids	124 – 128
Aerosol	Ultra-fine 'atomised' droplets deposited on surface	5 – 5mm	100	Liquids & any atomisable material	129, 131 – 134

Table 2.2: *Summary of selected direct write and direct metallisation processes*

Chapter 3:
Direct writing tests and substrate degradation

3.1 Introduction

This chapter describes in depth the direct writing process in Section 3.2 and lays down the experimental procedures in Section 3.3 before discussing the results of the initial tests in Section 3.4. These tests reveal that, while laser induced reduction is effective at producing silver nanoparticles, it also causes degradation of the polyimide substrate. This degradation causes warping of the metal tracks, which in turn reduces the uniformity of the seed layer for subsequent electroless plating. Substrate degradation and silver particle growth are therefore examined in Section 3.5 and the mechanisms affecting these are studied to reduce their deleterious effects. The work in Sections 3.4 and 3.5 was carried out collaboratively with Jack Ng.

3.2 Detailed process description

The method of forming metal tracks on polyimide is relatively straightforward. Polyimide film is surface-modified using a strong alkali solution then doped with silver ions. These ions are selectively reduced to silver nanoparticles by exposure to a UV light source. Any remaining ions in unexposed areas subsequently rinsed away, leaving silver tracks which are then electrolessly plated. As previously discussed in Section 1.3 and highlighted in Figure 3.1 below, this manufacturing process originally formulated by Ng *et al.* [6] consists of seven steps.

Firstly, the silver ions must be embedded into the substrate, which is accomplished in the first two steps of the process. To achieve this, advantage is taken of the chemical structure of the polyimide chain. The imide monomer, called pyromellitic dianhydride-co-4,4’-oxydianiline (PMDA-ODA), contains two functional imide groups, highlighted in red in Figure 3.2 below.

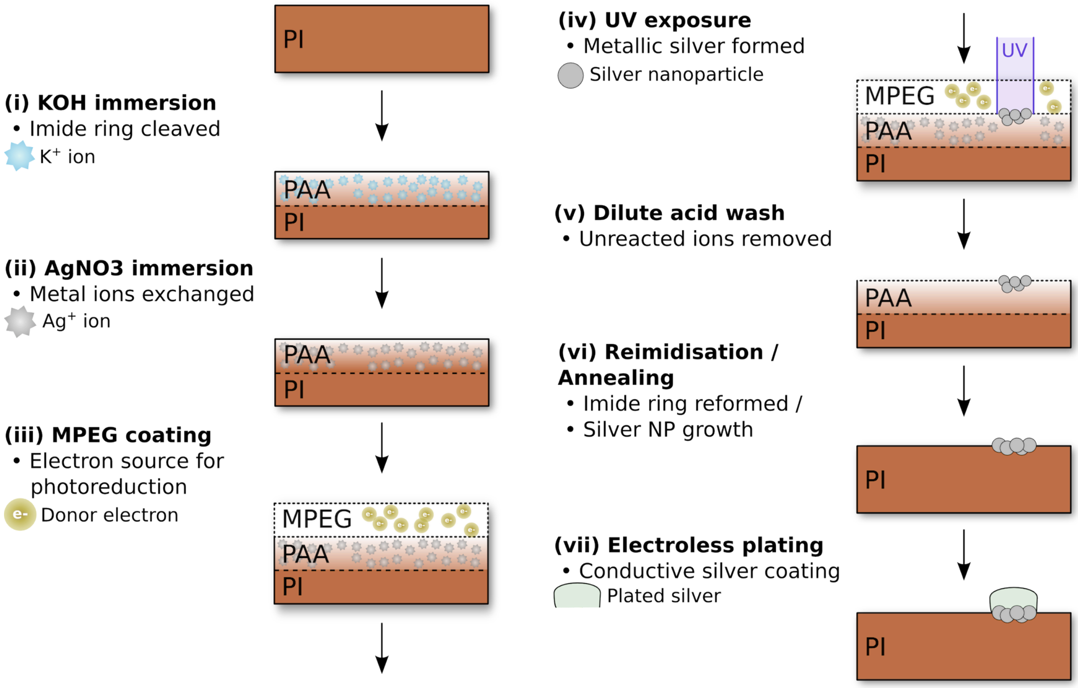

Figure 3.1: *Full procedure for substrate preparation for metal patterning of polyimide substrate.*

This imide sub-structure can be cleaved, breaking one of the two C–N bonds by exposing the polyimide to a strong base, such as potassium hydroxide (KOH). Potassium ions in the solution dissociate from their hydroxyl –OH bonds in solution and form electrostatic bonds with the hydroxyl groups in the polyimide, splitting the imide ring. The resulting molecule is a type of polyamic acid (PAA) or potassium polyamate, shown in Figure 3.3 below.

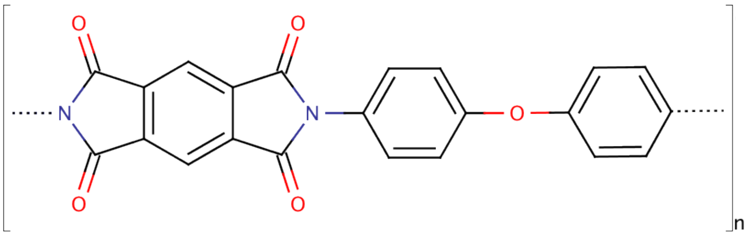

Figure 3.2: *PMDA-ODA monomer. Functional imide groups highlighted in red.*

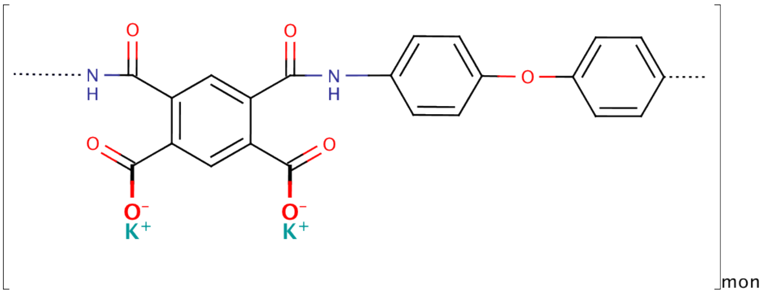

Figure 3.3: *Potassium polyamate acid monomer.*

In the second process step, the substrate, which now consists mainly of polyimide with a thin layer of PAA on the surface, is then submersed in a silver nitrate solution ($AgNO_3$). The silver half reaction, i.e., half of a reduction-oxidation (redox) reaction, has a reduction potential of 0.80 V, higher than the potassium half reaction potential of -2.92 V [136]. This means that silver cations will more readily associate with the negative carboxylic ions of the PAA than the potassium cations and thus displace them, forming silver polyamate on the substrate surface by an ion-exchange process [2, 84].

The silver ions are then reduced to their zero valent atomic state in steps three and four of the process as shown in Figure 3.1. This is achieved by initiating the silver reduction reaction:

$$Ag^{+} + e^{-} \rightleftharpoons Ag_{0} \tag{3.1}$$

Silver more readily exists in its neutral zero valence state than in its ionic state electrostatically bound to a negatively charged polymer, but it requires a source of electrons. Chemicals known as electron donors are ideal for this. Such chemicals have a low ionisation energy and so will readily oxidise, or donate electrons, if a chemical species with suitable electron affinity is present to receive these electrons. As noted in the previous chapter, water, poly(vinyl pyrrolidone) (PVP) and alcohol have all been used in this capacity [87, 137, 138] but methoxy-(poly)ethylene glycol (MPEG) has also been used in redox reactions [85] and was discovered to be more effective when first deployed in the present fabrication process [84]. The mere application of such an electron donor to the substrate is not sufficient to trigger the reduction reaction however, although reduction in this case will happen naturally over a period of weeks. An input of energy into the system is required to catalyse and accelerate the reaction. This increase in speed can be accomplished thermally, chemically, or, in the case of the direct writing process under examination, photo-chemically in the form of UV light irradiation. Photons from the light source excite electrons in the donor to an energy level from where they can escape more easily. At this higher excited level, the electrons are in a much better position to combine with the silver cations on the substrate and reduce the silver to a stable, neutrally charged state, as seen in Figure 3.1, step (iv) above.

This phenomenon is exploited to create patterns of silver nanoparticles wherever the silver ions are exposed to the UV light. As previously mentioned the reduction of silver occurs naturally on a long timescale. This is undesirable as this reduction could cause electrical problems, such as current leakage or short circuits between adjacent silver tracks. To circumvent this, the substrate is submerged briefly in dilute sulphuric acid (H_2SO_4). This has the effect of removing any unreacted silver ions from the substrate by a second ion exchange process. Hydrogen ions in the acid solution displace the silver ions within the PAA in the same way the silver ions displaced the potassium ions previously. Neither the substrate nor the newly created silver nanoparticles are affected by this reaction. The next stage is to reform the imide ring that was cleaved in step one. This reimidisation reforms the bonds as depicted in Figure 3.2, leaving the silver nanoparticles embedded in the substrate between the polymer chains, but without the potassium ions being present. Reimidisation can be performed chemically or thermally, with the thermal option being the more practical. This is simply achieved by heating the substrate in an oven.

Finally, the substrate is placed in an electroless plating bath. The silver patterns act as a seed layer to initiate the autocatalytic plating reaction, which forms metal on top of the silver nanoparticles, lending the tracks enough bulk mass to become electrically conductive.

The following section deals with this, using a UV laser to pattern the polyimide and investigate the effect that different energy doses have on the substrate and silver.

3.3 Detailed experimental procedure

The scope of this thesis is to improve the basic process laid out by Ng *et al.* [84]. In that respect, the experimental methods are explicitly laid out below, with more recent refinements to handling procedures included. A description of how equipment and chemicals are utilised is provided here.

As mentioned in Chapter 1, part of the remit of this project is to develop and refine the process such that it becomes cost effective enough to enable its wider usage. As such, the majority of equipment can be found in any standard laboratory with the exception of a laser and the electroless plating bath, although the cost of lasers is decreasing and the expense of the bath comes from the chemical ingredients; all equipment required for the plating step is also standard laboratory fare. In the subsequent sections, 3.3.1 – 3.3.8, experimental parameters previously reported by Ng *et al.* are used. Any parameters changed in forthcoming experimental descriptions will be clearly indicated.

3.3.1 Cleaning process and sample preparation

Before conducting the experiments, a standard cleaning procedure for sample substrates and any glassware used was carried out to minimise the presence of impurities. Acetone followed by isopropanol (IPA) then deionised (DI) water were used to rinse the substrate on both sides and the inside of beakers used for the experiments. The substrate was then placed in a clean beaker containing DI water with a few millilitres of Decon-90, a strong detergent, which was then placed in an ultrasonic bath at 40^{o}C for 5 minutes to remove traces of the solvents. Next, the substrate was thoroughly showered with DI water and placed in another beaker of DI water in the ultrasonic bath for 5 minutes, to remove traces of the detergent, before being thoroughly showered again. This is very similar to the preparation for glassware such as stirrers and pipettes, but in the case of beakers they are rinsed out with DI water 2-3 times after each step, rather than being submerged. The clean sample is now ready to be processed.

3.3.2 Step 1 – Imide ring cleavage

A 1 M solution of potassium hydroxide was prepared by dissolving 56.106 grams of KOH pellets in 1 litre of water in a beaker. The beaker was placed on a hotplate stirrer set to 50^{o}C controlled by a temperature probe and 200 rpm with a magnetic stirbar. After approximately 5 minutes, the pellets were completely dissolved. Once the desired temperature was reached, the stirring function was deactivated and the temperature probe was used to stir a few times in the opposite direction to the stirbar. The beaker was then left to settle for 2 minutes. Cessation of agitation during immersion was necessary to achieve a more uniform hydrolysis of the polyimide. A sample substrate placed in the beaker with the stirbar still activated would indeed cause greater hydrolysis at the 'leading edge' of the substrate, or the areas of contact on the polyimide where the flow velocity induced by the stirbar was greatest. The substrate was then submerged in the beaker for 5 minutes up to approximately 80–90% of its height, with the remaining area of substrate untreated to allow for subsequent handling of the sample. It was held in place by a pair of tweezers secured in a clamp, as seen in Figure 3.4 below. The substrate was then removed from the beaker, rinsed and submerged in DI water before being hung from a clamp stand to dry.

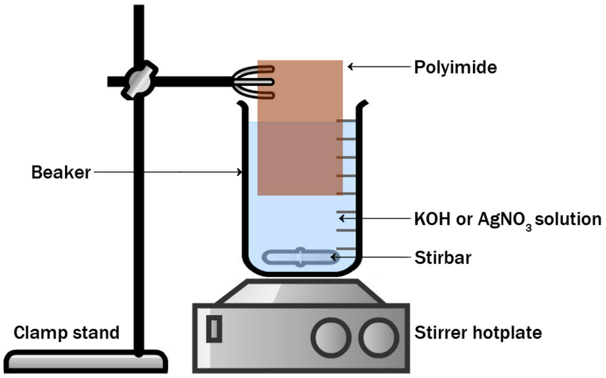

Figure 3.4: *Apparatus for KOH and* $AgNO_3$ *immersion steps.*

3.3.3 Step 2 – Silver-potassium ion exchange

A 0.1 M silver nitrate solution was prepared by stirring 16.987 g of silver nitrate for every litre of DI water in a large beaker until fully dissolved. Some of this solution was then decanted into the smaller ion-exchange beaker. A sample of imide ring-cleaved PI was then submerged in the solution for 15 minutes before being rinsed and submerged in DI water, clamped with tweezers in a clamp stand and left to dry as in Section 3.3.2 and Figure 3.4 above.

3.3.4 Step 3 – Reduction agent coating for silver nanoparticle formation

Methoxy Polyethylene Glycol (MPEG) was dissolved in ethanol at 60^{o}C at a concentration of 60 g/L on a stirrer hotplate. The PI was then coated with this solution while still hot, as MPEG recrystallises at lower temperatures. Two methods of applying the coating were employed.

Spin coating application

The first method involved spin coating in the same manner photoresists are deposited during photolithographic procedures. Prior to spin coating the flexible polyimide substrate must be fixed to a flat base to allow a fully airtight adhesion to the vacuum chuck of the spin coater. This is achieved by exploiting the 'stickiness' of a silicone rubber sheet to temporarily attach it to a sheet of Poly(methyl methacrylate) (PMMA).

Both the PMMA and silicone sheets are cleaned with Decon 90 and rinsed in DI water. The silicone sheet is then placed onto the PMMA before using a roller to apply pressure across the sheet to ensure no air bubbles are trapped as shown in Figure 3.5(a) below. The polyimide sheet to be coated is carefully placed on top of the silicone sheet and gently rolled flat in a similar manner to increase uniformity of adherence to the silicone. If the silicone loses its 'stickiness', as can happen after a number of polyimide samples have been processed, rubbing with IPA and allowing this to evaporate will restore its adhesion properties.

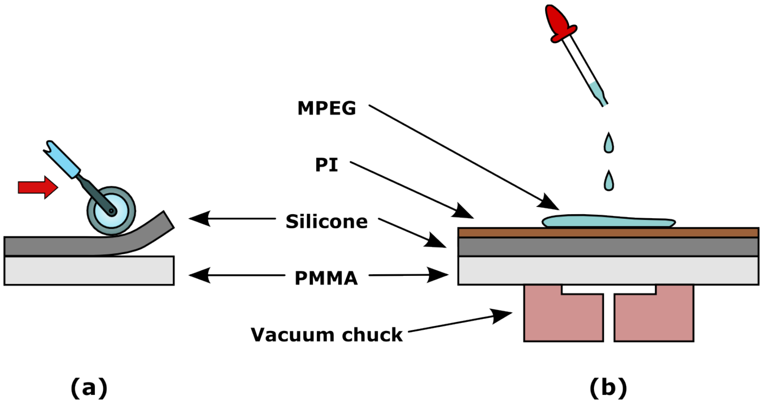

Figure 3.5: *Preparation for spin coating of MPEG.*

The PMMA-silicone holder is then placed on the vacuum chuck of the spin coater and a few drops of MPEG solution are dispensed onto the centre of the substrate directly from a bottle on a hotplate at 60°C as shown in Figure 3.5(b) above. An approximate rule of thumb for dispensing is to use 1 ml of solution for every inch of diameter of the sample being coated. Typical spin coating parameters can be seen in Table 3.1. Due to the ethanol of the coating evaporating relatively quickly it is difficult to measure the thickness of the MPEG coating accurately, but the spinning parameters in Table 3.1 provide a coating thickness of approximately 5 μm.

Acceleration ($rpm \cdot s^{-1}$)	Top speed (rpm)	Total spin time (s)
200	2000	50

Table 3.1: *Spin coating parameters for 5 μm thick MPEG coating.*

Spray coating application

The second method of applying the electron donating MPEG is spray coating. This was carried out using an artist's spray paint gun with pure nitrogen as the propellant. The polyimide substrate was taped to a horizontal surface before the hot MPEG solution was pipetted into the feed cup of an airbrush. An illustration of the spray coating experimental setup can be seen in Figure 3.6 below. While spray coating allows for finer coating thicknesses, it suffers from a greater degree of variability due to the manual processing. Height above the substrate, propellant release rate and MPEG solution release rate are all factors that are controlled manually and are thus not easily quantifiable.

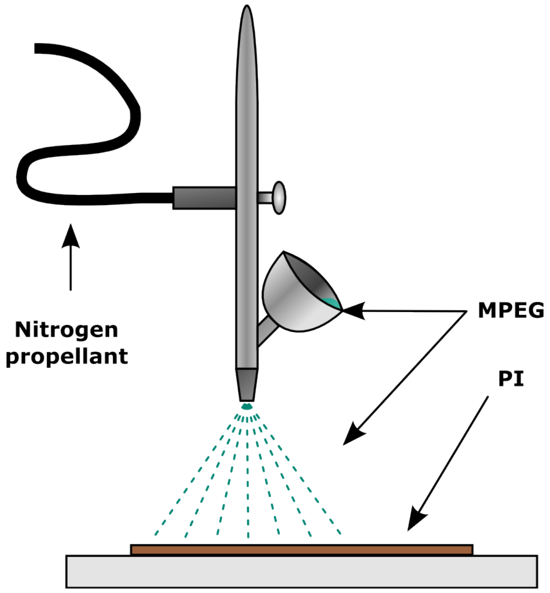

Figure 3.6: *Spray coating of MPEG onto PI.*

3.3.5 Step 4 – Silver ion reduction and patterning by UV exposure

After the MPEG coating has been given a few minutes to dry, the substrate is then ready for silver ion reduction via exposure to UV light from a broad beam lamp or laser source. The laser is used to define the smallest linewidths but patterning using collimated output from a UV lamp and a photomask provides a means to create larger areas of silvered polyimide.

Broad beam exposure

The sample was placed in a Tamarack 152R UV mask aligner system, where it was exposed to a constant beam of collimated UV light from a mercury arc lamp source for various time periods ranging from a number of minutes to a few hours. Once the patterning is completed, the MPEG is rinsed off with DI water.

Laser exposure

A laser was fixed above an X-Y translation stage to which the sample was attached. This allowed positional control of the sample to pattern fine linewidths the approximate size of the laser beam diameter. Once the patterning is completed, the MPEG is rinsed off with DI water.

Safety considerations

A class IV UV laser was used for laser based reduction and so safety goggles filtering the sub 400 nm wavelength range were required. The laser was also placed in a laboratory fitted with an interlock cut-off switch connected to the door, ensuring anyone inadvertently entering would not be exposed to the beam or any reflected rays. An exhaust was fitted adjacent to the beam delivery output, a few centimetres above the translation stage. As well as removing any ablated particles, this also took care of the small quantities of gases produced by the decomposition of PI, such as carbon monoxide and carbon dioxide [139].

Similar precautions were required for the broad beam photomask patterning route. Even though the power of the light source was considerably less, it was still hazardous enough to cause damage to the eyes if observed directly or via a reflection. As the silver formation took place over a much longer time in this route, an exhaust for fumes was not required with a well ventilated laboratory being sufficient.

3.3.6 Step 5 – Unreduced silver ion removal

To remove any unreacted silver ions, the substrate was then submersed in 1% w/w sulphuric acid solution to stop silver from forming in undesirable areas, via thermal reduction in the following step. The hydrogen ions in the acid exhibit a much greater affinity to the amide anions and so displace the silver ions. The solution is created by very slowly adding 10g sulphuric acid to 1 kg of DI water. After the solution is thoroughly mixed the substrate is submersed in this solution for 15 minutes to ensure all unreacted ions have been removed. If this step is not carried out, the following reimidisation step can cause silver particles to form in undesirable places. After submersion in the dilute acid the substrate is rinsed thoroughly with, and then dipped in, deionised water.

3.3.7 Step 6 – Reimidisation of polyimide

The substrates are placed in an oven and cured at various times at 300^{o}C to reimidise the PAA at the surface of the polyimide, restoring the substrate to its original state, as shown in Figure 3.1(vi) above.

3.3.8 Step 7 – Electroless plating

10 litres of the ESM 100 electroless silver plating bath were prepared by following the guidelines outlined below. More details can be found on the PK Plating website [140]. Preparation involves combining different components of the ESM 100 system in a particular order. The chemical in the ESM 100 system of primary importance is silver cyanide. Providing high enough levels of cyanide in a new bath are maintained and that it is constantly agitated, the silver will remain in this compound form. Should these levels become too low the silver will precipitate, rendering the bath unusable. Once a bath is prepared and its optimal temperature, pH and silver:cyanide ratio are all reached, electroless plating can be performed.

A 10 litre beaker was placed on a stirrer hotplate and 6 litres of DI water are added along with a stir bar, making sure agitation is turned on. 1000 ml of bath component ESM 100 A were added and allowed to mix thoroughly. ESM 100 A's primary contents are silver cyanide and sodium cyanide. 1500 ml of bath component ESM 100 B containing a small percentage of sodium hydroxide was then added and allowed to mix fully before 1000 ml of ESM 100 C is added and mixed in completely. The hotplate was then turned on to heat the bath to 50^{o}C. Once at this temperature the pH is carefully increased to 10.0 by slowly adding ESM 100 pH increase solution, which predominantly contains sodium hydroxide. DI water is then added to top up the bath to 10 litres and its temperature is increased to the bath operating temperature of 67^{o}C. pH is checked once this temperature is reached and increased or decreased accordingly. Decreasing the pH is achieved by slowly adding boric acid powder to the bath.

Before attempting to plate, the concentrations of silver and cyanide in the bath should be measured. Testing these concentrations requires taking a sample of the bath and examining it with a spectrophotometer or colourimeter. A freshly prepared bath should have a cyanide to silver ratio of 1.35:1. This is too high for electroless plating to commence, but when the bath is left at operating temperature, the cyanide will gradually break down and evaporate in the form of hydrogen cyanide. After approximately 2-3 hours the cyanide level should be tested again. By this point it should have reached target ratio for optimal bath performance of 1:1. Once this is reached a sample to be plated can be placed in the bath. Plating will occur on any suitable metallic surface or seed layer, such as silver or nickel. Since it is an autocatalytic reaction, silver deposition will continue as long as there are still silver ions in solution and the cyanide to silver ratio does not become too high. This means that the thickness of deposited silver can be chosen simply by adjusting the length of time a sample is treated for.

Once the bath is running, samples are plated by immersion in the bath for an amount of time to give the desired thickness. Since the plated silver is plated electrolessly it will grow isotropically, which will increase the width of any seed layer tracks. After immersion, the samples are removed and thoroughly rinsed then dipped in DI water before being hung up to dry.

With the process now defined and fully explained, the following sections of this chapter look at experiments carried out which identified areas requiring improvement. In Section 3.4 laser based experiments were performed to observe their effects on the silver particles and substrate. The results from this lead directly on to the second experiment described in Section 3.5.

3.4 UV Laser induced patterning of substrates

3.4.1 Aim

To test the effects of the process, an experiment was set up to determine the energy dose required for optimal silver pattern formation. The quantity of energy imparted by the laser can be varied in two ways: firstly by adjusting the output power and secondly by varying the speed at which the laser scans across the substrate. A lower speed means that the laser will be incident on a given area of substrate for longer, resulting in a higher energy dose per unit area. It is therefore reasonable to predict that a high power, low speed combination will be more likely to have a greater effect, but there will be a level of energy dose above which there will be damage to the substrate, to any silver nanoparticles formed or both. It is also feasible that there may be a difference between a fixed quantity of energy delivered over a longer or shorter period of time, that is to say, the energy from a laser beam with high power and high scanning speed can be matched with a lower power and a corresponding lower speed.

For calculation of the energy imparted to the substrate, it is necessary to look first at the profile of the laser beam, then at how the energy within the beam is transferred. Two typical beam profiles, Gaussian and ‘top hat’ are shown in Figure 3.7 below.

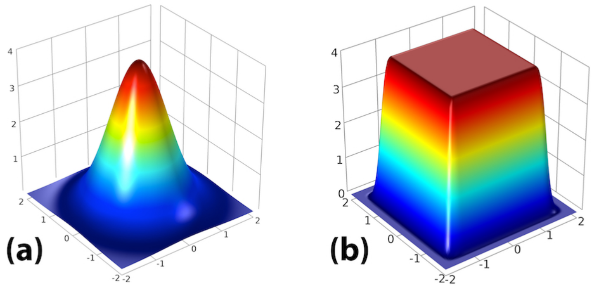

Figure 3.7: *Typical laser beam profiles showing (a) Gaussian and (b) square “top hat” profile. Axis values are arbitrary.*

Lasers more often have a Gaussian beam profile as shown in Figure 3.7(a), whose peak intensity, I_{peak}, can be defined by:

$$I_{peak} = \frac{P_{laser}}{\pi w^2/2} \tag{3.2}$$

Where P_{laser} is the output power of the laser and w is the Gaussian beam radius for a given distance from the laser source. For the purposes of initial laser testing however, a fully flat or 'top hat' beam profile was assumed. In this case, the intensity, I, can be more simply approximated to the power divided by the beam's cross-sectional area, A:

$$I = \frac{P_{laser}}{A} \tag{3.3}$$

If ideal (lossless) beam delivery apparatus is assumed, the irradiance on the surface of the substrate, E_e, can be said to be equivalent to the intensity, I. For more real measurements of the power, P, a laser power meter can be used instead such that:

$$E_e = \frac{P}{A} \tag{3.4}$$

A value for the total energy dose, H_e, can then be defined as the irradiance of the substrate for a given time, t:

$$H_e = E_e \cdot t \tag{3.5}$$

This total tells us the amount of energy per unit area imparted by the laser at the surface of the substrate. Calculating this quantity for each laser-written track power-speed combination allows for example, a direct comparison of low laser power imparted at low speed, producing a given dose, to a high laser power at high speed, producing a similar dose, as described above. Since the laser is moving, the time in the above equation can be defined by the beam diameter, d, divided by the laser speed, v:

$$H_e = E_e \cdot \frac{d}{v} \tag{3.6}$$

Thus we can compare the effects on the substrate of a beam at low power and low speed, delivering a given energy dose, with a beam delivered at higher power and higher speed, delivering the same dose.

3.4.2 Equipment and procedure

A class IV Helium Cadmium (HeCd) laser a maximum output of 400 mW at 325 nm was fixed to an optical bench, with the beam directed vertically downwards onto the substrate. The substrate was taped to an Aerotech XY-translation stage setup, whose axes each comprised a linear motor stage, ALS 20060 in the X-direction and ALS 20030 in the Y-direction, driven by an Ndrive HP-20 servo/stepper amplifier and controlled using LabView software. The stage was programmed to produce a simple series of adjacent straight lines of varying powers and speeds. This experimental setup was the same as that previously used by [6], seen in Figure 3.8 below, but with the rotational part of the equipment removed. The maximum incident power of the laser at the substrate surface, after passing through the fibre optic beam focussing and delivery apparatus, was measured to be 12 mW, therefore the range of laser power used in the experiment was 1 – 12 mW. The translation stage speeds investigated were in the range 0.1 – 200 mm·s^{-1}. After application of the laser beam, the substrate was rinsed and the unreduced silver ions were removed before the polyimide was reimidised as described in Sections 3.3.6 and 3.3.7 above. A Zygo Viewmeter 5200 white light phase shifting interferometer (Zygo) was used to provide a profile of the tracks created.

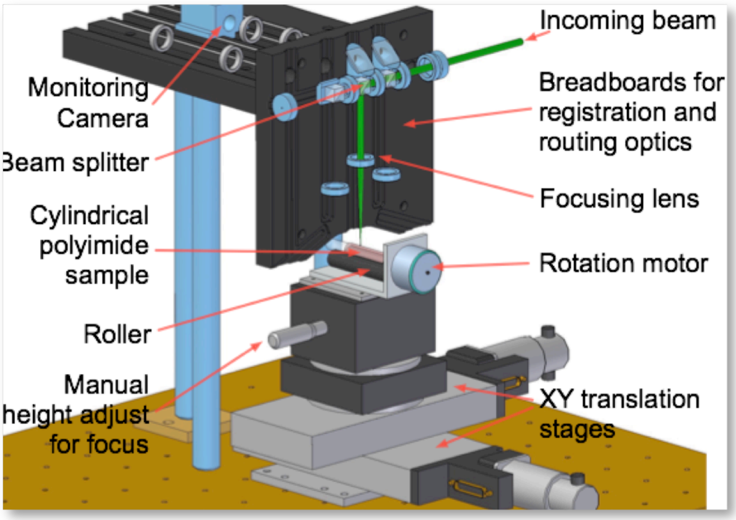

Figure 3.8: *Experimental setup of direct laser writing with translation stage. Taken from Ng* et al. *[6].*

3.4.3 Results and discussion

The colour of the reliefs from the Zygo plots indicates the relative height of any feature: blue being the lowest point within each image, red being the highest. Colours cannot be therefore compared between samples, but the colours of the flat surfaces either side of the tracks can be used to measure the change in height where the laser struck. Black areas indicate that the Zygo has not been able to obtain a signal from the material. Zygo plots of the various speed-power combinations can be seen in Figure 3.9 below. At a power of 1 mW, the fastest scans of 50 mm·s^{-1} and above were too faint to be discernable by the interferometric method and so were omitted.

Although the laser beam width was constant for all lines, it is clear there is a greater modification of the surface at higher powers and lower speeds, with the sample receiving the greatest energy dose (highest power at lowest speed) showing the largest area of change. Such an alteration of the substrate for any power should perhaps not be surprising, given that polyimide is known to strongly absorb light energy in the UV range [39].

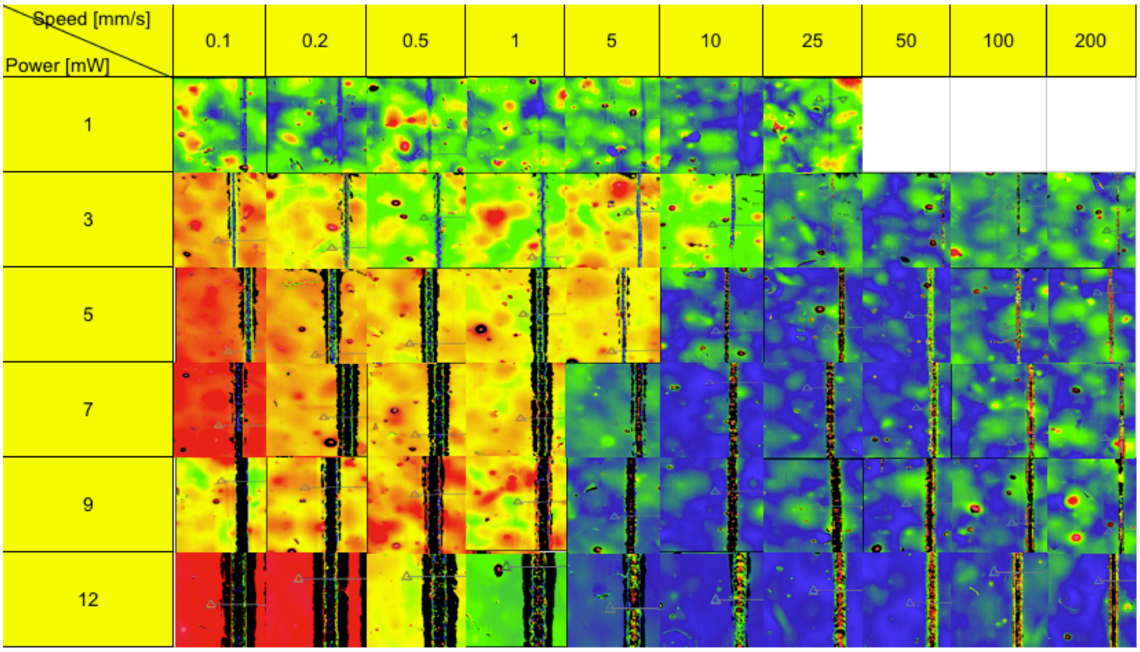

Figure 3.9: *Matrix of interferometry images of laser tracks formed with varying speed and power combinations as seen from above. Colour represents height. Within each individual image lowest to highest areas are mapped from blue to red across the standard visible spectrum.*

The colour of the unmodified areas either side of the tracks should be noted. The unmodified areas of the tracks written at higher speeds appear more blue with the tracks themselves being more yellow and red, while the surrounding area at lower speeds is red, with the tracks being more green to blue. This indicates that tracks at lower energy doses have become raised from the substrate, while at higher doses they have become recessed. This is perhaps most apparent in the tracks written with a power of 5 mW. At higher powers, and thus also higher doses, this is not as distinct, with larger (black) areas without height data and also more irregular heights in the areas where a reflection was picked up by the Zygo. Clearly the energy imparted by the laser has a large effect on the substrate and it appears that initially there is some form of swelling before material is ejected. This is better illustrated by comparing cross-sections of the tracks for the same total irradiance but delivered using different laser powers, as seen in Figure 3.10 below. For the low energy dose trials of 12 $J \cdot cm^{-2}$ (column 4, Figure 3.10), the track profile is broadly similar for the laser powers tested. All show a peak or swelling with a small trench either side lower than the surrounding substrate. This suggests that the polyimide initially undergoes some swelling when it absorbs the laser energy.

The intrinsic physical properties described in the datasheet of Kapton HN, the PI used in this experiment, mean that it does not melt and also has a low coefficient of thermal expansion [141]. Therefore the heated polymer is not melting and expanding. A possible reason for the swelling is the build up of gas underneath the surface of the PI. Using mass spectrometry Ortelli *et al.* have shown that during UV laser induced decomposition of PI, gases formed from the breaking up of the polymer chain are indeed formed [139, 142]. Comparing column 4 to the other higher energy density columns, it can be seen that the swelling becomes more pronounced, that is the width of the tracks becomes larger, and that the peak becomes more jagged and that some sections have no data.

While some jagged peaks on the Zygo plot represent a highly uneven area of the surface, some jagged areas are artefacts of the software interpretation of the data and so are not accurate reflections of the surface profile, so care must be taken when analysing these samples. A typical example of such a needle-like peak where it is likely there is no actual surface peak can be seen on the profile of the 6 mW sample in column 3.

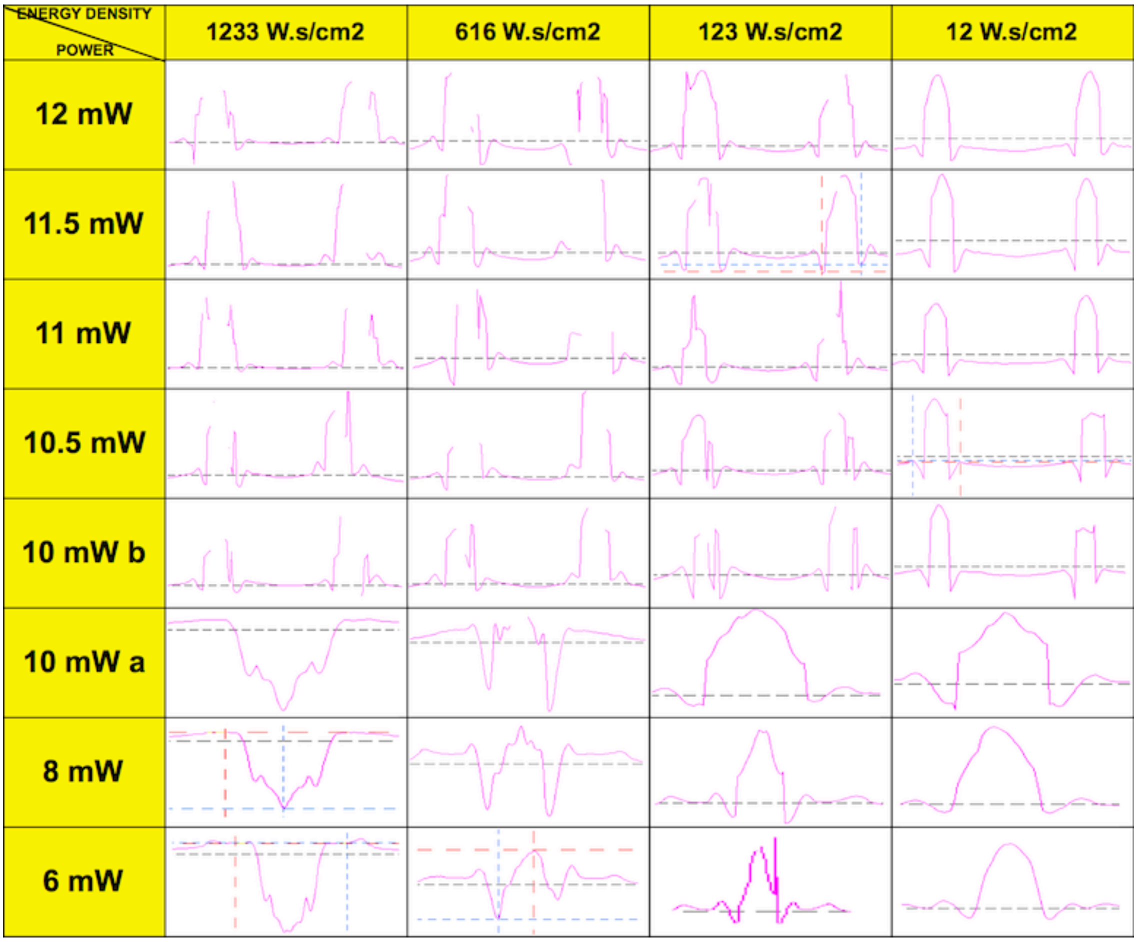

Figure 3.10: *Matrix of interferometry profiles of laser tracks created for each of four different irradiance (energy density) values. Descending incident power corresponds to descending laser speed. The first five rows show two tracks per profile while the final three show only one.*

Returning to the jagged peaks not due to reading error, the unevenness at higher energy density can be explained by the fact that the main gases formed from the polymer decomposition are the volatile carbon monoxide, hydrogen cyanide and acetylene. At the higher local temperature of laser impact it is reasonable to assume some explosive combustion may occur. This is confirmed by the SEM image of a laser-written track from a previous study by Ng *et al.* [6] in Figure 3.11 below. Silver nanoparticles will hold a much greater electrical charge than the PI film in the SEM and this manifests as the charged areas/particles appearing lighter, with the uncharged areas being darker. As well as there being a prevalence of silver nanoparticles as expected where the laser passed, there are many points scattered either side of the track, again indicating some sort of explosion. Also of interest is the area of track on the right hand side of the picture, where it shows a slightly lighter colour almost folded back on itself, with higher density silver areas underneath, although this underlying area has an irregular aerated sponge-like structure, possibly indicating where pockets of gas have formed before an explosion released these gases.

Perhaps the most intriguing information in Figure 3.10 above is the marked difference in profile between the low and high power written tracks at high energy densities (columns 1 and 2). Allowing for day-to-day variation in experimental conditions such as the manual focussing of the laser beam and the slight non-uniformity in flatness of the PI when secured to the translation stage, there is a change in profile at high to low power from swollen or exploded peak to large trench (column 1) or trenches (column 2) at a laser power of approximately 10 mW. Since a 6 mW beam must travel slower than a 12 mW beam to deliver the same irradiance, the time taken to do so and thus dose will increase (equation 3.5). It is clear that this increased dose affects the way in which the PI is modified, with the greatest dose-irradiance combination (column 1, 6 mW) showing a slightly ablated profile.

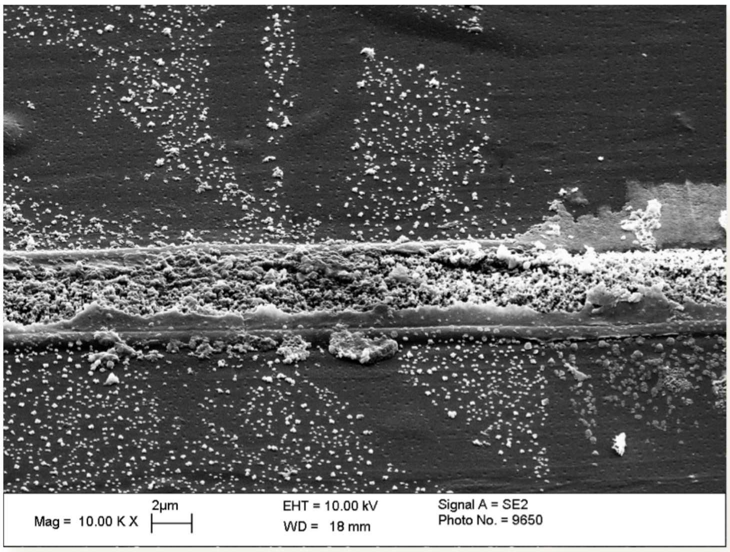

Figure 3.11: *Laser written track at high energy dose taken from Ng* et al. *[6].*

3.4.4 Conclusions

It is clear that the high energy of the laser has a significant effect on the PI substrate. Additionally, this effect will differ depending on how the laser energy is delivered. The laser causes a swelling of the PI that increases if the laser power, and therefore the irradiance, is increased, as seen in Figure 3.10. At higher powers, the Zygo has greater difficulty providing height data across the full area, indicating that the surface is more irregular and possesses areas with near vertical features. This strongly suggests a higher irradiance has a more pronounced effect. If the irradiance is kept constant for different powers by varying the speed and thus varying the energy dose, this also has an effect, with part of the polyimide being ablated at higher doses. The results above certainly tie in with the effects of UV at approximately the same wavelength (300 – 330 nm) at irradiances an order of magnitude higher than that deployed here (10 kW·cm^{-2}) [143], where the polymer was completely ablated.

It can be expected that such swollen and ablated irregularities caused by laser treatment will have an effect on subsequent electroless plating since the silver nanoparticle containing area of the PI near the surface may have been removed, causing non-uniformities in the silver seed layer. Since electroless plating is isotropic, the plated silver would be inconsistent with the intended laser patterned path. Furthermore, it is highly likely the local mechanical properties of the polyimide have been altered, potentially causing areas of weakness close to the silver tracks. From the different sizes of silver clusters noted in Figure 3.11, it is also worth considering the effects of the laser on the newly created silver nanoparticles and how the energy may or may not contribute to their growth. It is therefore beneficial to examine these effects in greater detail.

3.5 Polyimide degradation and silver nanoparticle growth investigation

3.5.1 Aim

As noted in Section 3.4, the laser irradiance has a significant effect on the PI. One option to better analyse the changes in the PI is to considerably lower the power of the light source. Naturally this means that the exposure time will need to be increased a significant amount to supply energy doses similar to the levels of the previous experiment. This can be realised by using a broad beam UV lamp exposure as utilised in photolithographic micropatterning processes. Spreading the energy dose at a lower irradiance over a longer time should lessen the rapid local heating and deformation of the substrate. It is also worth investigating the effects of the reimidisation step described in Section 3.3.7 at this stage. This part of the process is undertaken at elevated temperatures of 300°C so any effects from this more controlled heating process should be taken into account when examining the samples and could also provide a useful comparison for both PI and silver nanoparticles to the heating effects caused by laser-induced patterning. Finally, effects of laser writing and reimidisation should all be considered with respect to the effects on the final electroless plating process step.

3.5.2 Equipment and procedure

The standard preparation steps described in Sections 3.3.1–3.3.4 were undertaken. A Tamarack mask aligner whose light source is a collimated broadband mercury arc lamp was used to carry out the UV exposure step. The output irradiance at the sample surface was measured to be 50 $mW\cdot cm^{-2}$, the spectral distribution of which can be seen in Figure 3.12 below. Samples were exposed for periods ranging from 1 to 8 hours. After exposure the substrate was rinsed and unreacted ions were removed as described in Section 3.3.6 before the samples were reimidised for durations of between 1 and 8 hours. Finally samples were plated as outlined in Section 3.3.8.

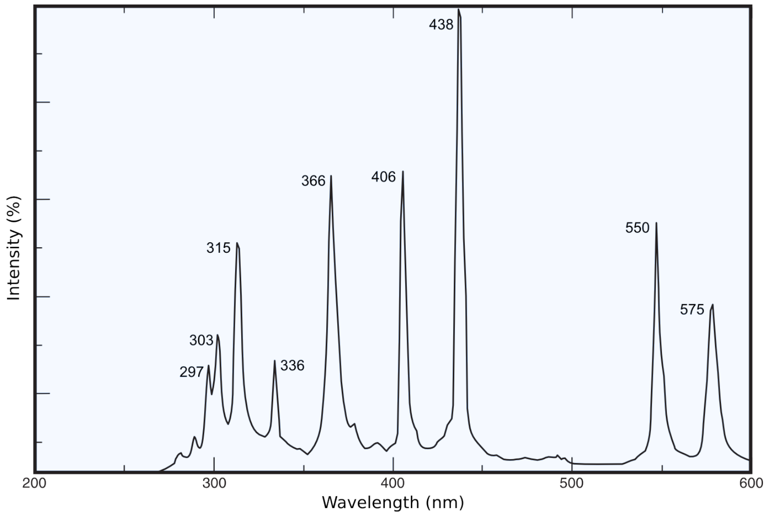

Figure 3.12*: Typical spectral distribution of mercury arc lamp output.*

For analysis and characterisation a Leo 1530 VP Field Emission Scanning Electron Microscope (FESEM) and an Olympus SZX10 stereomicroscope were used to examine the silver nanoparticle formations. A Veeco Dektak 3 stylus profilometer and the Zygo Viewmeter 5200 performed profiling of the patterns produced. Reflectivity measurements were undertaken with a continuous wave HeNe gas laser at 632.8 nm (NEC Corporation, Model GLG 5380) and a Newport 1830-C optical power meter. The Fourier transform infrared (FTIR) examination was performed with a Perkin Elmer Spectrum 100. Electroless plating was carried out as described in Section 3.3.8, with any variations noted in the discussion section below.

3.5.3 Results and discussion

Initially the effect of the UV energy on both silver growth and polymer modification will be discussed followed by an examination of the effects of the heat treatment required for PI reimidisation. After finding that there are degradative effects from both photo and thermal energy regimes and examining the reasons behind this in greater detail, some electroless plating results are presented and discussed.

During the photoreduction process silver atoms are formed from the silver ions reduced by the addition of electrons from the MPEG coating. These atoms then nucleate immediately into larger particles as presented in Figure 3.13. The PI backbone is depicted by irregular horizontal lines, with the lines in the generally vertical direction representing the negatively charged carboxyl groups formed from the cleaved imide rings within the polymer chain, to which metallic ions become attracted. After the silver atoms are formed, they begin to coalesce with their neighbours to form crystalline nanoparticles.

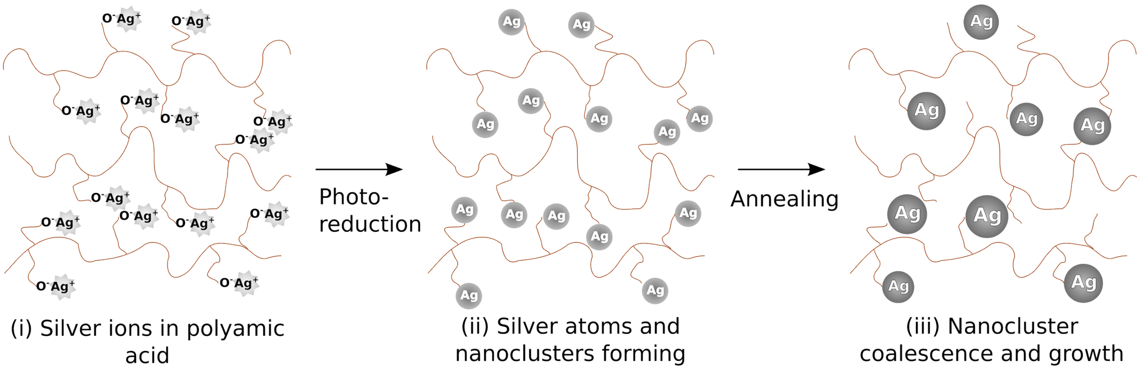

Figure 3.13: *Reduction and subsequent nucleation of silver atoms within the brown polyimide matrix.*

The optimal energy dose from the UV would photoreduce all exposed silver ions. A visual inspection of a sample can give an indication as to how complete the photoreduction process is. Figure 3.14 shows a grid of silver test structures directly photo-patterned over a range of UV doses, taken before the annealing step. Given the irradiance of the Tamarack's light source is 50 mW·cm^{-2}, Equation 3.5 tells us that the energy dose will be 180 J·cm^{-2} for every hour of exposure. A dose of less than 180 J·cm^{-2} produced a barely visible pattern and it was only once the dose was over 300 J·cm^{-2} that the patterns were observably silver to the naked eye. FESEM images in Figure 3.15 below confirm that increasing energy dose does indeed increase the density of silver nanoparticles formed, indicating that the silver ions are being reduced as expected. At energy doses of above 720 J·cm^{-2} however, some form of degradation within the polymer substrate is observed. Small gaps emerge and continue to develop as the energy dose increases. By the time the maximum energy dose in this study was reached, the polymer was noticeably rougher to the naked eye. The silver colour had decreased and the PI had become more opaque. An indication of when all silver ions within the substrate are exhausted is shown by the silver particle size. There is no discernible increase in size beyond an energy dose of 900 J·cm^{-2} or 5 hours of exposure. This exposure time is therefore the maximum required for silver nanoparticle formation and nucleation but, on the whole, it may be desirable to decrease this further due to detrimental effects the UV imparted energy has on the polyimide substrate.

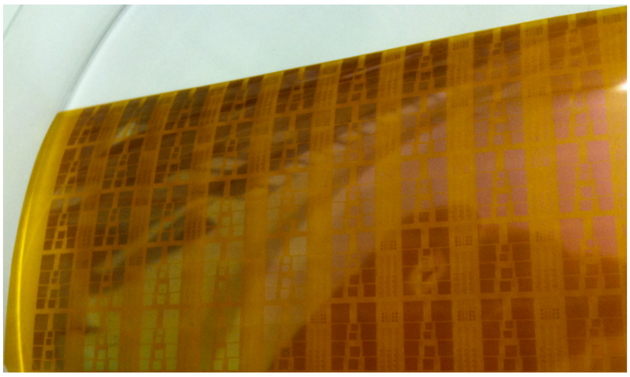

Figure 3.14: *Test structures showing an increasing silver colour with increasing UV exposure time from left to right of 1 hour to 4 hours.*

Once the silver particles are formed and any ions, which have not been photoreduced, are rinsed out, the next stage in the process is the reimidisation of the polyimide. This thermal treatment also has an effect on the silver however, causing the nanoparticles to coalesce further. To investigate the sole effect of heat on the silver, reflectivity measurements across the angle of 0 to 60 degrees, were taken of samples annealed for times varying between 2 and 5 hours exposed to the same UV energy dose of 720 J·cm^{-2}, the results of which can be seen in Figure 3.16.

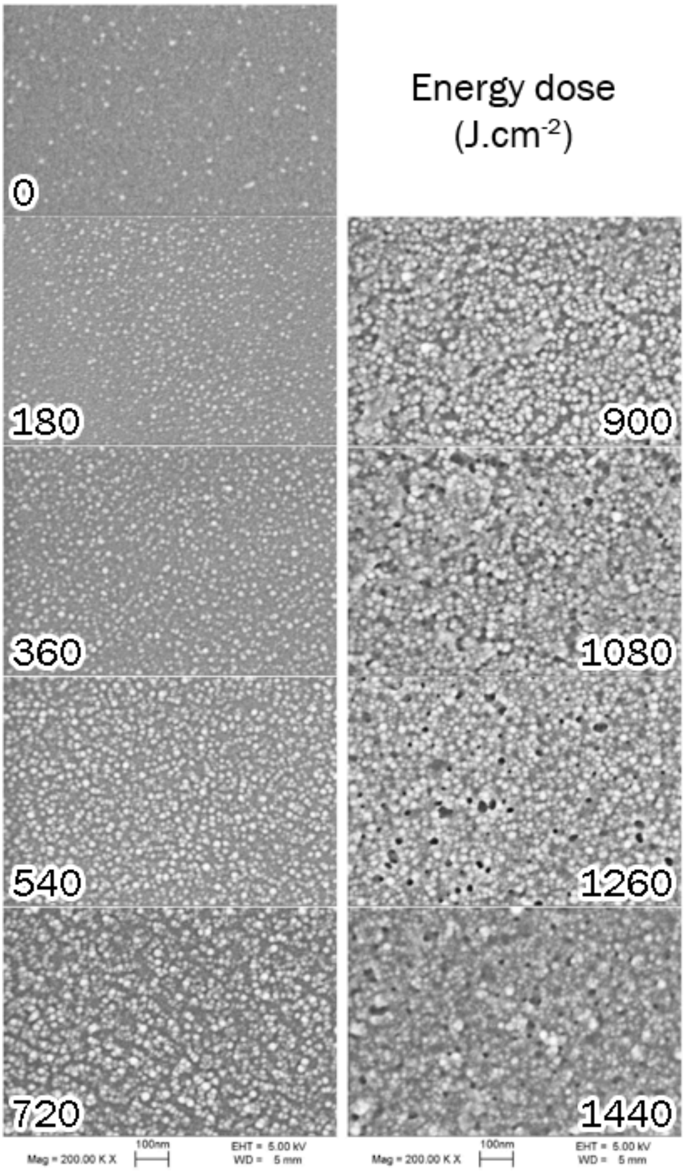

Figure 3.15: *SEM images of silver nanoparticle growth due to UV exposure.*

Prior to annealing, the samples exhibited a small amount of reflectivity. This reflectivity had increased slightly after the first hour and continued increasing with the greatest values recorded after 4 hours, while the readings after 2 and 3 hours were also close to these levels. After 4 hours however, there was a significant decrease in measured reflectivity, giving a relative brightness around half that of a sample with no heat treatment. This is more clearly shown by averaging the reflected intensity value over the range of angles for each annealing time, as show in Figure 3.17.

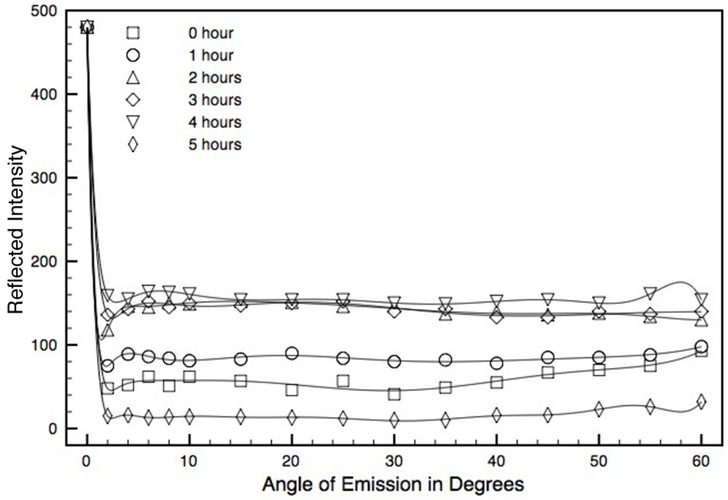

Figure 3.16: *Reflectivity measurements of silvered PI at fixed energy dose for varying anneal times.*

These results, combined with the more opaque appearance of polyimide exposed to larger energy doses discussed above, indicate that degradation of the polymer by UV energy is aggravated further by thermal energy.

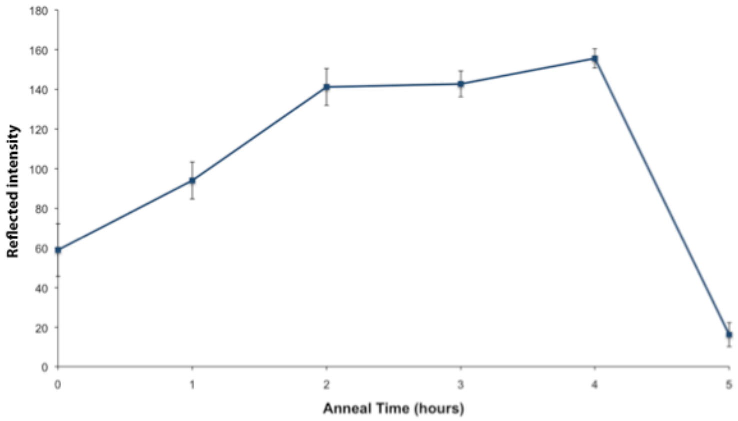

Figure 3.17: *Relative reflected intensity of silver seed layer as a function of anneal time. Relative brightness values are the average of measurements of emission angles between 2 and 60^{o} inclusive.*

With regard to the polymer it is clear the heat treatment step should be the minimum time necessary for complete reimidisation to occur, the most quoted figure in the literature being 30 minutes at temperatures of between 250^{o}C and 350^{o}C [87, 144-147]. However Figure 3.16 above intimates that such a treatment time is sub-optimal in terms of silver nanoparticle growth, indicating in turn that such a treatment regime may not be ideal for creation of the seed layer for electroless plating. Since these effects occur concurrently, it is worth comparing samples annealed for various times that have undergone only specific previous stages of the sample preparation. This should help identify the extent of the contribution of each step to silver formation and PI degradation. A set of samples for each of the following conditions of polyimide was prepared: A – pristine; B – exposed to UV only; C – imide rings cleaved by KOH immersion only; D – as C but subsequently exposed to UV; E – as C but potassium-silver ion-exchange subsequently carried out; F – as E but with UV exposure. This is better represented in tabular form as in Table 3.2 below. UV dose was 720 J·cm^{-2} and only UV-exposed sample sets B, D and F were coated with MPEG prior to exposure (see Section 3.3.4). Samples in sets C – F underwent chemical surface modification and so were rinsed with dilute sulphuric acid before the annealing tests (see Section 3.3.6). All samples were annealed for times between 0 and 5 hours.

Sample set	**Sample preparation step**			**Preparation summary**
	1: KOH immersion	2: $AgNO_3$ immersion	4: UV exposure	
A				
B			✓	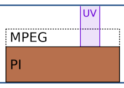
C	✓			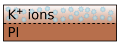
D	✓		✓	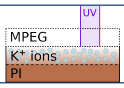
E	✓	✓		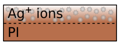
F	✓	✓	✓	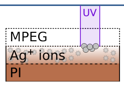

Table 3.2: *Pre-heat treatment sample preparation regimes. Only sets B, D and F were subjected to the third MPEG coating step. UV energy dose was 720 J·cm^{-2}.*

Figure 3.18 below shows SEM images of samples annealed for 0 to 5 hours for each of the six preparation regimes described above. For the purposes of this analysis, treatment regimes will be referred to as 'sample sets' or 'sets' and specific samples will be defined first by their sample set letter then by their annealing time, for example the untouched polyimide sample with no heat treatment is 'A-0,' while the sample that underwent the full preparation routine and was annealed for 5 hours is 'F-5.' This also corresponds to their position in the SEM matrix of Figure 3.18.

Unsurprisingly, given the resistance of polyimide to heat, the pristine samples in column A show no discernable change. Similarly, no change is noticeable in any sample from sets B or C. Although it is clear from set B that UV treatment has little effect on the surface morphology of unchanged polyimide, it is also clear from comparing the surface modified samples in columns C and D that it does have an effect on the hydrolysed surface. The samples without heat treatment from these sets (C-0 and D-0) differ in appearance, with the UV process roughening the surface. When heat is applied, the morphology changes once more and root-like growths are formed although they do not vary significantly for increased heat treatment times. Also the degradation seen in sample sets E and F is not observed in set D, suggesting the silver ions, particles or both are largely influential in the thermal degradation. Sample set E, with silver ions in the modified substrate but no UV exposure initially appears not to be degraded (E-0), similar to initial samples C-0 and D-0. This remains relatively unchanged for the first two hours, E-1 and E-2, but then degradation begins to occur and worsens over time. The final sample set, F, is the only one with observable silver nanoparticles, although given that silver ions can be thermally reduced [145, 148], it is possible that reduction has occurred to a small extent in the E-5 sample, but there is little or no further coalescence of silver as with prior UV exposure, depicted in Figure 3.18 (iii). The nanoparticle growth observed in sample set F however is consistent with particles before annealing of approximately 20–30 nm in diameter, growing steadily to diameters of 70 – 80 nm after 5 hours of heat treatment. Although the silver particles are largest in F-5 they have become recessed into the polymer. This declining number of particles at the surface explains the diminished reflectivity values observed in Figure 3.17. While the increasing silver particle size is desirable for electroless plating, it is evident that PI degradation is occurring concomittantly, with deterioration becoming more severe as heat treatment time continues. Since the only difference between this set of samples and sample set B is the addition of chemical treatment processes, it must be these processes that cause alteration of the polymer.

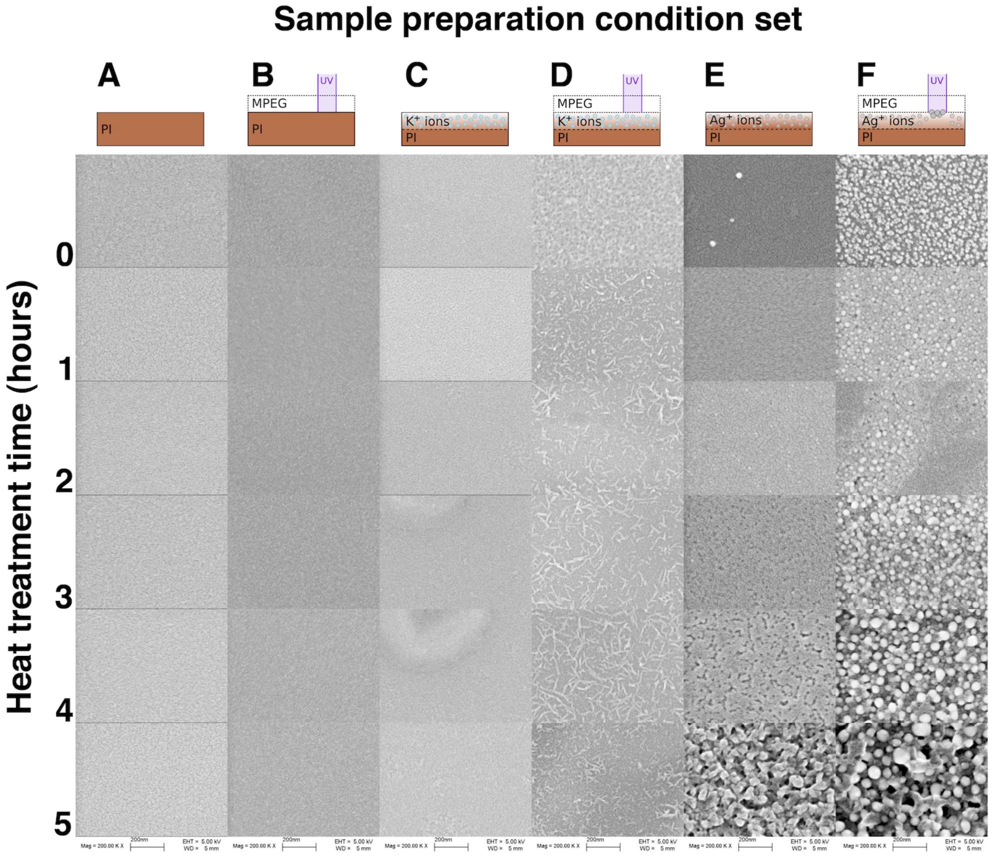

Figure 3.18: *SEM images of polyimide degradation and silver coalescence of samples with different treatment conditions for various heat treatment times.*

Such deterioration from both heat and UV sources in air can be rationalised in terms of oxidative degradation. As described at the beginning of this chapter, the surface of chemically modified polyimide is a metal polyamate acid, either potassium or silver polyamate depending on which process steps have been carried out. After the dilute sulphuric acid wash in step 5, the mobile metal ions are replaced by hydrogen ions and polyamic acid is formed. The 5 hour anneal image in Figure 3.18, Column E, plainly shows that these ion containing polymers do not have the thermal stability of the fully imidised PI film. Free radicals formed at the carbon atom of the carboxylic acid, shown in Figure 3.3 above, and the tertiary carbon atoms of the aromatic benzene ring to which they are attached are longer lasting at increased temperatures, making them more prone to attack from oxygen [139, 146]. These carbon atoms can be lost through oxidation as carbon monoxide or carbon dioxide gases [139, 149, 150], resulting in some polymer chains being broken and therefore weakening the polyamic acid chain. Further, Kapton is a strong absorber of UV energy [146, 151] so more free radicals are created from the interaction of this energy with the carbon bonds, which then further react with atmospheric oxygen, increasing the level of degradation. This explains the worsened degraded state of UV exposed sample set F compared to set E at all stages of heat treatment. The heat treatment also has a reimidising effect, with the C–N–C bond being reformed. However, since it has been shown that degradation has occurred, complete reimidisation will not be possible due to the loss of carbon atoms and breaking of polymer chains discussed above. Studies by Ortelli *et al.* support this theory with evidence of free radical formation at the C–N bonds within the imide ring (and therefore carbon atom loss) and decomposition of the polymer chain at the phenyl–O bonds [142, 152], seen on the right half of the molecule in Figure 3.2 above. This therefore suggests that the physical characteristics of polyimide hydrolysed then reimidised in air, particularly with the added step of UV exposure, will not be the same as flawless polyimide, at the surface of the modified areas at least.

Further to these degradation processes, another degenerative effect was observed in UV irradiated, annealed regions. Under Zygo examination, these patterned regions were found to be sunken into the substrate, as shown in Figure 3.19(a) below. This recess can be attributed to the oxidative degradation effect described above but it is worth noting that the depth is reasonably uniform across the UV-patterned area.

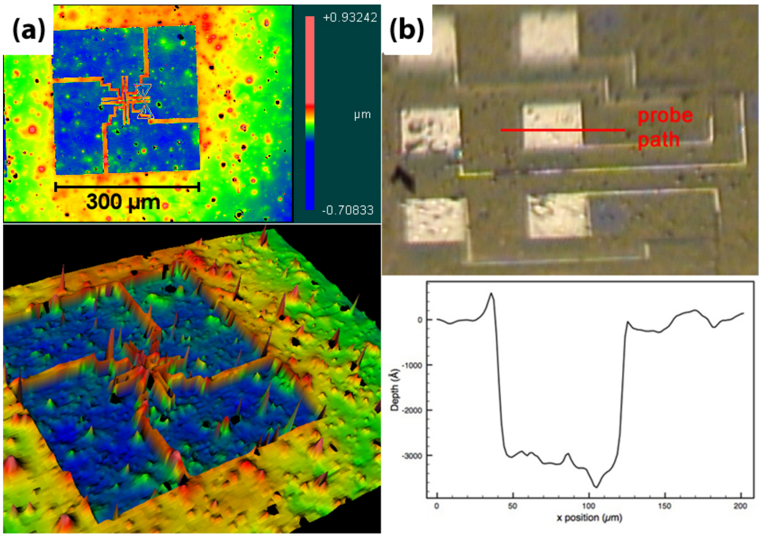

Figure 3.19: *(a) Interferometry and (b) Stylus probe profiles of UV-patterned silver microstructures. Recession depth was approximately 300 nm for a UV dose of 720 J.cm-2 and anneal time of 4 hours.*

Dektak stylus profiler measurements shown in Figure 3.19(b) confirm this, with the silver seed layer at the bottom of these depressed areas. To validate the previously discussed hypothesis of oxidative degradation caused by a combination of UV irradiation and heat treatment, the influence of these process steps was investigated. Results of this analysis are shown in Figure 3.20 below. Evidently, the longer a sample is annealed for, the greater the recess depth. However, it appears that no further degradation occurs after between approximately 4 to 6 hours, depending on the previous UV energy exposure time, where a plateau is reached. The shorter UV exposure times, i.e., the samples with the lower energy doses before annealing, take longer to reach a plateau than those irradiated with UV for longer. It is also evident from Figure 3.20 that the UV does indeed play a part in the degradation, with recess depths from an 8-hour UV exposure being approximately 50% greater than a 2-hour exposure. These results clearly indicate that the polymer shrinkage can be attributed to a combination of both photo-based and thermal effects.

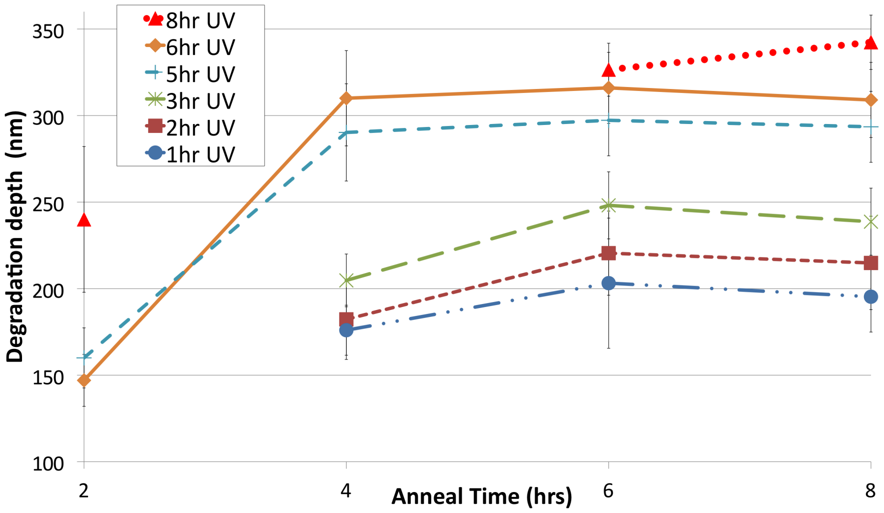

Figure 3.20: *Deterioration depth as a function of annealing time for selected UV exposure times.*

To articulate how these effects combine to produce the phenomenon, a hypothesis of the physical mechanisms at the molecular level is now proposed. The longer the UV exposure time, the more silver nanoparticles will coalesce [87]. Also, it has been shown that incompletely imidised polyimide is liable to break down into smaller molecules, mainly in the form of carbon dioxide [139, 142, 149, 150, 152]. Furthermore, it has been reported that the presence of silver on a polyamic acid interface can inhibit reimidisation [153]. It is possible that this effect, combined with the silver particles acting as thermal radiators, during both the photochemical and thermal steps of the process, will accelerate the decomposition on the polyimide substrate.

The final part of the investigation into the effects of UV irradiation and heat on the substrate and silver involves the examination of the final stage of the process: electroless plating of the silver test structures. A brief description of the workings of such a plating process is given here before scrutinising specific samples. Since it is a chemically fomented process, electroless plating has the advantage over electro plating in that no applied voltage is required and so electrical contacts and the determination of electric field distribution in the bath are not necessary. An electroless bath comprises specifically selected chemicals at particular concentrations, where the ions are converted to metal by a redox reaction instead of an electric current, where the bath will remain stable until electron transfer occurs [136]. Plating will commence when a suitable catalyst such as a silver seed layer is introduced into the bath at a given pH and temperature (among other factors, discussed below). This catalyst acts as a nucleation site, where the metal ions in the bath are reduced onto its surface. The commercial ESM100 bath from PK Plating Tech was chosen for stability and ease of control as recipes from the literature [154, 155] tested in-house were found to be less stable during plating and would precipitate more readily, resulting in more time-consuming bath preparation. Furthermore the ESM100 bath is autocatalytic, meaning any silver deposited from the bath onto the catalyst surface will itself act as a seed layer for further deposition.

The samples used for electroless plating were subjected to 720 $J{\cdot}cm^{-2}$ of UV irradiance to ensure all silver ions were reduced to silver nanoparticles and therefore maximise the available catalytic area. Heat treatment time was varied to compare the effect of silver particle size on the plating, with samples treated for 2 – 4 hours since they were found to be most reflective (see Figures 3.16 and 3.17). A sample with no heat treatment time was also tested for comparison. As well as the temperature and pH being key parameters in the ESM100 bath, the third major factor is the cyanide to silver ion ratio. Before any seed layer is added, the silver is in a silver cyanide compound in the bath. The cyanide ligand of this compound prevents the release of free silver ions into the bath. Therefore if the CN:Ag ratio is too high, plating will not ensue and if it is too low, plating occurs too rapidly and the plated layer detaches easily form the substrate. CN:Ag ratios of 0.79 – 1.1 were tested. The optimum operating temperature of the bath was 67°C but temperatures down to 55°C were tested and it was found that if the temperature was too low, plating would not occur. Similarly for the pH, variations between 9.8 and 10.3 were tested with 9.9 found to be most favourable.

When the sample with no heat treatment was immersed in the bath, all silver nanoparticles dissolved into the solution implying that there is no reimidisation without heat treatment so the modified layer is vulnerable to attack by the plating solution. After 2 hours of heat treatment, plating had not initiated after 10 minutes. This indicates the seed layer did not have enough activation energy since plating should visibly occur within a minute if there is sufficient catalytic activity. After 3 hours, plating did transpire on the seed layer areas on the substrate. However the plated layer soon detached from the substrate into the bath. The 4 hour heat treatment samples provided the best seed layer for plating at a temperature of 67°C, pH of 9.9 and CN:Ag ratio of 1.06. An example of the plated sample can be seen in Figure 3.21 below.

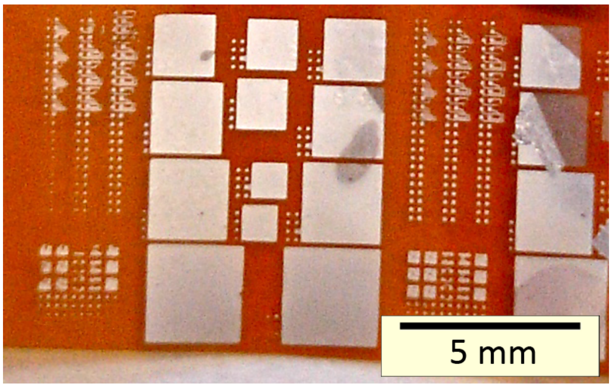

Figure 3.21: *Electrolessly plated test structures.*

On closer inspection under a microscope, the smaller feature sizes do not appear so uniform. The smallest feature size where deposited silver remained was approximately 30 µm. Tracks with lower linewidths appeared to have been attacked by the plating bath as no plated layer was found on these patterns. Furthermore, the original seed layer had also disappeared. It is possible that, at such narrow linewidths, the plating bath could more readily attack the degraded polymer underneath the silver nanoparticle layer, resulting in detachment between the two. This is shown in Figure 3.22(a) below.

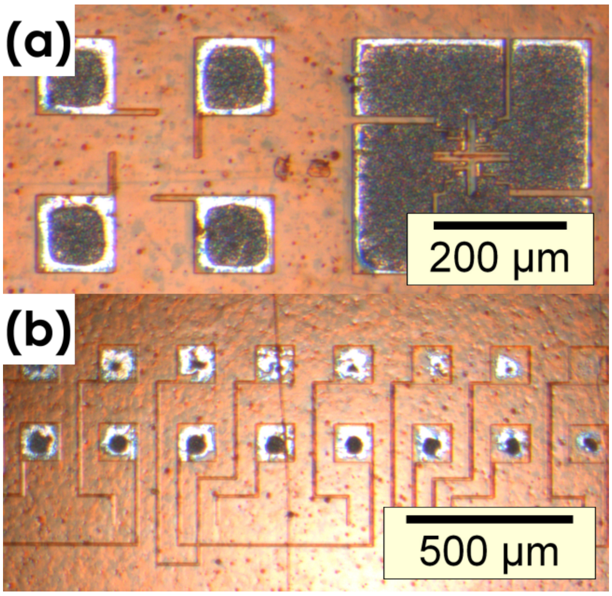

Figure 3.22: *Microscope image of plated microstructures.*

Figure 3.22(b) shows a sample submersed in the bath for a longer period. Here even the larger bond pads in the top-right have also begun to disappear. It appears that the detachment is not between the plated silver and the seed layer like the one seen in Figure 3.19(b). The degradation discussed above, perhaps best exemplified by Figure 3.18(F) at this point, must impair the mechanical interlocking between polymer and silver nanoparticles, resulting in poor adhesion of the electrolessly plated metal. Additionally, it can be seen from these SEM images that the silver particles are not closely packed together. This low density would not provide a high strength to metal deposited on top and would also expose more of the polymer to attack by the plating solution.

3.5.4 Conclusions

This set of experiments has investigated the effects of various process parameters on the production of a suitable silver conductive layer generated on top of polyimide. The application of UV irradiation and heat treatment times were examined with respect to their influence on the polymer substrate. An increased UV energy dose results in greater numbers of silver nanoparticles being formed up until a critical energy dose is employed and all the silver ions available in the exposed areas are photoreduced. At energy doses above 720 $J{\cdot}cm^{-2}$, the modified surface of the polyimide deteriorates, so an energy dose of 540 $J{\cdot}cm^{-2}$ was found to produce optimal for silver formation for subsequent plating, when judged by both reflectivity measurements and substrate degradation depth. As well as when silver ions were present, the surface morphology of the KOH treated PI was also observed to change slightly but remained constant for increased heat treatment times as shown in Figure 3.18(D). Heat treatment of the silver nanoparticle samples, Figure 3.18(E,F), prompted two conflicting effects of silver particle growth and polymer deterioration. This degeneration has been attributed to oxidative degradation. Increased silver growth from longer heat treatment times provides a better catalyst for electroless plating, however the increased time also reduces the polymer integrity, leading to poor adhesion between polymer and silver. The maximum density of silver nanoparticles can be improved by increasing the silver ion loading of the modified substrate, which can be achieved by increasing the initial degree of polyimide modification by KOH in the first processing step. However, a more aggressive KOH treatment regime has been shown to considerably degrade the rigidity of the film [6]. A compromise must therefore be reached between increasing the density of silver and degradation of the substrate.

3.6 Chapter conclusions

This chapter defined the direct laser writing process being developed in this thesis and the experimental procedures required for each step before examining a series of metal tracks produced by this process. While silver tracks were created, the underlying polymer was found to swell and/or ablate depending on the laser irradiance and energy dose used, with increased doses causing greater ablation. This prompted a closer investigation into these degradative effects and also into the effects of energy dose on the silver nanoparticles. The results of this indicate that increased energy from both photo and thermal sources are positive for silver particles but negative for the polymer substrate. It is therefore necessary to investigate ways to circumvent or at least mitigate this degradation at the same time as increasing the silver seed layer density to maximise adhesion. The following chapter explores in-situ silver particle formation by chemical reduction to compare with the photo-reduction based methods above.

Chapter 4:
An alternative metallisation route

4.1 Introduction

Having experimentally tested the direct writing process in Section 3.3 and subsequently characterised both the degradative effects occurring within the polyimide and the development of the silver nanoparticles caused by thermal and photothermal energy in Section 3.4, it is evident that the process would benefit from minimising the detrimental effects on the PI, while maintaining a suitably propitious level of silver coverage. A possible way to avoid such degradation could be to reduce the silver ions by chemical rather than photothermal means. Such a method has been shown as experimentally viable, with polyimide being fully coated with copper [156] and more recently silver [92]. Selectively patterning small enough feature sizes to be useful for microelectronic applications is a significant hurdle to overcome with this method. Nevertheless, attempts to pattern polyimides have been made using dimethylamine borane (DMAB) as a reducing agent in combination with inkjet printing [87] and screen printing processes [88] to form copper tracks. In both cases the minimum feature size achieved was 200 µm. Silver features created by screen printing and DMAB reduction were also recently demonstrated [157], but again the feature size was 200 µm. A fabrication flow of the chemical reduction with photoresist patterning route used in this chapter can be seen in Figure 4.1 below.

This chapter investigates the feasibility of chemical reduction by first determining in Section 4.2 suitable parameters for this process. These results are compared to the thermally induced degradation seen in Section 3.5 to better understand the silver formation process. Section 4.3 tackles the issue of patterning with this method by introducing a novel photoresist. Section 4.4 sums up what was learned about chemical reduction with the aim to manufacture circuits.

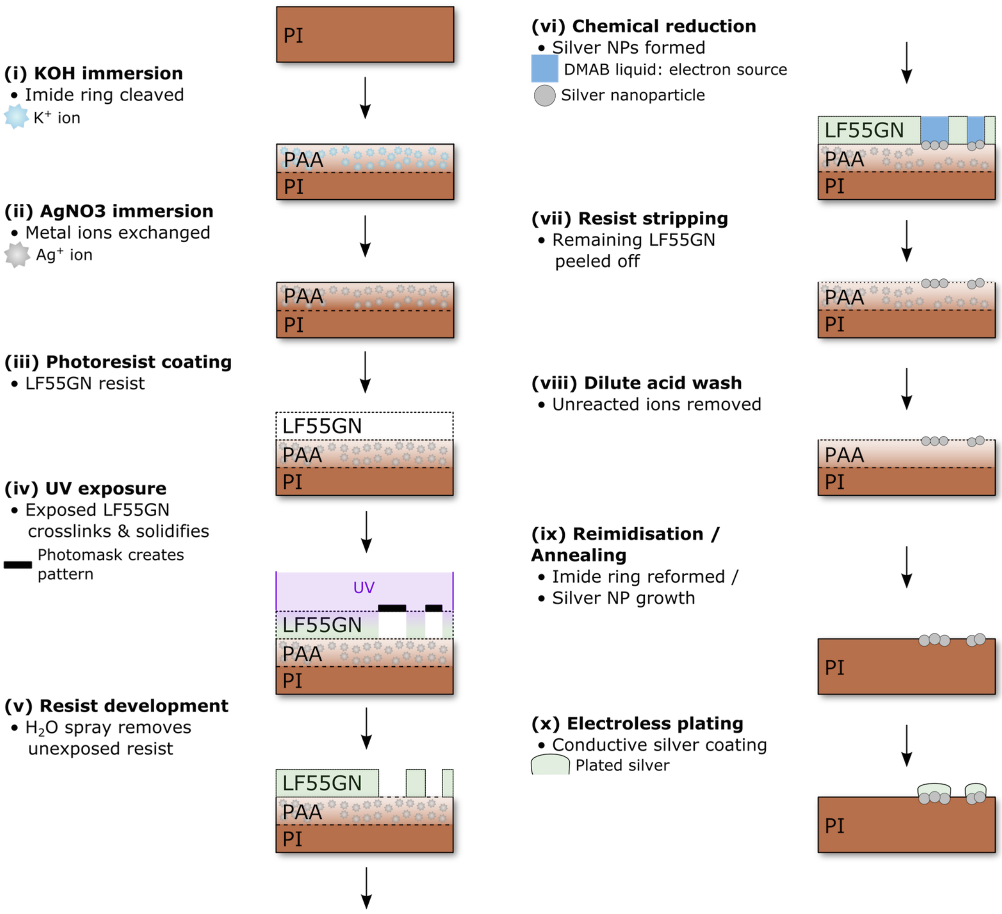

Figure 4.1: *Alternative selective metallisation route employing chemical reduction and photoresist patterning.*

4.2 DMAB concentration for silver particle growth

4.2.1 Aim

The aim of these experiments was to investigate the chemical reduction method of polyimide metallisation and determine the optimal concentration of the reduction solution and immersion time for silver seed layer growth for subsequent patterning and plating experiments. Results were assessed by microscope and SEM images and also by four-point probe resistivity measurements.

4.2.2 Equipment and procedure

Three approximately A5 sized sheets of 50 µm thick Kapton HN were cut and processed as described in Sections 3.3.1 – 3.3.3 to give surface modified polyimide loaded with silver ions. These sheets were then cut into 1 x 2 inch pieces. To minimize experimental error from these preparation steps each piece was then semi-randomly allocated immersion parameters of concentration and time in such a way to ensure that each concentration level contained at least 1 sample from each of the original A5 sheets.

DMAB solutions with concentration in the range of 1 – 500 mM were prepared by dissolving DMAB crystals in deionised water in a beaker. Since DMAB is not particularly soluble in water, especially if heavily concentrated, a magnetic stirbar and stirrer plate were used to accelerate the process. Samples of silver-ion-containing surface modified polyimide were then taped to the bottom of a glass Petri dish before approximately 40 ml DMAB solution was decanted into the dish to completely submerge the sample. Duration of submersion was varied between 30 seconds and 10 minutes. Samples were then removed and rinsed thoroughly with DI water. Excess water was then removed by covering the sample with a particle free cloth without applying any pressure before being left to dry. Reimidisation was performed at 250°C.

Microscope images were taken using an Olympus SZX10 with a Colorview iii-u CCD camera and Dino-Lite USB microscope models AM413T and AM4113ZT4. SEM images were taken using a Quanta 3D FEG from FEI. Four point probe measurements were carried out using a Jandel Engineering multi-height probe station with tungsten probe tips of 1 mm spacing and 60 g maximum force. This was connected to an RM3000 test unit, also from Jandel. Forward and reverse currents were taken to ensure validity of measurements, of which 3 were taken at different positions and the average value of these was taken.

4.2.3 Results and discussion

An array containing a typical sample of each of the time-concentration combinations can be seen in Figure 4.2 below. From the top left the rows depict concentrations of 1, 5, 10, 50, 100 and 500 mM descending the array, while the columns portray times of 0.5, 1, 2, 5 and 10 minutes, respectively.

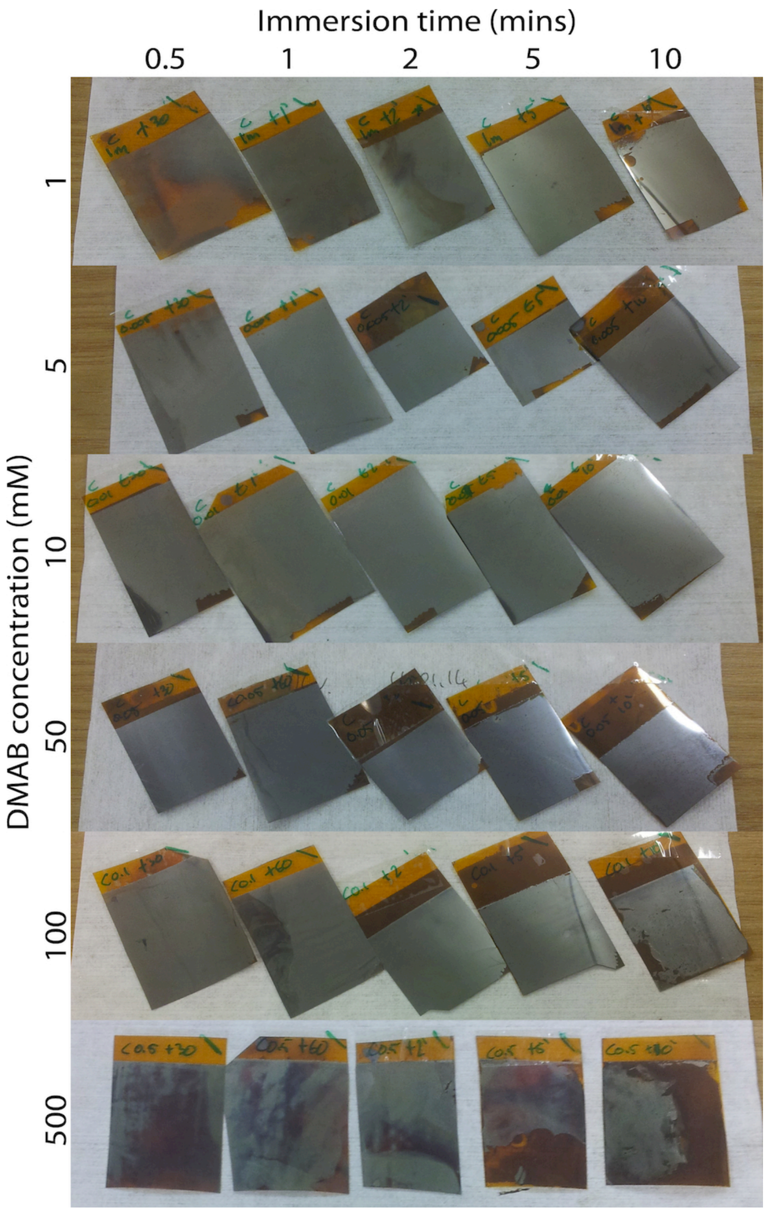

Figure 4.2: *DMAB immersion reduced samples. Increasing immersion time from left to right, increasing DMAB solution concentration from top to bottom.*

For all concentration and time permutations silver reduction was initiated within the first 15 seconds, with the majority of samples appearing to have silvered completely by the end of their submersion period. Only on the samples treated with 1 mM DMAB was the silver formation gradual enough to be observable between the different reaction durations; the 30 seconds, 1 and 2 minutes samples in particular highlight continuing silver particle formation. This can also be seen to a lesser extent on sample exposed to 5 mM DMAB for 30 seconds. Throughout the reduction reaction at all concentrations between 10 mM and 500 mM inclusive, gaseous bubbles began to form. Numerous bubbles were visible at all these concentrations after 5 minutes, with their onset noticeable after 2 minutes for concentrations of 50, 100 and 500 mM. Imprints at the locations of these bubbles were found on the silvered substrate after cleaning. Figure 4.3(a) below shows an example of these bubbles during immersion in a 50 mM solution for 10 minutes. Figure 4.3(b) shows the substrate after rinsing and drying at 90x magnification where it can be seen that the size of these holes was approximately in the range 100 – 300 µm, while Figure 4.3(c) shows an increased magnification image of a typical hole of approximately 300 µm.

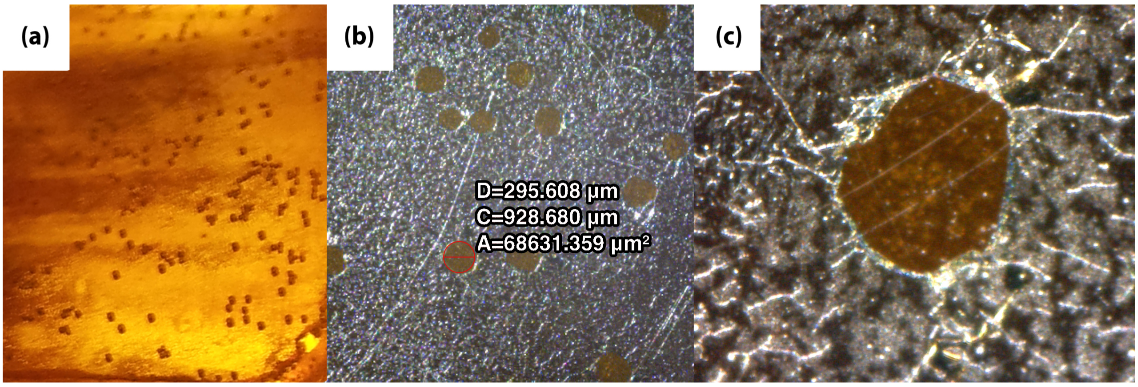

Figure 4.3: *(a) Gases forming during reduction reaction in Petri dish, area shown is approximately 1 square inch. (b) Microscope image of coating after rinsing. Highlighted hole has approximate diameter 295 µm. (c) Higher magnification of hole of approximately 300 µm.*

The silver layer at the top left of the hole in Figure 4.3(c) appears to have been folded back onto itself, indicating it had been forced out of the way by the gas escaping from below. This gas could be hydrogen formed as a by product of the silver-DMAB redox reaction [158] or possibly as a result of the DMAB reacting with the hydroxyl groups within the modified polyamic acid layer on the surface of the polyimide according to the following reaction [159]:

$$(CH_3)_2NH \cdot BH_3 + OH^- \rightarrow (CH_3)_2NH + BH_3OH^- \tag{4.1}$$

If the hydroxyl groups of the PAA are combining with the borane in solution, this could expose other sections of the polymer chain, allowing reaction with the carbon or nitrogen atom, which would have a negative effect on the integrity of the polymer chains. Break down of the PAA chains may result in reduced bond strength with the unmodified bulk polyimide underneath. Such a possibility is evidenced by the most stringently treated samples. As well as being widely 'pock-marked,' two samples, 500 mM, 5 and 10 minute treatment regimes, displayed such degradation that the silver detached from the substrate. The detachment occurred as a single sheet which was flexible but very fragile and disintegrated easily upon handling. The flexible nature with which it remained as a single piece suggests some quantity of PAA was also present in the removed material. Further evidence suggesting this can be seen in the interferometry profiles of the silver voids in Figure 4.4.

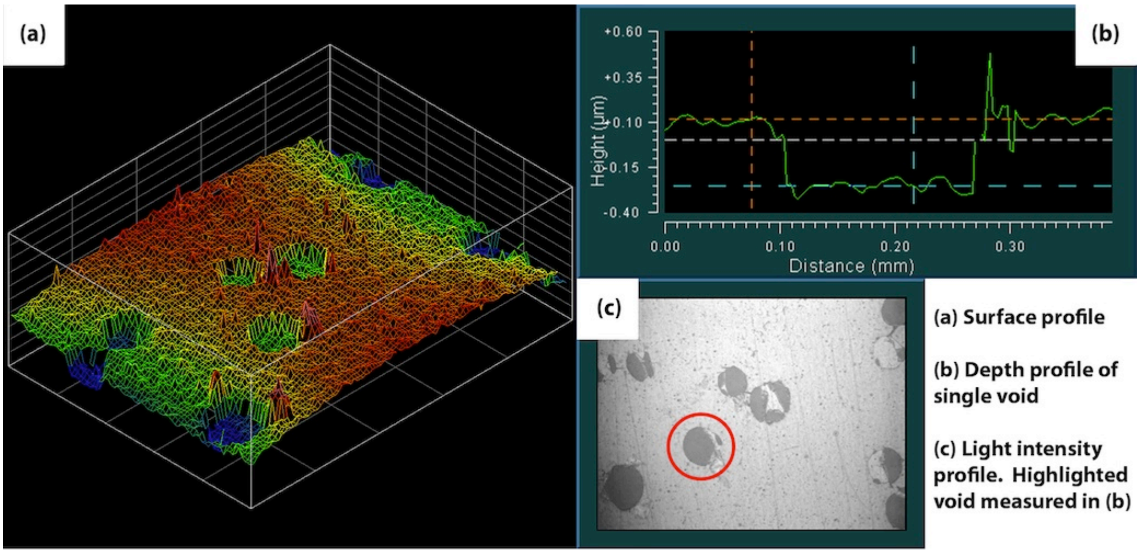

Figure 4.4: *Interferometry analysis of sample immersed in 50 mM DMAB for 5 minutes.*

The depth of the voids was approximately 300 nm, although it can be seen there is a fair amount of variation due to surface roughness. This depth is comparable to the depth of degradation observed underneath the silver patterned areas investigated in Chapter 3. When taken together, both these observations indirectly indicate the depth of surface modification carried out during step 1 of the process. Indeed, the regime used in this work of immersion in 1M KOH at 50^{o}C for 5 minutes fits this depth and agrees reasonably well with the surface modification depth observed by Stoffel *et al.* using Rutherford back scattering (RBS) spectrometry [160]. Their line fit for 60^{o}C, seen in Figure 4.5 below, suggests 5 minutes at this temperature should give 300 nm of modification, however this is a best fit line which leaves scope for experimental uncertainty. Further, their chosen substrate Kapton H, is a “special version” [161] of Kapton HN so it is reasonable to assume that some proprietary treatment or additives may have affected its resilience to alkaline attack.

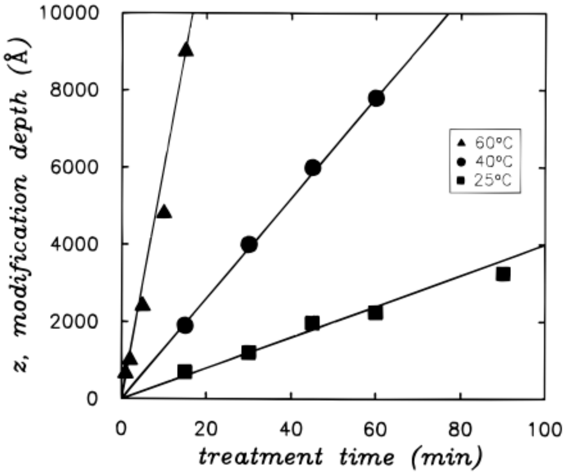

Figure 4.5: *Modification depth of Kapton-H for a 1 M KOH treatment [160].*

Stoffel *et al.* also experimentally confirmed the earlier assumption by Lee *et al.* that there is a relatively sharp interface between modified and unmodified polyimide [77]. This supports the above proposition that, at higher concentrations of DMAB solution and longer immersion times, the silver forms in the PAA layer but loses its adhesion to the underlying PI, perhaps originating at the areas where the gas bubbles have formed.

The three 500 mM samples with shorter treatment duration are also noteworthy. Although reduction was seen to initiate after similar time to samples with the lower concentration of DMAB, silver formation did not appear to progress as rapidly or as uniformly. While this may suggest a slower reaction, closer inspection suggests that the silver is actually forming much more quickly as shown in the SEM images of samples treated for 30 seconds at all the different concentrations in Figure 4.6 below. All concentrations up to 100 mM display signs of small particles forming within the substrate, with formations slightly larger in the 100 mM sample. The 500 mM sample however has already formed much larger nanoparticles on the surface. It is evident that a concentration of 500 mM is not suitable for uniform, reproducible silver reduction. However, on these samples the lack of imprint left at the site of bubbles indicates that time may be a more important factor in terms of delamination of the surface modified area, with durations of 5 minutes and over exhibiting the largest change.

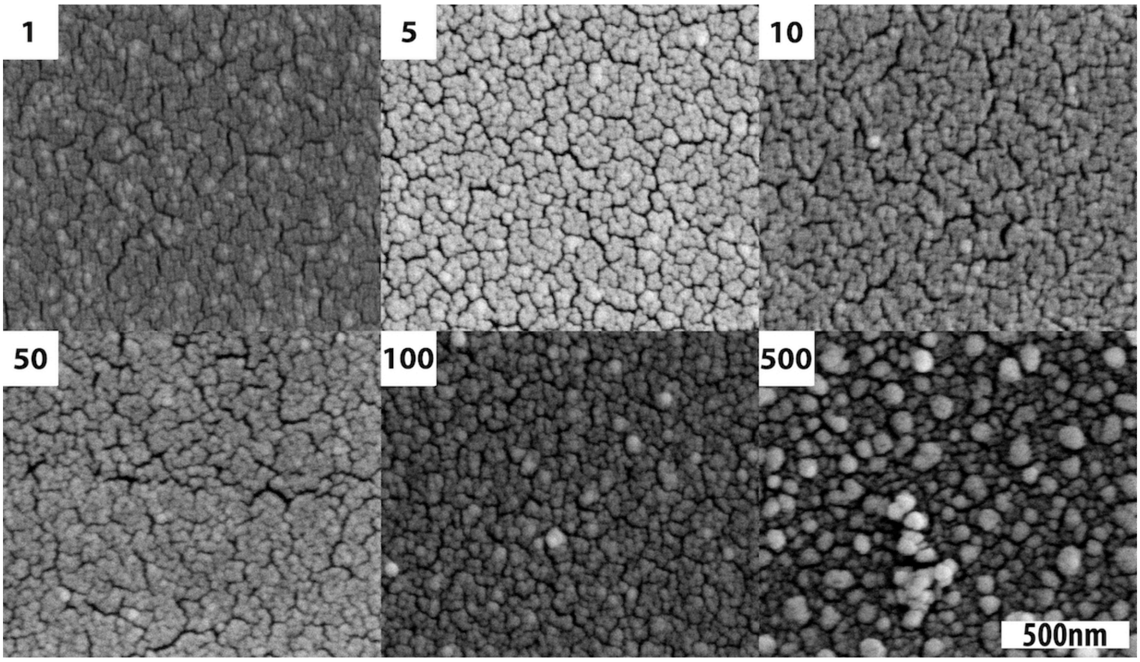

Figure 4.6: *SEM images of samples immersed in solutions of various concentrations for 30 seconds. Concentrations in mM indicated in top-left of each image.*

On this evidence the formation of bubbles should be minimised to maintain substrate integrity through lower DMAB concentration and a limit to the immersion time. To confirm this, surface resistivity measurements were taken of all samples using a four point probe. Such a measurement is useful as it provides an indication of the uniformity and density of the reduced silver. Average readings for each sample are shown in Table 4.1 below.

Valid readings were only obtained for the 5 mM and 10 mM samples for both un-annealed and annealed samples. While it could be expected that a current could not be passed through either the 1 mM samples, given their less silvered visual appearance than other higher concentrations, or the 500 mM samples, which showed very poor uniformity, it is perhaps surprising that a value could not be obtained by 50 mM and 100 mM samples, particularly after annealing.

As can be seen from the 5 mM and 10 mM samples, the reimidisation/annealing step clearly had a positive effect on the resistivity, with a reduction of typically around two orders of magnitude. These results compare favourably with resistivity reported by Mu *et al.*, who used ascorbic acid to reduce silver onto PI fibers and reported resistivities of approximately 100 Ω/square [162]. This can be better observed by plotting resistivity against treatment time for the conductive samples, as in Figure 4.7 below.

Conc. (mM)	Anneal	Time (mins) 0.5	1	2	5	10
1		NC				
	✓					
5		37.40×10^{6}	6.86×10^{6}	1.15×10^{3}	1.35×10^{3}	93.14
	✓	[111.77]	[70.95]	58.47	16.12	13.08
10		18.5×10^{3}	44.53×10^{3}	51.28×10^{3}	31.16×10^{3}	7.38×10^{3}
	✓	[28.16×10^{3}]	58.80	10.40	108.13	18.69
50		NC				
	✓	NC	Inv.	Inv.	Inv.	NC
100		NC				
	✓					
500						
	✓					

Table 4.1: *Resistivity measurements by four point probe method. Units are Ω/square. NC – not conductive enough to obtain a reading, Inv. – forward and reverse currents were not in close enough agreement for the reading to be considered valid. Samples in brackets appeared slightly patchy to the eye, perceived 'best' area was chosen for measurements.*

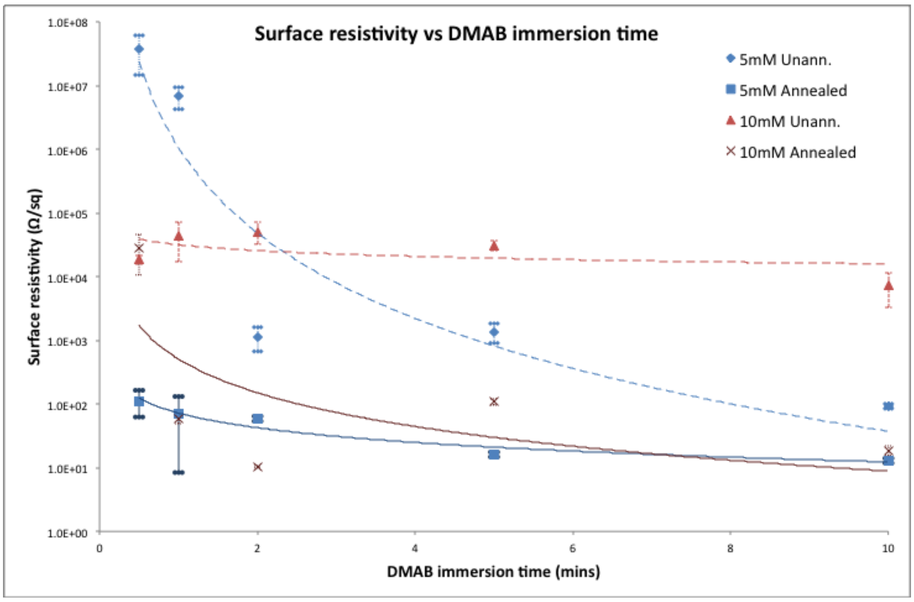

Figure 4.7: *Surface resistivity as a function of immersion time for 5 mM (blue) and 10 mM (red) samples. Best-fit curves have been added for both un-annealed (dashed lines) and annealed samples (solid lines).*

While there was a large variation in readings from the 10 mM annealed samples, there is still a clear reduction in surface resistivity with longer immersion durations, indicating a more conductive silver surface morphology. The lower concentration of 5 mM provides a better surface in this respect, certainly at longer treatment times. The annealing process however removes this advantage somewhat, with both annealed samples possessing similar resistivity after 10 minutes. To further investigate the changes to the surface undergone, SEM images of all 5 mM and 10 mM samples were taken and are in Figure 4.8 below.

Typically in SEM images the difference in contrast within the individual images provides an indication of the charge build up, with lighter areas representing areas of greatest charge accumulation. It is therefore reasonable to assume that the bright roughly spherical shapes of around 100 nm diameter prominent in some of the annealed samples are silver nanoparticles. Whether they contribute to the lower resistivity or not is not clear although it is suspected that they do not. The sample with greatest conductivity treated with 10 mM for 2 min and annealed (bottom, centre in Figure 4.8 below). This was found to have few particles sitting atop a surface, which had regions of high continuity and less height variation, suggesting more homogenous growth. Silver forming in this manner would lead to larger connected areas and therefore lower resistivity.

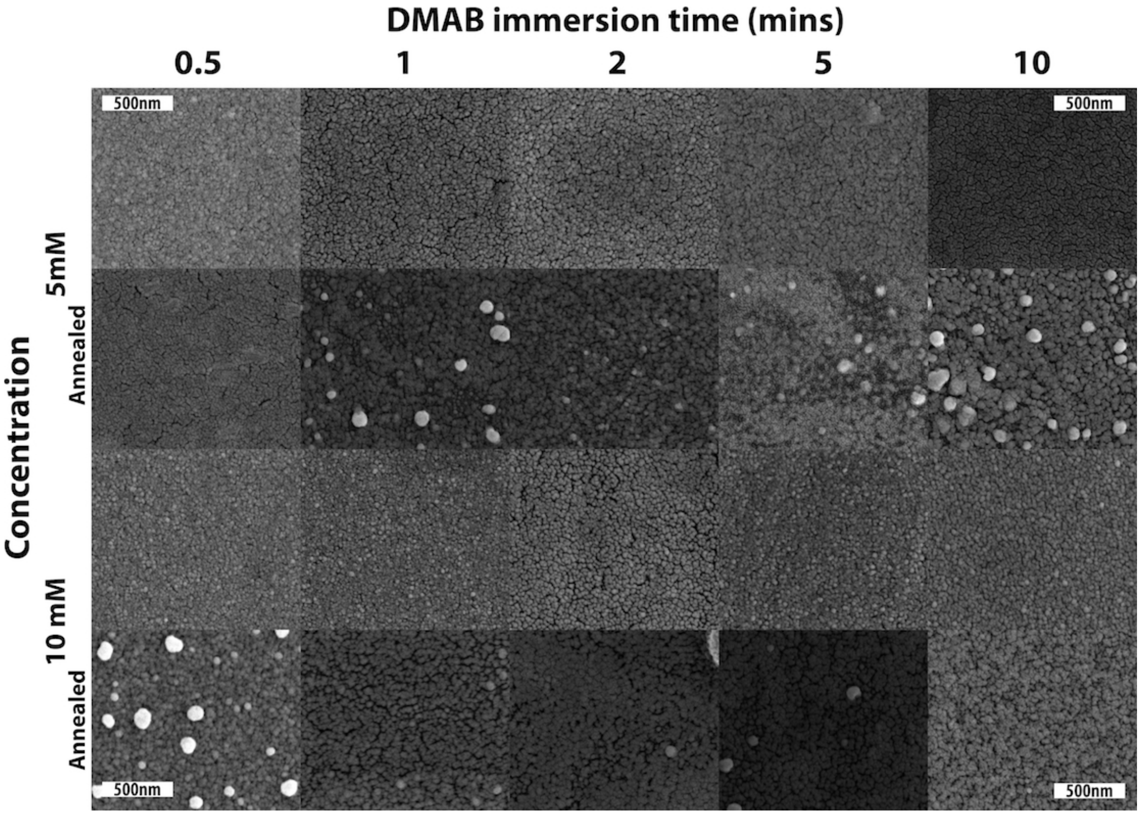

Figure 4.8: *SEM images of 5 mM and 10 mM treated samples before and after annealing.*

The only place NPs must be gaining their additional silver atoms from is within the polymer matrix. Akamatsu *et al.* noted the silver tendency of NPs to migrate towards the surface under UV exposure [2] so that, if the DMAB solution here has not diffused or penetrated the PAA to a great depth, it is possible that the silver will accumulate at a greater rate at the surface. Also silver attracts silver and so since the silver ions on the surface will be the first to undergo reduction, they will have a pulling effect on the remaining ions and newly formed NPs.

The 5 mM samples with lowest resistivity had longest immersion time and while these show NPs forming on top of the surface, there are also some continuous areas bright enough to indicate silver presence, so it would appear that the morphology of best conductivity is a combination of continuous silver rich regions and (relatively) pure silver NPs resting on the surface.

4.2.4 Conclusions

In-situ chemical reduction of silver is an effective way to produce uniform coatings of silver in a relatively short reaction time. Silver growth was controlled by modifying both reduction solution concentration and immersion time. It was found that 1 mM concentration was too low to produce a conductive surface for all times tested. 5 mM and 10 mM produced the only samples from which resistivity measurements could be made, with 5 mM generally providing the lower values. While the visual inspection of highest 500 mM concentration showed highly erratic silver covering and was therefore deemed unsuitable for plating, it was perhaps surprising that concentrations of 50 and 100 mM failed to yield conductive samples given their similar appearance to the 5 and 10 mM samples. The other previously reported patterning of chemically reduced silver on PI by Yang *et al.* [157] did not disclose the concentration used but the minimum concentration to reduce copper in the literature was 100 mM at an elevated temperature of 50^{o}C, although copper ions require two electrons for reduction as opposed to silver's one. It is evident that the DMAB also has a negative influence on the PAA, causing detachment from underlying PI at higher concentrations and immersion times.

While the samples with large (~100+ nm) silver NPs are more likely to catalyse electroless plating, they tended to occur in the samples of higher concentration and when combined with the resistivity measurements, correlate with the lack of conductivity of these samples. Therefore the parameters chosen for subsequent patterning experiments were immersion in 5 mM solution for 5 minutes.

Also, more indirect evidence of the surface modification depth of KOH treatment was demonstrated, showing good agreement with the depth profiles of the UV exposure metallisation process discussed in the previous chapter.

A suitable patterning process could complement this method to allow fast creation of circuits. The next section combines the above reduction route with a recently developed photoresist to form metallic features. Although photolithography is not 'direct writing', the photoresist in question is environmentally friendly and does not require harsh chemical treatment and so eliminates at least one of the other drawbacks of this fabrication route.

4.3 Circuit patterning with chemically reduced silver

4.3.1 Aim

Once an acceptable regime of chemical reduction of silver ions has been found that compares favourably to previous photoreduction experiments both in terms of silver nanoparticle formation and degradation of the polyimide substrate, the question of how to control the location of silver formation then arises. Patterning is obviously necessary to create functioning circuitry. One such method of patterning would be by well-established photolithography techniques. This photolithographic step would integrate into the overall fabrication process after the silver ion-exchange step, where photoresist application and patterning would occur. The substrate with photo-patterned resist on top would then be submerged in DMAB solution to initiate silver formation as normal. The remaining photoresist would then be stripped off before the standard step of rinsing in dilute acid to remove any unreacted silver ions. This process variation replaces steps (iii) and (iv) of the photoreduction process seen in Figure 3.1 with the photoresist patterning and chemical reduction steps of (iii) – (vii) in Figure 4.1 above.

Preliminary studies using photoresists from AZ Electronic Materials found that commonly used compounds were incompatible with our fabrication process due to chemicals present in their developing or stripping solutions. Typical developer/stripper solutions contained either KOH [163], seen in the present study to attack polyimide, or N-Methylpyrrolidone (NMP) [164], a powerful solvent for polyimides and numerous other plastics [165]. The hydrolysed surface of the PI substrate proved highly susceptible to these chemicals, resulting in any silvered polyimide being washed away during photoresist development. To circumvent this issue, it was necessary to find a photoresist whose developer solution would not interfere with the substrate in any way. A promising option is LF55GN from MacDermid Printing Solutions, USA. Although not widely utilised, LF55GN has been deployed in various applications, with the primary uses in the literature being as a mask for powder blasting [166-169], or for creating high aspect ratio structures [170] and microwave antennae [171]. This polyurethane-based compound acts as a negative photoresist, contains no solvents, which would require a pre-bake exposure step to remove, and only requires a jet of water to develop. As well as being advantageous for the current process, these handling requirements are also environmentally beneficial. Since metallic reduction using this resist as a patterning mask has not previously been undertaken, the final fabricated linewidths will be of particular interest when compared to both the mask geometries and the structures produced by photoreduction in the previous chapter.

4.3.2 Equipment and procedure

After the standard imide ring cleavage and silver-potassium ion-exchange steps were performed, LF55GN was spin coated onto the substrate using a Spin150 spin coater from SPS, Europe. Following the effect of rotational speed on spin coating thickness by Sayah *et al.* [168], a top speed of 2,000 rpm for 60 s was chosen to provide a thickness of approximately 90-100 μm. While this is a relatively high value for photoresists in general, it was chosen here for two reasons. Unexposed LF55GN is in a liquid state so, to prevent the photoresist sticking to the photomask, and thereby dirtying it for future exposures, a thin disposable acetate film was placed between the two to protect the photomask. The delicate manual nature of applying the protector meant that too thin a coating of resist could result in the LF55GN being sandwiched out of the gap between substrate. A thicker application reduced the chances of this happening. Secondly, once exposed, the cross-linked polymer forms a rubbery solid. As the coating thickness decreases, this solid has the tendency to come apart more easily, breaking into several smaller pieces rather than a few larger ones, making it more problematic and time consuming to remove. The covering of the surface of the LF55GN without air gap also removes the opportunity for any oxygen to come into contact with the resist. The presence of oxygen during UV exposure prohibits cross-linking of the polymer and is therefore undesirable. UV exposure was performed with the same Tamarack 152R mask aligner as used for the experiments described in Section 3.5. Patterning was accomplished with an acetate photomask supplied by JD Phototools, UK, which comprised of test structures with linewidths of 500, 250, 100, 50 and 15 µm. To achieve full polymer cross-linking a fixed energy dose of 200 mJ across the entire Tamarack exposure area was employed. The film was then developed by thorough rinsing in deionised water using a spray gun. Reduction of the silver ions was carried out by submersion in 5 mM DMAB solution for 5 minutes, followed by an ample rinsing in DI water. Prior to resist removal, the sample was subjected to a further 200 mJ UV exposure. This caused the remaining photoresist to assume a more rubbery form, facilitating easier removal. The remainder of the fabrication process was carried out with standard parameters of a 15-minute 0.1 M sulphuric acid bath and annealing in an oven at 250°C for 30 minutes followed by electroless plating in ESM500 electroless bath for 8 minutes at 70°C, pH 6.6. On the advice of PK Plating Tech, an additional post-plating bake at 150°C for 40 minutes was undertaken to encourage higher conductivity and adhesion. Linewidth deviation, height profile and any substrate degradation were characterised by an Olympus SZX10 optical microscope and Zygo Viewmeter 5620 interferometer, while adhesion was assessed using the standard "Scotch tape" test [172].

4.3.3 Results and discussion

Typical seed layers of linewidths 250, 100 and 50 µm can be seen in Figure 4.9 below. The 500 µm tracks were similar to the bulk coverings of the bond pads seen at the edges of these images and so have not been given their own image. However the 250 µm and 100 µm test structures are very well patterned and there is also evidence of reduction activity on the 50 µm structures.

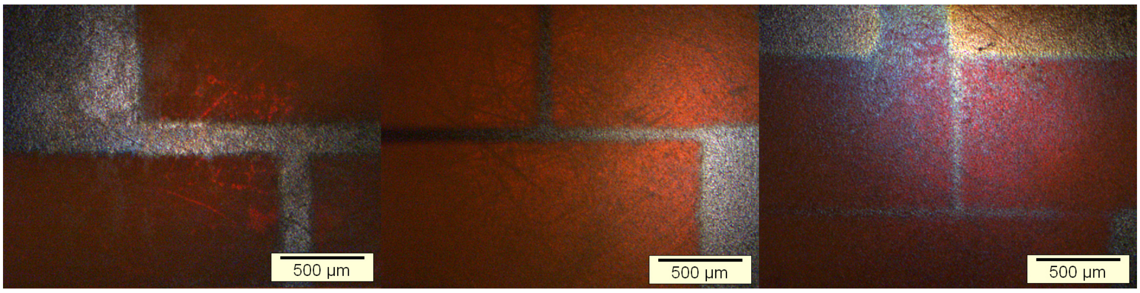

Figure 4.9: *Test structures with linewidths of 250, 100 and 50 µm.*

Images of the 15 µm test structures are not shown as they exhibited zero silver, possibly due to the swelling effect exhibited by the LF55GN liquid resist during development or indicating that the channel width of the LF55GN was too narrow for the surface tension of the DMAB to overcome. Closer investigation of the linewidths reveals that, although the DMAB produced tracks are clearly visible, the seed layers are slightly bigger than the linewidths of the mask at this stage, highlighted in Figure 4.10 below.

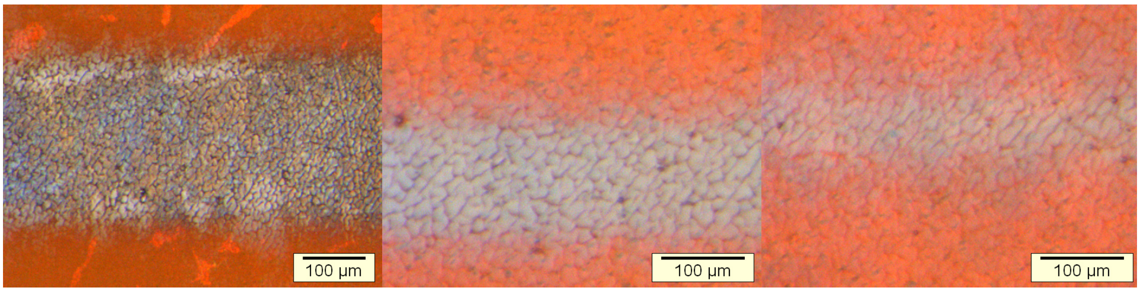

Figure 4.10*: High magnification microscope images of test structures. From left to right – 250, 100 and 50 µm.*

Rather than a clear divide between plastic and metal being visible, there is a more gradual transition, with the density of silver nanoparticles decreasing as the distance from the track centre increases. This could be due to the DMAB partially diffusing into the silver-polyamate underneath the LF55GN mask. This assumption is reinforced when examining a sample that was overexposed during the post-resist-development step, highlighted in Figure 4.11 below.

This second UV exposure, used to further harden the resist for easier removal, has caused silver to form in an approximately circular shape, around the four bond pads at the extremities of the test structure. The whole substrate was exposed but only a circular area of additional silver was formed near the features. This suggests that additional silver formation was not caused solely by UV exposure. It is possible that DMAB has seeped beneath the LF55GN, perhaps indicating that the adhesion of LF55GN to the substrate is less near patterned areas when compared with the bulk away from the edges. This is hypothesised because the water jet spray used to develop the unexposed liquid LF55GN is very powerful and was seen to dislodge improperly cured resists in preliminary tests.

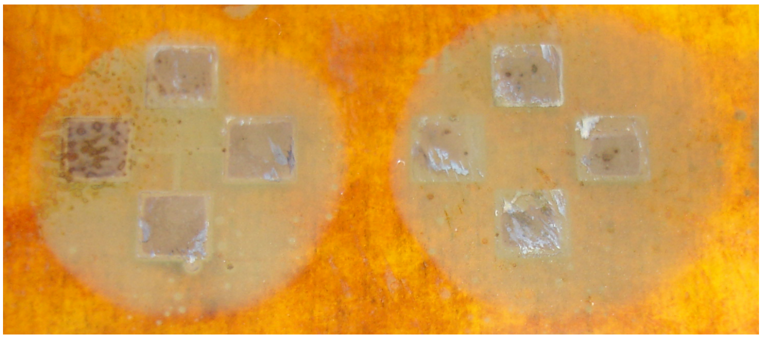

Figure 4.11: *Overexposed samples indicating that the LF55GN did not contain the DMAB solution within the patterned area.*

To compare the photo and chemical methods of silver formation for any degradation sustained, interferometer surface profiles were taken and can be seen in Figure 4.12 below. The absence of recessed pattern on the chemical sample indicates that there is no degradation of the polymer under the silvered areas as seen in the last chapter with UV exposure. This confirms the hypothesis in the previous chapter that UV irradiation, extended high temperature heat treatment or both, degrade the substrate.

Figure 4.13 shows microscope images of the same test structures from Figures 4.9 and 4.10 after electroless plating. It is clear from these images that the linewidth of plated tracks is not always uniform. The edges of the 250 µm and 100 µm tracks are not completely straight, while the 50 µm tracks were found to be discontinuous. No plating was observed on the seed layers with 15 µm linewidth and while the 500 µm samples did plate successfully, they were not deemed to provide further insights than the 250, 100 and 50 µm samples and therefore neither are presented here.

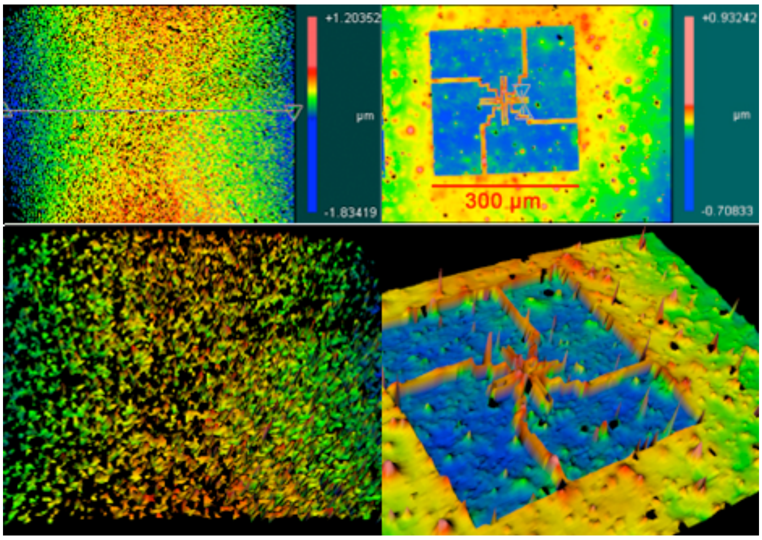

Figure 4.12: *Interferometry profiles of chemically reduced (left) and photo-reduced (right) test structures.*

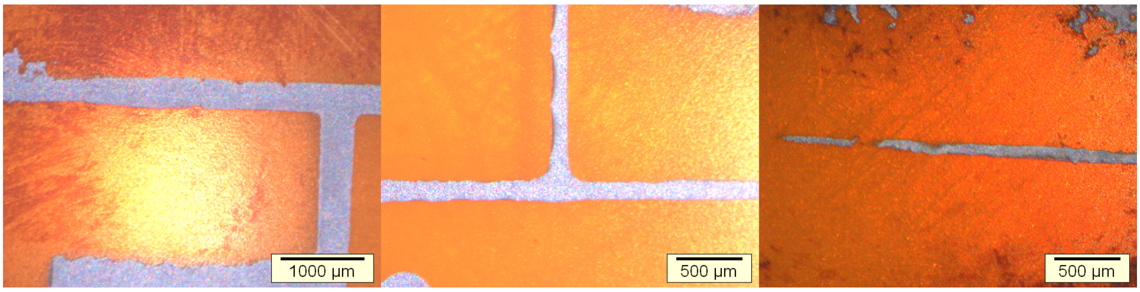

Figure 4.13: *Typical plated test structures with linewidths of 250, 100 and 50 µm respectively.*

This non-uniformity is attributed to incomplete removal of the liquid LF55GN resist prior to DMAB reduction, resulting in small patches or very thin films of resist remaining on the substrate. Even though it is reasonably water soluble in its liquid state, LG55GN is a very jelly-like and tacky substance and it was prone to accumulate in deposits on the substrate during developing that could not be removed without physical brushing of the substrate, which adversely affects silver formations. If small areas of resist were to remain, this could indeed hinder silver reduction. A similar situation also occurred after the silver reduction step when the remaining resist was stripped off. An example of a large accumulation of resist can be seen in Figure 4.14 below.

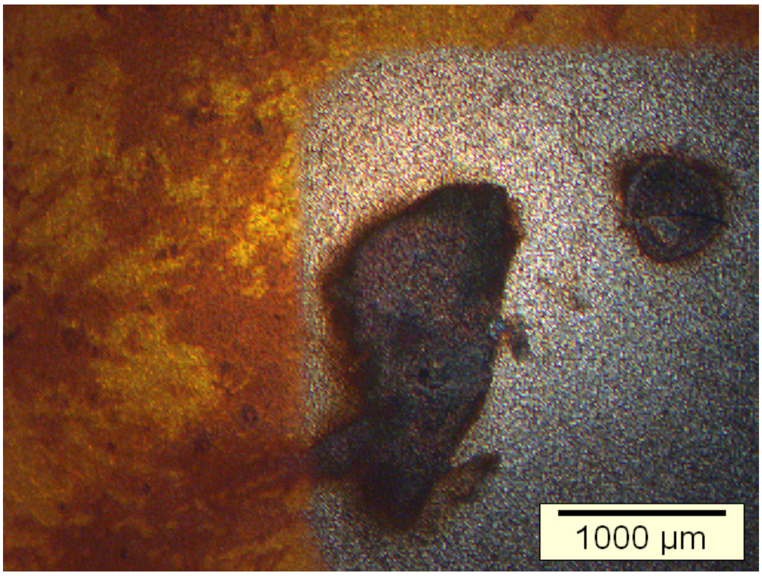

Figure 4.14: *Residual photoresist on the bond pad of a test structure after stripping.*

Higher magnification micrographs of the samples seen in Figure 4.13 can be seen in Figure 4.15 below. Although the silver plating is clearly uniform and densely packed, these images highlight the irregularity of the linewidth after plating, which points to the incomplete development of LF55GN, resulting in small areas along the side of the tracks that were shielded from the DMAB solution during the reduction step.

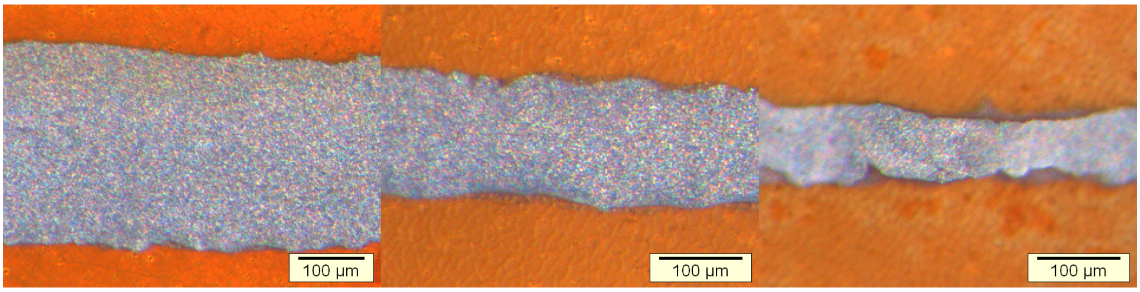

Figure 4.15: *Plated test structures. Linewidths of photomask used were 250, 100 and 50 µm, respectively.*

Interferometry analysis of typical plated tracks with 250 µm and 100 µm linewidth can be seen in Figure 4.16 below. The limited change in colour over the plated area indicates a uniform height over the whole track. Height of the plated areas was measured to be approximately 3.5 µm. The larger spikes along the outside of the 100 µm track are most likely artefacts from the signal processing as opposed to spiked deposits of silver.

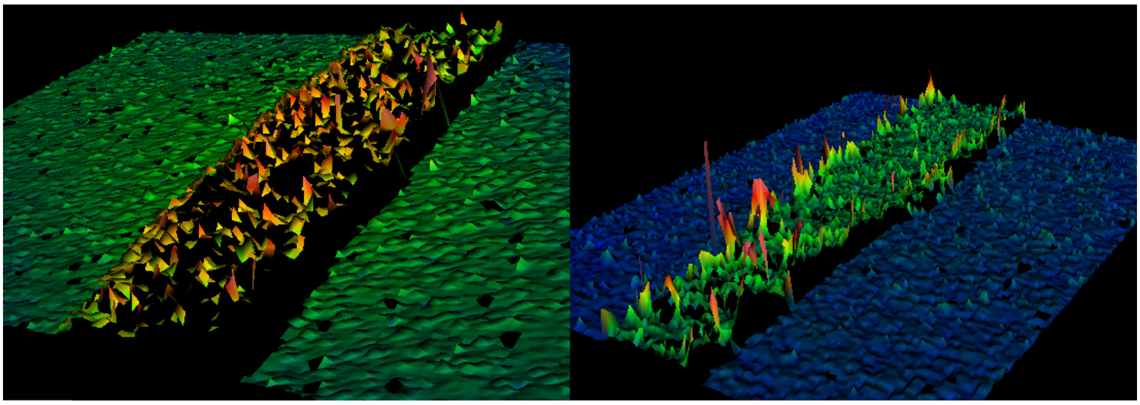

Figure 4.16: *Interferometry profiles of plated tracks of 250 µm and 100 µm linewidth respectively. Height was measured at approximately 3.5 µm in both cases.*

Obtaining an accurate figure for the linewidth of reduced silver before plating was problematic due to the gradient of silver formation seen in Figure 4.10 above. However once plating was performed the boundary between track and substrate was much more clearly defined, allowing a comparison between the intended and actual linewidths. Since the photoresist development process affected the linewidth as discussed above, measurements of track width were taken at sections with least deviation. Average linewidths for each corresponding test structure size can be seen in Table 4.2 below.

Test structure linewidth (µm)	Approximate plated linewidth (µm)
500	560
250	313
100	133
50	72
15	No plating occurred

Table 4.2: *Linewidth deviation in LF55GN fabrication process.*

Even allowing for approximately 7 µm of width increase due to the isotropic nature of the electroless plating bath, that is assuming there is an equal silver growth on each side of the track as that for the height measured in Figure 4.16 above, it is clear that the seed layer is considerably larger than the intended linewidths. Since LF55GN is a negative resist, any diffractive effects of the photomask would cause the linewidth to decrease, therefore the electrons within the DMAB solution must be able to diffuse and penetrate the substrate during chemical reduction outwith the intended bounds of the LF55GN.

Despite these hindrances, uniform plating of the larger area bond pads was achieved, an example of which be seen for the 100 µm test structures in Figure 4.17 below. Larger areas are useful to obtain a better understanding of adhesion testing and also to obtain values for the resistivity.

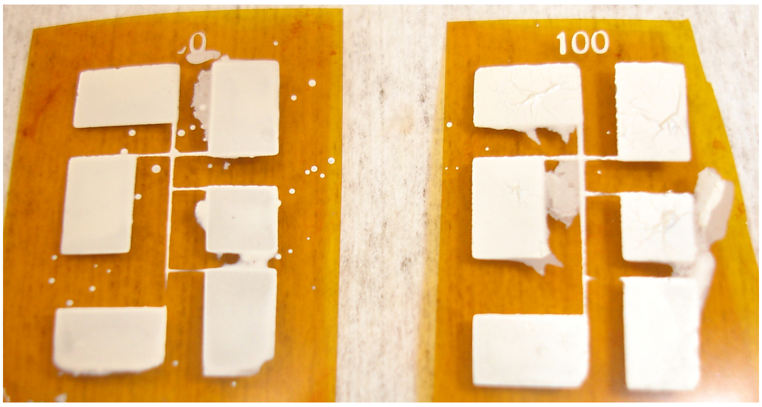

Figure 4.17: *Electrolessly plated 100 µm test structures.*

The resistivity was found by first measuring the resistance. Resistances were measured by 2-point probe testing with an ohmmeter along the longest silver path between the bond pads. As can be seen in Figure 4.17, the five rectangular bond pads can be connected via the central track in six different ways to obtain the maximum path length, which was 10 mm. For each of the different linewidth tests, the average value of these six resistances was calculated and are given in Table 4.3. Resistivity, ρ, was then estimated using the relationship:

$$\rho = \frac{RA}{l} \tag{4.2}$$

where R is the average resistance over the length of the test structure, A is the cross-sectional area, obtained by multiplying the plated linewidth values in Table 4.2 with 3.5 µm, the height of plating measured in Figure 4.16, and l is the 10 mm length. Any values where the reading was infinite due to a broken track were excluded from the calculation. No unbroken 10 mm tracks were found on the 50 µm and 15 µm samples so no data for these could be taken.

These values compare favourably with the value of bulk silver resistivity, which is 1.6 µΩ·cm [8], being only one order of magnitude greater. The increase in resistivity of the 100 µm sample can be attributed to the variance in track width. The variance was broadly similar for all track dimensions and therefore becomes proportionally more significant as linewidths decrease. This is best understood by referring to the high magnification images of the plated tracks Figure 4.15.

Test structure linewidth (µm)		Average resistance (Ω)	Estimated resistivity (Ω·m)
Target	Measured		
500	560	1.4	2.74×10^{-7}
250	313	2.4	2.63×10^{-7}
100	133	9.9	4.61×10^{-7}

Table 4.3: *Test structure average resistances over 10 mm path length.*

Finally peel tests were carried out on the 100 µm structures to test the adhesion of the metal structures to the polyimide, highlighted in Figure 4.18. While the majority of the plating on the test tracks was removed, the majority of the bond pads remained in tact, with only parts of the edges being removed. The silver tracks still being present on the substrate shows that strong adhesion at the metal-polymer interface is achieved.

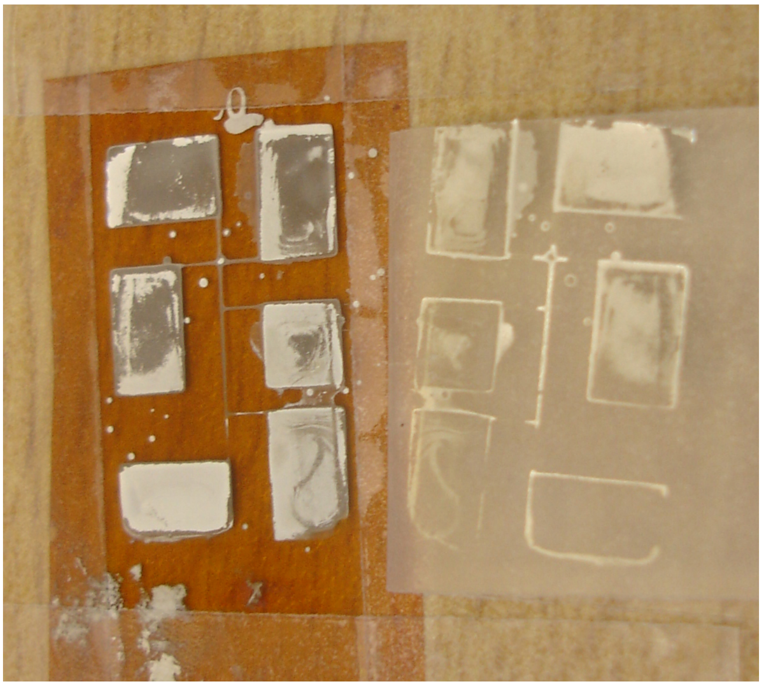

Figure 4.18: *"Scotch tape" test of 100 µm tracks.*

4.3.4 Conclusions

An alternate flexible circuit fabrication route has been investigated with moderate success. While the minimum feature size attained was only 100 µm, this may be enough for some applications. The smaller test structures of 50 µm and 15 µm were incomplete. More problematic is the variation in width of the track, mainly due to the way the undeveloped LF55GN photoresist is removed before DMAB immersion. Although the resist is slightly water soluble, it relies largely on the mechanical impact of the water for removal. As well as the possibility of incomplete resist elimination, this process also appears to weaken the adhesion between LF55GN and substrate, meaning track diameters become larger than designed. It is envisioned that a complete clearing of the undeveloped resist would allows for feature sizes of approximately 50 μm to be reliably produced but the lack of seed layer on the 15 μm samples suggests that the DMAB was not in contact with the substrate due to surface tension. While a thinner coating of photoresist may help this, it becomes more challenging to both remove the undeveloped resist after UV exposure and also to strip the developed resist after chemical reduction. For this reason, it was deemed unsuitable to continue with the chemical reduction route. Though the majority of the plating on the test tracks was removed during the peel test, the fact a remainder was left behind suggests that adhesion between the silver seed layer and the polymer is sound and more work is required on the plating.

4.4 Chapter conclusions

In-situ chemical reduction of silver nanoparticles in polyimide was demonstrated. From the permutations tested an immersion time/concentration combination of 5 mM for 5 minutes was chosen for subsequent patterning attempts. The higher concentration tests indicated that chemical reduction with DMAB, in a similar fashion to the UV exposure in the previous chapter, caused unwanted degradation of the PAA of the substrate while forming silver NPs and so a compromise was necessary. The KOH modification depth of approximately 300 – 350 nm was also indirectly confirmed.

Chemical patterning with the aid of water-based photoresist LF55GN was successfully demonstrated down to mask feature sizes of 50 μm, however due to the rubbery composition of the resist, the result tracks were larger than the intended linewidth. Furthermore the chemical reduction spread to areas underneath the resist areas, in a similar way to over etching in traditional CMOS processes. This also resulted in a large variation of linewidth along the length of the patterned features.

When compared to UV photoreduction the chemically reduced silver before annealing was of similar if not better uniformity. Also, with the optimally chosen parameters, degradation of the substrate was not observed. This method would also be more suitable for larger linewidth connections or features such as capacitor pads, where silver could be produced over a large substrate area because of the lengthy broad beam exposure required by the photoreduction method. The process at this scale however faces competition on several fronts and so photoreduction is still the preferred method for small feature fabrication. Additionally, extra photoresist processing steps are necessary to achieve selective metallisation, increasing fabrication time and therefore cost, making the direct laser writing route more attractive.

Chapter 5:
Biologically inspired fabrication

5.1 Chapter introduction

The source of the degradation of the polyimide seen in Chapter 3 was attributed to both thermal and oxidative effects, whereby oxygen radicals attack the silver polyamate at the surface of the polyimide. Indeed, a recent study by Rasmussen *et al.* investigating degradation by both thermal and UV radiation routes provides more in-depth study of this phenomenon [173]. Firstly their analysis of thermal degradation found two competing mechanisms at work: one which causes oxygen radical generation and is more dominant at temperatures greater than 250°C, markedly so at 300°C and above, and a second which caused radical termination, leading to stabilisation of the material. This second mechanism prevailed at 100°C, with both mechanisms competing approximately equally at 200°C. This suggests that although higher temperatures are necessary for reimidisation of the polyamate layer, a lower temperature than the 300°C used in Chapter 3 would be preferable, particularly since 250°C is high enough to achieve almost complete imidisation for PMDA-ODA, while having negligible effect on the mechanical properties [174]. While this will mitigate overall degradation to some degree, there is still the issue of UV triggered decomposition. In that respect, Rasmussen *et al.* found the best fit for the kinetics of the reaction was a bi-exponential decay, indicating that at least two degradation mechanisms occur simultaneously. One suggested mechanism was secondary thermal degradation caused by the UV radiation heating the sample. A way to alleviate this could be to use a higher wavelength, and thus lower energy, radiation source, particularly since Kapton is highly absorbent in the UV region [39]. Figure 5.1 below shows the emission spectrum of the mercury light source used in Chapter 3 with the UV-vis absorption spectrum of Kapton [175]. Although the peaks of both spectra are not on the same scale and so cannot be directly compared, it is clear that the energy produced by the mercury arc lamp below approximately 400 nm will begin to be absorbed by the polyimide, potentially causing undesirable heating of the substrate during the UV exposure step of the process.

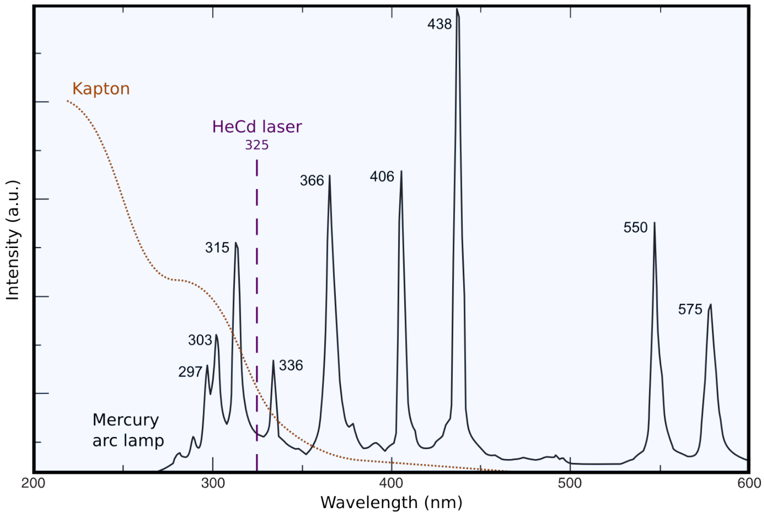

Figure 5.1: *Mercury arc lamp emission spectrum with Kapton absorption spectrum superimposed [175]. Wavelength of laser used in Chapter 3 also indicated.*

If the wavelength of the excitation source is moved slightly into the visible area of the spectrum this will minimise the heat generated through UV absorption by the polyimide substrate. To keep the excitation wavelength as low as possible, and thus excitation energy as high as possible, while remaining in a range transparent to the PI substrate a blue light source should be used. This modification has additional impact on the process however. Depending on the wavelength chosen, the MPEG electron donor coating may need to be replaced. MPEG has a similar UV-vis curve to that of Kapton above, in that it only begins to become absorbent to light below about 400 nm, although there is a second absorbance peak at approximately 530 nm [85]. Therefore an energy source emitting between 400 and 500 nm or above 550 nm will have little effect in initiating the silver-MPEG redox reaction. With the notion of minimising both cost and environmental impact in mind, an interesting possibility with which to replace the MPEG is to attempt to mimic the most widely known and used photochemical process: photosynthesis.

Despite much research in artificial photochemical conversion dating back at least 35 years [176], natural photosynthesis is still the most efficient method for converting and storing solar energy, although man-made methods are on the verge of surpassing this [177, 178]. Very briefly, natural photosynthesis in green plants captures light energy for the creation of oxygen via photosystems one and two (PS-I and PS-II). These photosystems typically consist of a reaction centre surrounded light harvesting complexes (LHCs). Reaction centres typically consist primarily of chlorophyll-a while LHCs consist of several antenna pigments such as chlorophyll-b and various other carotenoids like lycopene, ß-carotene and xanthophyll. Within a given photosystem, antenna pigments will absorb the photons, whose energy will be passed by resonant energy transfer to reaction centre molecules such as chlorophyll-a, where oxygen is created along with protons and electrons.

Perhaps the most commonly recognised pigment by name is chlorophyll. As well as being abundant in nature, existing in various forms in the majority of plant, bacterial and algal life on the planet, it can be easily extracted at low cost using ethanol, although such methods do not isolate chlorophyll molecules from other ethanol-soluble molecules, which is considerably more expensive. By replacing the MPEG coating with spinach extract dissolved in ethanol, it is hoped that the energy efficiency of the direct metallisation process studied in this thesis can be improved.

This chapter investigates whether the combination of blue light sources and pigments present in the light harvesting complexes found in spinach leaves can provide enough energy to form silver as readily as UV exposure of MPEG coated substrates while incurring less damage to the polyimide substrate. Initial tests verify this theory using spinach extract, first proposed by Jack Ng, and test whether the presence of ethanol affects the process in Section 5.2 before direct writing of silver tracks with a blue laser is demonstrated in Section 5.3. The crude method of chlorophyll extraction used for these initial tests cannot definitively ascertain that chlorophyll is the sole actor in the metallisation process as several other pigments are also present in the complex photosystems involved in photosynthesis. Therefore Section 5.4 examines the photosynthesis process more closely before Section 5.5 investigates whether isolated pigments can provide the same photoreductive efficiency as spinach extract. Section 5.6 provides conclusions to the chapter.

5.2 Initial chlorophyll tests

5.2.1 Aim

Preliminary tests were set up to confirm the feasibility of chlorophyll as an electron donor for silver formation. Since the cost of ordering pure chlorophyll is very high due to the complex extraction methods required to isolate it from the other antenna and reaction centre proteins, the most practical way of obtaining it is by extraction from spinach. Once the chlorophyll was obtained, it could be used to replace MPEG as the electron donor on a silver ion doped substrate.

5.2.2 Equipment and procedure

For chlorophyll extraction, 100 g of spinach leaves were placed in a standard kitchen blender with 200 ml of absolute ethanol and mixed for 60 seconds. Various solvents such as acetone or hexane could also be used but ethanol was chosen as it is both cheaper and easier to dispose of. The ethanol-spinach mixture was then filtered using Whatman No. 1 filter paper to remove any fibres or debris from the spinach leaves larger than 11 μm. The resulting solution was then spin coated onto the silver ion doped polyimide substrate. Since ethanol has a low viscosity the spin coating regime employed was rapid acceleration to a moderate cruising speed for a short duration, shown in Table 5.1 below. This length was sufficient for all ethanol to evaporate, leaving the substrate ready for immediate exposure.

Acceleration (rpm·s^{-1})	Top speed (rpm)	Total spin time (s)
500	2000	30

Table 5.1: *Ethanol spin coating parameters.*

Standard procedure for preparation of silver ion doped substrates was observed, as shown in steps (i) and (ii) of Figure 3.1. The substrate was then exposed to blue light from a Prizmatix UHP-460 LED source emitting at 460 nm and rated at 1 W output power. This particular model was chosen because its output wavelength range was the best available match for accommodating the absorption regions of all pigments within photosystem I/II. The emission spectrum of the LED is overlaid upon the spectra of these pigments in Figure 5.2 below.

The LED was placed as close as possible to the substrate for a range of durations between 30 seconds and 10 minutes. Incident power at the surface was measured with a Thorlabs PM121D optical power meter setup. The observed spot diameter of 9 mm was input to the power meter software to obtain a maximum power reading of 740 mW, giving an irradiance at the meter surface of 11,361 W·m^{-2}. After exposure, samples were rinsed with ethanol then water before submersion in dilute sulphuric acid to remove any unreacted ions. The annealing step was not carried out since the focus of these experiments was the photoreduction step and the thermal effects have already been characterised in Chapter 3. Temperature was measured using a Sensirion SHT21 sensor. Microscope and interferometry measurements were taken with a Dinolite and Zygo Viewmeter 5200 respectively. SEM imaging was performed on Quanta 650 and Quanta 3D FEG instruments, both from FEI. EDX measurements were taken with an Oxford Instruments X-maxN 150 and transmission electron microscope (TEM) imaging was carried out by Shabir Ravji at the University of Glasgow using an FEI Tecnai T20.

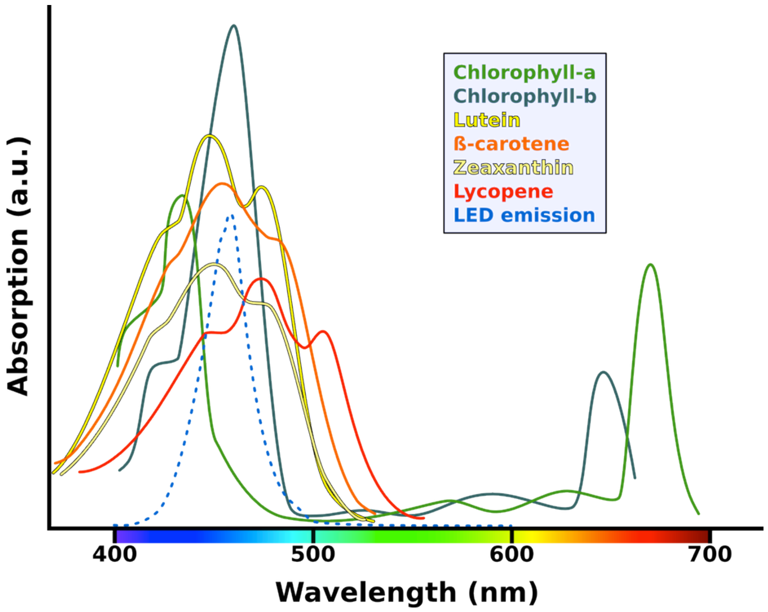

Figure 5.2: *Visible light absorption spectra of photosystem pigments with emission spectrum of LED with maximum emission at 460 nm. Adapted from [179], solvents used not stated so maxima may vary slightly.*

5.2.3 Initial results

Samples were exposed at maximum power for 30 seconds and 1, 2, 5 and 10 minutes, providing energy doses over the entire spot of about 22, 44, 89, 222 and 444 J respectively. Images of these spots can be seen in Figure 5.3 below.

Silver can be seen to have formed even at the lowest energy dose tested, with the silver apparently becoming denser as the energy dose increases. It is also noticeable from one minute onwards that silver formation is not uniform across the area of the spot. This could however provide clues to silver formation at different energy doses. Studying the photographs of the 1, 2 and 5 minute samples, it appears from the concentric patterning that there are three areas with slightly different silver formations and four different areas in the 10 minute sample, not including the thin, darker area at the spot extremity. This is most likely due to the light source providing a stronger energy dose in the centre of the spot than at the sides. Whether the incident light is modelled as being emitted from a point source, resulting in an irradiance inversely proportional to the square of the distance from the source, or more realistically in this case as a miniature spotlight with lower divergence, it is clear that radiant power is a contributing factor. The dark spot at the centre of the 10 minute sample appeared rough to the naked eye, possibly indicating burning. This is discussed further later. To get an idea of formation activity at the microscopic scale SEM images of spots created by the same varying exposure times were taken and can be seen below in Figure 5.4.

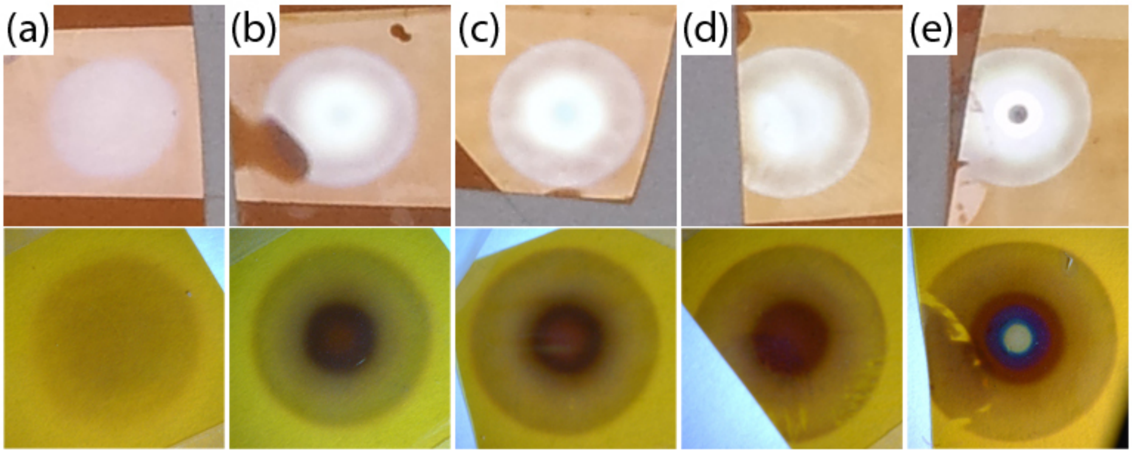

Figure 5.3: *Effect of varying doses of blue light on silver ion-doped PI. Top: photographs of spots. Bottom: increased magnification microscope images. (a) – (e) correspond to exposure times of 30 s, 1, 2, 5 and 10 minutes or energy doses of 22, 44, 89, 222 and 444 J respectively. Spots are approximately 9 mm in diameter.*

Silver particles clearly formed on all samples, however variation in their size can be seen across both the different exposure times and regions of the exposed area. The largest particles toward the outer edges of the spot after 30 seconds are approximately 50 nm in diameter and near spherical in shape. This increases to the 80 – 100 nm range after 1 minute where it remains approximately constant up to 5 minutes. Looking at the 10 minute exposed sample (e) it appears the outermost ring consists of smaller particles of around 20 – 30 nm which have begun to coalesce into larger clusters often well over 150 nm in size, rather than the individual spheroid particles seen in the same area of the other samples with lower exposure time. Coalescence also occurs towards the centre of the spot, but the size of the constituent spheres is larger, indicating that a higher intensity of light causes larger silver particles to form but at the expense of the silver formations being more disconnected. This tendency to form larger silver particles at higher intensity could also be a factor in the degradation as the more rapid growth could be putting more pressure on the supporting polymer matrix. Also more energy can be absorbed by larger areas of silver, which could cause a more pronounced heating effect. This is most evident when comparing the outer regions of the spots along the top row to the inner regions at the very centre on the bottom row.

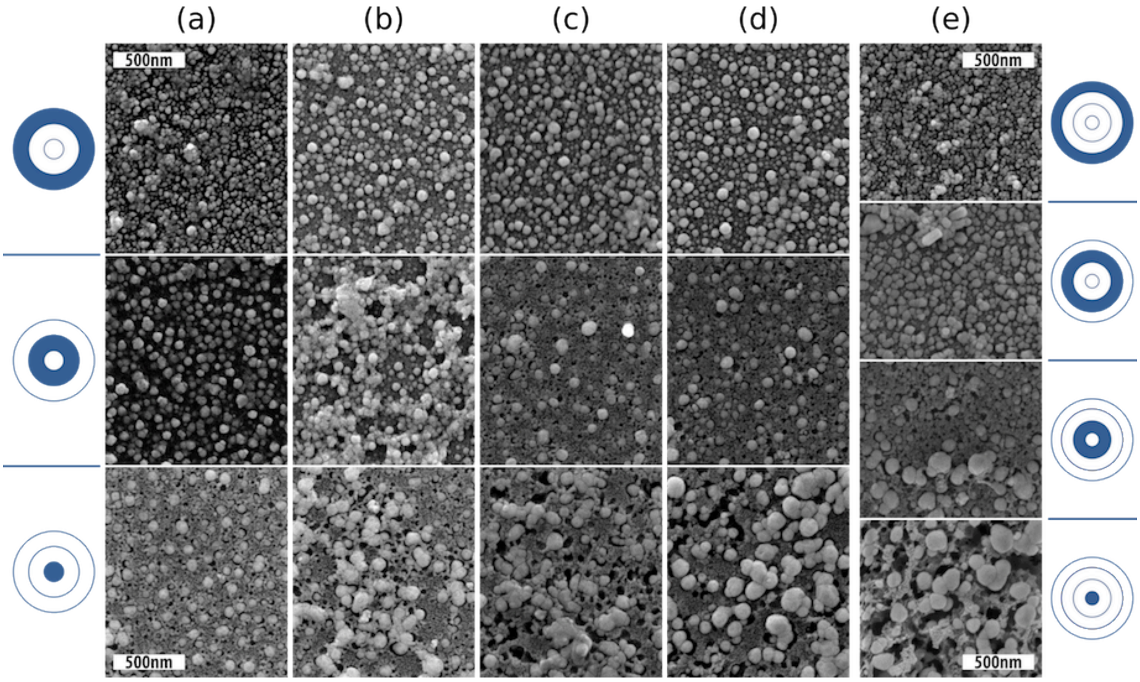

Figure 5.4: *SEM images of each energy dose on different regions of the spot. Approximate location with respect to Figure 5.3 is marked on the left for samples (a) 30 s, (b) 1 minute, (c) 2 minutes, (d) 5 minutes and on the right for sample (e) 10 minutes due to its noticeably different visual appearance.*

Comparing a single row of images shows exposure time also has a less conspicuous effect on particle size however, with growth occurring most noticeably in the centre region but also to a lesser extent in the outer region, although it could also be that a certain energy threshold must be met to trigger the nucleation process. A small degree of coalescence is also visible in small patches from one minute onwards but the spheroid shape of the constituent nanoparticles (NPs) is still visible.

Although morphology varies slightly between samples of different exposure times, a greater difference can be seen between different areas of the same sample, that is different intensities of light. Further evidence of this is seen in the compositional results from EDX analysis seen in Table 5.2 below. Measurements were taken from the central and outer regions, confirming silver content of approximately 3 – 4% and 1% by atomic count respectively across all samples. If it is assumed that there is complete reduction of silver ions in the centre spot, despite the different visibly surface morphologies in Figure 5.4 above, then the lower intensity light at the spot edge can only partially reduce the silver. The high percentage of silver in the 10 minute edge sample was attributed to being taken in an area similar in appearance to the second row of column (e) in Figure 5.4, although it could also indicate that a longer exposure period will allow the more deeply embedded ions to diffuse towards the silver NPs where they will be more readily reduced.

Element	**Sample region / exposure time (mins)**									
	◉					◎				
	0.5	**1**	**2**	**5**	**10**	**0.5**	**1**	**2**	**5**	**10**
Ag	4.1	2.7	4.0	3.3	3.1	0.7	1.2	1.4	0.8	3.4
C	70.5	77.1	72.9	76.8	78.7	78.0	75.9	75.5	77.9	79.0
O	24.0	19.5	21.4	19.4	17.6	20.7	22.1	22.6	21.0	16.8

Table 5.2: *EDX elemental analysis at innermost and outermost regions of samples. Values are in percentage of atomic composition.*

The drop in oxygen levels of both 10 minute exposed areas could indicate oxidative degradation, however it should be noted that at the submicron scale, EDX measurements are somewhat crude. This is especially true when taking into account that they provide information of material composition up to several microns deep within the sample. Since the silver loaded PAA layer is only approximately 300 nm deep, this means that the composition will be mostly the carbon of the underlying polymer as the silver only occupies a small fraction of the total volume examined. Carbon and oxygen values were included as a comparison to pristine PI, which consists of around 75% carbon and 24% oxygen, as can be calculated from its chemical formula $C_{22}H_{14}N_2O_7$. Hydrogen is not included, as it cannot be detected by EDX. The EDX spectra were broadly similar in shape across all samples, with silver peaks reduced for the outer edge samples. A typical spectrum is shown in Figure 5.5 below:

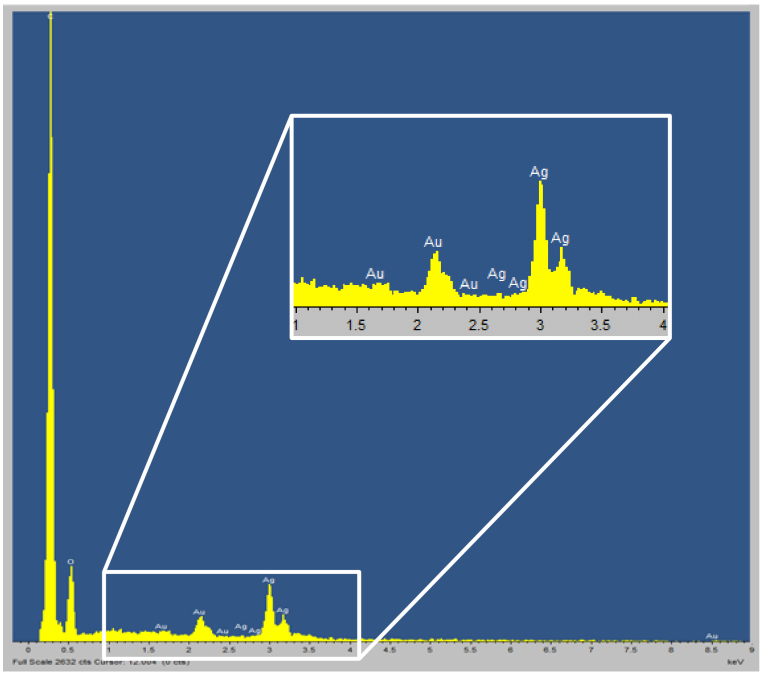

Figure 5.5: *EDX spectrum from centre of 5 minute exposed spot. Peaks at 0.3 and 0.5 keV indicate carbon and oxygen respectively. Inset: magnified silver peaks. Gold peaks are registered from the sputter coating as part of sample preparation for SEM/EDX analysis.*

TEM imaging was also performed on the centre region of the five minute sample to obtain a cross section for further observation of silver NP formation and bright field images can be seen in Figure 5.6 (a – c) below. It was necessary to coat the sample in aluminium and platinum at different stages of sample preparation, which are the darkest two bands to the bottom left of images (a) and (b). The lighter grey areas are PI or PAA as marked in Figure 5.6 (a). Spheroid silver NPs appear darker than the PAA and can clearly be seen on the surface, ranging in size from approximately 20 to 70 nm, although a few elongated shapes are also visible. Perhaps unexpectedly there is also a band of smaller silver NPs embedded within the PAA layer, beginning approximately 100 nm below the larger surface NPs and continuing to a depth of around 250 nm. This distinctly uniform belt, best observed in Figure 5.6 (b) below, consists of NPs in the 5 – 10 nm range for the most part, with slightly larger sizes up to 15 nm occurring furthest from the surface, or to the right hand side of the belt in the image. Directly under the larger surface NPs, the top 100 nm of substrate is bereft of silver, suggesting that either unreduced silver cations or newly formed silver atoms migrate towards the surface. When irradiation begins, the surface silver ions are closest to the electron source of the chlorophyll coating, and so will form silver atoms, which begin to coalesce with their nearby counterparts. Furthermore, the surface of these agglomerations then acts as a catalytic site where further reduction of local silver ions occurs [180]. Thus atoms which are first formed at the surface start to aggregate, while the reduction of silver atoms embedded more deeply in the substrate lags behind slightly. Since the first formed surface spheroid particles will grow first, attracting and appropriating surrounding silver ions, a depleted region will occur where the ions have all migrated towards the surface, rather than forming smaller localised NPs as in the embedded band.

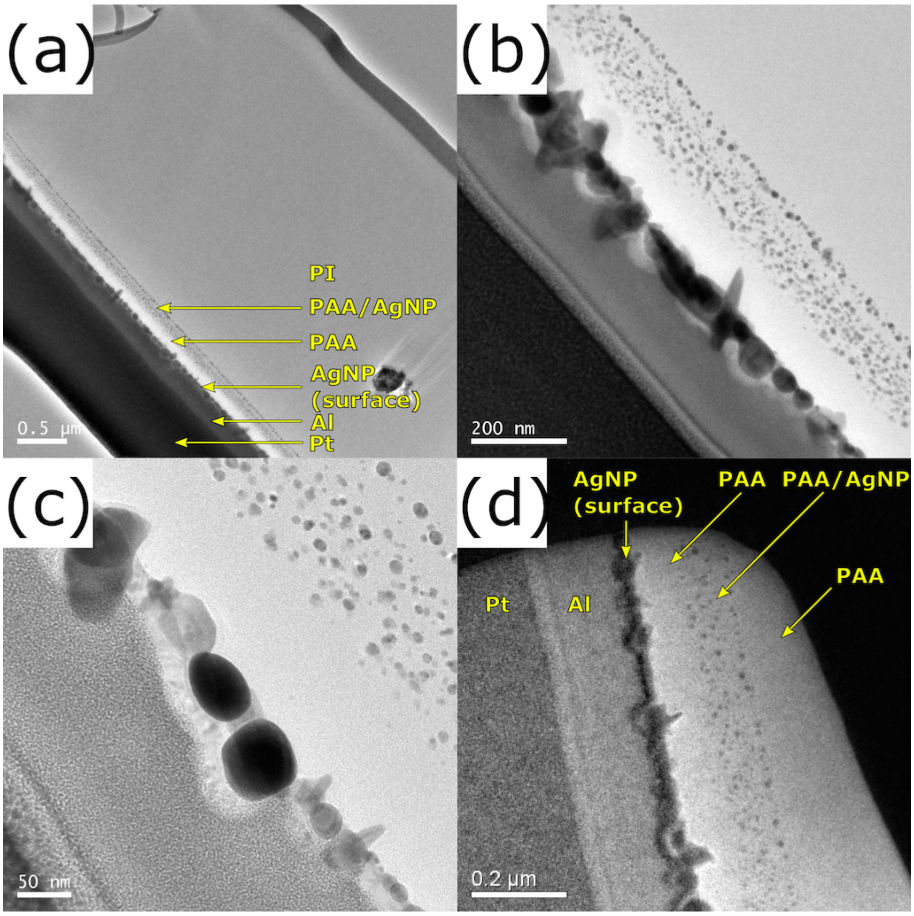

Figure 5.6: *Cross sections of 5 minute exposed spot. (a) – (c) TEM images, (d) carbon map. Scale bars are 500, 200, 50 and 200 nm, respectively.*

Although this morphology is markedly different to that created using UV irradiation by Akamatsu *et al.* [2], a region devoid of metal between the surface and deeply embedded NPs has been observed when a thermal reduction method was employed by Li *et al.* [181]. Comparable TEM images from both these reports are shown in Figure 5.7 below.

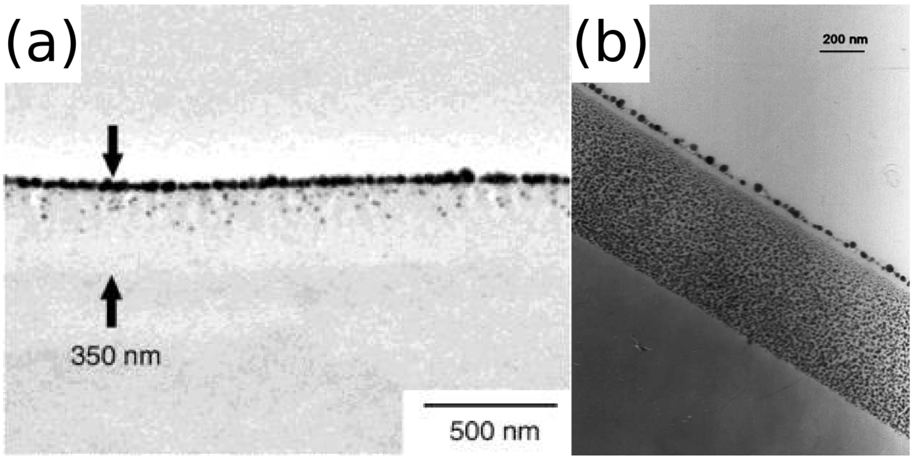

Figure 5.7: *TEM images from surface metallisation of PI by (a) UV exposure for 60 minutes [2] and (b) thermal annealing at 250°C for 30 minutes [181].*

Two concurrent silver evolution mechanisms are therefore proposed: thermal and plasmon resonance triggered growth. The comparison of the TEM photographs in Figure 5.6 to those in Figure 5.7 indicates the metal-free region could come from thermal rather than EM energy sources. Thermal energy is a still a possibility in this experiment as the high power LED was only around 4 mm from the sample, at which distance a temperature of 106°C was measured, although this may be exaggerated slightly due to heating of the packaging of the micro-thermometer used. Silver NP growth in ink formulations has been demonstrated at slightly higher temperatures [182] while sintering of silver to form conductive coatings has also been carried out at room temperature using pulsed white light excitation [183]. While both these examples were in tailored chemical environments they demonstrate that silver NP formation and growth is possible when exposed to only slightly raised temperatures. Similar particle free areas have been observed in PAA-copper matrices by Kim *et al.*, who noted that a thermal gradient could cause such an effect due to the high mobility of copper salts within the PAA [144].

A thermal source would not depend on the substrate depth and so initial reduction could occur anywhere, although the surface would still have better access to the electron source of the chlorophyll. In the absence of a plentiful source of donor electrons at the substrate-donor interface, the more deeply embedded silver could possibly 'steal' electrons from the carboxylic branches in the surrounding PAA, given enough thermal energy. This would also contribute to the degradation through oxidation of the PAA as seen previously in Chapter 3. The limited access to free electrons would also impede the growth of the NPs, and would explain the slightly larger nucleations at the lower edge of the band as silver ions there will have a larger volume of PAA from which to harvest electrons. The carbon map shown in Figure 5.6 (d) above supports this theory, with brighter areas indicating higher concentrations of carbon. The brightest area of the PAA is directly underneath the surface silver NPs, indicating the highest concentration of carbon, which in turn suggests a lower concentration of oxygen. What it does not explain however, is why the 150 nm deep band of smaller silver NPs does not extend more than 250 nm into the substrate, given that the surface modification depth discussed in Chapters 3 and 4 is approximately 350 nm. The discrepancy could be due to the majority of the light energy being absorbed by the silver above before it reaches this depth and so it would be insufficient to trigger reduction. This is illustrated in the proposed formation scheme in Figure 5.8 below, which also introduces the second mechanism of growth.

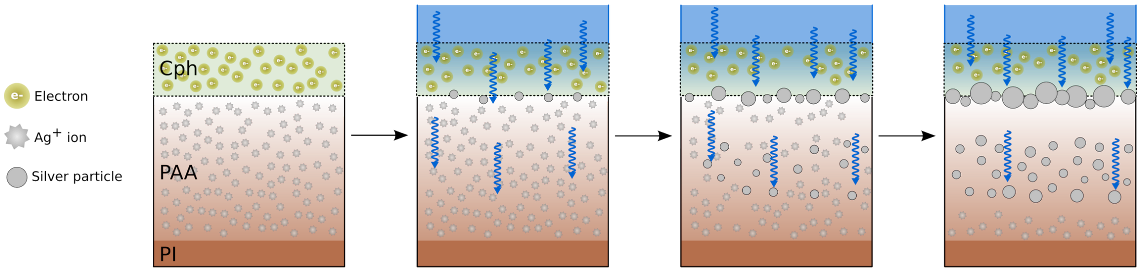

(i)
Ion doped substrate with chlorophyll electron donor coating

(ii)
460 nm light exposure induces rapid reduction at the surface due to large electron mobility

(iii)
Direct reduction then also occurs through direct photolysis due to LSPR. This also accelerates the growth of the NPs at the surface.
Ions migrate towards newly formed particles, preferring the larger particles at the surface

(iv)
Reduction continues until all adjacent ions are used up at the same time as coalesence continuing to form larger particles.

Figure 5.8: *Proposed formation of silver NPs in PI under blue light irradiation. LSPR: localised surface plasmon resonance.*

Localised surface plasmon resonance (LSPR) could also have an enhancing effect on NP growth, triggering direct photolysis. A brief description of LSPR follows. Light waves are accompanied by time varying electric field. When a metal nanoparticle is irradiated with EM energy, if the wavelength of the incident EM waves is much larger than the size of the metal object, as is the case here, free electrons displaced from the metallic lattice will collectively oscillate. When the excitation frequency is a particular value these oscillations will be in resonance with incident light, causing very strong oscillation of the surface (of the metal NP) electrons [184]. These oscillations can contribute to charge transfer, which accelerates the overall reduction rate. Indeed visible light radiation has been shown to be effective at reducing silver ions in solution, with a broad plasmon peak at 420 nm increasing in both intensity and bandwidth as silver NPs formed and increased in size as exposure time increased [185]. A similar effect has also been observed in absorption spectra of silver NPs sandwiched between two BDPA-PDA type PI films [186]. As NP sizes increased from around 5 – 8 to 18 – 20 nm, the absorbance peak red shifted from 450 to 550 nm. The peak amplitude was also seen to increase, meaning that all particles in this size range would be absorbent at the 460 nm wavelength used in the present experiments. Furthermore, spherical silver NPs with diameter 50 – 80 nm have been shown to have peak plasmon resonance at 460 nm [187]. Once the NPs reach a critical size, their growth could then accelerate over this size range due to the LSPR, increasing the rate at which unreduced ions are used up. This would agree with the markedly larger particles on the surface than those in the embedded band, as they would be first to grow to a size where LSPR occurs at 460 nm. Furthermore, since LSPR is dependent on angle of incidence, this could also contribute to the non-uniform silver formation of the LED spots in Figure 5.4 above.

A detailed review of metal nanoparticle synthesis using light broadly categorises two methods by which nanoparticles can form and grow: direct photolysis and photosensitisation [120]. Schemes of each are shown below in Figure 5.9 (a) and (b) respectively. By these definitions, the use of MPEG or chlorophyll as an electron donor film can be classed as employing a sensitizer as in Figure 5.9 (b), while the LSPR effect discussed above is direct photolysis. It is therefore likely that when a UV laser is used for photoreduction, the photosensitisation route is dominant, while when using a broadband mercury UV lamp, LSPR could play a role since its emission spectrum possesses peaks at around 406 and 438 nm, as seen in Figure 3.12, which correspond to absorption peaks of 10 nm silver particles [188] and particles of around 40 – 60 nm [187], respectively. In the case of the chlorophyll coating and blue LED used in this chapter, it is likely that both NP formation methods occur at the surface as both chlorophyll and silver NPs are strongly absorbent around the excitation wavelength, while the smaller NPs within the substrate could form from LSPR alone.

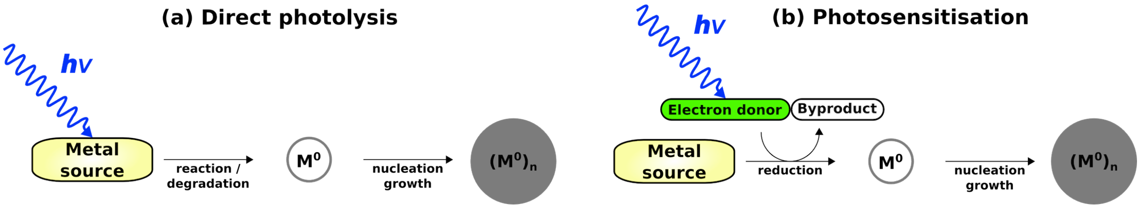

Figure 5.9: *The two general routes of photochemical synthesis. Direct photolysis (a) and reduction assisted by an electron donor or photosensitiser (b).*

The 10 minute exposed spots appeared slightly burned to the naked eye. The surface plasmon effect could also contribute to this through localised heating of the silver NPs causing the degradation seen in Figure 5.4 above and discussed in Chapter 3. Further to this, experiments carried out by Pyun *et al.* indicate that a 6FDA-based polyamic acid, structurally similar to PMDA-ODA, is slightly absorbent at the wavelengths used here [189], which could further contribute to thermal degradation.

5.2.4 Eliminating ethanol as an electron source

Another possible factor that could produce the rapid reduction witnessed above is the solvent in which the chlorophyll was dissolved. To test this hypothesis, samples were prepared with three different coating conditions: the chlorophyll coating as described above, an ethanol only coating and no coating at all. Samples were again exposed for 30 s, 1, 2, 5 and 10 minutes, but this time a quartz photomask was introduced. This was done to demonstrate the patterning possibilities of the process but also helped mitigate the heat effect from the LED discussed above. The temperature under the mask was 67^{o}C but the extra 3 mm width of photomask between LED and substrate also meant that irradiance dropped to 200 mW·cm^{-2} compared to 740 mW·cm^{-2} in the previous experiment.

Microscope images of the various exposures are shown in Figure 5.10 below. Comparing the top two rows, it is clear that the presence of chlorophyll greatly accelerates silver formation, with silver forming in great enough quantities to be plainly visible after 30 seconds, while ethanol without the chlorophyll takes 5 minutes to reach a comparable level. Compared to exposure with no coating the effect of ethanol on its own appears minimal at best, despite the reported success of its use to create 10 nm silver NPs under microwave radiation [190].

Higher magnification images of test structures resulting from the ten minute mask exposure can be seen in Figure 5.11 below. The edge of the capacitor pad and connectors shown in Figure 5.11 (a) were approximately central relative to the LED spot while the test structure in (b) was further toward the edge and would therefore have experienced a lower energy dose. It does however demonstrate a 5 μm wide track, indicating that the process is feasible for producing features finer than current inkjet methods for example.

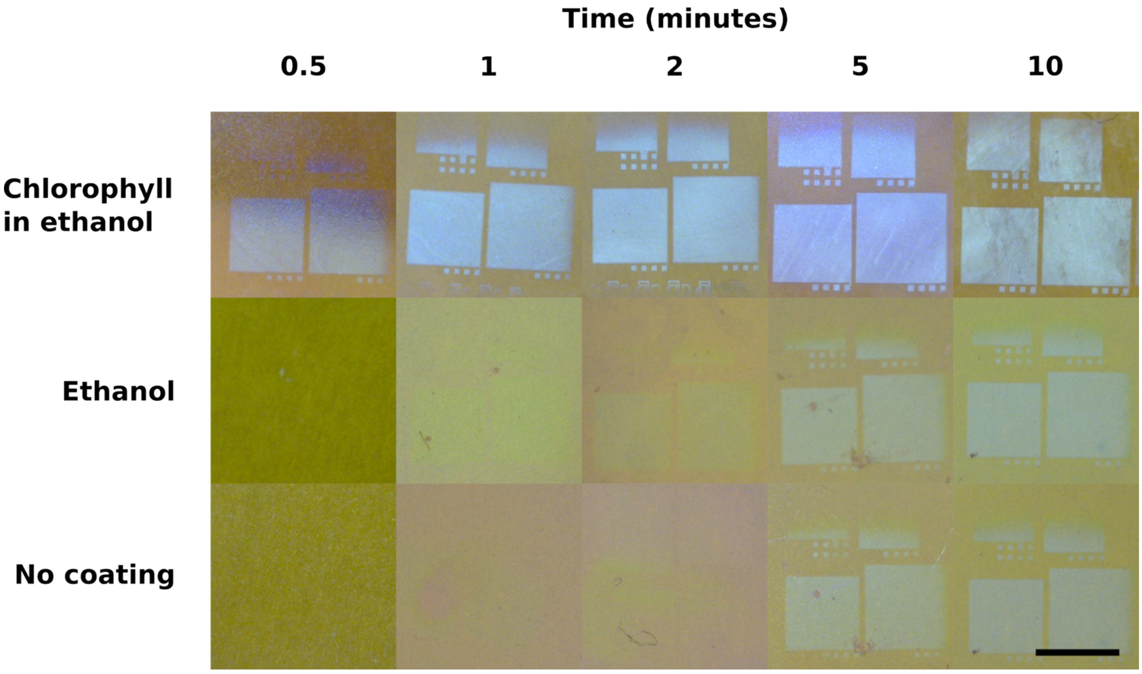

Figure 5.10: *Mask exposure with different coating conditions. Scale bar is 2 mm.*

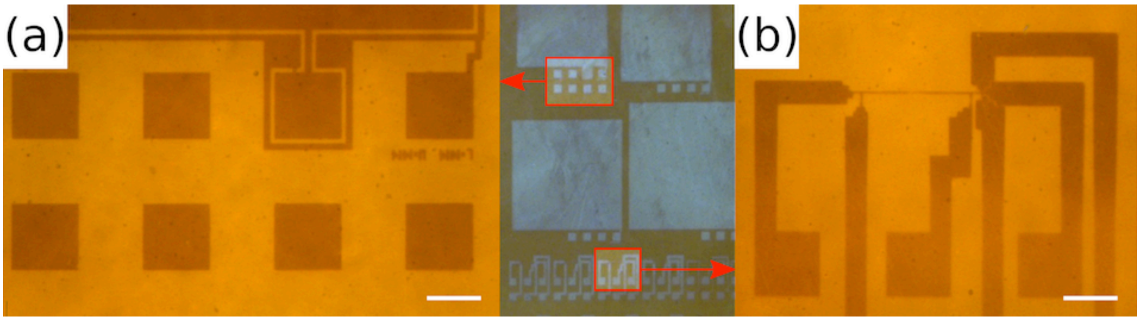

Figure 5.11: *Patterning of polyimide created by blue LED mask exposure. (a) side of capacitor pad, (b) 5 μm test structure. Scale bars are 100 μm.*

5.3 Laser power-speed tests

5.3.1 Aim

After the efficacy of the blue light process was successfully demonstrated, with spinach extract coating shown to significantly reduce the energy dose required for silver formation, the next step was to test with a blue laser, since the primary goal of this thesis is rapid laser manufacturing.

5.3.2 Equipment and procedure

Samples preparation was identical to procedures described above. A 457 nm blue laser with maximum power 400 mW was obtained from Edinburgh Instruments and coupled with optical fiber to produce a focussed spot of approximately 9 μm. Maximum output power from the fiber was measured at 132 mW, although this was defocussed so as not to damage the power meter sensor. Irradiance of the substrate would therefore be approximately 207 $kW{\cdot}cm^{-2}$. This was fixed above a Zaber LSM200B-T4 X-Y translation stage for patterning. The stage was controlled by an AMCB2 controller and software, also from Zaber. The maximum speed of the stage was measured to be 55 $mm{\cdot}s^{-1}$. The superior stage used for the high-speed UV laser experiments in Section 3.4 was unavailable at the time of the experiments in this section.

5.3.3 Results and discussion

Control software was used to move the stage to create a series of line pairs at different speeds, starting at 55 $mm{\cdot}s^{-1}$ and decreasing by 40% each time, creating lines with speeds of 4, 7, 12, 20, 33 and 55 $mm{\cdot}s^{-1}$. Microscope images of the tracks can be seen in Figure 5.12(a) below, with (b) – (g) providing higher magnification for each of the speeds from 4 – 55 $mm{\cdot}s^{-1}$, respectively.

As well as obvious silver colouring across the majority of the width of all tracks, some darker brown colouring can be seen at the edges. This is likely a combination mainly of formation of smaller silver particles, which appear brown at low densities and sizes, but also partial reimidisation of the PAA. The accelerated silver formation due to LSPR may cause sufficient localised heating for this to occur. Typical linewidths for each track are shown in Table 5.3 and plotted against scan speed in Figure 5.13 below, with values given both including and excluding the brown edge areas. Irradiance and energy dose were estimated by multiplying the power by the time taken for the laser to travel the distance of the spot diameter.

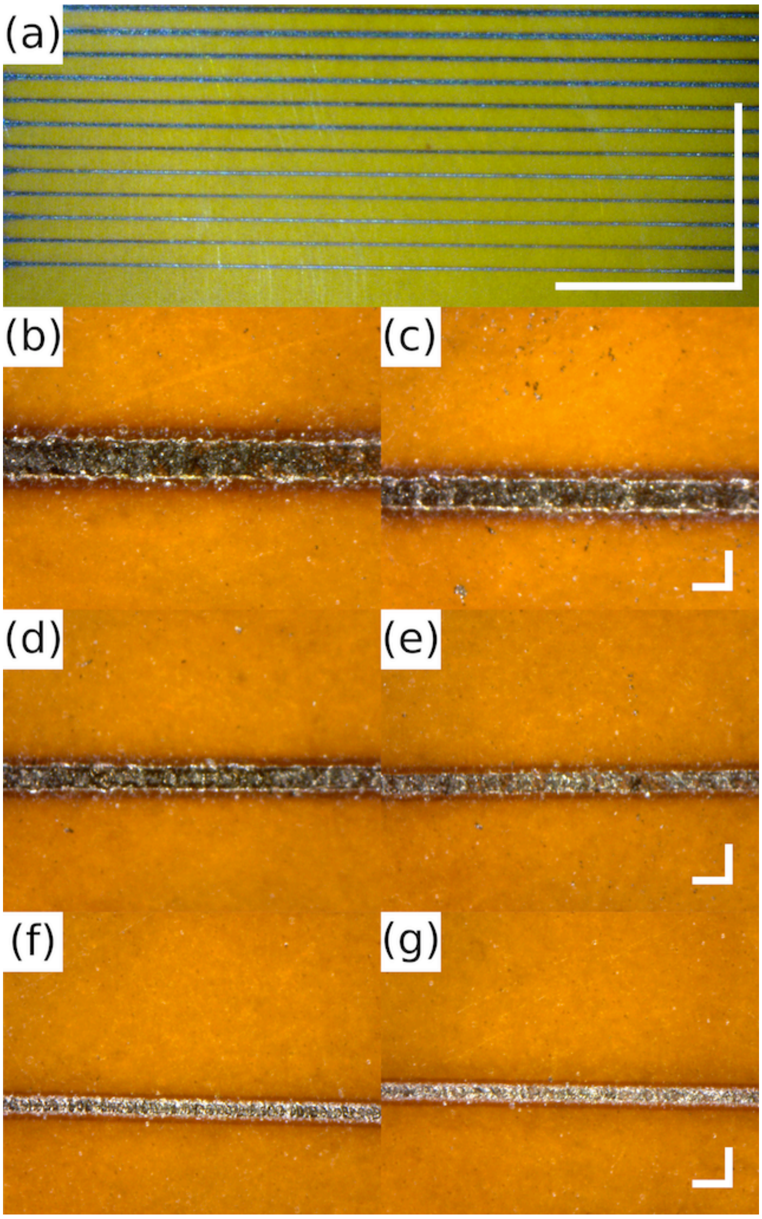

Figure 5.12: *Microscope images of direct laser written tracks. (a) all tracks, scale bar is 2 mm. Increased magnification images of individual tracks at scan speed: (b) 4, (c) 7, (d) 12, (e) 20, (f) 33 and (g) 55 mm·s^{-1} with scale bars of 0.1 mm.*

Assuming that the brown edges are not conductive or suitable for electroless plating, the 'outer' linewidth can be discounted. Even with regard to the 'inner' linewidth measurements, referred to simply as linewidth from here onwards, the size of track is considerably wider than the focussed beam for all speeds. This is most possibly due to two factors. Firstly inaccuracies in focussing may cause the spot size to increase. Dealing with flexible substrates can be problematic in this respect. Secondly, due to the thermal and LSPR effects discussed above reduction is unlikely to be constrained to the immediate area of the spot due to the intensity of the spot. As well as readily absorbing blue light, colloidal silver NPs have been observed to fluoresce in the 400 – 500 nm region, suggesting that this secondary emitted energy could trigger reduction nearby [191]. The best-fit curve for the linewidth in Figure 5.13 following the form:

$$\text{Linewidth} \approx 141 \text{ x } (\text{Laser write speed})^{-0.303} \qquad (5.1)$$

was software generated from the values given in Table 5.3. Extrapolating this would suggest a linewidth of approximately 34 μm for a writing speed of 100 mm.s^{-1} with exactly the same optical setup, assuming that no other factors affect the writing process. Such factors could be the requirement of a minimum energy dose or threshold fluence. It is also evident that the slower speeds conferring higher energy doses create a more uneven, disjointed silver surface in a similar, if less empathic, manner to treatment from high energy UV as seen in Figure 3.11. More continuous and uniform silver tracks are observed at higher speeds with lower energy doses, which is promising in that higher speeds than those currently demonstrated are a necessity for adequate upscaling of the process.

Scan speed (mm·s^{-1})	Energy dose (J·cm^{-2})	Equivalent energy dose (μJ)	'Outer' linewidth (μm)	'Inner' linewidth (μm)	Figure 5.12
4	519	330	160	93	(b)
7	297	189	138	84	(c)
12	173	119	109	64	(d)
20	104	66	90	52	(e)
33	63	40	73	48	(f)
55	38	24	62	45	(g)

Table 5.3: *Linewidth of laser tracks for varying scan speed.*

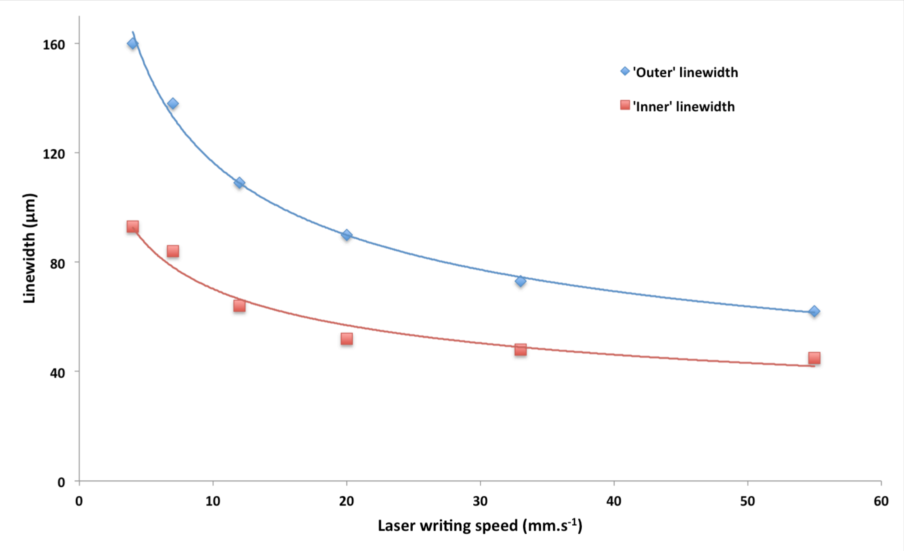

Figure 5.13: *Linewidth as a function of laser scan speed*

5.4 Chapter conclusions

Spinach extract has been shown to considerably accelerate the reduction of silver ions embedded in the modified surface of polyimide, meaning far less energy is required than the UV light used previously. While ethanol may have a slight contributory effect, this is not much greater than the effect of blue light with no additional coating. This is likely due to pigment compounds that exist within photosystems I and II, whose function is efficient light energy absorption and electron transfer, in particular the chlorophyll molecules chlorophyll-a and chlorophyll-b. EDX measurements confirmed the presence of silver in the exposed substrates as well as suggesting a loss of oxygen from the polymer but a different characterisation method is necessary to obtain more accurate composition data and the confirmation of any oxygen loss.

The mechanism of silver formation at this wavelength has been proposed to occur predominantly by energy transfer through both heat and LSPR, with the latter being the primary driver through a combination of direct photolysis and highly efficient electron donation of the spinach extract coating.

It seems slightly wasteful that silver particle formation occurs within substrate, separate from the surface growth however. The presence of the silver free region may adversely affect adhesion, although such a region may or may not be present when the irradiance is increased to laser levels. Indeed, it has been shown that a more rapid thermal energy transfer reduces the particle free area due to a greater thermal gradient [144]. This indicates that the thermal gradient induced by a high power, tightly focussed laser would decrease the gap between surface and embedded silver particles when compared to exposure from a large area LED exposure providing a lower energy dose. Also, examining the morphology across the LED spots in Figure 5.4 suggests that a higher irradiance forms more continuous silver, which is certainly beneficial for creating circuitry. More investigation would be needed to ensure more uniform growth however.

Direct writing has also been successfully demonstrated with a blue laser. This method requires far less energy than the previous UV setup and although speeds of only 55 $mm \cdot s^{-1}$ were shown, with continuous sub-50 μm tracks being written. Increasing the speed will require a different laser setup, and more accurate focussing is also possible as there was not insubstantial variation in the fiber delivery optics employed here. A further advantage of increased speed is the projected decrease of linewidth, although this will be limited to the beam size, or most likely slightly larger than the beam size due to thermal and surface plasmon effects. The plasmon effects occur due to the absorbance peak of silver particles of size from a few up to around 150 nm being in the 400 – 500 nm range. While it is likely this effect occurred to some extent during the broadbeam UV experiments in Section 3.3 due to the mercury lamp emission peaks seen in Figure 5.1, it is highly unlikely this occurred when using the HeCd laser at 325 nm. The 460 nm LED and 457 nm laser used in this chapter however are much more likely to trigger LSPR in the particles within the size range mentioned above.

Another point that was not discussed was that active ingredient of the spinach extract is not in fact solely chlorophyll a or b, but may consist of several light harvesting proteins as well as chlorophyll. This has great potential for further investigation, which the final chapter discusses in more detail in the future work section.

Chapter 6:
Process diversification: a new substrate

6.1 Introduction

The previous chapters described the development and enhancement of the direct writing method of silver on polyimide through the investigation of different parameters throughout the fabrication process. Improvements were made, for example, by using a longer illumination wavelength during the silver reduction, resulting in less damage to the polymer and considerably more efficient silver nanoparticle formation. Alternative patterning methods were also established using new photoresists devised for processing without the need for harsh etchants.

A further aim of this work is to broaden the scope of the fabrication process to expand the number of possible applications as a major area of interest is in polymer metallisation [145, 148, 192-194]. While polyimide has received particular attention [2, 58, 83, 90, 195] due to the excellent properties of this material that include strong resistance to temperature and chemicals, good mechanical strength and biocompatibility, thereby allowing its use in a wide range of applications, the metallisation method could potentially be applied to other plastics. This chapter looks at one such candidate: polyetherimide.

6.2 Polyetherimide substrate

6.2.1 Introduction to polyetherimide

Polyetherimide (PEI) has physical properties comparable to PI, such as excellent dielectric properties over a range of temperatures, high yield strength and Young's modulus, high heat and radiation (UV and Gamma ray) resistance [196-199] and suitability for medical devices manufacture, being USP Class VI compliant. PEI can be employed in a variety of applications, with the most prevalent one being the fabrication of moulded interconnect devices (MIDs) [200]. Gaikwad and Rout recently suggested PEI as a potential candidate for ion-exchange substrate surface modification, although no thorough characterisation of the metallisation process was achieved [198]. Ion-exchange methods offer a simple way to produce metal nanoparticles and metal-polymer composites, which could provide a quicker route involving fewer processing steps to realising interconnects within MIDs or aid in the creation of 3D circuits. The surface modification of imide based polymers and the subsequent in-situ ion exchange requires hydrolysis of the polymer, discussed in depth in earlier chapters of this thesis. This chapter presents the applicability of the surface modification, ion exchange and metallic salt reduction method to PEI and therefore determines its suitability for metallisation via the laser-direct writing methods.

The similarity in physical properties between PEI and PI is partly explained by their similar monomers as shown in Figure 6.1 below.

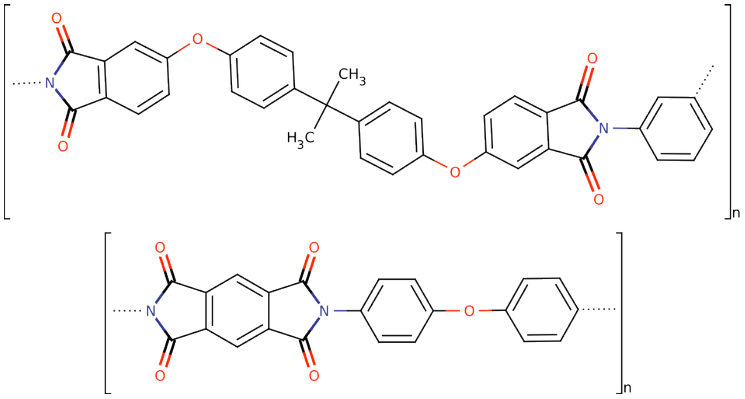

Figure 6.1: *PEI (top) and PMDA-ODA (bottom) monomers with imide groups highlighted.*

As both materials contain two imide groups, which are instrumental in the surface modification and ion exchange steps of the fabrication process, it is a strong possibility that PEI might also be suitable for direct metallisation using photochemical or chemical effects.

6.2.2 Equipment and procedure

The PEI used for these tests was 75 µm thick Ultem 1000B. FTIR measurements were taken with a Perkin Elmer Spectrum 100 FT-IR spectrometer in ATR mode, SEM imaging was carried out using a Quanta 3D FEG, manufactured by FEI Company and XRD measurements were obtained with a Bruker Corporation D8 Discover in transmission mode using X-ray wavelength $\lambda = 1.5418$ Å. Minitab 14 software package was used to perform the full factorial Design of Experiments (DOE) analysis.

The process steps followed were identical to the polyimide silvering methods described previously but with changes in certain parameters as described further. Preliminary tests found that the conditions for successfully hydrolysing polyimide, submersion in 1 molar KOH at 50°C for 5 minutes, had a negligible effect on PEI. Since several different factors could affect hydrolysis, DOE was implemented to determine the optimum parameters that would achieve full cleavage of the imide ring, such that the polymer surface could be converted into polyetheramic acid as shown in Figure 6.2 below.

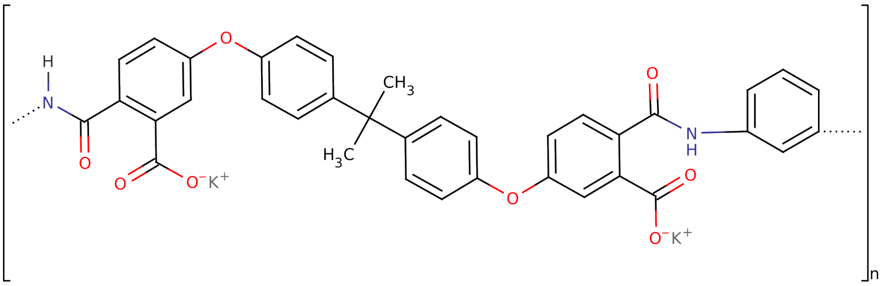

Figure 6.2: *Polyetheramic acid after successful imide ring cleavage in KOH.*

A two-level, full factorial design was chosen to explore the effect of each parameter and any combination of factors. According to Antony [201], such an experimental design was an apposite fit for this experiment, given the number of parameters and the lack of previous knowledge of PEI hydrolysis. The full factorial DOE comprised temperature, concentration, immersion time and type of alkali used as parameters. A 'low' and 'high' level were chosen for each of the continuous variable parameters – temperature, concentration and time – while the 'alkali type' parameter was restricted to two discrete values: 'sodium hydroxide' (NaOH) and 'potassium hydroxide' (KOH). The various parameter permutations for each experimental run and their randomised running order are shown in Table 6.1 below. The running order was randomised to mitigate the influence of experimental error.

Following the cleaving, ion-exchange was carried out with the normal parameters of submersion in 0.1M silver nitrate solution at room temperature for 15 minutes. For experimental expediency, the chemical reduction route using DMAB as the reducing agent was chosen for silver nanoparticle formation, with different samples immersed in 5 mM DMAB solution for 1 and 7 minutes. After a standard acid washing in 1% w/w sulphuric acid to remove any unreacted silver ions, reimidisation was carried out at 250°C in air, nitrogen or vacuum atmospheres for 30, 60 and 90 minutes.

Experiment number	Randomised run order	Temperature (°C)	Concentration (M)	Time (min)	Alkali
1	10	50	5	20	NaOH
2	2	80	5	20	NaOH
3	8	50	15	20	NaOH
4	9	80	15	20	NaOH
5	6	50	5	40	NaOH
6	13	80	5	40	NaOH
7	5	50	15	40	NaOH
8	16	80	15	40	NaOH
9	11	50	5	20	KOH
10	7	80	5	20	KOH
11	12	50	15	20	KOH
12	15	80	15	20	KOH
13	4	50	5	40	KOH
14	3	80	5	40	KOH
15	1	50	15	40	KOH
16	14	80	15	40	KOH

Table 6.1: *Run order of PEI hydrolysis experiment.*

6.2.3 Results and discussion

Table 6.2 below shows the results for all the experimental runs. The FTIR spectra for untreated PEI and for Run 16, which showed the greatest change, are displayed in Figure 6.3, also below. The peaks at ~1780 cm^{-1}, ~1710 cm^{-1}, and ~1370 cm^{-1} correspond to the C=O double bond asymmetric, C=O symmetric and C–N–C imide ring stretches, respectively, and their presence confirms that there is complete imidisation of the polymer chain. Peaks at 1660 cm^{-1} and 1550 cm^{-1} indicate amide I and II vibrations, respectively, which indicate that hydrolysis has taken place [6]. The amide groups are the newly created branches in the polymer chains where the metal ions bond to, as seen in Figure 6.2 above.

To quantify the degree of hydrolysis for each run, the magnitude of the most prominent imide peaks (1710 cm^{-1}) was divided by that of the peak at ~1500 cm^{-1}, a peak which is associated with one of the benzene ring breathing modes [80, 202], of which five exist in the PEI monomer. For more accurate comparison between samples, the spectra were normalised with respect to the peak at 1010 cm^{-1}, also known to indicate in-plane C–H benzene ring breathing [203]. The normalised peak ratio for each run was then divided by the normalised peak ratio for untreated PEI to give an approximate percentage of imide content at the surface of the substrate as indicated in the last column of Table 6.2.

Run number	Temp. (^{o}C)	Conc. (M)	Time (min)	Alkali	1750 cm^{-1} C=O peak	1500 cm^{-1} benzene peak	$\frac{1750\text{ peak}}{1500\text{ peak}}$ ratio	Relative surface imide content (%)
Pristine	**-**	**-**	**-**	**-**	**2.88357**	**1.32336**	**2.17893**	**100**
1	50	5	20	NaOH	2.89947	1.33491	2.17203	99.6
2	80	5	20	NaOH	1.11149	1.28438	0.86500	39.7
3	50	15	20	NaOH	2.90063	1.33059	2.17996	100
4	80	15	20	NaOH	1.17719	1.31504	0.89517	41.1
5	50	5	40	NaOH	2.89517	1.32879	2.17880	100
6	80	5	40	NaOH	1.49238	1.33448	1.11832	51.3
7	50	15	40	NaOH	2.95424	1.34880	2.19027	100
8	**80**	**15**	**40**	**NaOH**	**0.35783**	**1.62320**	**0.22045**	**10.1**
9	50	5	20	KOH	3.13159	1.39502	2.24483	100
10	80	5	20	KOH	1.89049	1.37010	1.37010	62.9
11	50	15	20	KOH	2.79193	1.37519	2.03021	93.1
12	**80**	**15**	**20**	**KOH**	**0.17839**	**1.70683**	**0.10452**	**4.8**
13	50	5	40	KOH	3.21812	1.42541	2.25768	100
14	80	5	40	KOH	1.06623	1.37064	0.77791	35.7
15	50	15	40	KOH	2.28878	1.38691	1.65027	75.7
16	**80**	**15**	**40**	**KOH**	**0.01919**	**1.80382**	**0.01064**	**0.4**

Table 6.2: *Relative imide content of modified PEI. Runs of note highlighted in bold.*

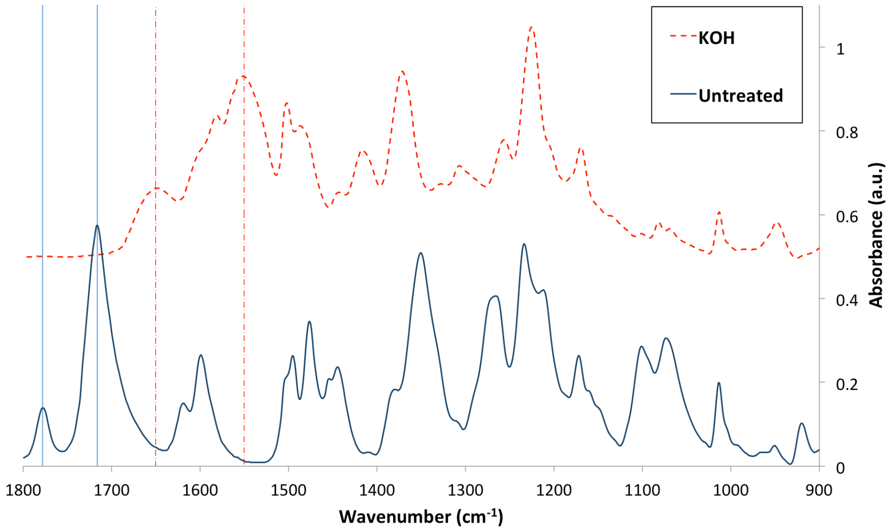

Figure 6.3: *FTIR-ATR spectra of untreated (solid line) and fully hydrolysed (dashed line) PEI.*

Most complete hydrolysis occurs either when all parameters are 'high' (Runs 8 and 16) or for Run 12 where a high temperature, high KOH concentration and low time have been used. Further evidence of hydrolysis is given by the formation of a carboxylic group, as seen in Figure 6.4, highlighted by peaks at ~1650 cm^{-1} and 1750 cm^{-1} on these runs. As explained earlier, Run 16 is shown on the uppermost in Figure 6.3. The spectra for the other two runs exhibiting great ring cleavage are not presented here due to their high similarities with Run 16. Both alkalis display broadly similar FTIR results, with KOH generally providing a higher surface imide content, as would be expected for this stronger base.

It does appear that only runs with high temperature and high concentration produce a thorough hydrolysis. The standardised effects from the DOE analysis and its corresponding Pareto chart are shown in Figure 6.4 below. The greater the value for the standardised effect of each term in the Pareto chart in Figure 6.4(a), the greater its effect on the reaction. A term can refer either to independent variables (i.e. individual parameters), or confounding variables (the interaction between independent variables). Similarly for the standardised effects plot shown in Figure 6.4(b), the further away from the central cluster a parameter effect or parameter interaction effect is, the more strongly it influences the reaction. The normal probability plot in Figure 6.4(c) indicates the suitability of the DOE analysis chosen for the problem. As seen here, the data points do not stray far from the linear best fit line, indicating that the experiment has been designed appropriately and that the plots in (a) and (b) are valid. A non-linear trend amongst the data would have indicated a more complicated parameter interaction and, as such, would have required a higher order DOE analysis.

Clearly the most important factor in the cleaving process is temperature (A), with concentration (B) also being somewhat significant. The other factors of time (C) and alkali type (D) were less influential. The interaction between temperature and concentration (AB) enhances however the hydrolysis reaction on top of the individual effects of each single factor. The threshold for a significant degree of hydrolysis appeared to be at 80°C using a 15 M concentration of alkali. On the basis of these results, a PEI hydrolysis regime of 15 M KOH at 80°C for a minimal treatment time of 20 minutes was chosen for the investigation and characterisation of subsequent process steps.

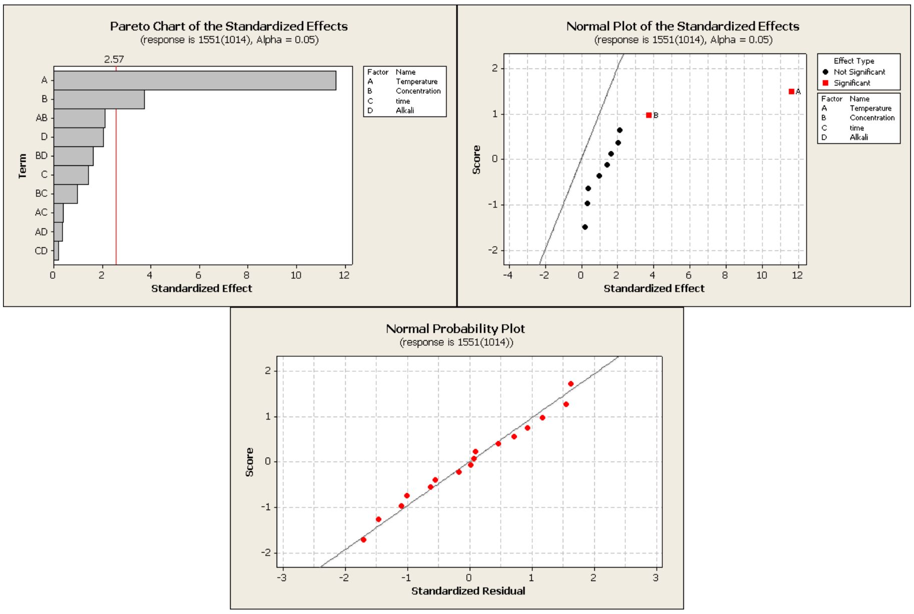

Figure 6.4: *Clockwise from top-left: (a) Pareto chart of standardised effects, (b) standardised effects plot and (c) normal probability plot of residuals.*

Effects of the reimidisation process were then investigated by studying the annealing of the samples treated in DMAB for one minute. The samples were annealed at 250°C in air or nitrogen at ambient pressure. Samples were treated for 30, 60 and 90 minutes in each of these atmospheres. The heating regime consisted of a 20 minute heating ramp from room temperature to 250°C, where the temperature was held for either 30, 60 or 90 minutes before a cooling down period of approximately 15 minutes to bring it back to under 100°C before being removed from the oven and allowed to cool further to room temperature. The samples were also annealed under vacuum but the heating regime differed slightly from the method above due to the length of time the vacuum oven took to vary the temperature. Samples were placed in the vacuum oven at 160°C, with approximately 30 minutes to reach the desired temperature. The cooling ramp of 15 minutes for the air and nitrogen samples was not possible to achieve while maintaining a vacuum, so samples were removed directly from the oven with no extended cooling down period.

Samples were annealed after different stages of the process to assess substrate behaviour with and without silver particles or ions being present. More precisely, the annealing step was carried out after the hydrolysis (omitting steps 2 and 3 in Figure 3.1), after the ion exchange (omitting step 3) and finally after the chemical reduction step (no steps omitted). FTIR spectra of the samples annealed in each curing environment for 90 minutes immediately after the KOH imide ring cleavage step can be seen in Figure 6.5 below. The samples treated for 30 and 60 minutes showed broadly similar spectra with little variation and so have been omitted for clarity.

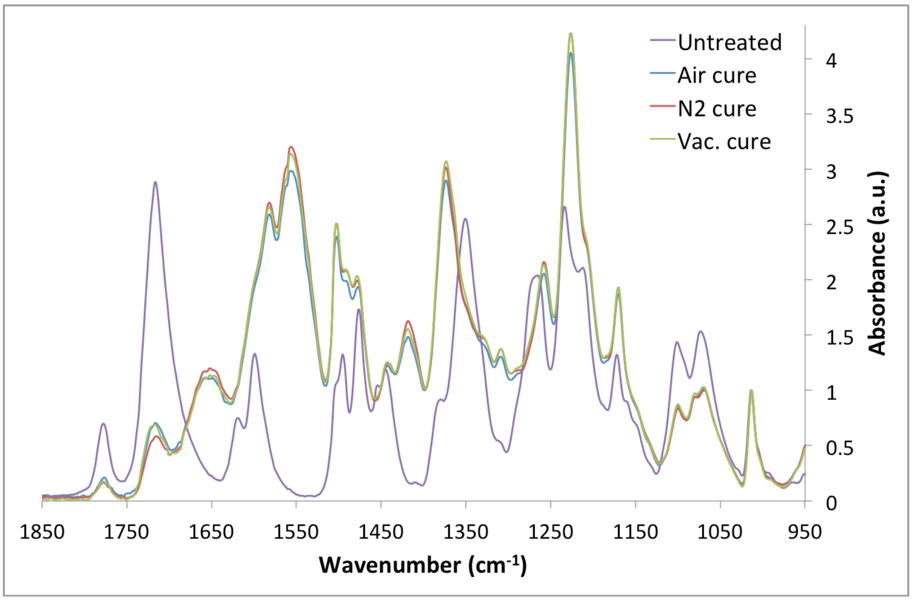

Figure 6.5: *FTIR spectra of PEI samples heat treated for 90 minutes immediately after the imide ring cleaving step.*

Reimidisation has not occurred at this stage in any of the curing environments, with amide peaks (1650 cm^{-1} and 1550 cm^{-1}) clearly visible and the imide ring peaks (1780 cm^{-1} and 1710 cm^{-1}) much less pronounced than the untreated spectrum. This is notable as a temperature of 250^{o}C has previously been used to cure PEI [198] and can also suitably reimidised PI as discussed at length in previous chapters of this thesis. Since neither of these studies carried out reimidisation with potassium ions present, an explanation could be that these ions hinder the reimidisation process, although this is not likely as reimidisation does occur after the silver ion-exchange step in most cases, as displayed in Figure 6.6 below.

The samples with unreduced silver ions showed a distinct colour change, with the PEI becoming a dark orange/brown much like PMDA-ODA polyimide, suggesting that a small degree of thermally induced reduction occurred. The curing environment can also be seen to have an effect. The colour of the air and vacuum cured samples were very similar with the nitrogen cured samples exhibiting a less pronounced colour change. This effect can be partially explained by the comparison of their FTIR spectra in Figure 6.6.

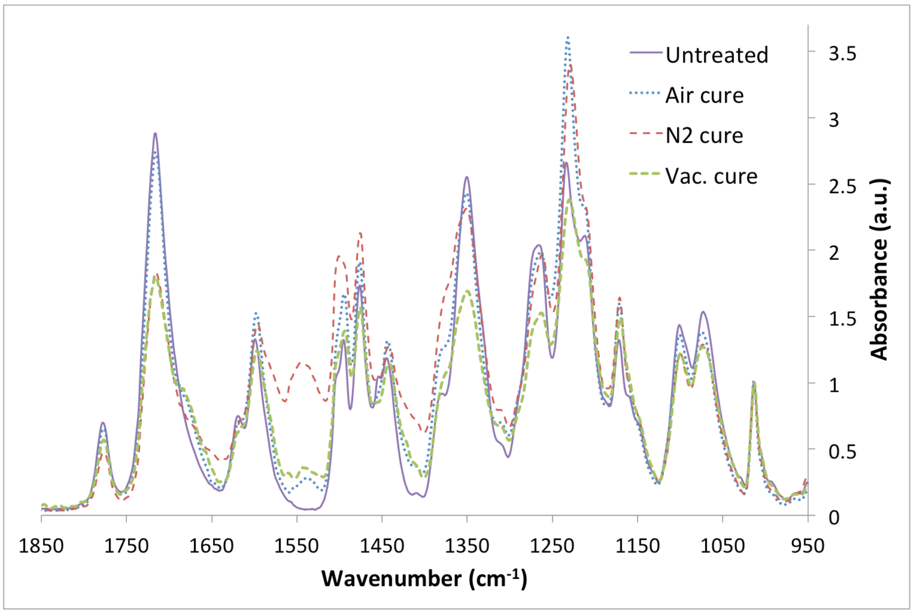

Figure 6.6: *FTIR spectra of PEI samples annealed for 90 minutes in different atmospheres after the ion exchange step.*

As with Figure 6.5, the 30 and 60 minute anneal times are not shown for clarity. While all samples have substantially regained their imide peaks and lost their amide(I) peak, there is still a noticeable amide(II) peak at 1550 cm^{-1} in all samples, indicating that complete reimidisation may not have occurred. Although these peaks in the air and vacuum cured samples have decreased enough to be considered negligible, the peak in the nitrogen cured samples remains prominent. Examining the nitrogen curing environment over the differing treatment times indicates that reimidisation is taking place but at a more gradual pace than the air and vacuum atmospheres. This is shown in Figure 6.7 below.

It also appears that the presence of silver nanoparticles has an effect on reimidisation, accelerating the process. This effect has been previously observed and characterised by Qi *et al.* [82]. Figure 6.8 below shows the FTIR spectra from the samples cured for 90 minutes in a nitrogen atmosphere. Each plot represents a measurement taken after each process step with two taken after the silver ion reduction step; one with a DMAB immersion time of 1 minute and a second with an immersion time of 7 minutes. This suggests that the silver nanoparticles may have a positive effect on reimidisation, possibly due to the added thermal conductance of the silver around the polymer chains.

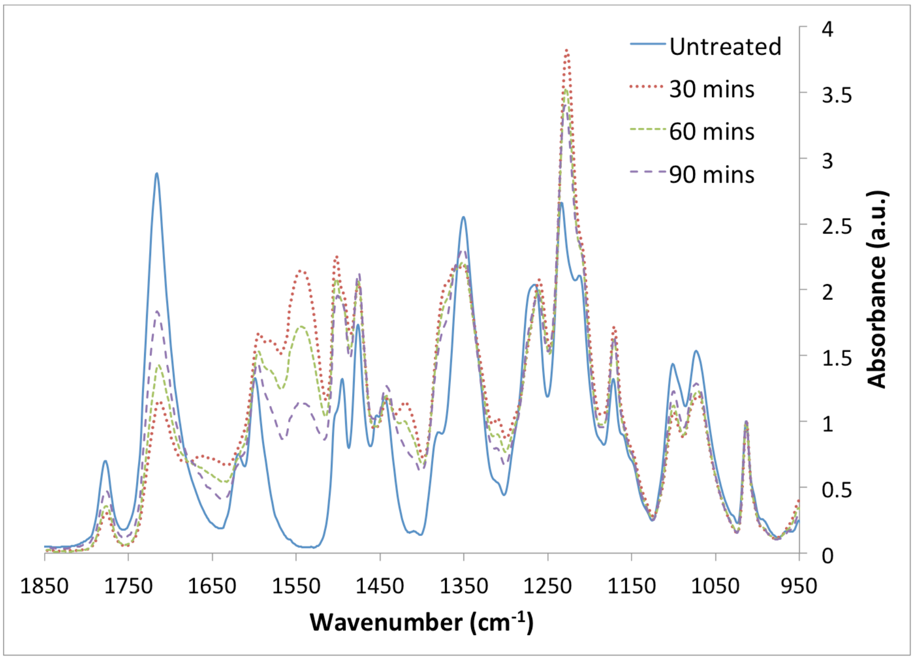

Figure 6.7: *FTIR spectra of PEI samples annealed in nitrogen atmosphere for various times after ion-exchange step.*

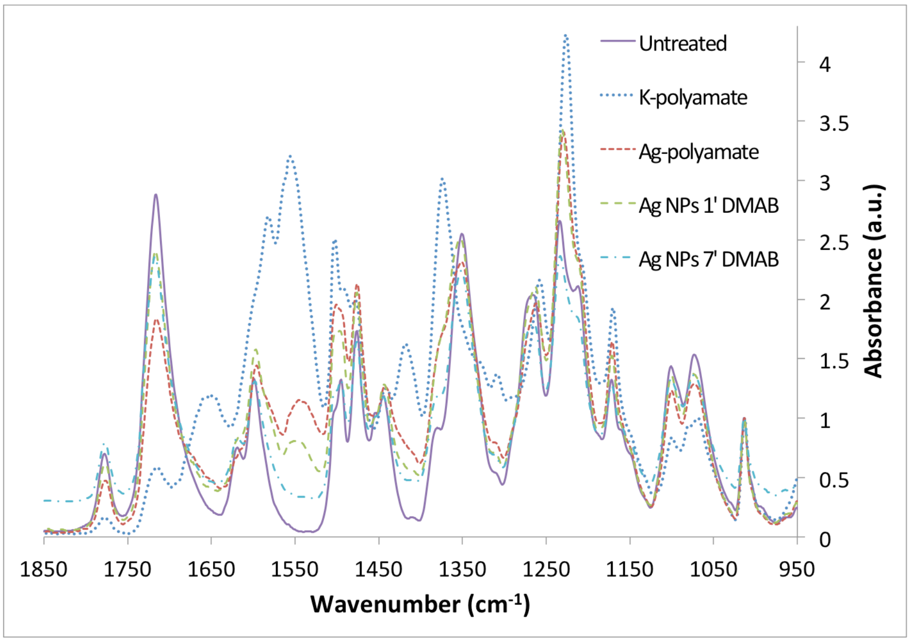

Figure 6.8: *FTIR spectra of PEI samples annealed for 90 minutes in nitrogen after each process step.*

To summarise the FTIR findings, the polyetherimide tested here undergoes a comparable degree reimidisation to polyimide under the same heating conditions when silver nanoparticles, and to a lesser degree silver ions, are present, in a vacuum or air atmosphere, however the rate of reimidisation is much slower in a nitrogen environment.. Also it can be inferred from Figures 6.5 – 6.8 that reimidisation is incomplete for all samples. Therefore a higher temperature than 250oC should be considered while bearing in mind the higher risk of degradation seen in Chapter 3. Reimidisation does not occur to an appreciable extent when potassium ions are still present, however this is not of great concern for the metallisation process, other than highlighting proper rinsing and cleaning of substrates should be carried out.

To further characterise the process, images of the samples taken by FESEM and optical microscope can be seen below in Figures 6.9 and 6.10, respectively. Clearly the surface morphology and formation of the silver nanoparticles depend strongly on the annealing atmosphere. Despite these images, FTIR analysis of the samples exposed to 7 minutes DMAB reduction and annealed for 90 minutes provided broadly similar results across the different annealing atmospheres. Although these results indicate that reimidisation has occurred across all annealing atmospheres, the SEM images in the final row of Figure 6.9 show markedly different patterns of silver growth. The air and vacuum annealed samples seem to show good coverings of silver, with the vacuum annealed sample showing greater uniformity. The nitrogen sample appears to show a reasonably densely packed layer of silver nanoparticles with a few isolated, possibly detached, agglomerations on top of this.

Figure 6.10 below shows that all three annealing environments produce a largely continuous layer of silver although the morphologies are different. Before reduction of the silver ions, the nitrogen cured samples appear to have a much greater difference in surface texture as indicated in B (i) & (ii) compared to A/C (i) & (ii) in both figures.

Figure 6.11 shows the same samples seen in Figure 6.9 and 6.10. This photograph clearly indicates the changes occurring at each stage of the process, with all DMAB treated samples showing a definite silver colour. The vacuum cured sample (C (iii)) appears slightly whiter. This white form of silver is similar to electroless plated silver as previously examined in chapters 3 and 4 but is not present in high enough concentrations to be conductive.

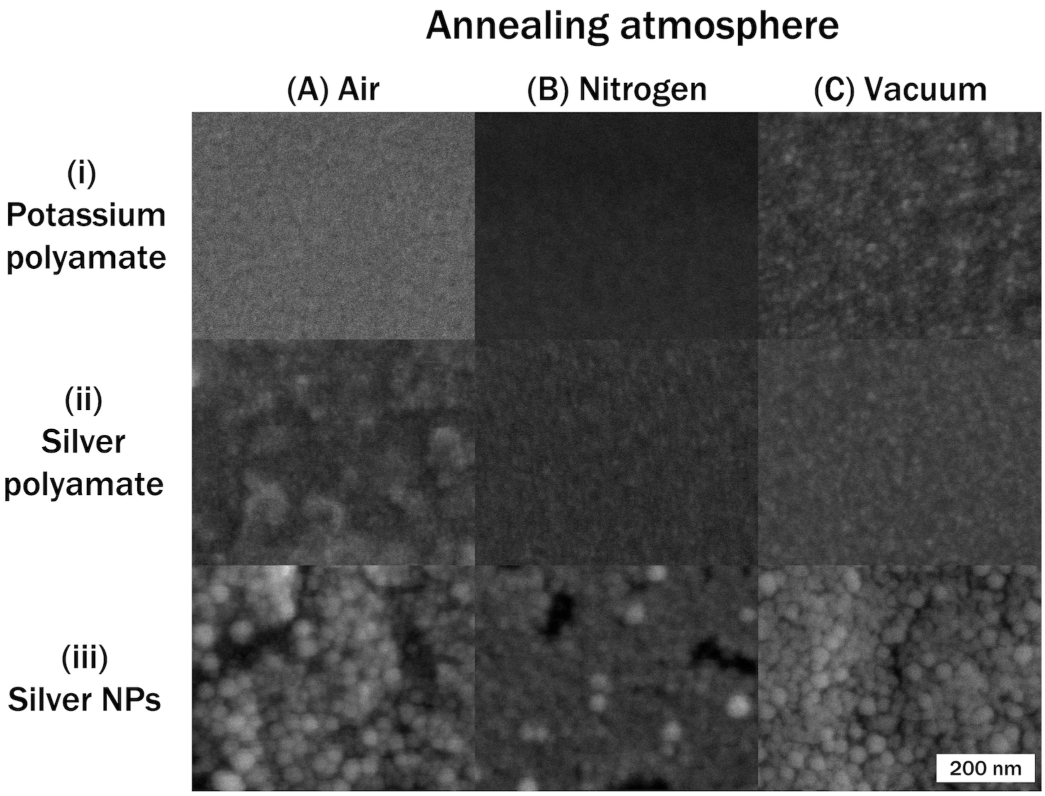

Figure 6.9*: FESEM of the samples annealed for 90 minutes in different atmospheres after: (i) process step 1 in Figure 3.1; (ii) step 2 and (iii) step 3. Scale bar is 200 nm.*

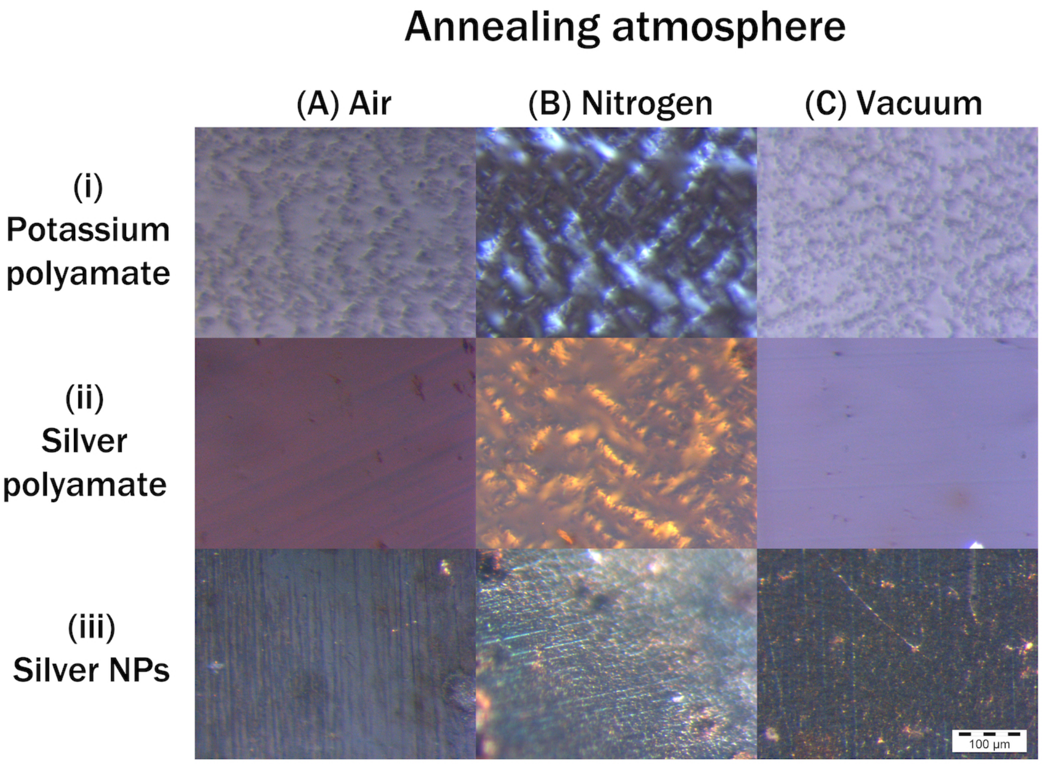

Figure 6.10: *Microscope images of the samples annealed for 90 minutes in different atmospheres after: (i) process step 1 in Figure 3.1; (ii) step 2 and (iii) step 3. Scale bar is 100 µm.*

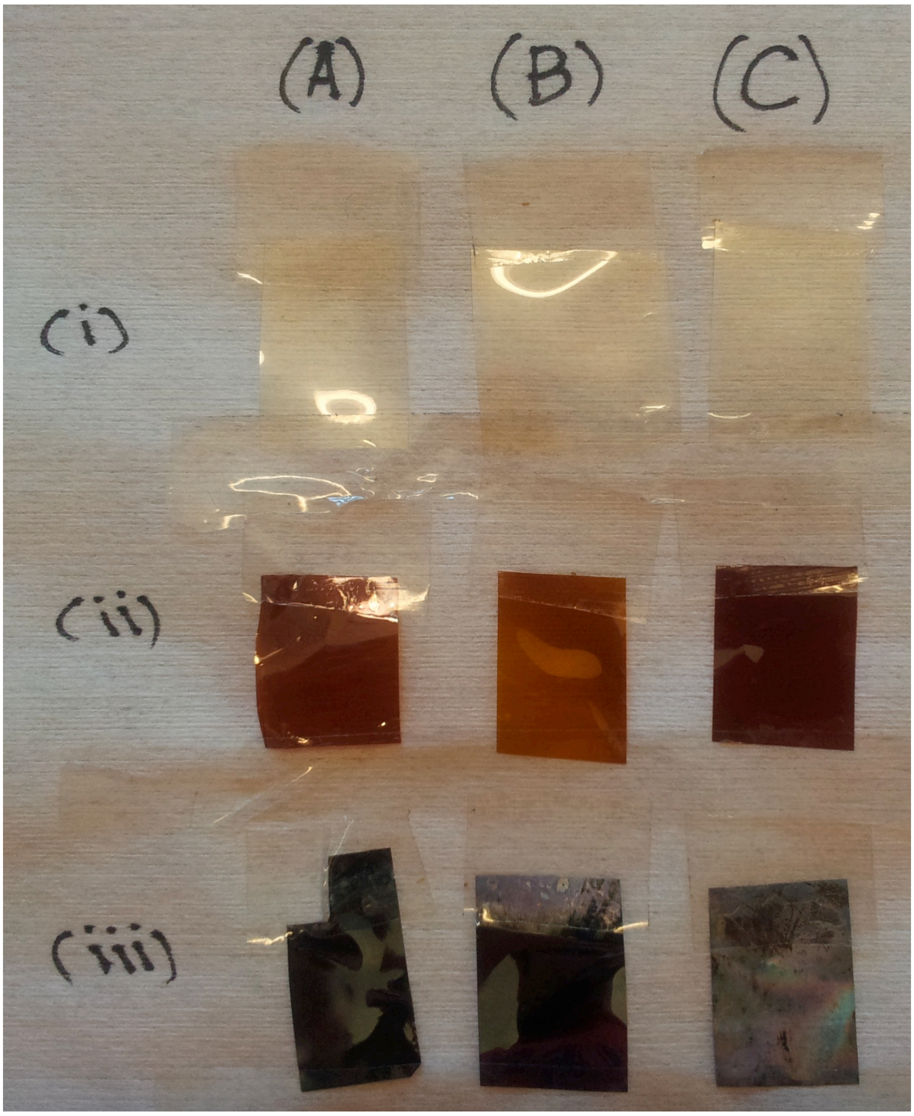

Figure 6.11: *Photographic image of samples shown in Figures 6.9 and 6.10 above. Sample sizes are approximately 2 cm x 3 cm.*

The final characterisation method performed was XRD to confirm the presence of reduced, metallic silver. Figure 6.12(a) below shows the diffraction pattern from a sample that has been the subject of the ion-exchange process but no reduction has taken place. No crystalline diffraction peaks stand out, indicating an amorphous sample. Figure 6.12(b) shows the spectrum from sample C(iii) in figures 6.9, 6.10 and 6.11, after the reduction step but before heat treatment. A crystalline peak at 38.2^{o} is clearly seen, with slight peaks at 45 and 77 degrees also visible. These coincide with silver diffraction peaks of crystalline structure (111), (200) and (311), respectively [204], confirming the presence of crystalline silver within the sample. The lack of prominence of the peaks can be attributed to the low volume fraction of silver in the sample.

Samples cured in the nitrogen atmosphere showed the largest peaks, with the air cured peaks displaying only slightly smaller peaks than the vacuum annealed samples. Although the difference is not large, it suggests either that the absence of oxygen has a positive effect on in-situ silver nanoparticle formation and that the vacuum environment somehow retards silver growth or that silver oxide is formed, which does not exhibit the same peaks as pure silver.

The diffraction peak at 38.2° in Figure 6.12(b) also allows an estimate of the average crystalline correlation length for the silver crystals, τ, to be made using the Scherrer formula [205]:

$$\tau = \frac{K\lambda}{\beta\cos\theta} \tag{6.1}$$

where K is the dimensionless shape factor (=1), λ is the X-ray wavelength (1.5418 Å), β is the full width half maximum (FWHM) of the peak value in radians (7.4 x 10^{-3}), and θ is the Bragg angle (19°). This estimate gives a mean silver crystal size of approximately 20 nm, which agrees well with the SEM images in row (iii) of Figure 6.9, giving a silver nanoparticle size of 20 – 30 nm. These nanoparticles may be composed of single crystals, but nanoparticles with more than one single crystal or with crystalline defects, would be consistent with a lower crystalline correlation length.

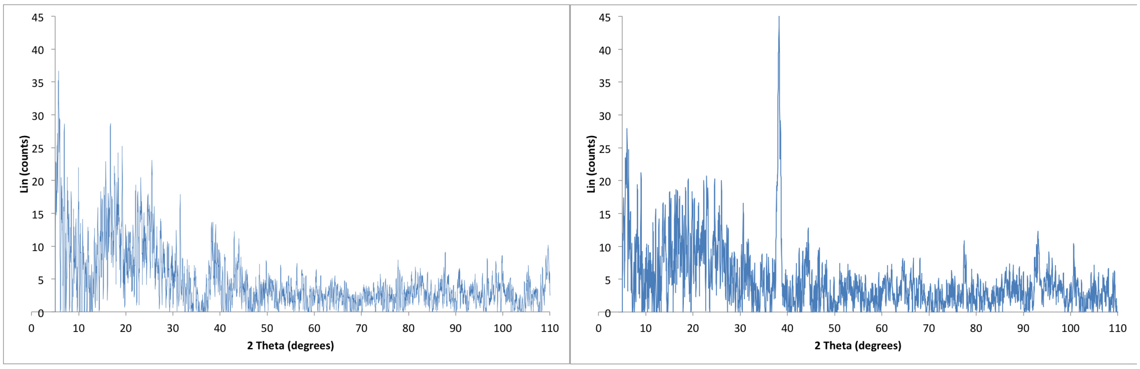

Figure 6.12: *XRD samples of PEI with (a) ion-exchange only with no chemical reduction and (b) chemically reduced silver nanoparticles.*

6.2.4 Conclusions

The fabrication process has been successfully adapted for use with a different substrate in the form of polyetherimide. Hydrolysis has been demonstrated to be possible on this polymer albeit with more aggressive parameters being required. Of the continuous variables, temperature was found to be the key factor in this reaction, with concentration also playing a somewhat significant role. Ion exchange of silver and potassium ions within the modified substrate and subsequent in-situ reduction of the silver ions have also been demonstrated and experimentally verified, with the potassium solution providing greater efficacy. This exploratory work opens up interesting opportunities towards achieving direct metallisation onto PEI. Despite PEI having the same number of cleavable imide rings in its monomer as Kapton, the main polyimide studied in this thesis, PEI has a greater molecular weight per repeat unit. It is therefore not expected that the maximum achievable densities of silver nanoparticles on the surface of PEI will be as high as that on PI, in its PMDA-ODA form at least.

6.3 Chapter conclusions

Polyetherimide has been tested and verified as a suitable new substrate receptive to the fabrication process. The initial hydrolysis step was found to require a much more aggressive treatment than standard Kapton polyimide. Silver nanoparticle formation was also achieved by chemical reduction and although the best covering of silver nanoparticles after reimidisation appeared to be on the vacuum cured samples, the air environment also provided a useful covering of silver amenable to further electroless plating.

Chapter 7
Conclusions and future work

7.1 Introduction

This thesis has investigated and developed a novel direct writing technique for site selective metallisation of polyimide substrates. An in-depth review of up to date direct writing and direct metallisation technologies was provided in Chapter 2 to both justify the choice of fabrication route and highlight the large variety of competing techniques and their relative prominences within the field. Specific attention was paid to ion exchange of polyimide to provide the reader with a solid background when reading the subsequent experimental chapters. The outcomes of each of these chapters are discussed in Section 7.2. Section 7.3 then proposes future areas of research to further develop and improve the process before Section 7.4 ends the thesis with some concluding remarks.

7.2 Outcomes

The work in this thesis builds on previous research by Akamatsu *et al.* [2] and Ng *et al.* [6]. It has been summarised in Figure 7.1 with respect to the initial fabrication process when studies were commenced. The most significant and novel contributions are listed here:

- The combination of a new electron donor coating of spinach extract combined with a blue light source appropriate to the absorption band of chlorophyll was demonstrated to require significantly lower energy doses to achieve metallisation. This results in faster laser scanning speeds being possible, meaning higher fabrication rates. A 5 μm test structure using a photomask combined with spinach extract and blue light source was demonstrated.

Further preliminary investigations on individual photosystem proteins were subsequently carried out, identifying ß-carotene as a potentially even cheaper electron donor source than spinach extract. This is discussed further in Section 7.3.3 below.

- Polyetherimide was shown to be a suitable substrate for the metallisation procedure, increasing the potential scope of the process. PEI is widely used in the production of MIDs so this work has opened up a large scope for new manufacturing methods in moulded device production. The factors affecting initial surface modification were also well characterised.

  Another novel substrate was also found in the latter stages of the research and is discussed briefly in Section 7.3.8 below. Cellulose was found to be both substrate and electron donor combined, removing the need to apply an extra donor material. Such substrate material has potential anti-bacterial applications such as that in water treatment.
- Before the spinach extract was tested, silver tracks created with a scan speed of 0.5 $m \cdot s^{-1}$ were demonstrated – a very high speed compared to other current technologies. The subsequent characterisation of degradation experienced during UV exposure led directly to experiments involving blue light sources and spinach extract.
- Site selective chemical reduction was demonstrated with the aid of a new environmentally friendly photoresist. Although this was not strictly the aim of the research, it does add other fabrication routes to the process

The following subsections encapsulate the work undertaken in each chapter in slightly more detail and state how this has contributed to developing the process in each case. The significant preliminary work on potentially improving and extending the process to different substrates seen in the final column of Figure 7.1 can be found in Sections 7.3.3 and 7.3.8. below.

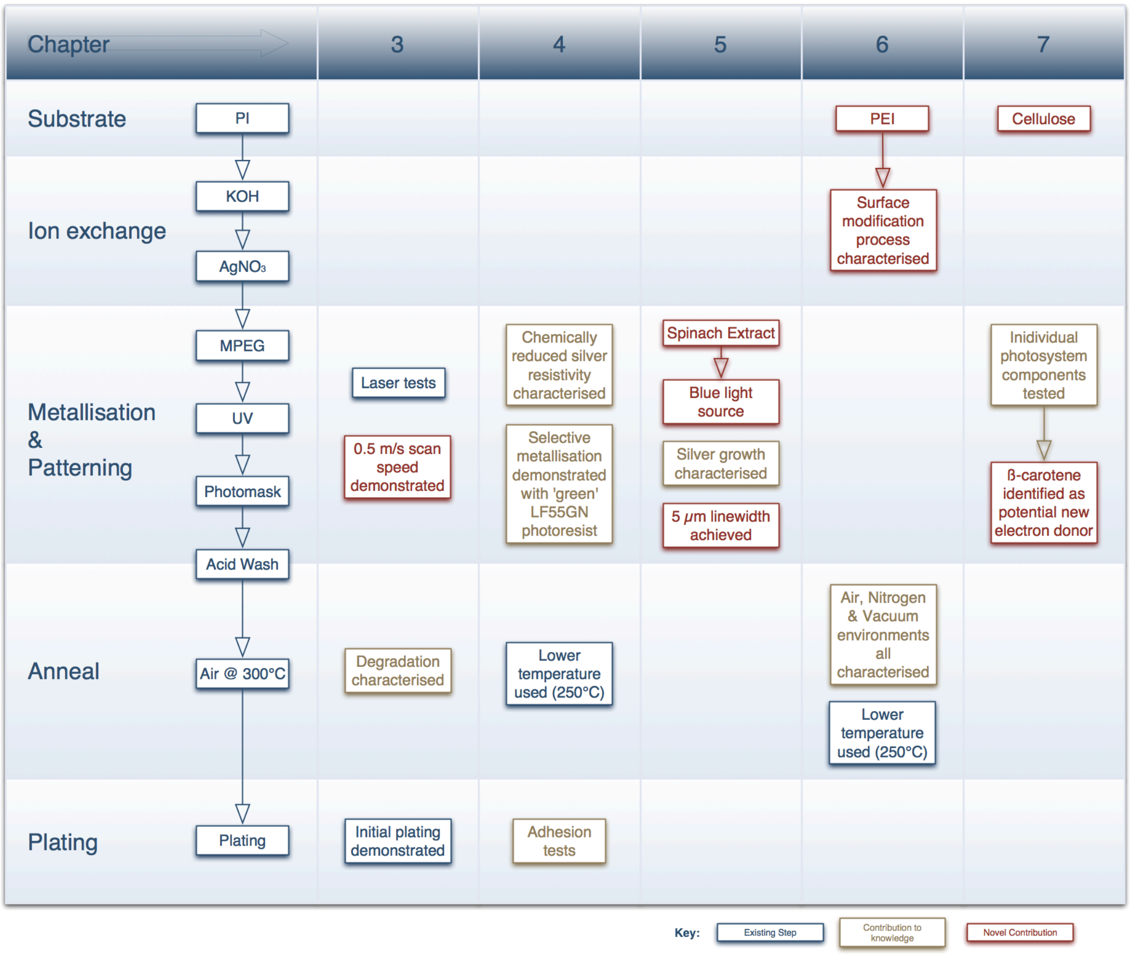

Figure 7.1: *Summary of work presented in this thesis with respect to process steps.*

7.2.1 Laser direct writing tests and degradation of polyimide

A UV laser was used to write a series of silver tracks, at different laser powers and scanning speeds. When the energy dose was too great, ablation of the polymer was observed resulting in irregular, recessed tracks. At a lower dose, swelling of the polymer under the silver was observed. Neither of these effects was desirable for subsequent circuit fabrication steps so further investigation was carried out to determine steps to reduce or eliminate such occurrences.

Detailed investigation of physical effects of UV induced metallisation on both polyimide and silver particles was then carried out. Greater doses of energy were found to cause a greater number of silver nanoparticles to form, with these particles also growing in size through coalescence with neighbouring particles as time progressed. At the same time, energy doses above 720 J·cm^{-2} were seen to cause deterioration in the modified layer of the polyimide, resulting in a trade-off between larger energy doses providing a better seed layer for electroless plating while also causing oxidative degradation in the polymer, which resulted in poor polymer-metal adhesion.

7.2.2 Chemical metallisation route

As a way to diversify the process, an alternate reduction method was investigated, where photoreduction was replaced by chemical reduction. Surface morphology over a variety of concentration and immersion time parameters was observed and their surface resistivities were measured. Workable values of 5 mM for the concentration and 5 minutes for the immersion time were found, with higher values demonstrated to indirectly confirm the KOH modification depth of 300 – 350 nm in agreement with the degradation seen in Chapter 3.

Once suitable values were finalised, the problem of selectively patterning using chemical reduction was addressed using an environmentally water-soluble photoresist. Although this method requires more process steps than direct writing, the silver formed is much more uniform at the micron scale, which is desirable for better conductivity. 100 μm linewidths were demonstrated although there was quite large variation along different parts of the test structures created. This was attributed to the DMAB reducing agent diffusing underneath the slightly rubbery photoresist.

While successful at producing medium to large feature sizes, the chemical reduction method combined with LF55GN resist was deemed unsuitable for fine feature creation. Even at larger feature sizes there are already many well established fabrication processes and so it was decided to revert to examining how to improve the photoreduction process instead.

7.2.3 Direct writing improvements

In an attempt to reduce the energy used to create silver tracks and thereby decrease polymer degradation, the UV light sources were replaced by blue light sources. Taking a leaf from the book of photosynthesis, nature's primary energy transfer mechanism, spinach extract was demonstrated to be an excellent electron donor in combination with the blue light sources. While the enhancement was primarily attributed to chlorophyll molecules, the action of other molecules within the light harvesting complex was not ruled out. Indeed, this is discussed further in Section 7.3 below. It was also shown that even without a spinach extract coating, blue light was capable of direct photolysis of silver ions.

The readiness with which silver particles were created using blue light radiation was attributed to a combination of the photoreduction of the silver ions, heat effects, similar to those that triggered in part the degradation seen in Chapter 3, and localised surface plasmon resonance of silver nanoparticles, which accelerate the reduction and nucleation of surrounding silver ions.

7.2.4 Extending the process to new substrates

Finally, the process was also diversified to a different substrate in polyetherimide thanks to its similar imide ring-containing molecular structure to polyimide. PEI is less widely used than PI for electronics but is popular in the growing field of moulded interconnect devices due to its malleability, transparency and high chemical resistance and mechanical strength. Such a material was found to require a much more aggressive alkali hydrolysis regime than PI, with a 20 minute immersion in 15 M KOH at 80°C to achieve greater than 95% imide ring cleavage, compared to 5 minutes immersion in 1M KOH at 50°C for polyimide. Nevertheless silver ion exchange followed by chemical reduction then reimidisation in different atmospheres was successfully demonstrated to produce uniform silver coatings.

7.3 Future process development

To conclude the thesis suggestions for improvements and future areas of study are given chronologically with regard to each step of the process. The regions regarded by the author as most important and potentially fruitful for investigation to improve and develop the process are discussed in Subsections 7.3.3 and 7.3.4, which covers the electron donor coating and direct writing steps respectively. Subsection 7.3.6, which deals with the reimidisation step, also presents some opportunity for alternate polyimide curing and silver annealing and sintering investigations. The remaining sections are regarded as lower priority by the author, but this is not to say that improvements cannot be made. Indeed there are several areas in which the process could be investigated to improve adhesion for example.

7.3.1 Alkali hydrolysis by KOH treatment

While the polyimide hydrolysis part of the process is not complex, it is still important in terms of metal-polymer adhesion.

The degradation from UV exposure seen in Section 3.5 was attributed mainly to the effects of the silver particles, however the samples without UV irradiation but with heat treatment did not display any patterning. The recessive effect was therefore not witnessed on these sample sets. Selective KOH modification of a PI substrate should be carried out to be able to directly assess any effect on degradation caused without silver particle formation.

Also it has been shown that the addition of ethylenediamine to the KOH solution improved adhesion between surface modified Kapton and nickel/copper plating on a palladium seed layer, as measured by 'T-peel' testing [206]. It is therefore worthwhile testing if a similar effect is observed with respect to silver seed layers should adhesion of silver tracks be poor.

Quantification of modification depth on polyetherimide would also be useful for any future work with that material as there is very little information on this in the literature.

There are many different polyimides that could be tested to expand the process further too, for example the numerous Kapton® and Upilex® sheets. Of particular interest for flexible display purposes are transparent blends, of which one type was recently demonstrated by the Akamatsu group to be compatible with the ion-exchange steps of the process [93].

Finally it is worth noting that while using the ratio of FTIR absorbance peaks to measure the relative degree of imidisation in both PI and PEI is reasonably accurate. Another characterisation method known as evolved gas analysis-mass spectrometry (EGA-MS) could determine absolute values as recently demonstrated for four different types of polyimides [207].

7.3.2 Ion-exchange by silver nitrate immersion

The second step of ion exchange is similarly straightforward to the first step, but again there is scope to investigate potential improvement here for both PI and PEI films. The group at Beijing University of Chemical Technology who are actively researching metallisation of polyimides employ a silver nitrate solution with a small amount of ammonia added to increase the rate of ion-exchange and improve subsequent reduction [208]. This was deemed a minor point with respect to this thesis due to both the small amount of extra preparation required and also the fact that the added ammonia increases the pH to alkaline levels and so could actively degrade the substrate. A similar issue was seen with the higher pH ESM 100 bath compared with better adhesion seen when using the low pH ESM 500 bath instead for example. Finally ammonia is a harmful substance for the environment.

It would however be useful to evaluate a direct comparison between the two solutions, especially in terms of whether the ion-exchange occurs throughout the entire KOH modified zone, or in other words whether the ion-exchange rate is diffusion dependent or more linear in both cases.

7.3.3 Electron donor coating

The most immediate area of further work is in the electron donor coating. As shown in Chapter 5, spinach extract provides a cheap and relatively green alternative to MPEG that provides very efficient photosensitisation. This was initially thought to be the work of the chlorophyll molecules, given other recent research involving other porphyrin ring-containing substances in both artificial photosynthesis [209, 210] and energy transfer [178]. However, preliminary tests indicate that other components of both light harvesting complexes and photosynthetic reaction centres, such as PS-I and PS-II, are also capable of energy transfer. Porphyrin rings can be seen to differentiate between chlorophylls and other pigment molecules in Table 7.1 below.

Figure 7.2 below shows images of reduction tests with various pigment molecules while Table 7.1 provides more information about the samples. Exposure time was 5 minutes at a relatively low irradiance of 400 mW·cm^{-2} to minimise the effect of heat, hence silvering is not as great as that observed previously. The carotenoid compounds were found to be less readily soluble in ethanol than the chlorophylls and so chloroform was used for these instead. A small sample of ion doped PI approximately 1.5 x 1.5 cm was coated by dropping around 300 µl of solution with a pipettor, then spread using surface tension at the interface between pipettor tip and liquid boundary, except for two of the spinach extract coatings, which are marked as such and discussed further below.

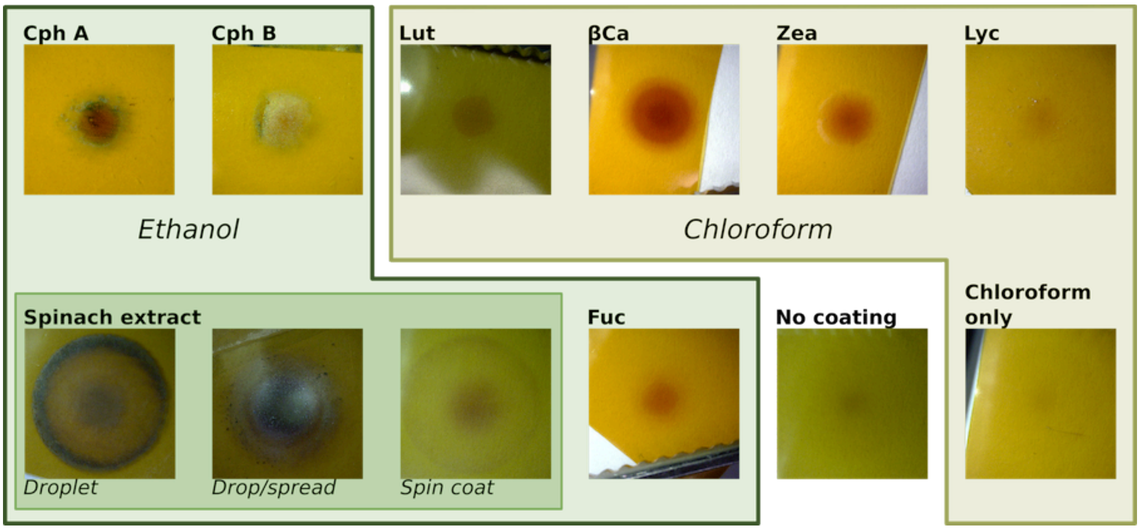

Figure 7.2: *Blue LED exposure of PI with drop/spread coating of selected photosynthetic molecules. Top row: selected PSI/II components from left to right: chlorophyll-a, chlorophyll-b, lutein, β-carotene, zeaxanthin and lycopene. Bottom row: reference samples from left to right: spinach extract coated by 3 different methods, brown algae extract fucoxanthin, uncoated sample and chloroform only coated sample. Solvent used for each sample shown by grouping.*

It is clear that the spinach extract provides the best silvering compared to individual molecules, however since ethanol was used in this extraction, it is reasonable to assume that not as much lutein, β-carotene or zeaxanthin was extracted from the spinach leaves as was potentially available due to the solubility issue mentioned above. Lycopene was found to be completely insoluble in ethanol and so it is expected none was present in the spinach extract, although it had little effect compared to the sample with no coating anyway. Given the molecular structure of the compounds, shown in Table 7.1 below, this is perhaps not surprising as it does not absorb 460 nm light as strongly as the other chemicals tested as highlighted in Figure 5.2, but is more responsive to longer wavelength light. This could be due to its structure lacking a hexagonal carbon ring (a type of alicyclic structure) termination at both ends like the other carotenoids shown or a porphyrin ring at one end like the chlorophyll molecules.

It would appear then, that the most efficient reducing coating at this radiation wavelength should contain not just chlorophyll, but other pigments present in PS-I, PS-II and LHC-II too. In particular β-carotene appears most effective individually out of the remainder. It is also interesting to note the different shapes of the spots, with lutein being more even over a smaller area and β-carotene creating an apparently larger spot size than the chlorophylls, although it must be stressed that these are preliminary results.

Photosensitising agent	Solvent	Approximate silver reduction efficacy	Molecular structure
Chlorophyll-a	EtOH	●●●●○	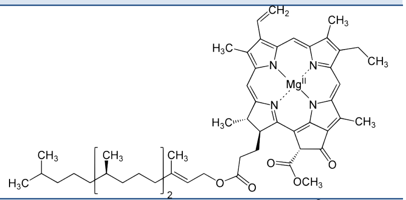
Chlorophyll-b	EtOH	●●●○○	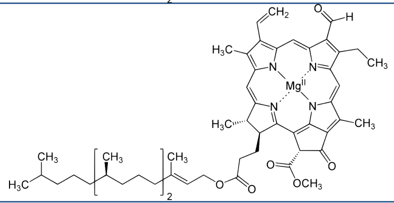
Lutein	Chlf	●●●○○	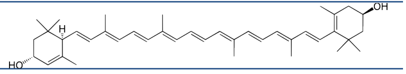
β-Carotene	Chlf	●●●●○	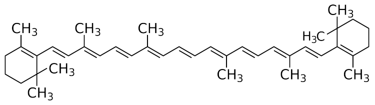
Zeaxanthin	Chlf	●●●○○	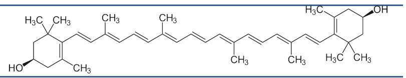
Lycopene	Chlf	●○○○○	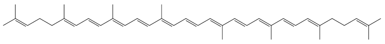
Spinach extract (droplet)	EtOH	●●●●●	-
Spinach extract (drop/spread)	EtOH	●●●●●	-
Spinach extract (spin coat)	EtOH	●●○○○	-
Fucoxanthin	EtOH	●●○○○	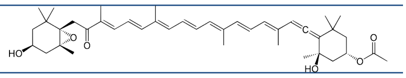
No coating	-	●○○○○	
Chloroform only	Chlf	●○○○○	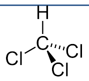

Table 7.1: *Approximate effectiveness of individual light harvesting molecules as a photosensitiser for reduction of silver ions in polyimide.*

Fucoxanthin, one if the main carotenoids found in brown algae but not in plants, was tested with the aim of finding out if other light harvesting compounds found in nature could be exploited for flexible substrate metallisation. It possesses a fairly broad absorption peak at 450 nm when dissolved in ethanol, with a shoulder at 467 nm [211]. Reduction was observed but not anything greater than seen by other individual carotenoids. This does however open up a huge array of natural compounds to test for their suitability to the current process, with a multi-wavelength laser system being tuned to irradiate a mixture of different photosensitising chemicals for example, although perhaps using a solar-simulating white light in a similar manner to Kang *et al.* and Hou *et al.* [212, 213] would yield the best results. Chloroform on its own was tested to eliminate its role in proceedings in a similar manner to the tests in Section 5.2.4. It is clear from comparing the chloroform only coated sample with the uncoated sample in Figure 7.2 that is has negligible effect.

Energy transfer within plants, algae and bacteria is non-trivial but steady progress is being made, especially in recent times. While only given a cursory mention in this thesis, some publications are suggested in Table 7.2 below as reading to compliment any experimental work carried out.

General topic	Reference(s)
Historical perspective on artificial light harvesting	• Hautala, Chapters 2, 5 and 8 [214]
Initial modelling of a light harvesting complex	• McDermott *et al.* [215]
Energy transfer in photosynthesis	• van Grondelle and Novoderezhkin [216]
PS-I absorption enhancement by metal nanoparticles	• Carmeli *et al.* [217]
PS-II: detailed analysis and its impact on artificial photosynthesis	• Barber [218]
LHC-II energy transfer	• van Amerongen and van Grondelle [219]
The role of carotenoids in photosynthesis in excess energy dissipation	• Janhs and Holzwarth [220] • Müller *et al.* [221]

Table 7.2: *Suggested background reading for experimental work on natural photosensitisers.*

As well as investigating different coatings, another highly important avenue for immediate research is refining the coating process for the spinach extract. It is clear from Figure 7.2 that the coating method plays a large role. Although challenging to measure the coating thickness, since the ethanol is left to evaporate in all cases, it is assumed that spin coating leaves the thinnest residue of the three coating methods tested here. This explains the less impressive silver formation and is preliminarily attributed to the lack of electron source material and also the lack of electron mobility in this coating. What is also interesting is the difference between a large droplet left to evaporate and a smaller volume of liquid spread over a larger area, with the silver pattern being almost inverted between the two samples. This could be due in part to coating thickness but also due to LSPR effects; which are dependent on the angle of incident light.

The coating thickness effect should be characterised, perhaps initially by repeated coating-evaporation cycles to 'build up' a thicker layer. Similarly studying the effect of collimated light at a range of incident angles could prove highly useful to the process, this is discussed further in the following subsection.

The concentration of the coating could also play a part. During the initial tests, it was found that the rapid evaporation of chloroform, and to a lesser extent ethanol, caused uneven distribution of photosensitising agents, sometimes leaving relatively large crystalline structures on the surface, which retarded silver growth. Since some of the compounds tested were very costly for small quantities, it was not possible to carry out many repetitions. A more rigorous testing of all compounds is essential to ensure repeatability and finding a way to slow down the evaporation rate to make testing more robust would be a part of this.

Finally, on the subject of materials costs, although some individual components are expensive, the most effective new potential candidate, β-carotene, is not. If looking at keeping the process low-cost, it is therefore recommended to either continue with spinach extract in ethanol, obtain spinach extract using a combination of solvents to better extract the active photosynthetic pigments or obtain a cheap source from which to extract β-carotene, such as carrots, although spinach is also rich in this carotenoid.

7.3.4 Direct laser writing and other photoreduction methods

The laser writing demonstrated in Section 5.3 requires more robust characterisation. This is perhaps the most significant next step and should be considered top priority. Adhesion and conductivity of tracks should be tested, further investigation of the silver formation with and without a photosensitising coating should be carried out and ways by which the particle free zone, seen in the TEM images in Figure 5.6, can be minimised to fully exploit the silver nucleation process for maximum conductivity. Recent work has indicated that the means of ion reduction plays a strong part in how the silver particles nucleate and coalesce [222].

A great deal of work has been done on controlling the geometry of silver particle growth at the nano scale by varying the irradiance parameters [223, 224]. Although exotic shapes are perhaps less relevant for forming continuous tracks, they highlight that it should be possible to tailor the incident light to produce exactly the right size and shape of silver NPs for optimal conductivity, subsequent electroless plating or both. Fragmentation of silver to form smaller NPs with a 532 nm light source has also been demonstrated [225], indicating that some form of dual laser (or LED) setup may be able to control size to within a given range and minimise particle-to-particle diameter variation. A good starting point for formulating a plan of attack is the review of light as a construction tool by Sakamoto *et al.* [120].

As touched upon in the previous subsection, the angle of incidence of the light is also a factor on the LSPR effect [226], which may partly explain the high silvering of the spot edge in the drop coated PI in Figure 7.2 above. It is also likely that polarisation of the incident light will have an effect [227], so there is great scope here for research to optimise the light source in conjunction with whatever natural photosensitiser, if any, is being tested. A good theoretical background to light interaction with nanoscale objects, introducing the particularly relevant Mie theory among other principles is given by Hagfeldt and Grätzel [228], which should assist in explaining the phenomena witnessed during the direct writing process of this thesis.

Due to the steady increase in processing power, simulations of LSPR can now be computed. Indeed Wei *et al.* have presented modelling of plasmon modes of silver 'nanorice' that agreed well with their experimental measurements [229]. Therefore there is a potential for work here on the theoretical and simulation side of silver formation, although this is of greater importance from an academic perspective than a circuit fabrication point of view.

Practically, there is scope for improving the optical setup of the blue laser to minimise variability in beam focus and diameter between experiments. The laser could also be upgraded, as higher power models at the same wavelength and better options of similar wavelengths have since become available. Other wavelengths could also be tested in tandem with any new reducing agents. Judging by the continuity of silver reported by Kang *et al.* [212], pulsing the light source would appear to be very beneficial to improving conductivity and should be tested, as should its effect on adhesion.

A larger translation stage or laser mount capable of higher speeds is necessary to find the absolute write speed limit for a given power, which it is hoped could reach a few metres per second. If a suitably fast translation stage cannot be found, another way to demonstrate the up-scalability of the process could be to parallelise the LDW step by using optical beam-splitters for example.

As well as characterising and improving the current process further, there is also scope to investigate a novel fabrication route for process diversification purposes. Fritsch *et al.* recently demonstrated a new silver complex derived from silver nitrate, which was dip-coated onto a substrate [230]. A pattern was then embossed into this new thin coating before UV exposure photoreduced the silver. The complex was found to be soluble in both water and ethanol. Using this coating instead of or in addition to a natural photosensitiser coating in the present process could provide a denser silver covering and possibly enhance the adhesion between embedded silver NPs and the additional silver from this new coating. This also leads to the theoretical possibility of having a system whereby such a coating is inkjet printed directly in front of a laser beam, which reduces the silver ions and evaporates the solvent at the same time. This would use less precursor material and so would be more useful for coatings, which were more expensive as the current spinach extract coating is relatively cheap.

Finally in this subsection, photoreduction of silver ions on PEI substrates is also a high priority area. Only non-selective chemical reduction was used to demonstrate the use of PEI in the process in Chapter 6, meaning the photoreduction methods of laser direct writing or photomask exposure still require validation.

7.3.5 Unreacted ion removal by dilute acid wash

This low complexity step does not have great scope for improvement as the ion-exchange mechanisms have been well studied elsewhere and discussed in Chapters 2 and 3. For minimising costs when up-scaling the process however, it will be necessary to reclaim unreacted silver ions from the spent solution after this stage. Although this will not be a complex chemical process, it still needs to be addressed.

7.3.6 Polymer reimidisation and silver annealing

This stage has the dual effect of reimidising the polyimide and also further growing/sintering the silver particles. As has been shown in this thesis, the latter is most likely to have a negative impact on the former. There are some possibilities to reduce this effect.

Magdassi *et al.* have shown some very nice looking SEM images of chemically sintered silver at room temperature [231]. A similar chemical could be used after imidisation to improve silver coating, or indeed it may even be possible to introduce it into the photosensitiser coating in step 3 of the present process.

Similarly, Kang *et al.* used intense light to perform room temperature sintering [212]. Although the results appear slightly crude, the concept may tie in better with the LDW fabrication method.

The final possibility is microwave sintering, which has been shown to provide well formed silver coatings at the micron scale on polyimide by Perelaer *et al.* [232]. Naturally all 3 of these suggestions could be investigated on both PI and PEI substrates.

7.3.7 Electroless plating

The area of electroless plating was somewhat neglected by this thesis, but a thorough testing of plating of blue laser created tracks is required, although thanks to the use of a stable proprietary electroless bath, it is not envisaged that much adjustment will be needed to optimise it. Resistivity measurements are not seen as essential since the bath is already seeing usage in the PV sector as well as other industries, but formal adhesion tests adhering to official standards would provide useful data. As a starting point, suggested test standards are BS 3900 E6, ISO 2409 and ASTM standards 3359D and 3302D, although these tend to require large coated areas of a few square millimetres.

7.3.8 Other improvements and developments

The final proposals for future work do not come under any single process step but could prove beneficial nonetheless. There are three areas covered here: rubbing of polyimide, chemical reduction route, and further substrate diversification.

Firstly, rubbing of polyimide is a substrate preparation process well known in the LCD industry to aid with liquid crystal alignment that has been found to align the polymer chains in the direction of rubbing [233] and aids in adhesion of liquid crystals to the surface [234]. Furthermore, alignment was shown to change depending on imidisation temperature [235]. Rubbing could therefore be used to modify the substrate and the silver-polymer interface by performing it at different points before and during the fabrication process, with literature available for characterisation methods and comparison [236, 237].

Secondly, although Chapter 4 showed that patterning was problematic, it did produce good silver coatings that were highly uniform. Trials could be carried out to find a more suitable photoresist for patterning or the DMAB could be aerosol printed for fine feature formation. Another potentially interesting outcome from this chapter is the detachment of the silver layer from the polyimide, which occurred at higher concentration tests. While undesirable for the present process, this could be a way of forming ultra thin silver layers of less than 300 nm thickness. The silver is presumed to be held together by polyamic acid and so it may even be possible to detach this silver-PAA matrix from the majority of the PI using strong DMAB solution, before re-imidising this matrix.

Finally substrate diversification is desirable to maximise the potential of the process. The many various polyimides have already been addressed above but a rather different substrate is suggested here.

Although the spinach extract coating undoubtedly accelerates silver nucleation and growth, the use of a blue light without additional coating is sufficient to facilitate metallisation. Indeed, a recent study by Hou *et al.* showed that silver ions can be readily reduced by sunlight in the presence of a range of materials they term 'natural organic matter' [213]. Similarly He *et al.* used chrysanthemum extract to create silver NPs [238].

To further illustrate the readiness by which silver can reduce in the presence of a suitable electron donor, another environmentally friendly and abundant compound shown to act as a reducing agent is cellulose [239]. Cellulose is the primary component of the most common filter papers so a preliminary check was conducted to test its ability to create silver particles under blue light.

Briefly, a sheet of Whatman No. 1 filter paper was immersed in 0.1 M silver nitrate and allowed to dry. This paper was then exposed to light from the same LED used in Section 5.2 at maximum power for an irradiance of 740 $mW\cdot cm^{-2}$ for 30 seconds. The result is shown in Figure 7.3 Below.

Although it is likely that other compounds in the paper contributed to the rapid nucleation seen here, it would appear that silver of some form has indeed been created within the cellulose matrix. As well as having great potential for anti-bacterial purposes, such as filtering water to remove pathogens susceptible to silver NPs, this quick and easy process could be used to create paper circuits or other flexible or wearable electronics. Indeed, copper has already been successfully printed onto a cellulose paper [76], silver particles have been embedded in cellulose filter paper [240] and for further substrate tailoring, work has been carried out to spin coat cellulose [241]. Further discussion on cellulose and its current applications can be found in a recent review by Abdul-Khalil *et al.* [242].

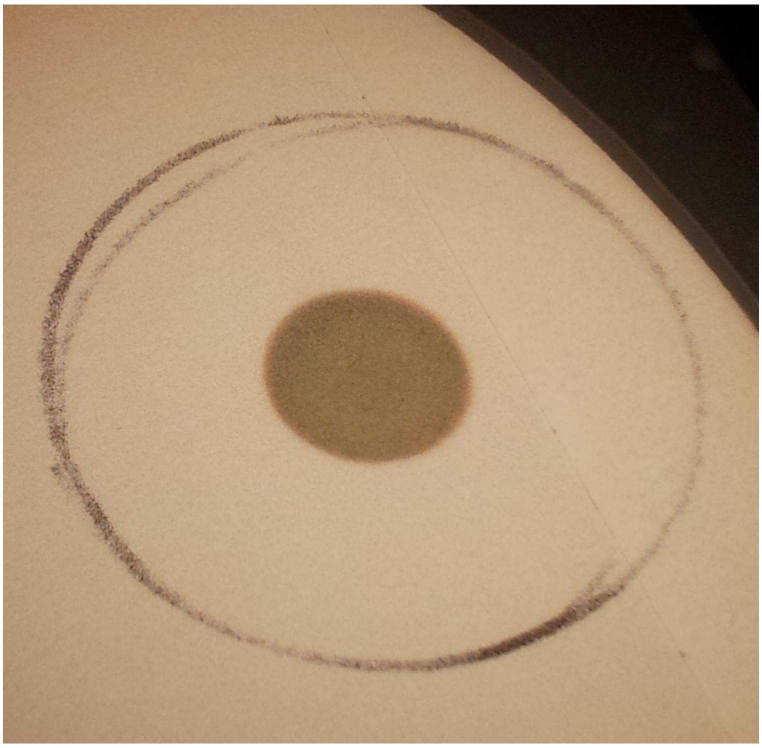

Figure 7.3: *Blue LED exposure of cellulose immersed in silver nitrate. Silver spot is approximately 1cm in diameter.*

7.4 Concluding remarks

This chapter has summarised the findings of the thesis and provided what is hoped is a sound basis for easy repetition of results, direction towards up-scaling and improving the overall process and some interesting avenues of future work from a theoretical viewpoint in the process. While the process is novel, it faces stiff competition if it is to find a niche in the printed and flexible electronic industry and so there is much work to be done to improve it, although hopefully there are enough suggestions in this chapter to see this achieved.

References

First appearing in:

Chapter 1

1. Ebisawa, F., T. Kurokawa, and S. Nara, *Electrical properties of polyacetylene/polysiloxane interface.* Journal of Applied Physics, 1983. **54**(6): p. 3255-3259.

2. Akamatsu, K., S. Ikeda, and H. Nawafune, *Site-selective direct silver metallization on surface-modified polyimide layers.* Langmuir, 2003. **19**(24): p. 10366-10371.

3. Qi, S.L., Z.P. Wu, D.Z. Wu, W.C. Wang, and R.G. Jin, *Double-Surface-Silvered Polyimide Films Prepared via a Direct Ion-Exchange Self-Metallization Process.* Chemistry of Materials, 2006. **19**: p. 393-401.

4. IOP, *Engineering Case Study – Plastic Electronics Engineering*, 2008, IOP: IOP Publishing.

5. IDTechEx, *Flexible Electronics Masterclass*, in *Plastic Electronics Europe*, S. Reuter, Editor 2012, IDTechEx: Berlin.

6. Ng, J.H.G., M.P.Y. Desmulliez, M. Lamponi, B.G. Moffat, A. McCarthy, H. Suyal, A.C. Walker, K.A. Prior, and D.P. Hand, *A direct-writing approach to the micro-patterning of copper onto polyimide.* Circuit World, 2009. **35**(2): p. 3-17.

Chapter 2

7. von Gutfeld, R.J., E.E. Tynan, R.L. Melcher, and S.E. Blum, *Laser enhanced electroplating and maskless pattern generation.* Applied Physics Letters, 1979. **35**(9): p. 651-653.

8. Hon, K.K.B., L. Li, and I.M. Hutchings, *Direct writing technology—Advances and developments.* CIRP Annals - Manufacturing Technology, 2008. **57**(2): p. 601-620.

9. Kwok, K. and W.K.S. Chiu, *Growth of carbon nanotubes by open-air laser-induced chemical vapor deposition.* Carbon, 2005. **43**(2): p. 437-446.

10. LaFratta, C.N., J.T. Fourkas, T. Baldacchini, and R.A. Farrer, *Multiphoton Fabrication.* Angewandte Chemie International Edition, 2007. **46**(33): p. 6238-6258.

11. Ashkin, A., *FORCES OF A SINGLE-BEAM GRADIENT LASER TRAP ON A DIELECTRIC SPHERE IN THE RAY OPTICS REGIME.* Biophysical Journal, 1992. **61**(2): p. 569-582.

12. Odde, D.J. and M.J. Renn, *Laser‐guided direct writing of living cells.* Biotechnology and bioengineering, 2000. **67**(3): p. 312-318.

13. Wee, L.M. and L. Li, *Multiple-layer laser direct writing metal deposition in electrolyte solution.* Applied Surface Science, 2005. **247**(1-4): p. 285-293.

14. Von Gutfeld, R., L. Romankiw, and R. Acosta, *Laser-enhanced plating and etching: mechanisms and applications.* Ibm Journal of Research and Development, 1982. **26**(2): p. 136-144.

15. Chen, Q., K. Imen, and S. Allen, *Laser Enhanced Electroless Plating of Micron‐Scale Copper Wires.* Journal of the Electrochemical Society, 2000. **147**(4): p. 1418-1422.

16. Manshina, A.A., A.V. Povolotskiy, T.Y. Ivanova, Y.S. Tver'Yanovich, S.P. Tunik, D. Kim, M. Kim, and S.C. Kwon, *Effect of salt precursor on laser-assisted copper deposition.* Applied Physics a-Materials Science & Processing, 2007. **89**: p. 755-759.

17. Kordás, K., J. Békési, R. Vajtai, L. Nánai, S. Leppävuori, A. Uusimäki, K. Bali, T.F. George, G. Galbács, and F. Ignácz, *Laser-assisted metal deposition from liquid-phase precursors on polymers.* Applied Surface Science, 2001. **172**(1): p. 178-189.

18. Kochemirovsky, V., S. Fateev, L. Logunov, I. Tumkin, S. Safonov, and E. Khairullina. *Laser-induced copper deposition with weak reducing agents*. in *Fundamentals of Laser Assisted Micro-and Nanotechnologies 2013*. 2013. International Society for Optics and Photonics.

19. Gross, M., A. Appelbaum, and P. Gallagher, *Laser direct‐write metallization in thin palladium acetate films.* Journal of Applied Physics, 1987. **61**(4): p. 1628-1632.

20. Aminuzzaman, M., A. Watanabe, and T. Miyashita, *Direct writing of conductive silver micropatterns on flexible polyimide film by laser-induced pyrolysis of silver nanoparticle-dispersed film.* Journal of Nanoparticle Research, 2010. **12**(3): p. 931-938.

21. Kim, J.H., B.S. Shin, J.S. Ko, J.S. Go, K.R. Kim, and Y.K. Jeong, *Direct Micro Fabrication of Flexible Copper Clad Laminate Using 355 nm UV Laser.* Japanese Journal of Applied Physics, 2008. **47**(8): p. 6883-6886.

22. Joo, S.C. and D.F. Baldwin, *Analysis of Adhesion and Fracture Energy of Nano-Particle Silver in Electronics Packaging Applications.* Ieee Transactions on Advanced Packaging, 2010. **33**(1): p. 48-57.

23. Buffat, P. and J.P. Borel, *Size effect on the melting temperature of gold particles.* Physical Review A, 1976. **13**(6): p. 2287.

24. Watanabe, A., *Laser Sintering of Metal Nanoparticle Film.* Journal of Photopolymer Science and Technology, 2013. **26**(2): p. 199-205.

25. Watanabe, A. and G. Qin. *Transparent conductive films based on the laser sintering of metal and metal oxide nanoparticles*. in *SPIE LASE*. 2014. International Society for Optics and Photonics.

26. Bohandy, J., B. Kim, and F. Adrian, *Metal deposition from a supported metal film using an excimer laser.* Journal of Applied Physics, 1986. **60**(4): p. 1538-1539.

27. Fardel, R., M. Nagel, F. Nuesch, T. Lippert, and A. Wokaun, *Laser-Induced Forward Transfer of Organic LED Building Blocks Studied by Time-Resolved Shadowgraphy†.* The Journal of Physical Chemistry C, 2010. **114**(12): p. 5617-5636.

28. Claeyssens, F., A. Klini, A. Mourka, and C. Fotakis, *Laser patterning of Zn for ZnO nanostructure growth: Comparison between laser induced forward transfer in air and in vacuum.* Thin Solid Films, 2007. **515**(24): p. 8529-8533.

29. Sanz, M., M. Walczak, M. Oujja, C. Domingo, A. Klini, E. Papadopoulou, C. Fotakis, and M. Castillejo, *Femtosecond laser deposition of TiO< sub> 2</sub> by laser induced forward transfer.* Thin Solid Films, 2010. **518**(19): p. 5525-5529.

30. Boutopoulos, C., A. Alloncle, I. Zergioti, and P. Delaporte, *A time-resolved shadowgraphic study of laser transfer of silver nanoparticle ink.* Applied Surface Science, 2013. **278**: p. 71-76.

31. Mattle, T., J. Shaw-Stewart, C.W. Schneider, T. Lippert, and A. Wokaun, *Laser induced forward transfer aluminum layers: Process investigation by time resolved imaging.* Applied Surface Science, 2012. **258**(23): p. 9352-9354.

32. Duocastella, M., J. Fernández-Pradas, J. Domínguez, P. Serra, and J. Morenza, *Printing biological solutions through laser-induced forward transfer.* Applied Physics A, 2008. **93**(4): p. 941-945.

33. Kim, H., R. Auyeung, S. Lee, A. Huston, and A. Piqué, *Laser forward transfer of silver electrodes for organic thin-film transistors.* Applied Physics A, 2009. **96**(2): p. 441-445.

34. Shaw-Stewart, J.R., T.K. Lippert, M. Nagel, F.A. Nüesch, and A. Wokaun, *Sequential printing by laser-induced forward transfer to fabricate a polymer light-emitting diode pixel.* ACS Applied Materials & Interfaces, 2012. **4**(7): p. 3535-3541.

35. Hopp, B., T. Smausz, Z. Antal, N. Kresz, Z. Bor, and D. Chrisey, *Absorbing film assisted laser induced forward transfer of fungi (Trichoderma conidia).* Journal of Applied Physics, 2004. **96**(6): p. 3478-3481.

36. Kattamis, N.T., P.E. Purnick, R. Weiss, and C.B. Arnold, *Thick film laser induced forward transfer for deposition of thermally and mechanically sensitive materials.* Applied Physics Letters, 2007. **91**(17): p. 171120.

37. Smausz, T., B. Hopp, G. Kecskemeti, and Z. Bor, *Study on metal microparticle content of the material transferred with absorbing film assisted laser induced forward transfer when using silver absorbing layer.* Applied Surface Science, 2006. **252**(13): p. 4738-4742.

38. Brown, M.S., N.T. Kattamis, and C.B. Arnold, *Time-resolved study of polyimide absorption layers for blister-actuated laser-induced forward transfer.* Journal of Applied Physics, 2010. **107**(8): p. 083103.

39. LaFemina, J.P., G. Arjavalingam, and G. Hougham, *Electronic structure and ultraviolet absorption spectrum of polyimide.* The Journal of Chemical Physics, 1989. **90**: p. 5154.

40. Kattamis, N.T., N.D. McDaniel, S. Bernhard, and C.B. Arnold, *Ambient laser direct-write printing of a patterned organo-metallic electroluminescent device.* Organic Electronics, 2011. **12**(7): p. 1152-1158.

41. Piqué, A., D. Chrisey, R. Auyeung, J. Fitz-Gerald, H. Wu, R. McGill, S. Lakeou, P. Wu, V. Nguyen, and M. Duignan, *A novel laser transfer process for direct writing of electronic and sensor materials.* Applied Physics A, 1999. **69**(1): p. S279-S284.

42. Riggs, B., A. Dias, N. Schiele, R. Cristescu, Y. Huang, D. Corr, and D. Chrisey, *Matrix-assisted pulsed laser methods for biofabrication.* Mrs Bulletin, 2011. **36**(12): p. 1043-1050.

43. Chrisey, D., A. Pique, R. Modi, H. Wu, R. Auyeung, and H. Young, *Direct writing of conformal mesoscopic electronic devices by MAPLE DW.* Applied Surface Science, 2000. **168**(1): p. 345-352.

44. Zhang, C., D. Liu, S.A. Mathews, J. Graves, T.M. Schaefer, B.K. Gilbert, R. Modi, H.-D. Wu, and D.B. Chrisey, *Laser direct-write and its application in low temperature Co-fired ceramic (LTCC) technology.* Microelectronic Engineering, 2003. **70**(1): p. 41-49.

45. Kinzel, E.C., X. Xu, B.R. Lewis, N.M. Laurendeau, and R.P. Lucht, *Direct Writing of Conventional Thick Film Inks Using MAPLE-DW Process.* J. Laser Micro-Nanoeng, 2006. **1**: p. 74-78.

46. Mir-Hosseini, N., M.J.J. Schmidt, and L. Li, *Growth of patterned thin metal oxide films on glass substrates from metallic bulk sources using a Q-switched YAG laser.* Applied Surface Science, 2005. **248**(1–4): p. 204-208.

47. Kuznetsov, A., J. Koch, and B. Chichkov, *Laser-induced backward transfer of gold nanodroplets.* Optics express, 2009. **17**(21): p. 18820-18825.

48. Young, D., R. Auyeung, A. Piqué, D. Chrisey, and D.D. Dlott, *Plume and jetting regimes in a laser based forward transfer process as observed by time-resolved optical microscopy.* Applied Surface Science, 2002. **197**: p. 181-187.

49. Duocastella, M., H. Kim, P. Serra, and A. Piqué, *Optimization of laser printing of nanoparticle suspensions for microelectronic applications.* Applied Physics A, 2012. **106**(3): p. 471-478.

50. Shaw-Stewart, J., T. Lippert, M. Nagel, F. Nüesch, and A. Wokaun, *A simple model for flyer velocity from laser-induced forward transfer with a dynamic release layer.* Applied Surface Science, 2012. **258**(23): p. 9309-9313.

51. Mézel, C., A. Souquet, L. Hallo, and F. Guillemot, *Bioprinting by laser-induced forward transfer for tissue engineering applications: jet formation modeling.* Biofabrication, 2010. **2**(1): p. 014103.

52. Shafeev, G.A., *Laser-assisted activation of dielectrics for electroless metal plating.* Applied Physics a-Materials Science & Processing, 1998. **67**(3): p. 303-311.

53. Kordas, K., A.E. Pap, J. Saavalainen, H. Jantunen, P. Moilanen, E. Haapaniemi, and S. Leppavuori, *Laser-induced surface activation of LTCC materials for chemical metallization.* Ieee Transactions on Advanced Packaging, 2005. **28**(2): p. 259-263.

54. Wang, Y., Q. He, X. Hu, Y. Zhang, and H. Chen, *A polymeric dual-channel amperometric biosensor chip capable of symmetrically splitting sample bands for parallel micro flow injection determination of glucose and lactate.* Analytical Methods, 2012. **4**(7): p. 2031-2038.

55. Yung, K.C., C. Chen, and C.P. Lee, *Laser induced activation of circuit lines and via-holes on AlN for electroless metal plating.* Applied Surface Science, 2011. **257**(15): p. 6601-6606.

56. Xu, J., Y. Liao, H. Zeng, Y. Cheng, Z. Xu, K. Sugioka, and K. Midorikawa, *Mechanism study of femtosecond laser induced selective metallization (FLISM) on glass surfaces.* Optics Communications, 2008. **281**(13): p. 3505-3509.

57. Song, J., Y. Liao, C. Liu, D. Lin, L. Qiao, Y. Cheng, K. Sugioka, K. Midorikawa, and S. Zhang, *Fabrication of Gold Microelectrodes on a Glass Substrate by Femtosecond-Laser-Assisted Electroless Plating.* JLMN-Journal of Laser Micro/Nanoengineering, 2012. **7**(3): p. 334-338.

58. Zhou, Q., H. Chen, and Y. Wang, *Region-selective electroless gold plating on polycarbonate sheets by UV-patterning in combination with silver activating.* Electrochimica Acta, 2010. **55**(7): p. 2542-2549.

59. Montazer, M. and V. Allahyarzadeh, *Electroless plating of silver nanoparticles/nanolayer on polyester fabric using AgNO3/NaOH and ammonia.* Industrial & Engineering Chemistry Research, 2013. **52**(25): p. 8436-8444.

60. Lili, L., Y. Dan, W. Le, and W. Wei, *Electroless silver plating on the PET fabrics modified with 3 ‐ mercaptopropyltriethoxysilane.* Journal of Applied Polymer Science, 2012. **124**(3): p. 1912-1918.

61. Schlenoff, J.B., *Retrospective on the Future of Polyelectrolyte Multilayers†.* Langmuir, 2009. **25**(24): p. 14007-14010.

62. Malikova, N., I. Pastoriza-Santos, M. Schierhorn, N.A. Kotov, and L.M. Liz-Marzán, *Layer-by-layer assembled mixed spherical and planar gold nanoparticles: control of interparticle interactions.* Langmuir, 2002. **18**(9): p. 3694-3697.

63. Parakhonskiy, B., M. Bedard, T. Bukreeva, G. Sukhorukov, H. Mohwald, and A. Skirtach, *Nanoparticles on polyelectrolytes at low concentration: controlling concentration and size.* The Journal of Physical Chemistry C, 2010. **114**(5): p. 1996-2002.

64. Azzaroni, O., Z. Zheng, Z. Yang, and W.T.S. Huck, *Polyelectrolyte Brushes as Efficient Ultrathin Platforms for Site-Selective Copper Electroless Deposition.* Langmuir, 2006. **22**(16): p. 6730-6733.

65. Huang, S.-C., T.-C. Tsao, and L.-J. Chen, *Selective electroless copper plating on poly (ethylene terephthalate) surfaces by microcontact printing.* Journal of the Electrochemical Society, 2010. **157**(4): p. D222-D227.

66. Kimura, M., H. Yamagiwa, D. Asakawa, M. Noguchi, T. Kurashina, T. Fukawa, and H. Shirai, *Site-selective electroless nickel plating on patterned thin films of macromolecular metal complexes.* ACS Applied Materials & Interfaces, 2010. **2**(12): p. 3714-3717.

67. Zabetakis, D. and W.J. Dressick, *Selective electroless metallization of patterned polymeric films for lithography applications.* ACS Applied Materials & Interfaces, 2009. **1**(1): p. 4-25.

68. Skirtach, A., C. Dejugnat, D. Braun, A. Susha, A. Rogach, and G. Sukhorukov, *Nanoparticles distribution control by polymers: aggregates versus nonaggregates.* The Journal of Physical Chemistry C, 2007. **111**(2): p. 555-564.

69. Cerdà, J.J., B. Qiao, and C. Holm, *Modeling strategies for polyelectrolyte multilayers.* The European Physical Journal Special Topics, 2009. **177**(1): p. 129-148.

70. Carrillo, J.-M.Y. and A.V. Dobrynin, *Layer-by-layer assembly of polyelectrolyte chains and nanoparticles on nanoporous substrates: molecular dynamics simulations.* Langmuir, 2011. **28**(2): p. 1531-1538.

71. Garcia, A., T. Berthelot, P. Viel, A. Mesnage, P. Jégou, F. Nekelson, S.b. Roussel, and S. Palacin, *ABS polymer electroless plating through a one-step poly (acrylic acid) covalent grafting.* ACS Applied Materials & Interfaces, 2010. **2**(4): p. 1177-1183.

72. de Saint-Aubin, C., J. Hemmerlé, F. Boulmedais, M.-F. Vallat, M. Nardin, and P. Schaaf, *New 2-in-1 polyelectrolyte step-by-step film buildup without solution alternation: From PEDOT-PSS to polyelectrolyte complexes.* Langmuir, 2012. **28**(23): p. 8681-8691.

73. Basarir, F., *Fabrication of Gold Patterns via Multilayer Transfer Printing and Electroless Plating.* ACS Applied Materials & Interfaces, 2012. **4**(3): p. 1324-1329.

74. Barbey, R., L. Lavanant, D. Paripovic, N. Schüwer, C. Sugnaux, S. Tugulu, and H.-A. Klok, *Polymer brushes via surface-initiated controlled radical polymerization: synthesis, characterization, properties, and applications.* Chemical Reviews, 2009. **109**(11): p. 5437-5527.

75. Azzaroni, O., *Polymer brushes here, there, and everywhere: Recent advances in their practical applications and emerging opportunities in multiple research fields.* Journal of Polymer Science Part A: Polymer Chemistry, 2012. **50**(16): p. 3225-3258.

76. Guo, R., Y. Yu, Z. Xie, X. Liu, X. Zhou, Y. Gao, Z. Liu, F. Zhou, Y. Yang, and Z. Zheng, *Matrix‐Assisted Catalytic Printing for the Fabrication of Multiscale, Flexible, Foldable, and Stretchable Metal Conductors.* Advanced Materials, 2013. **25**(24): p. 3343-3350.

77. Lee, K.W., S.P. Kowalczyk, and J.M. Shaw, *Surface modification of PMDA-oxydianiline polyimide. Surface structure-adhesion relationship.* Macromolecules, 1990. **23**(7): p. 2097-2100.

78. Stephans, L.E., A. Myles, and R.R. Thomas, *Kinetics of alkaline hydrolysis of a polyimide surface.* Langmuir, 2000. **16**(10): p. 4706-4710.

79. Plechaty, M.M. and R.R. Thomas, *Chemical Surface‐Modification of a Polyimide: Characterization and a Kinetic Study on the Diffusion of Ions in a Modified Polymer.* Journal of the Electrochemical Society, 1992. **139**(3): p. 810-821.

80. Okumura, H., T. Takahagi, N. Nagai, and S. Shingubara, *Depth Profile Analysis of Polyimide Film Treated by Potassium Hydroxide.* J Polym Sci Part B: Polym Phys, 2003. **41**: p. 2071-2078.

81. Thomas, R.R., *Quantification of ionizable functional groups on a hydrolyzed polyimide surface.* Langmuir, 1996. **12**(22): p. 5247-5249.

82. Qi, S., Z. Wu, D. Wu, W. Yang, and R. Jin, *The chemistry involved in the loading of silver (I) into poly (amic acid) via ion exchange: A metal-ion-induced crosslinking behavior.* Polymer, 2009. **50**(3): p. 845-854.

83. Ikeda, S., K. Akamatsu, and H. Nawafune, *Direct photochemical formation of Cu patterns on surface modified polyimide resin.* Journal of Materials Chemistry, 2001. **11**(12): p. 2919-2921.

84. Ng, J.H.G., M.P.Y. Desmulliez, K.A. Prior, and D.P. Hand, *Ultra-violet direct patterning of metal on polyimide.* Micro & Nano Letters, 2008. **3**(3): p. 82-89.

85. Mallick, K., M. Witcomb, and M. Scurrell, *Silver nanoparticle catalysed redox reaction: An electron relay effect.* Materials Chemistry and Physics, 2006. **97**(2–3): p. 283-287.

86. Chen, D., Q. Lu, and Y. Zhao, *Laser-induced site-selective silver seeding on polyimide for electroless copper plating.* Applied Surface Science, 2006. **253**(3): p. 1573-1580.

87. Akamatsu, K., S. Ikeda, H. Nawafune, and H. Yanagimoto, *Direct patterning of copper on polyimide using ion exchangeable surface templates generated by site-selective surface modification.* Journal of the American Chemical Society, 2004. **126**(35): p. 10822-10823.

88. Su, W., P. Li, L. Yao, F. Yang, L. Liang, and J. Chen, *Direct Patterning of Copper on Polyimide by Site‐Selective Surface Modification via a Screen‐Printing Process.* ChemPhysChem, 2011. **12**(6): p. 1143-1147.

89. Matsumura, Y., Y. Enomoto, M. Sugiyama, K. Akamatsu, and H. Nawafune, *Direct metallization of nickel on polymeric template patterns for fabrication of copper circuits on glass substrates.* Journal of Materials Chemistry, 2008. **18**(42): p. 5078-5082.

90. Matsumura, Y., Y. Enomoto, T. Tsuruoka, K. Akamatsu, and H. Nawafune, *Fabrication of Copper Damascene Patterns on Polyimide Using Direct Metallization on Trench Templates Generated by Imprint Lithography.* Langmuir, 2010. **26**(14): p. 12448-12454.

91. Yoon, S.S., D.O. Kim, S.C. Park, Y.K. Lee, H.Y. Chae, S.B. Jung, and J.D. Nam, *Direct metallization of gold patterns on polyimide substrate by microcontact printing and selective surface modification.* Microelectronic Engineering, 2008. **85**(1): p. 136-142.

92. Cui, G., D. Wu, Y. Zhao, W. Liu, and Z. Wu, *Formation of conductive and reflective silver nanolayers on plastic films via ion doping and solid–liquid interfacial reduction at ambient temperature.* Acta Materialia, 2013. **61**(11): p. 4080-4090.

93. Ikeda, S., Y. Kobayashi, Y. Fujiwara, K. Akamatsu, and H. Nawafune. *All-Wet Metallization Process for Transparent Polyimide Films*. in *Journal of Physics: Conference Series*. 2013. IOP Publishing.

94. Kim, J.Y., T.V. Byk, S.H. Cho, C.H. Noh, K.Y. Song, J.M. Kim, and T.V. Gaevskaya, *Selective electroless deposition using photoinduced oxidation of Sn(II) compounds on surface-modified polyimide layers.* Electrochemical and Solid State Letters, 2006. **9**(12): p. H118-H122.

95. Zhan, J., G. Tian, S. Qi, Z. Wu, D. Wu, and R. Jin, *Fabrication and mechanism study of CuO layers on double surfaces of polyimide substrate using surface modification.* Composites Science and Technology, 2012. **72**(9): p. 1020-1026.

96. Cui, G., W. Liu, L. Yuan, D. Wu, and Z. Wu, *Transition of polyimide/α-Fe 2 O 3 to polyimide/Fe 3 O 4 nanocomposite films by adjusting thermal treatment surroundings of ion-doped substrates.* RSC Advances, 2013. **3**(34): p. 14390-14396.

97. Halper, S.R. and R.M. Villahermosa, *Cobalt-containing polyimides for moisture sensing and absorption.* ACS Applied Materials & Interfaces, 2009. **1**(5): p. 1041-1044.

98. Zheng, Z., Z. Wang, Q. Feng, Y. Du, and C. Wang, *Preparation of surface-silvered graphene-CNTs/polyimide hybrid films: Processing, morphology and properties.* Materials Chemistry and Physics, 2013. **138**(1): p. 350-357.

99. Han, E., D. Wu, S. Qi, G. Tian, H. Niu, G. Shang, X. Yan, and X. Yang, *Incorporation of Silver Nanoparticles into the Bulk of the Electrospun Ultrafine Polyimide Nanofibers via a Direct Ion Exchange Self-Metallization Process.* ACS Applied Materials & Interfaces, 2012. **4**(5): p. 2583-2590.

100. Song, J., J.H. Jeon, I.K. Oh, and K. Park, *Electro‐active Polymer Actuator Based on Sulfonated Polyimide with Highly Conductive Silver Electrodes Via Self‐metallization.* Macromolecular Rapid Communications, 2011. **32**(19): p. 1583-1587.

101. SeokáChi, W., J. WooáHan, D. KyuáRoh, and J. HakáKim, *Employing electrostatic self-assembly of tailored nickel sulfide nanoparticles for quasi-solid-state dye-sensitized solar cells with Pt-free counter electrodes.* Chemical Communications, 2012. **48**(76): p. 9501-9503.

102. Tian, G., D. Wu, L. Shi, S. Qi, and Z. Wu, *Nonvolatile electrical switching behavior observed in a functional polyimide thin film embedded with silver nanoparticles.* RSC Advances, 2012. **2**(26): p. 9846-9850.

103. Deng, T., F. Arias, R.F. Ismagilov, P.J. Kenis, and G.M. Whitesides, *Fabrication of metallic microstructures using exposed, developed silver halide-based photographic film.* Analytical Chemistry, 2000. **72**(4): p. 645-651.

104. Tian, B. and J. Zhang, *Morphology-controlled synthesis and applications of silver halide photocatalytic materials.* Catalysis Surveys from Asia, 2012. **16**(4): p. 210-230.

105. Matsubayashi, A., K. Fukunaga, and K. Tanaka, *Metal ions/ion clusters transport in glassy polymer films: construction of multi-layered polymer and metal composite films.* Journal of Materials Chemistry, 2012. **22**(31): p. 15578-15585.

106. Fleancu, M., N. Olteanu, C.A. Lazar, A. Meghea, and M. Mihaly, *Controlled Size Gold Nanoparticles Obtained by Tuning Synthesis Parameters in Microemulsion Templates.* REVISTA DE CHIMIE, 2013. **64**(7): p. 729-732.

107. Carp, O., C.L. Huisman, and A. Reller, *Photoinduced reactivity of titanium dioxide.* Progress in solid state chemistry, 2004. **32**(1): p. 33-177.

108. Fujishima, A., X. Zhang, and D.A. Tryk, *TiO2 photocatalysis and related surface phenomena.* Surface Science Reports, 2008. **63**(12): p. 515-582.

109. Riassetto, D., F. Roussel, L. Rapenne, H. Roussel, S. Coindeau, O. Chaix, F. Micoud, M. Chatenet, and M. Langlet, *Synthesis and functionalities of noble metal nanoparticles formed through simple all-inorganic photochemical procedures.* Journal of Experimental Nanoscience, 2010. **5**(3): p. 221-243.

110. Byk, T.V., V.G. Sokolov, T.V. Gaevskaya, E.V. Skorb, D.V. Sviridov, C.H. Noh, K.Y. Song, Y.N. Kwon, and S.H. Cho, *Photochemical selective deposition of nickel using a TiO2-Pd 21 layer.* Journal of Photochemistry and Photobiology a-Chemistry, 2008. **193**(1): p. 56-64.

111. Baum, T.H., E.E. Marinero, and C.R. Jones, *Projection printing of gold micropatterns by photochemical decomposition.* Applied Physics Letters, 1986. **49**(18): p. 1213-1215.

112. Dicks, M.H., G.M. Broxton, J. Thomson, J. Lobban, J.T.M. Stevenson, and A.J. Walton, *Characterization of platinum films produced by UV exposure of a novel photosensitive organometallic material.* Ieee Transactions on Semiconductor Manufacturing, 2004. **17**(2): p. 91-97.

113. Byun, Y., E.-C. Hwang, S.-Y. Lee, Y.-Y. Lyu, J.-H. Yim, J.-Y. Kim, S. Chang, L.S. Pu, and J.M. Kim, *Highly efficient silver patterning without photo-resist using simple silver precursors.* Materials Science and Engineering: B, 2005. **117**(1): p. 11-16.

114. Korchev, A., M. Bozack, B. Slaten, and G. Mills, *Polymer-initiated photogeneration of silver nanoparticles in SPEEK/PVA films: direct metal photopatterning.* Journal of the American Chemical Society, 2004. **126**(1): p. 10-11.

115. Bernabò, M., A. Pucci, H.H. Ramanitra, and G. Ruggeri, *Polymer nanocomposites containing anisotropic metal nanostructures as internal strain indicators.* Materials, 2010. **3**(2): p. 1461-1477.

116. Kim, S.J., C.S. Ah, and D.-J. Jang, *Laser-induced growth and reformation of gold and silver nanoparticles.* Journal of Nanoparticle Research, 2009. **11**(8): p. 2023-2030.

117. Charbonnier, M., M. Romand, and Y. Goepfert, *Ni direct electroless metallization of polymers by a new palladium-free process.* Surface and Coatings Technology, 2006. **200**(16): p. 5028-5036.

118. Lee, S.W., D. Liang, X. Gao, and R.M. Sankaran, *Direct writing of metal nanoparticles by localized plasma electrochemical reduction of metal cations in polymer films.* Advanced Functional Materials, 2011. **21**(11): p. 2155-2161.

119. Grzelczak, M. and L.M. Liz-Marzán, *The relevance of light in the formation of colloidal metal nanoparticles.* Chemical Society Reviews, 2014.

120. Sakamoto, M., M. Fujistuka, and T. Majima, *Light as a construction tool of metal nanoparticles: synthesis and mechanism.* Journal of Photochemistry and Photobiology C: Photochemistry Reviews, 2009. **10**(1): p. 33-56.

121. Martin, G.D., S.D. Hoath, and I.M. Hutchings. *Inkjet printing-the physics of manipulating liquid jets and drops.* in *Journal of Physics: Conference Series*. 2008. IOP Publishing.

122. Derby, B., *Inkjet printing of functional and structural materials: fluid property requirements, feature stability, and resolution.* Annual Review of Materials Research, 2010. **40**: p. 395-414.

123. Chen, C., C. Chen, T.-Y. Dong, T. Chang, M. Chen, H. Chen, and I. Chen, *Using nanoparticles as direct-injection printing ink to fabricate conductive silver features on a transparent flexible PET substrate at room temperature.* Acta Materialia, 2012. **60**(16): p. 5914-5924.

124. Wu, J.-T., S.L.-C. Hsu, M.-H. Tsai, and W.-S. Hwang, *Inkjet printing of low-temperature cured silver patterns by using AgNO3/1-dimethylamino-2-propanol inks on polymer substrates.* The Journal of Physical Chemistry C, 2011. **115**(22): p. 10940-10945.

125. Wu, J.-T., S.L.-C. Hsu, M.-H. Tsai, and W.-S. Hwang, *Direct inkjet printing of silver nitrate/poly (N-vinyl-2-pyrrolidone) inks to fabricate silver conductive lines.* The Journal of Physical Chemistry C, 2010. **114**(10): p. 4659-4662.

126. Lee, Y.-I. and Y.-H. Choa, *Adhesion enhancement of ink-jet printed conductive copper patterns on a flexible substrate.* Journal of Materials Chemistry, 2012. **22**(25): p. 12517-12522.

127. Choi, K.H., M. Zubair, and H.W. Dang, *Characterization of flexible temperature sensor fabricated through drop-on-demand electrohydrodynamics patterning.* Japanese Journal of Applied Physics, 2014. **53**(5S3): p. 05HB02.

128. Murata, K. *Direct fabrication of super-fine wiring and bumping by using inkjet process*. in *Polymers and Adhesives in Microelectronics and Photonics, 2007. Polytronic 2007. 6th International Conference on*. 2007. IEEE.

129. Mahajan, A., C.D. Frisbie, and L.F. Francis, *Optimization of Aerosol Jet Printing for High-Resolution, High-Aspect Ratio Silver Lines.* ACS Applied Materials & Interfaces, 2013. **5**(11): p. 4856-4864.

130. Optomec, *Aerosol Jet® Printed Electronics Overview (white paper)*, online: http://www.optomec.com/whitepapers.

131. Jones, C.S., X. Lu, M. Renn, M. Stroder, and W.-S. Shih, *Aerosol-jet-printed, high-speed, flexible thin-film transistor made using single-walled carbon nanotube solution.* Microelectronic Engineering, 2010. **87**(3): p. 434-437.

132. Ha, M., J.-W.T. Seo, P.L. Prabhumirashi, W. Zhang, M.L. Geier, M.J. Renn, C.H. Kim, M.C. Hersam, and C.D. Frisbie, *Aerosol Jet Printed, Low Voltage, Electrolyte Gated Carbon Nanotube Ring Oscillators with Sub-5 μs Stage Delays.* Nano Letters, 2013. **13**(3): p. 954-960.

133. Yang, C., E. Zhou, S. Miyanishi, K. Hashimoto, and K. Tajima, *Preparation of Active Layers in Polymer Solar Cells by Aerosol Jet Printing.* ACS Applied Materials & Interfaces, 2011. **3**(10): p. 4053-4058.

134. Li, S., J.G. Park, S. Wang, R. Liang, C. Zhang, and B. Wang, *Working mechanisms of strain sensors utilizing aligned carbon nanotube network and aerosol jet printed electrodes.* Carbon, 2014. **73**(0): p. 303-309.

135. Hoey, J.M., A. Lutfurakhmanov, D.L. Schulz, and I.S. Akhatov, *A review on aerosol-based direct-write and its applications for microelectronics.* Journal of Nanotechnology, 2012. **2012**.

Chapter 3

136. Redinger, D.H., *Solution processing techniques for low-cost circuit fabrication*. Vol. 68. 2006.

137. Washio, I., Y. Xiong, Y. Yin, and Y. Xia, *Reduction by the end groups of poly (vinyl pyrrolidone): a new and versatile route to the kinetically controlled synthesis of Ag triangular nanoplates.* Advanced Materials, 2006. **18**(13): p. 1745-1749.

138. Ayyappan, S., R.S. Gopalan, G. Subbanna, and C. Rao, *Nanoparticles of Ag, Au, Pd, and Cu produced by alcohol reduction of the salts.* Journal of Materials Research, 1997. **12**(02): p. 398-401.

139. Srinivasan, R., R.R. Hall, W.D. Loehle, W.D. Wilson, and D.C. Allbee, *Chemical transformations of the polyimide Kapton brought about by ultraviolet laser radiation.* Journal of Applied Physics, 1995. **78**(8): p. 4881-4887.

140. Website. *PK Plating Tech*. 2013; Available from: http://pkplatingtech.com/.

141. Datasheet, *Kapton HN Technical Data Sheet*, DuPont, Editor 2011, DuPont.

142. Ortelli, E.E., F. Geiger, T. Lippert, J. Wei, and A. Wokaun, *UV-laser-induced decomposition of Kapton studied by infrared spectroscopy.* Macromolecules, 2000. **33**(14): p. 5090-5097.

143. Srinivasan, R., *Etching polymer films with ultraviolet laser pulses of long (10–400 μs) duration.* Journal of Applied Physics, 1992. **72**(4): p. 1651-1653.

144. Kim, Y.-H., G. Walker, J. Kim, and J. Park, *Adhesion and interface studies between copper and polyimide.* Journal of Adhesion Science and Technology, 1987. **1**(1): p. 331-339.

145. Southward, R.E., C.M. Boggs, D.W. Thompson, and A.K. St. Clair, *Synthesis of Surface-Metallized Polyimide Films via in Situ Reduction of (Perfluoroalkanoato)silver(I) Complexes in a Poly(amic acid) Precursor.* Chem. Mater., 1998. **10**(5): p. 1408-1421.

146. Hill, D.J.T., F.A. Rasoul, J.S. Forsythe, J.H. O'Donnell, P.J. Pomery, G.A. George, P.R. Young, and J.W. Connell, *Effect of simulated low earth orbit radiation on polyimides (UV degradation study).* Journal of Applied Polymer Science, 1995. **58**(10): p. 1847-1856.

147. Liou, H.-C., P.S. Ho, and R. Stierman, *Thickness dependence of the anisotropy in thermal expansion of PMDA-ODA and BPDA-PDA thin films.* Thin Solid Films, 1999. **339**(1): p. 68-73.

148. Thompson, D.S., L.M. Davis, D.W. Thompson, and R.E. Southward, *Single-Stage Synthesis and Characterization of Reflective and Conductive Silver Polyimide Films Prepared from Silver(I) Complexes with ODPA/4,4,-ODA.* ACS Applied Materials & Interfaces, 2009. **1**(7): p. 1457-1466.

149. Dinetz, S.F., E.J. Bird, R.L. Wagner, and A.W. Fountain, *A comparative study of the gaseous products generated by thermal and ultra-violet laser pyrolyses of the polyimide PMDA-ODA.* Journal of Analytical and Applied Pyrolysis, 2002. **63**(2): p. 241-249.

150. Sazanov, Y.N., A.V. Gribanov, and V.A. Lysenko, *The role of nitrogen atoms in forming the carbon structure in the carbonization of polymer composites.* Fibre Chemistry, 2008. **40**(4): p. 355-364.

151. Dumont, T., R. Bischofberger, T. Lippert, and A. Wokaun, *Gravimetric and profilometric measurements of the ablation rates of photosensitive polymers at different wavelengths.* Applied Surface Science, 2005. **247**(1-4): p. 115-122.

152. Ortelli, E.E., F. Geiger, T. Lippert, and A. Wokaun, *Pyrolysis of Kapton in Air: An in Situ DRIFT Study.* Applied Spectroscopy, 2001. **55**(4): p. 412-419.

153. Young, J.T., W.H. Tsai, and F.J. Boerio, *CHARACTERIZATION OF THE INTERFACE BETWEEN PYROMELLITIC DIANHYDRIDE OXYDIANILINE POLYIMIDE AND SILVER USING SURFACE-ENHANCED RAMAN-SCATTERING.* Macromolecules, 1992. **25**(2): p. 887-894.

154. Kumar, V., R. Singh, and S.K. Chakarvarti, *Novel electroless template based synthesis of silver microtubules and their characterization.* Digest Journal of Nanomaterials and Biostructures, 2007. **2**(1): p. 163-167.

155. Hashimoto, Y., Y. Matsuo, and K. Ijiro, *Fabrication of silver nanowires by selective electroless plating of DNA stretched using the LB method.* Chemistry Letters, 2005. **34**(1): p. 112-113.

Chapter 4

156. Ikeda, S., H. Yanagimoto, K. Akamatsu, and H. Nawafune, *Copper/polyimide heterojunctions: Controlling interfacial structures through an additive-based, all-wet chemical process using ion-doped precursors.* Advanced Functional Materials, 2007. **17**(6): p. 889-897.

157. Yang, F., W. Su, L.B. Yao, L.F. Liang, Y.X. Liu, S.J. Yu, and Y.F. Zhu, *Screen-Printing-Based Fabrication of Silver Patterns on Polyimide Substrate.* Advanced Materials Research, 2012. **510**: p. 176-181.

158. Homma, T., A. Tamaki, H. Nakai, and T. Osaka, *Molecular orbital study on the reaction process of dimethylamine borane as a reductant for electroless deposition.* Journal of Electroanalytical Chemistry, 2003. **559**(0): p. 131-136.

159. Sadik, O.A., H. Xu, and A. Sargent, *Multi-electron transfer mechanism of dimethylamine borane in electroless gold deposition.* Journal of Electroanalytical Chemistry, 2005. **583**(2): p. 167-175.

160. Stoffel, N.C., M. Hsieh, S. Chandra, and E.J. Kramer, *Surface Modification Studies of Polyimide Films Using Rutherford Backscattering and Forward Recoil Spectrometry.* Chemistry of Materials, 1996. **8**(5): p. 1035-1041.

161. Bulletin. *GS-96-7*. 2013 [cited 2014; Available from: http://www.cirlex.com/pdf/Kapton_General_Properties.pdf.

162. Mu, S., Z. Wu, S. Qi, D. Wu, and W. Yang, *Preparation of electrically conductive polyimide/silver composite fibers via in-situ surface treatment.* Materials Letters, 2010. **64**(15): p. 1668-1671.

163. Website. *Photoresist Developers*. 2013; Available from: http://www.azem.com/en/Products/Litho-technology/Photoresist Developers.aspx.

164. Website. *Photoresist Strippers*. 2013; Available from: http://www.azem.com/en/Products/Litho-technology/Photoresist Strippers.aspx.

165. Website. *N-Methylpyrrolidone (NMP)*. 2013; Available from: http://www2.basf.us/diols/bcdiolsnmp.html.

166. Lacrotte, Y., J.P. Carr, R.W. Kay, and M.P.Y. Desmulliez. *LTCC package manufacturing using powder blasting technology*. in *Design, Test, Integration and Packaging of MEMS/MOEMS (DTIP), 2012 Symposium on*. 2012.

167. Lacrotte, Y., J. Carr, R. Kay, and M.Y. Desmulliez, *Fabrication of a low temperature co-fired ceramic package using powder blasting technology.* Microsystem Technologies, 2013. **19**(6): p. 791-799.

168. Sayah, A., V. Parashar, A.-G. Pawlowski, and M. Gijs, *Elastomer mask for powder blasting microfabrication.* Sensors and Actuators A: Physical, 2005. **125**(1): p. 84-90.

169. Sayah, A., P.-A. Thivolle, V.K. Parashar, and M.A. Gijs, *Three-dimensional mixers with non-planar microchannels in a monolithic glass substrate using oblique powder blasting.* Journal of Micromechanics and Microengineering, 2010. **20**(8): p. 085028.

170. Sayah, A., V.K. Parashar, and M.A.M. Gijs, *LF55GN Photosensitive Flexopolymer: A New Material for Ultrathick and High-Aspect-Ratio MEMS Fabrication.* Microelectromechanical Systems, Journal of, 2007. **16**(3): p. 564-570.

171. Jungkwun, K., C. Xiaoyu, A. Hyochun, D.S. Elles, and Y. Yong-Kyu. *Lithographically defined integrable air-lifted bow-tie antennas*. in *Micro Electro Mechanical Systems (MEMS), 2010 IEEE 23rd International Conference on*. 2010.

172. Kim, Y.H., J. Kim, G.F. Walker, C. Feger, and S.P. Kowalczyk, *Adhesion and interface investigation of polyimide on metals.* Journal of Adhesion Science and Technology, 1988. **2**(1): p. 95-105.

Chapter 5

173. Rasmussen, K., G. Grampp, M.v. Eesbeek, and T. Rohr, *Thermal and UV degradation of polymer films studied in situ with ESR spectroscopy.* ACS Applied Materials & Interfaces, 2010. **2**(7): p. 1879-1883.

174. Coburn, J.C. and M.T. Pottiger, *Thermal curing in polyimide films and coatings*, in *Polyimides: fundamentals and applications*, M. Ghosh, Editor 1996, CRC Press. p. 226-227.

175. Hasegawa, M. and K. Horie, *Photophysics, photochemistry, and optical properties of polyimides.* Progress in Polymer Science, 2001. **26**(2): p. 259-335.

176. Bolton, J.R., *Solar energy conversion in photosynthesis—features relevant to artificial systems for the photochemical conversion of solar energy*, in *Solar Energy*1979, Springer. p. 31-50.

177. Blankenship, R.E., D.M. Tiede, J. Barber, G.W. Brudvig, G. Fleming, M. Ghirardi, M.R. Gunner, W. Junge, D.M. Kramer, A. Melis, T.A. Moore, C.C. Moser, D.G. Nocera, A.J. Nozik, D.R. Ort, W.W. Parson, R.C. Prince, and R.T. Sayre, *Comparing Photosynthetic and Photovoltaic Efficiencies and Recognizing the Potential for Improvement.* Science, 2011. **332**(6031): p. 805-809.

178. Son, H.-J., S. Jin, S. Patwardhan, S.J. Wezenberg, N.C. Jeong, M. So, C.E. Wilmer, A.A. Sarjeant, G.C. Schatz, and R.Q. Snurr, *Light-harvesting and ultrafast energy migration in porphyrin-based metal–organic frameworks.* Journal of the American Chemical Society, 2013. **135**(2): p. 862-869.

179. Koning, R.E. *Light. Plant Physiology Information Website*. 1994 [cited 2014 10th July]; Available from: http://plantphys.info/plant_physiology/light.shtml.

180. Mallick, K., M. Witcomb, and M. Scurrell, *Polymer stabilized silver nanoparticles: A photochemical synthesis route.* Journal of Materials Science, 2004. **39**(14): p. 4459-4463.

181. Li, Y., Q. Lu, X. Qian, Z. Zhu, and J. Yin, *Preparation of surface bound silver nanoparticles on polyimide by surface modification method and its application on electroless metal deposition.* Applied Surface Science, 2004. **233**(1): p. 299-306.

182. Ankireddy, K., S. Vunnam, J. Kellar, and W. Cross, *Highly conductive short chain carboxylic acid encapsulated silver nanoparticle based inks for direct write technology applications.* Journal of Materials Chemistry C, 2013. **1**(3): p. 572-579.

183. Kang, B.J. and J.H. Oh, *Geometrical characterization of inkjet-printed conductive lines of nanosilver suspensions on a polymer substrate.* Thin Solid Films, 2010. **518**(10): p. 2890-2896.

184. Rycenga, M., C.M. Cobley, J. Zeng, W. Li, C.H. Moran, Q. Zhang, D. Qin, and Y. Xia, *Controlling the synthesis and assembly of silver nanostructures for plasmonic applications.* Chemical Reviews, 2011. **111**(6): p. 3669-3712.

185. Sudeep, P. and P.V. Kamat, *Photosensitized growth of silver nanoparticles under visible light irradiation: a mechanistic investigation.* Chemistry of Materials, 2005. **17**(22): p. 5404-5410.

186. Lim, S.K., K.J. Chung, C. Kim, D.W. Shin, Y.-H. Kim, and C.S. Yoon, *Surface-plasmon resonance of Ag nanoparticles in polyimide.* Journal of Applied Physics, 2005. **98**(8): p. 084309-084309-4.

187. Mock, J., M. Barbic, D. Smith, D. Schultz, and S. Schultz, *Shape effects in plasmon resonance of individual colloidal silver nanoparticles.* The Journal of Chemical Physics, 2002. **116**(15): p. 6755-6759.

188. Alan-Creighton, J., *Ultraviolet–visible absorption spectra of the colloidal metallic elements.* Journal of the Chemical Society, Faraday Transactions, 1991. **87**(24): p. 3881-3891.

189. Pyun, E., R.J. Mathisen, and C.S.P. Sung, *Kinetics and mechanisms of thermal imidization of a polyamic acid studied by ultraviolet-visible spectroscopy.* Macromolecules, 1989. **22**(3): p. 1174-1183.

190. Pal, A., S. Shah, and S. Devi, *Microwave-assisted synthesis of silver nanoparticles using ethanol as a reducing agent.* Materials Chemistry and Physics, 2009. **114**(2): p. 530-532.

191. Zhang, A., J. Zhang, and Y. Fang, *Photoluminescence from colloidal silver nanoparticles.* Journal of Luminescence, 2008. **128**(10): p. 1635-1640.

Chapter 6

192. Cheng, K., M.H. Yang, W.W.W. Chiu, C.Y. Huang, J. Chang, T.F. Ying, and Y. Yang, *Ink-Jet Printing, Self-Assembled Polyelectrolytes, and Electroless Plating: Low Cost Fabrication of Circuits on a Flexible Substrate at Room Temperature.* Macromolecular Rapid Communications, 2005. **26**(4): p. 247-264.

193. Cui, W., W. Lu, Y. Zhang, G. Lin, T. Wei, and L. Jiang, *Gold nanoparticle ink suitable for electric-conductive pattern fabrication using in ink-jet printing technology.* Colloids and Surfaces A: Physicochemical and Engineering Aspects, 2010. **358**(1-3): p. 35-41.

194. Dos Santos Ferreira, O., A. Stevens, and C. Schrauwen, *Quantitative comparison of adhesion in metal-to-plastic systems.* Thin Solid Films, 2009. **517**(10): p. 3070-3074.

195. Kato, Y., K. Maki, S. Furukawa, and M. Kashino, *A Photosensitive Polyimide based Method for an Easy Fabrication of Multichannel Neural Electrodes*, in *30th Annual International IEEE EMBS Conference*2008, IEEE: Vancouver, BC. p. 5802-5805.

196. Carroccio, S., C. Puglisi, and G. Montaudo, *Thermal degradation mechanisms of polyetherimide investigated by direct pyrolysis mass spectrometry.* Macromol. Chem. Phys., 1999. **200**: p. 2345-2355.

197. Carroccio, S., C. Puglisi, and G. Montaudo, *Photo-oxidation products of polyetherimide ULTEM determined by MALDI-TOF-MS. Kinetics and mechanisms.* Polymer Degradation and Stability, 2003. **80**: p. 459-476.

198. Gaikwad, A.V. and T.K. Rout, *In situ synthesis of silver nanoparticles in polyetherimide matrix and its application in coatings.* J. Mater. Chem., 2011. **21**: p. 1234-1239.

199. Kim, S.-Y. and K.-H. Lee, *Effects of chemical transition of polyetherimide membranes having an integrally skinned asymmetric structure.* Current Applied Physics, 2009. **9**: p. e51-e55.

200. Eisenbarth, M. and K. Feldmann. *Pressfit technology for 3-D molded interconnect devices (MID) - A lead-free alternative to solder joints - challenges and solutions concepts*. in *Electronics Manufacturing Technology Symposium, 2002. IEMT 2002. 27th Annual IEEE/SEMI International*. 2002.

201. Antony, J., *Design of experiments for engineers and scientists*. Vol. 26. 2003: Butterworth-Heinemann.

202. Hsiao, Y.-S., W.-T. Whang, S.-C. Wu, and K.-R. Chuang, *Chemical formation of palladium-free surface-nickelized polyimide film for flexible electronics.* Thin Solid Films, 2008: p. 4258–4266.

203. Coates, J., *Interpretation of infrared spectra, a practical approach.* Encyclopedia of analytical chemistry, 2000.

204. JCPDS, *(Standard silver crystal). International Centre for Diffraction Data. Available:* http://www.icdd.com. card 4-0783.

205. Patterson, A.L., *The Scherrer Formula for X-Ray Particle Size Determination.* Physical Review, 1939. **56**(10): p. 978-982.

Chapter 7

206. Lee, H.-K., S.-H. Son, H.-Y. Lee, and S.-B. Koo, *Adhesion Enhancement of Electroplated Cu/Electroless Ni Composite Layer to (PMDA-ODA)-Type Polyimide Films.* Journal of Adhesion Science and Technology, 2008. **22**(1): p. 47-64.

207. Kim, B.-H., H. Park, H. Park, and D.C. Moon, *Degree of imidization for polyimide films investigated by evolved gas analysis-mass spectrometry.* Thermochimica Acta, 2013. **551**: p. 184-190.

208. Qi, S., Z. Wu, D. Wu, and R. Jin, *Controlled Formation of optically reflective and electrically conductive silvered surfaces on polyimide film via a direct ion-exchange self-metallization technique using silver ammonia complex cation as the precursor.* The Journal of Physical Chemistry B, 2008. **112**(18): p. 5575-5584.

209. Ishida, Y., T. Shimada, D. Masui, H. Tachibana, H. Inoue, and S. Takagi, *Efficient excited energy transfer reaction in clay/porphyrin complex toward an*

artificial light-harvesting system. Journal of the American Chemical Society, 2011. **133**(36): p. 14280-14286.

210. Hingorani, K., R. Pace, S. Whitney, J.W. Murray, P. Smith, M.H. Cheah, T. Wydrzynski, and W. Hillier, *Photo-oxidation of tyrosine in a bio-engineered bacterioferritin 'reaction centre'–a protein model for artificial photosynthesis.* Biochimica et Biophysica Acta (BBA)-Bioenergetics, 2014.

211. Yamano, Y., C. Tode, and M. Ito, *Carotenoids and related polyenes. Part 3. First total synthesis of fucoxanthin and halocynthiaxanthin using oxo-metallic catalyst.* Journal of the Chemical Society, Perkin Transactions 1, 1995(15): p. 1895-1904.

212. Kang, J., J. Ryu, H. Kim, and H. Hahn, *Sintering of inkjet-printed silver nanoparticles at room temperature using intense pulsed light.* Journal of electronic materials, 2011. **40**(11): p. 2268-2277.

213. Hou, W.-C., B. Stuart, R. Howes, and R.G. Zepp, *Sunlight-driven reduction of silver ions by natural organic matter: formation and transformation of silver nanoparticles.* Environmental science & technology, 2013. **47**(14): p. 7713-7721.

214. Hautala, R.R., R.B. King, and C. Kutal, *Solar energy: Chemical conversion and storage.* Solar Energy: Chemical Conversion and Storage, 1979. **1**.

215. McDermott, G., S. Prince, A. Freer, A. Hawthornthwaite-Lawless, M. Papiz, R. Cogdell, and N. Isaacs, *Crystal structure of an integral membrane light-harvesting complex from photosynthetic bacteria.* Nature, 1995. **374**(6522): p. 517-521.

216. van Grondelle, R. and V.I. Novoderezhkin, *Energy transfer in photosynthesis: experimental insights and quantitative models.* Physical Chemistry Chemical Physics, 2006. **8**(7): p. 793-807.

217. Carmeli, I., I. Lieberman, L. Kraversky, Z. Fan, A.O. Govorov, G. Markovich, and S. Richter, *Broad band enhancement of light absorption in photosystem I by metal nanoparticle antennas.* Nano Letters, 2010. **10**(6): p. 2069-2074.

218. Barber, J., *Photosystem II: Its function, structure, and implications for artificial photosynthesis.* Biochemistry (Moscow), 2014. **79**(3): p. 185-196.

219. van Amerongen, H. and R. van Grondelle, *Understanding the energy transfer function of LHCII, the major light-harvesting complex of green plants.* The Journal of Physical Chemistry B, 2001. **105**(3): p. 604-617.

220. Jahns, P. and A.R. Holzwarth, *The role of the xanthophyll cycle and of lutein in photoprotection of photosystem II.* Biochimica et Biophysica Acta (BBA)-Bioenergetics, 2012. **1817**(1): p. 182-193.

221. Müller, P., X.-P. Li, and K.K. Niyogi, *Non-photochemical quenching. A response to excess light energy.* Plant Physiology, 2001. **125**(4): p. 1558-1566.

222. Shen, F.-Y., S.-E. Huang, and W.-P. Dow, *Silver Metallization of Polyimide Surfaces Using Environmentally Friendly Reducing Agents.* ECS Electrochemistry Letters, 2013. **2**(11): p. D45-D48.

223. Stamplecoskie, K.G. and J.C. Scaiano, *Light emitting diode irradiation can control the morphology and optical properties of silver nanoparticles.* Journal of the American Chemical Society, 2010. **132**(6): p. 1825-1827.

224. Bordenave, M.D., A.F. Scarpettini, M.V. Roldán, N. Pellegri, and A.V. Bragas, *Plasmon-induced photochemical synthesis of silver triangular prisms and pentagonal bipyramids by illumination with light emitting diodes.* Materials Chemistry and Physics, 2013. **139**(1): p. 100-106.

225. Kamat, P.V., M. Flumiani, and G.V. Hartland, *Picosecond dynamics of silver nanoclusters. Photoejection of electrons and fragmentation.* The Journal of Physical Chemistry B, 1998. **102**(17): p. 3123-3128.

226. Brockman, J.M., B.P. Nelson, and R.M. Corn, *Surface plasmon resonance imaging measurements of ultrathin organic films.* Annual review of physical chemistry, 2000. **51**(1): p. 41-63.

227. Hao, F., C.L. Nehl, J.H. Hafner, and P. Nordlander, *Plasmon resonances of a gold nanostar.* Nano Letters, 2007. **7**(3): p. 729-732.

228. Hagfeldt, A. and M. Graetzel, *Light-Induced Redox Reactions in Nanocrystalline Systems.* Chemical Reviews, 1995. **95**(1): p. 49-68.

229. Wei, H., A. Reyes-Coronado, P. Nordlander, J. Aizpurua, and H. Xu, *Multipolar plasmon resonances in individual Ag nanorice.* Acs Nano, 2010. **4**(5): p. 2649-2654.

230. Fritsch, J., F.M. Wisser, K. Eckhardt, V. Bon, G. Mondin, B. Schumm, J. Grothe, and S. Kaskel, *A new molecular silver precursor for the preparation of thin conductive silver films.* Journal of Physics and Chemistry of Solids, 2013. **74**(11): p. 1546-1552.

231. Magdassi, S., M. Grouchko, O. Berezin, and A. Kamyshny, *Triggering the sintering of silver nanoparticles at room temperature.* Acs Nano, 2010. **4**(4): p. 1943-1948.

232. Perelaer, J., B.J. de Gans, and U.S. Schubert, *Ink‐jet printing and microwave sintering of conductive silver tracks.* Advanced Materials, 2006. **18**(16): p. 2101-2104.

233. Ha, K. and J.L. West, *Studies on the photodegradation of polarized UV‐exposed PMDA‐ODA polyimide films.* Journal of Applied Polymer Science, 2002. **86**(12): p. 3072-3077.

234. Son, P.K., J.H. Park, B.K. Jo, S.P. Lee, J.H. Lee, J.C. Kim, T.-H. Yoon, T.J. Lee, and M. Ree, *Anisotropy and Raman absorption of the polyimide surface irradiated by the ion beam for liquid crystal alignment.* Thin Solid Films, 2009. **517**(5): p. 1803-1806.

235. Hirosawa, I. and N. Sasaki, *Influence of annealing on molecular orientation of rubbed polyimide film observed by reflection ellipsometry.* Japanese Journal of Applied Physics, 1997. **36**(part 1): p. 6953-6956.

236. Suzuki, M., T. Maruno, F. Yamamoto, and K. Nagai, *Surface roughness of rubbed polyimide film for liquid crystals by scanning tunneling microscopy.* Journal of Vacuum Science & Technology A, 1990. **8**(1): p. 631-634.

237. Pidduck, A., G. Bryan ‐ Brown, S. Haslam, R. Bannister, I. Kitely, T. McMaster, and L. Boogaard, *Atomic force microscopy studies of rubbed polyimide surfaces used for liquid crystal alignment.* Journal of Vacuum Science & Technology A, 1996. **14**(3): p. 1723-1728.

238. He, Y., Z. Du, H. Lv, Q. Jia, Z. Tang, X. Zheng, K. Zhang, and F. Zhao, *Green synthesis of silver nanoparticles by Chrysanthemum morifolium Ramat. extract and their application in clinical ultrasound gel.* International journal of nanomedicine, 2013. **8**: p. 1809.

239. Johnson, L., W. Thielemans, and D.A. Walsh, *Synthesis of carbon-supported Pt nanoparticle electrocatalysts using nanocrystalline cellulose as reducing agent.* Green Chemistry, 2011. **13**(7): p. 1686-1693.

240. Sallum, L.F., F.L.F. Soares, J.A. Ardila, and R.L. Carneiro, *Optimization of SERS scattering by Ag-NPs-coated filter paper for quantification of nicotinamide in a cosmetic formulation.* Talanta, 2014. **118**: p. 353-358.

241. Kontturi, E., P.C. Thüne, and J. Niemantsverdriet, *Cellulose model surfaces simplified preparation by spin coating and characterization by X-ray photoelectron spectroscopy, infrared spectroscopy, and atomic force microscopy.* Langmuir, 2003. **19**(14): p. 5735-5741.

242. Abdul Khalil, H., A. Bhat, and A. Ireana Yusra, *Green composites from sustainable cellulose nanofibrils: a review.* Carbohydrate Polymers, 2012. **87**(2): p. 963-979.